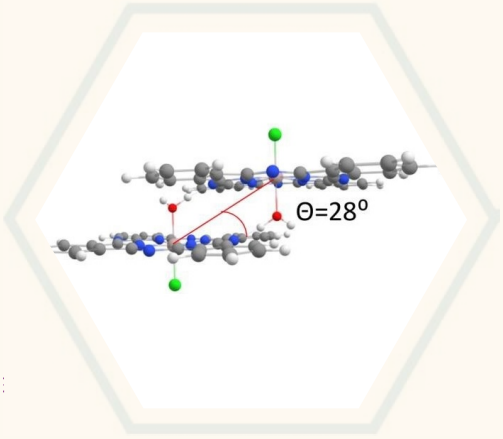
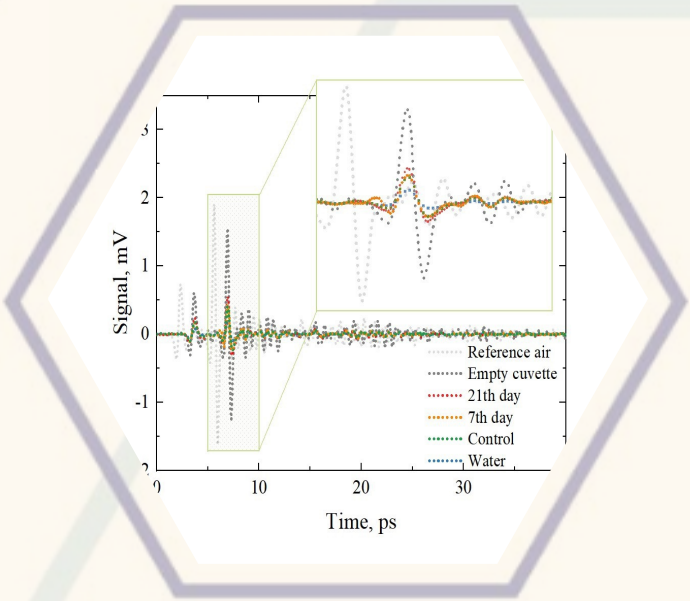
Vol 9, No 3, 2023

Journal of Biomedical Photonics & Engineering





Editor-In-Chief:
Valery Tuchin

Guest Editors:
Ammasi Periasamy,
Murukeshan Vadakke Matham,
and Santhosh Chidangil

©2023 J-BPE

Journal of Biomedical Photonics & Engineering

by Samara National Research University

Volume 9, Issue 3 (September 2023)

Guest Editors

Ammasi Periasamy
University of Virginia, U.S.A
Murukeshan Vadakke Matham
Nanyang Technological University, Singapore
Santhosh Chidangil
Manipal Academy of Higher Education, India

Editor-In-Chief

Valery V. Tuchin - Saratov National Research State University, Russian Federation;
Institute of Precision Mechanics and Control RAS, Russian Federation; a corr.-member of RAS

Deputy Editor-In-Chief

Valery P. Zakharov - Samara National Research University, Russian Federation

Postal address:
39B Lukacheva st., room #301
Samara 443086, Russian Federation

Used Figures from this issue on the Cover

Inna V. Klimenko et al. Molecular Aggregation of Aluminum Phthalocyanine Chloride in Organic and Water-Organic Media, 030301, Fig. 7(a).

Olga P. Cherkasova et al. Terahertz Spectroscopy of Mouse Blood Serum in the Dynamics of Experimental Glioblastoma, 030308, Fig. 1.

© 2023 J-BPE

Contents

Reviews

Nonlinear Optics of Skin: Enhancement of Autofluorescence and Second Harmonic Generation Signals by Immersion Optical Clearing 030201
Anton Yu. Sdobnov, Jurgen Lademann, Valery V. Tuchin, and Maxim Darvin

Articles

Molecular Aggregation of Aluminum Phthalocyanine Chloride in Organic and Water-Organic Media 030301
Inna V. Klimenko, Tatiana Yu. Astakhova, Elena N. Timokhina, and Anton V. Lobanov

Analysis of Medical Images Classification Methods: the Case of Neutrophil Nuclei 030302
Anna V. Neupokoeva, Semen A. Naydenov, and Elena V. Shevchenko

Estimating of Fraction of Weakly Deformable Erythrocytes in a Blood Sample Based on the Method of Laser Ektacytometry and a Database of Simulated Diffraction Patterns 030303
Vladislav D. Ustinov, Evgeniy G. Tsybrov, and Sergey Y. Nikitin

High-Resolution Ultra-Spectral Imager for Advanced Imaging in Agriculture and Biomedical Applications 030304
Maria M. Antony, C. S. Suchand Sandeep, Hoong-Ta Lim, and Murukeshan Vadakke Matham

C-MEMS Derived Glassy Carbon Glucose Sensor 030305
Naresh Mandal and Bidhan Pramanick

Lossy Mode Resonance Based Fiber Optic Sensor for the Detection of Acetone Concentration 030306
Asokan Prasanth, Varadharajan Kanchana Harini, Mohan Velumani, Subramaniyam Narasimman, and Zachariah C. Alex

The Role of Sm^{3+} Energy Transfer on White Emission of $La_{1.98}Dy_{0.02}MgTiO_6$ Double Perovskite Nano-Phosphors for Endoscopy and Laparoscopy LEDs 030307
Veena Vannadil Puthiyaveetil, Shilpa Cherlan Kottianmadathil, Jasira Seere Valappil, and Nissamudeen Kavukuzhi Meerasahib

Terahertz Spectroscopy of Mouse Blood Serum in the Dynamics of Experimental Glioblastoma 030308
Olga P. Cherkasova, Maria R. Konnikova, Maksim M. Nazarov, Denis A. Vrazhnov, Yury V. Kistenev, and Alexander P. Shkurinov

Fabrication of Polyvinyl Alcohol Doped CuO Thin Films for Improved Amperometric-Non Enzymatic Hydrogen Peroxide Sensing 030309
Navashree Nagarajan and Parthasarathy Panchatcharam

Concentration Dependent Thermal Diffusivity of Mn3O4 Nanoparticles Using Dual Beam Thermal Lens Technique 030310
Jayaprasad K. V., Titu Thomas, Manu Vaishakh, and Sheenu Thomas

Silver Anchored α-MnO_2 Nanorods Based SERS Substrates for Salivary Thiocyanate Detection and Application in Oral Cancer Diagnosis 030311
Navami Sunil, Rajesh Unnathpadi, and Biji Pullithadathil

Laser-Induced Crystallization of Standard Proteins on Ultra-Hydrophobic Surface and Characterization Using Raman Spectroscopy 030312
B. Sudarshan Acharya, Sajan D. George, and Abdul Ajees Abdul Salam

 © 2023 J-BPE

Cardiovascular Marker Proteins Detection in the Blood Serum Using an LSPR Chip Based on Au Nanobipyramid 030313
Prajna N. D., Tom Devasia, and Rajeev K. Sinha

Motion Estimation of Handheld Optical Coherence Tomography System Using Real-Time Eye Tracking System 030314
Abira Bright B., Lakshmi Parvathi M., and Vani Damodaran

Differences in the Effect of 40%-Glucose on the Optical Properties of Healthy and Stromal-Sarcoma Ovaries in Cats 030315
Aleksey A. Selifonov and Valery V. Tuchin

Spectrometer Design for an 840 nm Spectral Domain Optical Coherence Tomography System 030316
Lakshmi Parvathi M., Abira Bright B., and Vani Damodaran

Design of a Photonic Integrated Device with an on-Chip k-Clock and Tunable Reference Arm for Swept-Source Optical Coherence Tomography 030317
Ivan V. Stepanov, Evgeniy A. Talynev, Anton A. Ivanov, Ruslan V. Kutluyarov, and Elizaveta P. Grakhova

 © 2023 J-BPE

Nonlinear Optics of Skin: Enhancement of Autofluorescence and Second Harmonic Generation Signals by Immersion Optical Clearing

Anton Yu. Sdobnov[1*], Jurgen Lademann[2], Valery V. Tuchin[3,4,5], and Maxim E. Darvin[2]

[1] Faculty of Information Technology and Electrical Engineering, University of Oulu, 1 Pentti Kaiteran katu, Oulu 90570, Finland

[2] Center of Experimental and Applied Cutaneous Physiology (CCP), Department of Dermatology, Venerology and Allergology, Charité – Universitätsmedizin Berlin, corporate member of Freie Universität Berlin and Humboldt-Universität zu Berlin, 1 Charitéplatz, Berlin 10117, Germany

[3] Science Medical Center and Institute of Physics, Saratov State University, 83 Astrahanskaya str., Saratov 410026, Russia

[4] Laboratory of Laser Molecular Imaging and Machine Learning, Tomsk State University, 36 Lenin Ave., Tomsk 634050, Russia

[5] Institute of Precision Mechanics and Control, FRC "Saratov Scientific Centre of the Russian Academy of Sciences", 24 Rabochaya str., Saratov 410028, Russia

***e-mail:** sdobnovanton@mail.ru

Abstract. Multiphoton microscopy and especially two-photon microscopy are actively used in dermatology for the diagnosis and analysis of skin diseases. The typical skin probing depth for these methods is limited to 150–200 μm due to the strong scattering properties of skin. The application of the optical clearing method to biological tissues makes it possible to control their optical properties, namely light scattering, by matching the refractive indices of the structural components of tissues. Reducing the scattering of the upper layers of tissue increases the depth of probing for any method of optical imaging by increasing the intensity of the optical signal recorded from the depth up to 6.6 times. This paper presents a brief review of the methods of nonlinear optics used to assess the condition of the skin, discusses the possibility of improving the efficiency of diagnosing skin diseases through the use of the optical clearing method. In particular, this paper discusses the enhancement of the intensity of autofluorescence and second harmonic generation signals during two-photon microscopy of the skin. © 2023 Journal of Biomedical Photonics & Engineering.

Keywords: skin; optical clearing; fluorescence; second harmonic generation; imaging; stratum corneum; dermis; collagen.

Paper #8948 received 3 Apr 2023; revised manuscript received 30 May 2023; accepted for publication 31 May 2023; published online 3 Aug 2023. doi: 10.18287/JBPE23.09.030201.

1 Introduction

Fluorescence is one of the basic mechanisms of interaction between optical radiation and biological objects. In general, fluorescence corresponds to a spin-allowed optical transition between singlet or triplet levels characterized by a short lifetime (10^{-11}–10^{-6} s) and relatively large quantum yield [1]. The fluorescence methods of optical imaging are currently became one of the most popular and promising research directions for non-invasive diagnosis and monitoring of biological tissues, since their application makes it possible to obtain functional images of the studied objects and analyse the obtained data at the molecular level with high resolution [2, 3].

One of the most effective methods of fluorescence optical imaging is multiphoton microscopy (MPM) and,

particularly, two-photon microscopy (TPM) method, basing on a nonlinear two-photon fluorescence excitation process [4]. TPM uses both scattered and ballistic fluorescence photons excited at a wavelength longer than the second harmonic generation (SGH) wavelength considering the used laser excitation source and registered with a wide-aperture photodetector. TPM approach allows for three-dimensional analysis of chromophores distribution due to their excitation by a laser source in the near-infrared (NIR) region. Since biological objects have high transparency in the infrared spectral region, the excitation radiation reaches the deepest layers. Also, the low absorption in the infrared range reduces damage to biological objects. In case of two-photon excitation at 760 nm, fluorescence emission lies in the visible spectral range (410–680 nm) [5]. Recorded signal comes from focal volume of microscope and practically does not contain extraneous background noise.

TPM method combined with fluorescence lifetime imaging is widely used in dermatology for diagnosis and analysis of skin at the cellular level [5–12]. Nevertheless, strong light scattering properties of stratum corneum, living epidermis and dermis significantly limits penetration ability of probing light and reduce the detected signal. Therefore, analysis of fluorescence signal at depths exceeding 150–200 μm is difficult due to low fluorescence intensity as well as low signal-to-noise ratio value.

In order to increase the probing depth of optical methods in biological tissues and improve the quality of obtained images, the optical clearing (OC) method was developed [13, 14]. OC allows to control optical properties of investigated biological objects, significantly increase the efficiency of used optical imaging method, especially in case of highly scattering skin.

The current paper presents a brief review of results on investigation of OC application with the main aim to improve the skin assessment using MPM and TPM. In particular, the effects of optical clearing agents (OCAs) with different osmolarity on the intensity of SHG signal from skin is discussed.

2 Principles of Two-Photon Excitation

The theory of two-photon excitation was firstly described in 1931 by Maria Geppert-Mayer [15]. However, experimentally this effect has been confirmed only after the invention of lasers in 1961 [16]. In general, the standard one-photon fluorescence excitation is described as follows. A fluorophore in the ground state (S_0) can absorb a single photon, leading to the fluorophore excitation and transition to a higher energy state (S_1). After presence at the excited state fluorophore returns to the ground state at the same time emitting the fluorescence photon. Thus, the following condition must be satisfied for the single-photon excitation:

$$E_{S1} - E_{S0} = \frac{hc}{\lambda_{1p}}. \quad (1)$$

Here E_{S1} is the energy of the fluorophore at the excited state, E_{S0} is the energy of the fluorophore at the ground state, h is Planck's constant, c is the speed of light in a vacuum, λ_{1p} is the photon wavelength during one-photon excitation.

In the case of two-photon excitation two photons are simultaneously absorbed, and each of the photons has twice the energy of the photon comparing to one-photon excitation. Thus, since the energy of the photon is inversely proportional to its wavelength, the following condition must be satisfied for two-photon excitation:

$$E_{S1} - E_{S0} = 2\frac{hc}{\lambda_{2p}}. \quad (2)$$

Here, λ_{2p} is the wavelength of the two-photon excited fluorescence.

In case of SHG excitation, simultaneous absorption of two photons leads to transition to the virtual state and subsequent emission of a photon. Thus, for two-photon excitation of SHG, the following condition must be fulfilled:

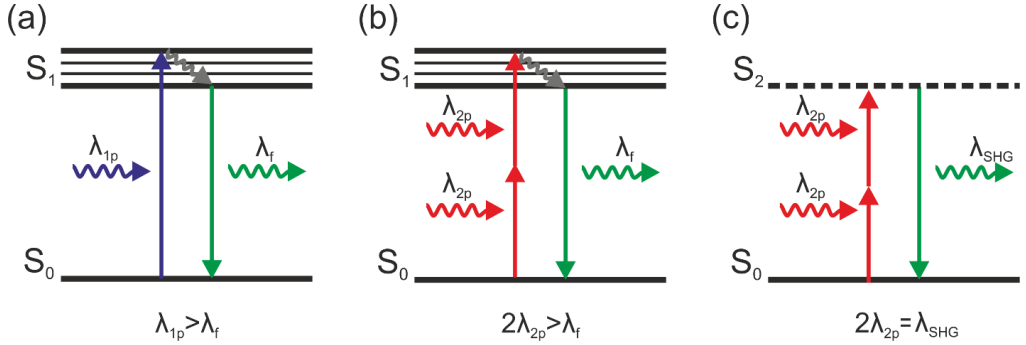


Fig. 1 Diagram showing the principle of single-photon excitation (a), two-photon excited fluorescence (b), and SHG excitation (c). S_0 is the ground state of the fluorophore; S_1 is the excited state of the fluorophore; S_2 is the virtual state of the fluorophore; λ_{1p} and λ_{2p} are the photon excitation wavelength for one-photon and two-photon excitation; λ_f is the photon excitation wavelength for one-photon and two-photon excited fluorescence; λ_{SHG} is the photon excitation wavelength for two-photon excited SHG.

$$E_{S2} - E_{S0} = 2\frac{hc}{\lambda_{2p}}, \quad (3)$$

where E_{S2} is the energy of the fluorophore at the virtual state and λ_{2p} is the wavelength of the excitation photon during two-photon excitation of SHG. Also, two-photon excited fluorescence is generated in the entire bandwidth, while SHG has a resonant character.

Fig. 1 shows diagrams of one- and two-photon fluorescence and SHG excitation processes.

As mentioned above, successful two-photon fluorescence excitation requires simultaneous absorption of two photons (the inter-event interval must be less than 10^{-18} s) [17]. Potentially, high-intensity continuous lasers can be used to increase the probability of this event. Nevertheless, in practice, pulsed sources with femtosecond pulse duration are used to work with biological objects, since they allow to reduce the tissue thermal damage due to short exposure at the same time maintaining a large number of photons in the beam [17].

The closest analogue to TPM method is confocal microscopy (CM) basing on single-photon excitation of fluorescence. However, in case of CM, fluorescence is generated not only in the focal area of the optical system, but also out of focus, which increases the noise in registered signal. Also, CM suffers from significant fluorescence photobleaching effects [18, 19] and possible phototoxicity [20]. At the same time, the use of a high-aperture lens in TPM setups allows to achieve small (sub-femtoliter) excitation volume [4]. Also, TPM allows to achieve higher probing depth and provides safer measurements due to significantly less phototoxicity and fluorescence photobleaching effects compared to CM [21].

Commercially available TPM systems allow to register autofluorescence (AF) and SHG signals by using different emission filters located before the photomultiplier tube [21, 22]. In case of skin imaging, AF signal is formed mainly by melanin, elastin, NAD(F)H, FAD and keratin. These fluorophores are unevenly distributed in skin layers. At the same time, SHG signal is formed by collagen type I molecules [22] located only in papillary and reticular layers of dermis at 50–300 μm depths. Thus, excitation and emission of light for collagen is attenuated due to high light scattering and absorption of skin epidermis. Collagen type I is not the sole source of SHG signal in the skin. Recently, the presence of crystallised urea dendriform structures in the stratum corneum of glabrous human skin has been discovered, which generate a strong SHG signal [23]. Also, AF intensity in the 400–480 nm region is attenuated due to absorption by other skin chromophores, such as, for example, hemoglobin, melanin, carotenoids [24, 25]. It should be noted that melanin presenting in the epidermis [26], is also a source of strong fluorescence signal in case of two-photon excitation [27, 28]. The JenLab TPM optical systems [21, 22], which have high spatial resolution of < 0.36 μm (horizontally) and < 1.7 μm (vertically), have proved to be a good tool for *in vivo* skin studies [9] allowing to obtain high quality skin images up to 150–200 μm in depth.

3 Second Harmonic Generation Signal Analysis for Skin Collagen Assessment

Relative changes in collagen type I content in dermis can be indicator of skin damage and skin aging processes [29–31]. Several studies showed that healthy skin of young people can be characterized by the interwoven structure of collagen fibers with embedded "hollows", as well as higher concentration of collagen type I compared to skin of older people [22, 32, 33]. Various studies showed that collagen content, structural organization, and morphology can change significantly in case of various diseases (e.g. diabetes [29], Ehlers-Danlos syndrome [34, 35], Goodpasture syndrome [36], cancer [37], etc.). The use of TPM, and particularly SHG signal analysis, is an extremely effective *in vivo* method for non-invasive measurement of concentration and visualization of spatial distribution of collagen type I in papillary and reticular dermis.

Series of works described the results of TPM application for histopathological analysis of human skin biopsy samples with the main aim to identify cancerous tumors [38–41]. In particular, it was shown that detection of extracellular matrix changes using TPM allows for monitoring metastasis and cancer progression [42].

Anker et al. [43] showed that AF and SHG signals analysis allows to evaluate the structural changes of epidermis related to keratinization disorder. SHG signal analysis has been also used for clinical studies of differences between healthy and mechanically damaged skin [44, 45]. In particular, it was shown that skin elasticity depends on isotropic properties of collagen. At the same time, for keloid tissues and scars, collagen fibers are straighten [46–48], which results in loss of skin elasticity. Decreased skin elasticity and alteration of collagen type I have recently been observed in tattooed skin [49]. A similar effect, as well as a decrease in the thickness of collagen fibers, was observed in the skin after transplantation [50]. Transdermal injection of collagen is actively used to increase the efficiency of skin scars and wounds healing. Ma et al. [51] suggested a method based on TPM use allowing for *in vivo* assessment of transdermal absorption of collagen in real time. Various methods are used to assess changes in collagen type I morphology. In particular, methods based on fast Fourier transform [52–56], Hilbert transform [57], as well as texture analysis [58] are widely used for SHG signal analysis. Kröger et al. [59] proposed a set of parameters for the methods described above with the main aim to *in vivo* classify different morphological structures of collagen type I in skin. Also the so-called "collagen index" defined as signal intensity ratio (SHG−AF)/(SHG+AF) was implemented to determine the concentration distribution of collagen type I in skin [32, 60]. This method is often used by dermatologist for *in vivo* estimation of collagen type I concentration [32, 60–63].

In addition to the standard TPM, polarization-sensitive SHG microscopy approach is also widely used

for collagen assessment in skin [64]. For this method SHG signal is registered at different orientations of linear polarization of laser source. After, the degree of depolarization in the registered signal is evaluated. A number of works showed high efficiency of this method for detection of various skin diseases [65, 66], as well as for monitoring of structural changes related to skin aging processes [67, 68].

4 Mechanisms of Optical Clearing

The strong light scattering of the skin significantly limits the applicability of the methods described above only to the upper layers of the skin, since the probing depth for TPM and MPT methods in skin is ≈ 150–200 μm. OC of skin allows to significantly increase the probing depth of TPM, as well as to improve the registered image quality by increasing the intensity of recorded SHG and AF signals. The most used OC method for skin imaging is local application of immersion OCAs. Currently, three OC mechanisms are generally accepted [69, 70]. The first mechanism is the refractive index matching of the skin components due to the penetration of OCA into tissue [69–73]. The second mechanism is related to the osmotic action of the OCA, resulting in dehydration of the biological tissue due to high hyperosmolarity [71–75]. The third mechanism is related to the reversible dissociation of collagen fibers after OCAs application and subsequent changes in collagen structure organization [74–76], which in turn considerably reduces light scattering caused by collagen structures [76, 77]. All three described mechanisms of OC acts simultaneously during tissue treatment with OCA. Nevertheless, the relative contribution of each mechanism is usually unequal and depends on the properties of the OCA and the biological tissue. Series of works showed that dehydration of the skin caused by the OCA application leads to scattering reduction due to the displacement of water from the areas between the collagen fibers. This process also contributes to the refractive index matching process between different skin components [71, 78]. In particular, the refractive index for human epidermis is 1.44 at 590 nm wavelength. For the same wavelength, the refractive index for dermis is 1.39, for water is 1.33, and, for example, for 70% glycerol solution in water is 1.43 [79, 80].

The OC efficiency depends on a number of factors, e.g. concentration of OCA and its refractive index, its osmolarity, treatment time, as well as the skin optical properties, its permeability to the molecules of a particular OCA, etc. In most works, OC efficiency is considered as the ratio between the intensity of signal recorded after OCA application and intensity of signal in case of absence of OCA treatment. In this way, values > 1 characterize OC efficiency according to the principle: the higher the value, the better the OC efficiency. In case of *in vivo* application, OCA effectiveness also depends on the physiological parameters of the skin, particularly on its temperature, blood saturation, metabolic response to OCA, etc. [81, 82]. Additionally, chemical enhancers such as DMSO, linoleic and oleic acids, ethanol, propylene glycol, etc., are widely used to increase OCA efficiency and improve OCA permeability into biological objects. [13, 83, 84]. Moreover, DMSO, propylene glycol, and oleic acid themselves can be considered as OCAs [82, 85–87]. In addition to the use of chemical enhancers, the various physical methods of skin surface pre-treatment (e.g. epidermis micro-damaging, removal of part of the stratum corneum by applying tape stripping procedure, microdermabrasion, photothermal and mechanical perforation, laser irradiation of the skin surface, electrophoresis, ultrasound, degreasing, etc.) are also widely used to improve OC efficiency [88–91].

5 Influence of the Optical Clearing on the SHG Signal Intensity

Work [92] presents results of investigation of 100% glycerol topical application on rodent tail tendon and skin dermis samples. It was shown that the use of glycerol resulted in 100-fold increase in skin optical transmittance for 400 to 700 nm wavelengths. At the same time, application of OCA resulted in a 3-fold decrease in SHG signal. This effect was reversible, and SHG signal intensity returned to the initial values after rehydration of the samples by placing them in physiological solution. The authors suggested that decrease in SHG signal was caused by the reversible dissociation and disturbance of collagen fibers organization in response to OCA application. The change in collagen fibers organization also leads to a decrease in optical transmittance, which is contradictory. A more reasonable explanation of this effect was given in work [93], where SHG polarimetry was implemented to study changes in SHG signal from chicken skin dermis before and after dehydration. It was shown that dehydration of the skin resulted in decrease in SHG signal intensity by ≈ 75%. Thus, it was suggested that the decrease in SHG signal intensity is related not to the efficiency of SHG signal generation in the skin, but mainly to the change of its linear optical properties, namely the scattering coefficient. Also, the possible reason of 3-fold decrease in SHG signal can be due to the fact that the volumetric density of the skin increases with dehydration, resulting in the increase of the linear absorption coefficient. At the same time the linear scattering coefficient may stay unchanged due to immersion effect of OCA. Further study of skin samples fixed in formalin showed that their SHG-polarization diagrams practically did not change. At the same time, the SHG signal increased. In this case tissue fixation resulted in formation of cross-links in collagen. Thus, it was suggested that cross-links formation does not influence the collagen fibers orientation but influences SHG signal intensity. In work [94] it was shown that application of sucrose (67.1%) and polyethylene glycol solution resulted in 2-fold decrease in SHG signal intensity from mouse skin. Moreover, reversible change in skin polarization and collagen fibers distribution after OCA application was observed.

Hovhannisyan et al. [95] demonstrated the influence of application of glycerol aqueous solutions with

different concentrations on SHG signals from the chicken tendons and skin. Authors showed that TPM method allows to separate in time the different processes occurring after OCA application to the skin. It was shown that during the tissue treatment with OCA, the primary process was a rapid dehydration of the skin with accompanying contraction of collagen fibers. This was followed by the process of relatively slow penetration of OCA into the interfibrillar space of collagen.

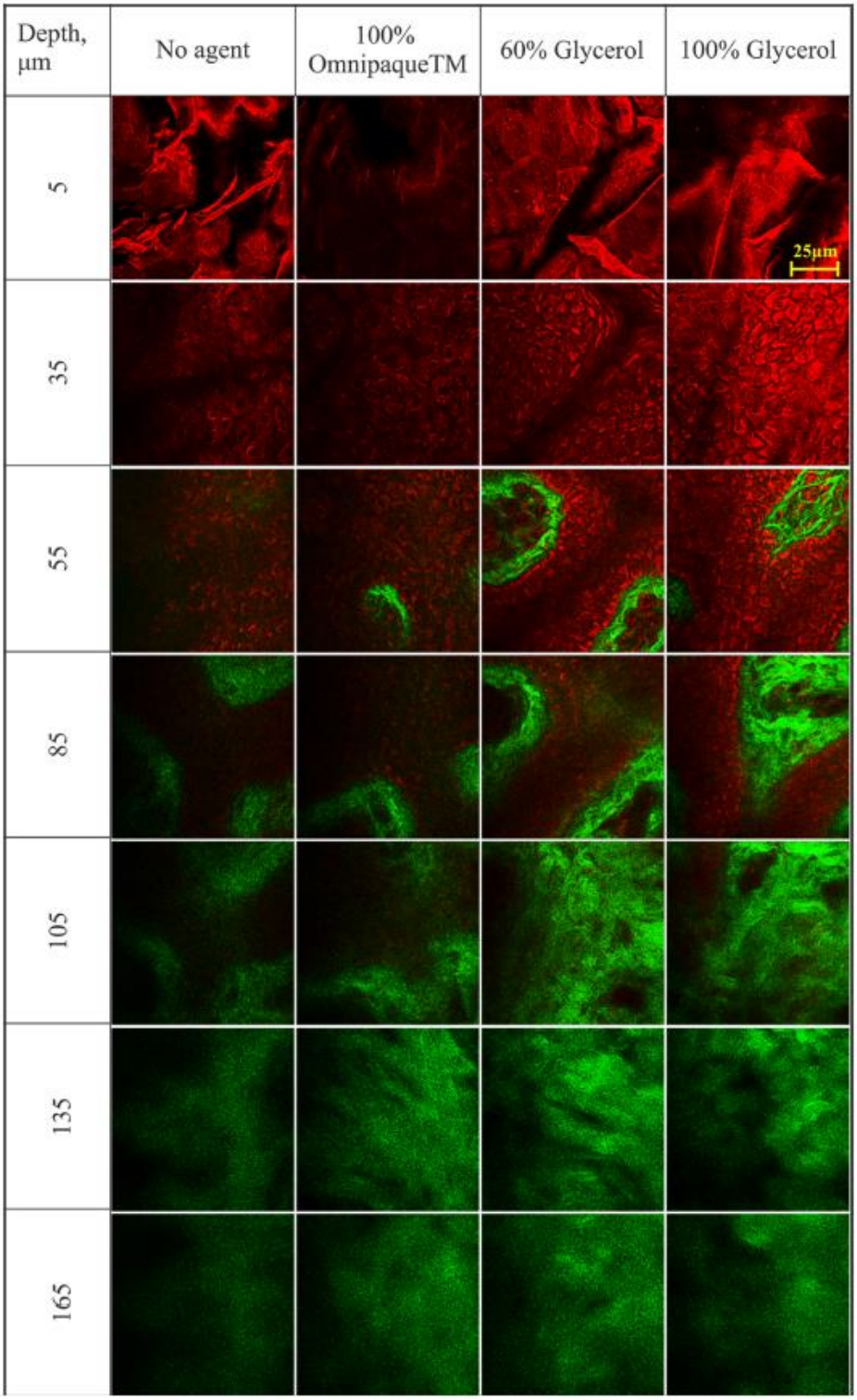


Fig. 2 Structural images for different porcine skin layers obtained *ex vivo* using TPM after Omnipaque and glycerol solutions applications, as well as for a control sample without OCA Red color corresponds to AF signal. Green color corresponds to SHG signal. Reprinted under CC BY 4.0 license from Ref. [79].

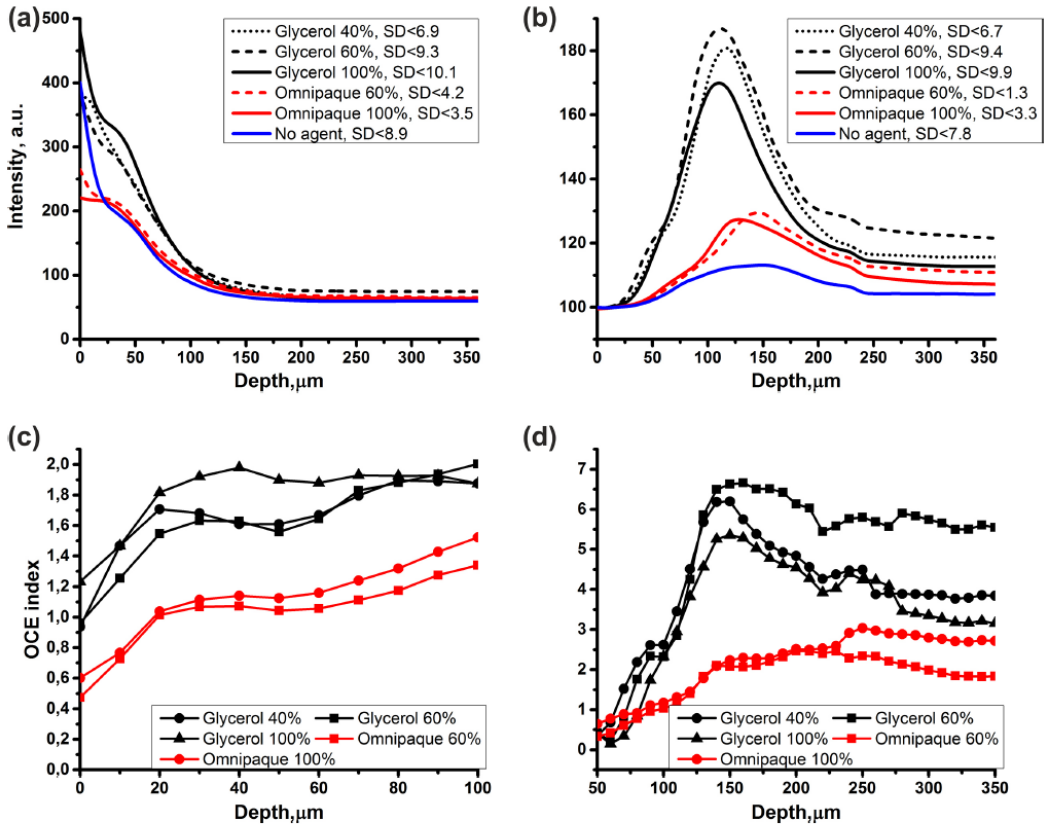


Fig. 3 Averaged in-depth AF (a) and SHG (b) signal intensity distributions obtained *ex vivo* using TPM after Omnipaque and glycerol solutions applications, as well as for a control sample without OCA. SD is the standard deviation for AF and SHG signals. The OC efficiency for AF (c) and SHG signals (d) after Omnipaque and glycerol solutions applications, as well as for a control sample without OCA. Reprinted under CC BY 4.0 license as is from Ref. [79].

It was demonstrated that application of higher concentrations of glycerol increased OCA efficiency and SHG signal intensity. In particular, 100% glycerol led to 4.75-fold enhancement in SHG signal, whereas a mixture of glycerol and phosphate buffer solution (50%/50%) led only to 1.7-fold enhancement. This effect may be related to the fact that when OCA penetrates into the skin, the skin water molecules are partially replaced by OCA molecules, leading to a decrease in refractive index values gradient between the different skin components. Thus, application of higher concentrations of glycerol has a greater OC effect due to a more pronounced replacement of skin water molecules by OCA molecules and the proximity of the refraction index values of glycerol (≈1.43) and skin components (for epidermis ≈1.44, for dermis ≈1.39) comparing to water (≈1.33). Authors demonstrated that use of OC allowed to increase the depth of SHG signal registration from 50 μm to 500 μm. It was also shown that the use of both 100% glycerol and a mixture of glycerol and phosphate buffer solution had reversible effects.

Wen et al. [96] showed that 30 min application of 75% glycerol solution to the rat skin reduced both tissue scattering and reflection coefficients. It was also noted that the thickness of the dermis during this time interval decreased by 1.13 times due to strong skin dehydration. Also, SHG signal was significantly reduced due to dissociation of collagen fibers. Nevertheless, for 10-min exposure by 20%-, 30%-, and 75%- glycerol solutions, SHG signals were higher comparing to the control skin samples without OCA treatment. Despite the collagen fibers compression (decrease of collagen fibers diameter up to 1.38 times), they did not dissociate and did not break off, which allowed to assume that one of the OC mechanisms relates to decrease of biological object layer thickness and subsequent more dense and orderly packing of collagen fibers.

Cicchi et al. [97] demonstrated the effects of different OCAs application on increment of the probing depth for SHG measurements, as well as on increment of contrast for obtained images. In particular, it was shown that the use of glycerol for 7 min allowed to increase the depth of SHG signal registration from 40 to 80 μm. Moreover, the contrast of the images increased thousands of times at a depth of 60–80 μm. The use of glucose and propylene glycol also resulted in a comparable increase in contrast. Authors showed that the contrast enhancement depends on OCA application time. It should be noted that stratum corneum provides the skin barrier function [98, 99] and prevents penetration of substances into the living epidermis and dermis. It has been shown that propylene glycol does not penetrate through the stratum corneum in a relatively short time [100], so the complete or partial

removal of the stratum corneum is implemented in practice to enhance OC [79, 90].

OCA application allows to reduce the tissue scattering and increase the further fluorescence yield until the OC front reaches the depth of the emitting fluorophores. In this case, the total path length of the photon that excites the fluorescence is significantly reduced. Thus, the probability of fluorescence excitation is reduced. On the other hand, with reduced scattering, the probability that the fluorescence photon still reaches the detector increases. On this basis, it should be kept in mind that a strong OC, e.g., due to prolonged exposure by OCA, can lead not only to an increase but also to a loss of the useful signal [101]. Particularly, it was shown in Ref. [100] that a 3-h *ex vivo* human skin treatment with DMSO solution leads to ≈1.4-fold decrease in the SHG signal intensity.

Sdobnov et al. [79] investigated effects of application of OCAs with different osmolarity on SHG and AF signals from porcine skin *ex vivo*. Topical application of iohexol (OmnipaqueTM(300)) and glycerol solutions with different concentrations within 1 h allowed to increase the probing depth in skin from 200 to 350 μm. It was shown that 100% glycerol had a lower OC efficiency for SHG signal comparing to aqueous solutions with lower concentrations. Particularly, 100% glycerol application increased SHG signal up to 5.4 times, whereas 40% and 60% glycerol solutions application increased the signal up to 6 and 6.6 times, respectively. This effect may be related to the high viscosity of 100% glycerol preventing OCA penetration into the skin. At the same time, in case of AF signal, the use of 100% glycerol resulted in higher OC efficiency comparing to 40% and 60% solutions (increase in AF signal up to 2, 1.8, and 1.8 times, respectively). Also, aqueous glycerol solutions showed higher OC efficiency comparing to aqueous iohexol solutions for both AF and SHG signals. In particular, AF and SHG signals were enhanced only 1.5- and 3-fold, respectively, after application of 100% iohexol solution. Possibly, higher enhancement in AF signal in case of glycerol application is achieved due to strong skin dehydration. At the same time, the use of glycerol resulted in changes in the cellular structure of epidermis. Fig. 2 demonstrates structural AF and TPM images for different porcine skin layers obtained *ex vivo* after Omnipaque and glycerol solutions applications, as well as for a control sample without OCA. Fig. 3 demonstrates the corresponding data on increase in the intensity of AF and SHG signals, as well as the efficiency of OC for different OCAs. It is also important to note that in case of iohexol solutions application AF signal at small depths (up to 50 μm) decreased in comparison with control skin samples and samples treated with glycerol solutions. The possible reason can be the fact that iodine contained in ihexol can decrease the fluorescence signal during its penetration into a biological sample. In particular, it was shown in Ref. [102] that interaction between iodine and fluorophores leads to dynamic quenching of fluorescence.

In work [103] the effect of 100% and 50% glycerol solutions application on SHG signal intensity and third harmonic generation (THG) signal intensity from the human skin was investigated *ex vivo* (see Fig. 4). It was shown that 100% glycerol application resulted in1.15-fold reduction of THG signal for stratum corneum and epidermis. For the dermis, the THG signal was slightly increased after OCA application. At the same time, in case of SHG signal, application of OCA resulted in 2-fold enhancement in the registered signal from dermis. Application of 50% glycerol solution resulted in 1.3-fold enhancement of THG signal from stratum corneum and epidermis. Intensity of SHG signal also increased significantly.

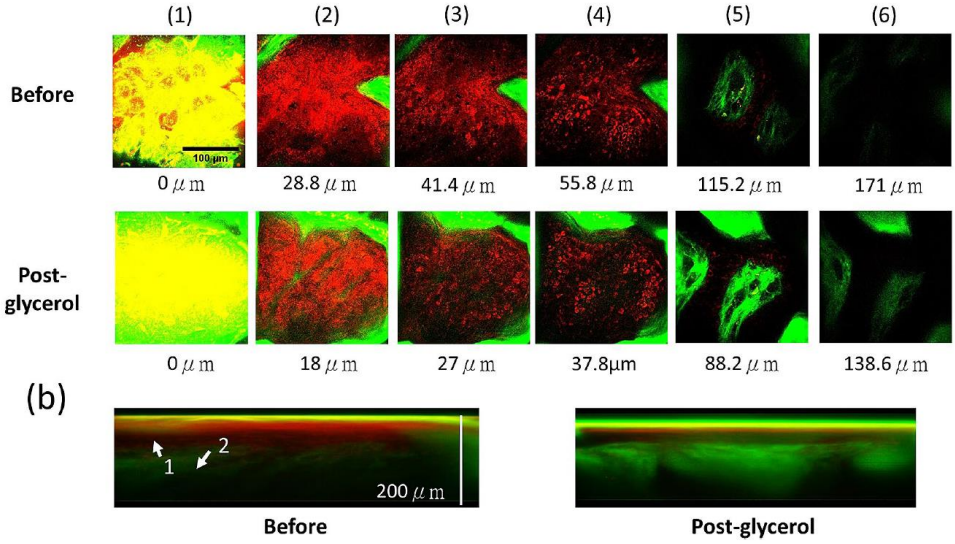


Fig. 4 (a) Structural images for different layers of human skin obtained *ex vivo* before and after treatment with 100% glycerol. Red color corresponds to the THG signal. Green color corresponds to the SHG signal. (b) Cross-sectional images of human skin samples obtained *ex vivo* before and after treatment with 100% glycerol. Reprinted under CC BY 4.0 license from Ref. [103].

Authors suggested that the use of 50% glycerol solution provides the compromise between the reduction of scattering and refractive indices matching between the skin components, leading to increase in signal intensity. It has also been suggested that the key role in skin OC is the interaction of OCA directly with the stratum corneum. In particular, stratum corneum shrinkage and refractive index matching due to OCA penetration contributed to increase in SHG signal intensity in dermis. One of the OC methods is mechanical compression of biological objects [104, 105], which is actually an analogue of skin shrinkage as a result of dehydration caused by the hyperosmotic action of OCAs. Also, the described result agrees well with other studies where it has been shown that glycerol concentrations in the range 40–60% are preferable for OC due to the low viscosity comparing to the pure glycerol (14-fold difference in viscosity), as well as due to lower decrease in the refractive index caused by dilution with water [106]. Also, the ratio between the water content in OCA and skin is important parameter. In particular, in stratum corneum and living epidermis the water concentration averages are 45% [107] and 60% [91, 107], respectively. In this case, water practically does not participate in diffusion processes and mainly glycerol molecules diffuse into the skin [108]. Each glycerol molecule binds about six water molecules [109] reducing the light scattering of superficial skin layers and leading to refractive index matching between the skin components. This theory agrees well with the results described above [79, 103], as well as with the results presented in works [106, 110, 111].

In addition to the skin, OC influence on SHG signal is actively studied for the other biological objects. For example, Genin et al. [112] showed that application of 50% aqueous glycerol solution on rodent tendons and striated muscles allowed to obtain information on SHG signal polarization response at the depths up to 200 μm due to reduction of light scattering in upper tissue layers. In Ref. [113] it was shown that OC with fructose solutions allowed to achieve 5-fold increase in probing depth for human cartilage. Zhang et al. [114] presented OC protocol allowing to achieve reversible temporal OC of a mouse skull. Also, the proposed method allowed to significantly increase both the probing depth (from 120 to 300 μm) and SHG signal intensity (more than 10-fold) during transcranial blood flow imaging in the mouse brain. In Ref. [115] it was shown that application of glycerol, DMSO and buffer solution allows to increase the depth of SHG signal detection in the anterior leaflet of sheep mitral valve up to 800 μm comparing to 100 μm in case of control samples without OC. At the same time, application of OCA led to strong dehydration of biological objects and conformational changes in collagen.

6 Conclusions

Various physical and chemical methods of skin pre-treatment are widely used to enhance the probing depth and image quality of skin TPM. The most effective and promising method is immersion OC and/or its combined use with the discussed optical methods. This article presents a brief review of works devoted mainly to the study of OC influence on SHG and AF signals from skin. The theory of two-photon excitation is given, and the basic principles and mechanisms of OC are described.

Despite the disagreement in interpretation of the experimental data, and particularly in the evaluation of contribution of different OC mechanisms to its overall efficiency, all the studies presented in this paper showed that the effect of OCA application on skin allows to increase the probing depth. In addition, OC method improves the overall quality of detected images due to a better focusing of laser radiation into the skin caused by reduced scattering. Also, OCA application leads up to 6.6-fold increase in intensity of skin SHG signal and up to 1.8-fold increase in intensity of skin AF signal by tissue dehydration, collagen dissociation and refractive index matching mechanisms. Thus, OC method is extremely promising for further *in vivo* and *ex vivo* use on mammalian skin and, in particular, for investigation of structural changes of collagen type I in the dermis at the depths exceeding 150 μm.

Disclosures

The authors declare no conflict of interest.

Acknowledgements

Valery Tuchin acknowledges the support of a grant under the Decree of the Government of the Russian Federation No. 220 of 09 April 2010 (Agreement No. 075-15-2021-615 of 04 June 2021).

References

1. J. R. Lakowicz (Ed.), Principles of fluorescence spectroscopy, Springer, New York, USA (2013).
2. G. A. Wagnieres, W. M. Star, and B. C. Wilson, "In vivo fluorescence spectroscopy and imaging for oncological applications," Photochemistry and Photobiology 68(5), 603 (1998).
3. B. Valeur, J. C. Brochon (Eds.), New trends in fluorescence spectroscopy: applications to chemical and life sciences, Springer Series on Fluorescence 1, Springer Berlin, Heidelberg (2012). ISBN: 978-3-642-56853-4.
4. E. A. Shirshin, B. P. Yakimov, M. E. Darvin, N. P. Omelyanenko, S. A. Rodionov, Y. I. Gurfinkel, V. V. Fadeev, and A. V. Priezzhev, "Label–free multiphoton microscopy: The origin of fluorophores and capabilities for analyzing biochemical processes," Biochemistry (Moscow) 84, 69–88 (2019).

5. M. Kröger, J. Scheffel, V. V. Nikolaev, E. A. Shirshin, F. Siebenhaar, J. Schleusener, J. Lademann, M. Maurer, and M. E. Darvin, "In vivo non–invasive staining–free visualization of dermal mast cells in healthy, allergy and mastocytosis humans using two–photon fluorescence lifetime imaging," Scientific Reports 10, 14930 (2020).
6. S. W. Perry, R. M. Burke, and E. B. Brown, "Two–photon and second harmonic microscopy in clinical and translational cancer research," Annals of Biomedical Engineering 40, 277–291 (2012).
7. J. Liu, "Two–photon microscopy in pre–clinical and clinical cancer research," Frontiers of Optoelectronics 8, 141–151 (2015).
8. M. Ulrich, Klemp, M. E. Darvin, K. König, J. Lademann, and M. C. Meinke,"In vivo detection of basal cell carcinoma: comparison of a reflectance confocal microscope and a multiphoton tomograph," Journal of Biomedical Optics 18(6), 061229 (2013).
9. M. Weinigel, H. G. Breunig, M. Kellner–Höfer, R. Bückle, M. E. Darvin, M. Klemp, J. Lademann, and K. König, "In vivo histology: optical biopsies with chemical contrast using clinical multiphoton/coherent anti–Stokes Raman scattering tomography," Laser Physics Letters 11(5), 055601 (2014).
10. M. Klemp, , Meinke, M. C., Weinigel, M., Röwert-Huber, H. J., König, K., Ulrich, M., J. Lademann, and M. E. Darvin, "Comparison of morphologic criteria for actinic keratosis and squamous cell carcinoma using in vivo multiphoton tomography," Experimental Dermatology 25(3), 218–222 (2016).
11. M. Kröger, J. Scheffel,, E. A. Shirshin, J. Schleusener, M. C. Meinke, J. Lademann, M. Maurer, and M. E. Darvin, "Label–free imaging of M1 and M2 macrophage phenotypes in the human dermis in vivo using two–photon excited FLIM," ELife 11, e72819 (2022).
12. O. G. L. Zakharkina, E. A. Sergeeva, M. Y. Kirillin, and N. Y. Ignatieva, "Analysis of laser–induced modification of collagen structure using nonlinear optical microscopy," Quantum Electronics 50(1), 76 (2020).
13. A. Y. Sdobnov, M. E. Darvin, E. A. Genina, A. N. Bashkatov, J. Lademann, and V. V. Tuchin, "Recent progress in tissue optical clearing for spectroscopic application," Spectrochimica Acta Part A: Molecular and Biomolecular Spectroscopy 197, 216–229 (2018).
14. A. Y. Sdobnov, J. Lademann, M. E. Darvin, and V. V. Tuchin, "Methods for optical skin clearing in molecular optical imaging in dermatology," Biochemistry (Moscow) 84, 144–158 (2019).
15. M. Göppert-Mayer, "Über elementarakte mit zwei quantensprüngen," Annalen der Physik 401(3), 273–294 (1931).
16. W. Kaiser, C. G. B. Garrett, "Two–photon excitation in Ca F 2: Eu 2+," Physical Review Letters 7(6), 229 (1961).
17. W. Denk, D. W. Piston, and W. W. Webb, "Two–photon molecular excitation in laser–scanning microscopy. In Handbook of biological confocal microscopy," Chapter in Handbook of Biological Confocal Microscopy, Springer, New York, USA (1995).
18. M. E. Darvin, N. N. Brandt, and J. Lademann, "Photobleaching as a method of increasing the accuracy in measuring carotenoid concentration in human skin by Raman spectroscopy," Optics and Spectroscopy 109, 205–210 (2010).
19. J. Schleusener, J. Lademann, and M. E. Darvin, "Depth–dependent autofluorescence photobleaching using 325, 473, 633, and 785 nm of porcine ear skin ex vivo," Journal of Biomedical Optics 22(9), 091503 (2017).
20. J. Icha, M. Weber, J. C. Waters, and C. Norden, "Phototoxicity in live fluorescence microscopy, and how to avoid it," BioEssays 39(8), 1700003 (2017).
21. K. König, A. Uchugonova, "Multiphoton imaging and nanoprocessing of human stem cells," Chapter 1 in Laser Imaging and Manipulation in Cell Biology, F. S. Pavone (Ed.), John Wiley & Sons, Weinheim (2010). ISBN:9783527632053.
22. K. König, "Clinical multiphoton tomography," Journal of Biophotonics 1(1), 13–23 (2008).
23. V. H. P. Infante, R. Bennewitz, M. Kröger, M. C. Meinke, and M. E. Darvin, "Human glabrous skin contains crystallized urea dendriform structures in the stratum corneum which affect the hydration levels," Experimental Dermatology (2023).
24. Y. P. Sinichkin, S. R. Utz, A. H. Mavliutov, and H. A. Pilipenko, "In vivo fluorescence spectroscopy of the human skin: experiments and models," Journal of Biomedical Optics 3(2), 201–211 (1998).
25. M. E. Darvin, J. Lademann, J. von Hagen, S. B. Lohan, H. Kolmar, M. C. Meinke, and S. Jung, "Carotenoids in human skin in vivo: Antioxidant and photo–protectant role against external and internal stressors," Antioxidants 11(8), 1451 (2022).
26. B. P. Yakimov, E. A. Shirshin, J. Schleusener, A. S. Allenova, V. V. Fadeev, and M. E. Darvin, "Melanin distribution from the dermal–epidermal junction to the stratum corneum: non–invasive in vivo assessment by fluorescence and Raman microspectroscopy," Scientific Reports 10, 14374 (2020).
27. K. Teuchner, J. Ehlert, W. Freyer, D. Leupold, P. Altmeyer, M. Stücker, and K. Hoffmann, "Fluorescence studies of melanin by stepwise two–photon femtosecond laser excitation," Journal of Fluorescence 10, 275 (2000).
28. A. M. Pena, E. Decencière, S. Brizion, P. Sextius, S. Koudoro, T. Baldeweck, and E. Tancrède–Bohin, "In vivo melanin 3D quantification and z–epidermal distribution by multiphoton FLIM, phasor and Pseudo–FLIM analyses," Scientific Reports 12, 1642 (2022).
29. V. Marcos-Garcés, P. Molina Aguilar, C. Bea Serrano, V. García Bustos, J. Benavent Seguí, A. Ferrández Izquierdo, and A. Ruiz-Saurí, "Age-related dermal collagen changes during development, maturation and ageing–a morphometric and comparative study," Journal of Anatomy 225(1), 98–108 (2014).

30. G. J. Fisher, S. Kang, J. Varani, Z. Bata–Csorgo, Y. Wan, S. Datta, and J. J. Voorhees, "Mechanisms of photoaging and chronological skin aging," Archives of Dermatology 138(11), 1462–1470 (2002).
31. D. S. James, P. J. Campagnola, "Recent advancements in optical harmonic generation microscopy: Applications and perspectives," BME Frontiers 2021, 3973857 (2021).
32. M. J. Koehler, K. König, P. Elsner, R. Bückle, and M. Kaatz, "In vivo assessment of human skin aging by multiphoton laser scanning tomography," Optics Letters 31(19), 2879–2881 (2006).
33. M. E. Darvin, H. Richter, Y.J. Zhu, M.C. Meinke, F. Knorr, S.A. Gonchukov, K. Köenig and J. Lademann, "Comparison of in vivo and ex vivo laser scanning microscopy and multiphoton tomography application for human and porcine skin imaging," Quantum Electronics 44(7), 646 (2014).
34. O. M. Vanakker, D. Hemelsoet, and A. De Paepe, "Hereditary connective tissue diseases in young adult stroke: a comprehensive synthesis," Stroke Research and Treatment 2011, 712903 (2011).
35. F. Malfait, M. Castori, C. A. Francomano, C. Giunta, T. Kosho, and P. H. Byers, "The ehlers–danlos syndromes," Nature Reviews Disease Primers 6, 64 (2020).
36. B. Shiferaw, V. Miro, C.Smith, J. Akella, W. Chua, and Z. Kim, "Goodpasture's disease: an uncommon disease with an atypical clinical course," Journal of Clinical Medicine Research 8(1), 52–55 (2016).
37. A. A. Plekhanov, A. L. Potapov, M. V. Pavlov, V. V. Elagin, E. V. Gubarkova, A. A. Sovetsky, L. A. Matveev, D. A. Vorontsov, A. L. Matveyev, A. Y. Vorontsov, S. V. Gamayunov, E. V. Zagaynova, M. A. Sirotkina, V. Y. Zaitsev, and N. D. Gladkova, "Side-by-Side OCE-Study of Elasticity and SHG-Characterization of Collagen Fibers in Breast Cancer Tissue before and after Chemotherapy," Journal of Biomedical Photonics & Engineering 9(2), 020305 (2023).
38. T. H. Tsai, S. H. Jee, C. Y. Dong, and S. J. Lin, "Multiphoton microscopy in dermatological imaging," Journal of Dermatological Science 56(1), 1–8 (2009).
39. S. J. Lin, S. H. Jee, and C. Y. Dong, "Multiphoton microscopy: a new paradigm in dermatological imaging," European Journal of Dermatology 17(5), 361–366 (2007).
40. J. Paoli, M. Smedh, and M. B. Ericson, "Multiphoton laser scanning microscopy—a novel diagnostic method for superficial skin cancers," Seminars in Cutaneous Medicine and Surgery 28(3), 190–195 (2009).
41. E. Dimitrow, M. Ziemer, M. J. Koehler, J. Norgauer, K. König, P. Elsner, and M. Kaatz, "Sensitivity and specificity of multiphoton laser tomography for in vivo and ex vivo diagnosis of malignant melanoma," Journal of Investigative Dermatology 129(7), 1752–1758 (2009).
42. R. de Andrade Natal, J. Adur, C. L. Cesar, and J. Vassallo, "Tumor extracellular matrix: lessons from the second–harmonic generation microscopy," Surgical and Experimental Pathology 4, 7 (2021).
43. P. Anker, L. Fésűs, N. Kiss, J. Noll, K. Becker, E. Kuroli, B. Mayer ,S. Bozsányi, K. Lőrincz, I. Lihacova,A. Lihachev, M. Lange, N. Wikonkál, and M. Medvecz, "Visualization of keratin with diffuse reflectance and autofluorescence imaging and nonlinear optical microscopy in a rare keratinopathic ichthyosis," Sensors 21(4), 1105 (2021).
44. P. J. Su, W. L. Chen, J. B. Hong, T. H. Li, R. J. Wu, C. K. Chou, and C. Y. Dong, "Discrimination of collagen in normal and pathological skin dermis through second–order susceptibility microscopy," Optics Express 17(13), 11161–11171 (2009).
45. Y. Liu, X. Zhu, Z. Huang, J. Cai, R. Chen, S. Xiong, G. Chen and H. Zeng, "Texture analysis of collagen second–harmonic generation images based on local difference local binary pattern and wavelets differentiates human skin abnormal scars from normal scars," Journal of Biomedical Optics 20(1), 016021 (2015).
46. J. P. Junker, J. Philip, E. Kiwanuka, F. Hackl, E. J. Caterson, and E. Eriksson, "Assessing quality of healing in skin: review of available methods and devices," Wound Repair and Regeneration 22(S1), 2–10 (2014).
47. N. Kumar, P. Kumar, S. N. Badagabettu, K. Prasad, R. Kudva, and R. C. Vasudevarao, "Surgical implications of asymmetric distribution of dermal collagen and elastic fibres in two orientations of skin samples from extremities," Plastic Surgery International 2014, 364573 (2014).
48. P. D. Verhaegen, P. P. Van Zuijlen, N. M. Pennings, J. Van Marle, F. B. Niessen, C. M. Van Der Horst, and E. Middelkoop, "Differences in collagen architecture between keloid, hypertrophic scar, normotrophic scar, and normal skin: an objective histopathological analysis," Wound Repair and Regeneration 17(5), 649–656 (2009).
49. M. Kröger, J. Schleusener, J. Lademann, M. C. Meinke, S. Jung, and M. E. Darvin, "Tattoo Pigments Are Localized Intracellularly in the Epidermis and Dermis of Fresh and Old Tattoos: In vivo Study Using Two–Photon Excited Fluorescence Lifetime Imaging," Dermatology 239(3), 478–493 (2023).
50. N. L. Rosin, N. Agabalyan, K. Olsen, G. Martufi, V. Gabriel, J. Biernaskie, and E. S. Di Martino, "Collagen structural alterations contribute to stiffening of tissue after split-thickness skin grafting," Wound Repair and Regeneration 24(2), 263–274 (2016).
51. S. Ma, G. He, W. Yang, and Y. Wang, "In Vivo Visualization of Collagen Transdermal Absorption by a Combined Second–harmonic Generation and Two–photon Excited Fluorescence Method," Preprint (Version 1) available at Research Square (2021).
52. M. L. Noorlander, P. Melis, A. Jonker, and C. J. V. Noorden, "A quantitative method to determine the orientation of collagen fibers in the dermis," Journal of Histochemistry & Cytochemistry 50(11), 1469–1474 (2002).

53. S. Wu, H. Li, H. Yang, X. Zhang, Z. Li, and S. Xu, "Quantitative analysis on collagen morphology in aging skin based on multiphoton microscopy," Journal of Biomedical Optics 16(4), 040502 (2011).
54. L. Mostaço–Guidolin, N. L. Rosin, and T. L. Hackett, "Imaging collagen in scar tissue: developments in second harmonic generation microscopy for biomedical applications," International Journal of Molecular Sciences 18(8), 1772 (2017).
55. G. Ducourthial, J. S. Affagard, M. Schmeltz, X. Solinas, M. Lopez-Poncelas, C. Bonod-Bidaud, R. Rubio–Amador, F. Ruggiero, J. M. Allain, E. Beaurepaire, and M. C. Schanne-Klein, "Monitoring dynamic collagen reorganization during skin stretching with fast polarization-resolved second harmonic generation imaging," Journal of Biophotonics 12(5), e201800336 (2019).
56. J. K. Pijanka, P. P. Markov, D. Midgett, N. G. Paterson, N. White, E. J. Blain, T. D. Nguyen, H. A. Quigley, and C. Boote, "Quantification of collagen fiber structure using second harmonic generation imaging and two-dimensional discrete Fourier transform analysis: application to the human optic nerve head," Journal of Biophotonics 12(5), e201800376 (2019).
57. K. Yang, K. Yu, and Q. Li, "Modal parameter extraction based on Hilbert transform and complex independent component analysis with reference," Mechanical Systems and Signal Processing 40(1), 257–268 (2013).
58. R. M. Haralick, K. Shanmugam, and I. H. Dinstein, "Textural features for image classification," IEEE Transactions on Systems, Man, and Cybernetics (6), 610–621 (1973).
59. M. Kröger, J. Schleusener, S. Jung, and M. E. Darvin, "Characterization of collagen I fiber thickness, density, and orientation in the human skin in vivo using second–harmonic generation imaging," Photonics 8(9), 404 (2021).
60. S. J. Lin, R. J. Wu, H. Y. Tan, W. Lo, W. C. Lin, T. H. Young, C. J. Hsu, J. S. Chen, S. H.Jee, and C. Y. Dong, "Evaluating cutaneous photoaging by use of multiphoton fluorescence and second–harmonic generation microscopy," Optics Letters 30(17), 2275–2277 (2005).
61. M. E. Darvin, H. Richter, S. Ahlberg, S. F. Haag, M. C. Meinke, D. Le Quintrec, O. Douceta, and J. Lademann, "Influence of sun exposure on the cutaneous collagen/elastin fibers and carotenoids: negative effects can be reduced by application of sunscreen," Journal of Biophotonics 7(9), 735–743 (2014).
62. S. Springer, M. Zieger, K. Koenig, M. Kaatz, J. Lademann, and M. E. Darvin, "Optimization of the measurement procedure during multiphoton tomography of human skin in vivo," Skin Research and Technology 22(3), 356–362 (2016).
63. S. J. Tseng, Y. H. Lee, Z. H. Chen, H. H. Lin, C. Y. Lin, and S. C. Tang, "Integration of optical clearing and optical sectioning microscopy for three–dimensional imaging of natural biomaterial scaffolds in thin sections," Journal of Biomedical Optics 14(4), 044004 (2009).
64. R. Cisek, A. Joseph, M. Harvey, and D. Tokarz, "Polarization–sensitive second harmonic generation microscopy for investigations of diseased collagenous tissues," Frontiers in Physics 9, 726996 (2021).
65. T. Yasui, Y. Takahashi, S. Fukushima, Y. Ogura, T. Yamashita, T. Kuwahara, T. Hirao and T. Araki, "Observation of dermal collagen fiber in wrinkled skin using polarization–resolved second–harmonic–generation microscopy," Optics Express 17(2), 912–923 (2009).
66. S. I. Fukushima, M. Yonetsu, and T. Yasui, "Polarization–resolved second–harmonic–generation imaging of dermal collagen fiber in prewrinkled and wrinkled skins of ultraviolet–B–exposed mouse," Journal of Biomedical Optics 24(3), 031006 (2018).
67. Y. Tanaka, E. Hase, S. Fukushima, Y. Ogura, T. Yamashita, T. Hirao, T. Araki, and T. Yasui, "Motion–artifact–robust, polarization–resolved second–harmonic–generation microscopy based on rapid polarization switching with electro–optic Pockells cell and its application to in vivo visualization of collagen fiber orientation in human facial skin," Biomedical Optics Express 5(4), 1099–1113 (2014).
68. I. Miler, M. D. Rabasovic, M. Aleksic, A. J. Krmpot, A. Kalezic, A. Jankovic, B. Korac, and A. Korac, "Polarization-resolved SHG imaging as a fast screening method for collagen alterations during aging: Comparison with light and electron microscopy," Journal of Biophotonics 14(3), e202000362 (2021).
69. E. A. Genina., A. N Bashkatov, and V. V. Tuchin, "Tissue optical immersion clearing," Expert Review of Medical Devices 7(6), 825–842 (2010).
70. I. Costantini, R. Cicchi, L. Silvestri, F. Vanzi, and F. S. Pavone, "In–vivo and ex–vivo optical clearing methods for biological tissues," Biomedical Optics Express 10(10), 5251–5267 (2019).
71. V. V. Tuchin (Ed.), Tissue Optics: Light Scattering Methods and Instruments for Medical Diagnostics, 3rd ed., SPIE Press, Bellingham, WA, USA (2015). ISBN: 9781628415162.
72. V. V. Tuchin, Optical clearing of tissues and blood, SPIE Press, Bellingham, WA, USA (2006). ISBN: 9780819460066.
73. D. K. Tuchina, R. Shi, A. N. Bashkatov, E. A. Genina, D. Zhu, Q. Luo, and V. V. Tuchin,"Ex vivo optical measurements of glucose diffusion kinetics in native and diabetic mouse skin," Journal of Biophotonics 8(4), 332–346 (2015).
74. K. V. Larin, M. G. Ghosn, A. N. Bashkatov, E. A. Genina, N. A. Trunina, and V. V. Tuchin, "Optical clearing for OCT image enhancement and in–depth monitoring of molecular diffusion," IEEE Journal of Selected Topics in Quantum Electronics 18(3), 1244–1259 (2011).

75. A. Jaafar, M. E. Darvin, V. V. Tuchin, and M. Veres, "Confocal Raman Micro–Spectroscopy for Discrimination of Glycerol Diffusivity in Ex Vivo Porcine Dura Mater," Life 12(10), 1534 (2022).
76. K. V. Berezin, K. N. Dvoretski, M. L. Chernavina, A. M. Likhter, V. V. Smirnov, I. T. Shagautdinova, E. M. Antonova, E. Y. Stepanovich, E. A. Dzhalmuhambetova, and V. V. Tuchin, "Molecular modeling of immersion optical clearing of biological tissues," Journal of Molecular Modeling 24, 45 (2018).
77. V. V. Tuchin, "A clear vision for laser diagnostics," IEEE Journal of Selected Topics in Quantum Electronics 13(6), 1621–1628 (2007).
78. A. Bykov, T. Hautala, M. Kinnunen, A. Popov, S. Karhula, S. Saarakkala, M. T. Nieminen, V. Tuchin, and I. Meglinski, "Imaging of subchondral bone by optical coherence tomography upon optical clearing of articular cartilage," Journal of Biophotonics 9(3), 270–275 (2016).
79. A. Sdobnov, M. E. Darvin, J. Lademann, and V. Tuchin, "A comparative study of ex vivo skin optical clearing using two-photon microscopy," Journal of Biophotonics 10(9), 1115–1123 (2017).
80. H. Ding, J. Q. Lu, W. A. Wooden, P. J. Kragel, and X. H. Hu, "Refractive indices of human skin tissues at eight wavelengths and estimated dispersion relations between 300 and 1600 nm," Physics in Medicine & Biology 51(6), 1479 (2006).
81. R. W. Sun, V. V. Tuchin, V. P. Zharov, E. I. Galanzha, and G. T. Richter, "Current status, pitfalls and future directions in the diagnosis and therapy of lymphatic malformation," Journal of Biophotonics 11(8), e201700124 (2018).
82. Y. Liu, X. Yang, D. Zhu, R. Shi, and Q. Luo, "Optical clearing agents improve photoacoustic imaging in the optical diffusive regime," Optics Letters 38(20), 4236–4239 (2013).
83. D. Zhu, K. V Larin., Q. Luo, and V. V. Tuchin, "Recent progress in tissue optical clearing," Laser & Photonics Reviews 7(5), 732–757 (2013).
84. A. Jaafar, M. H. Mahmood, R. Holomb, L. Himics, T. Váczi, A. Y. Sdobnov, V. V. Tuchin, and M. Veres, "Ex–vivo confocal Raman microspectroscopy of porcine skin with 633/785–NM laser excitation and optical clearing with glycerol/water/DMSO solution," Journal of Innovative Optical Health Sciences 14(05), 2142003 (2021).
85. P. Liu, Y. Huang, Z. Guo, J. Wang, Z. Zhuang, and S. Liu, "Discrimination of dimethyl sulphoxide diffusion coefficient in the process of optical clearing by confocal micro–Raman spectroscopy," Journal of Biomedical Optics 18(2), 020507 (2013).
86. B. Choi, L. Tsu, E. Chen, T. S. Ishak, S. M. Iskandar, S. Chess, and J. S. Nelson, "Determination of chemical agent optical clearing potential using in vitro human skin," Lasers in Surgery and Medicine: The Official Journal of the American Society for Laser Medicine and Surgery 36(2), 72–75 (2005).
87. V. Kalchenko, I. Meglinski, A. Sdobnov, Y. Kuznetsov, and A. Harmelin, "Combined laser speckle imaging and fluorescent intravital microscopy for monitoring acute vascular permeability reaction," Journal of Biomedical Optics 24(6), 060501 (2019).
88. O. F. Stumpp, A. J. Welch, T. E. Milner, and J. Neev, "Enhancement of transepidermal skin clearing agent delivery using a 980 nm diode laser," Lasers in Surgery and Medicine: The Official Journal of the American Society for Laser Medicine and Surgery 37(4), 278–285 (2005).
89. O. Stumpp, B. Chen, and A. J. Welch, "Using sandpaper for noninvasive transepidermal optical skin clearing agent delivery," Journal of Biomedical Optics 11(4), 041118 (2006).
90. A. Y. Sdobnov, V. V. Tuchin, J. Lademann, and M. E. Darvin, "Confocal Raman microscopy supported by optical clearing treatment of the skin—influence on collagen hydration," Journal of Physics D: Applied Physics 50(28), 285401 (2017).
91. A. Y. Sdobnov, M. E. Darvin, J. Schleusener, J. Lademann, and V. V. Tuchin, "Hydrogen bound water profiles in the skin influenced by optical clearing molecular agents—Quantitative analysis using confocal Raman microscopy," Journal of Biophotonics 12(5), e201800283 (2019).
92. A. T. Yeh, B. Choi, J. S. Nelson, and B. J. Tromberg, "Reversible dissociation of collagen in tissues," Journal of Investigative Dermatology 121(6), 1332–1335 (2003).
93. T. Yasui, T. Tohno, and T. Araki, "Characterization of collagen orientation in human dermis by two–dimensional second–harmonic–generation polarimetry," Journal of Biomedical Optics 9(2), 259 (2004).
94. C. Zhang, W. Feng, "Assessment of tissue-specific changes in structure and function induced by in vivo skin/skull optical clearing techniques," Lasers in Surgery and Medicine 54(3), 447–458 (2022).
95. V. Hovhannisyan, P. S. Hu, S. J. Chen, C. S. Kim, and C. Y. Dong, "Elucidation of the mechanisms of optical clearing in collagen tissue with multiphoton imaging," Journal of Biomedical Optics 18(4), 046004 (2013).
96. X. Wen, Z. Mao, Z. Han, V. V. Tuchin, and D. Zhu, "In vivo skin optical clearing by glycerol solutions: mechanism," Journal of Biophotonics 3(1–2), 44–52 (2010).
97. F. S. Cicchi, F. S. Pavone, D. Massi, and D. D. Sampson, "Contrast and depth enhancement in two–photon microscopy of human skin ex vivo by use of optical clearing agents," Optics Express 13(7), 2337–2344 (2005).
98. J. V. Smeden, M. Janssens, G. S. Gooris, and J. Bouwstra, "The important role of stratum corneum lipids for the cutaneous barrier function," Biochimica et Biophysica Acta (BBA)–Molecular and Cell Biology of Lipids 1841(3), 295–313 (2014).

99. M. E. Darvin, J. Schleusener, J. Lademann, and C. S. Choe, "Current views on noninvasive in vivo determination of physiological parameters of the stratum corneum using confocal Raman microspectroscopy," Skin Pharmacology and Physiology 35(3), 125–136 (2022).
100. M. Zimmerley, R. A. McClure, B. Choi, and E. O. Potma, "Following dimethyl sulfoxide skin optical clearing dynamics with quantitative nonlinear multimodal microscopy," Applied Optics 48(10), D79–D87 (2009).
101. E. V. Migacheva, A. B. Pravdin, and V. V. Tuchin, "Alterations in autofluorescence signal from rat skin ex vivo under optical immersion clearing," Journal of Innovative Optical Health Sciences 3(03), 147–152 (2010).
102. A. Hasanzadeh, G. Dehghan, M. Shaghaghi, Y. Panahi, A. Jouyban, and R. Yekta, "Multispectral and molecular docking studies on the interaction of human serum albumin with iohexol," Journal of Molecular Liquids 248, 459–467 (2017).
103. J. H. Lai, E. Y. Liao, Y. H. Liao, and C. K. Sun, "Investigating the optical clearing effects of 50% glycerol in ex vivo human skin by harmonic generation microscopy," Scientific Reports 11, 329 (2021).
104. P. D. Agrba, M. Y. Kirillin, A. I. Abelevich, E. V. Zagaynova, and V. A. Kamensky, "Compression as a method for increasing the informativity of optical coherence tomography of biotissues," Optics and Spectroscopy 107, 853–858 (2009).
105. E. K. Chan, B. Sorg, D. Protsenko, M. O'Neil, M. Motamedi, and A. J. Welch, "Effects of compression on soft tissue optical properties," IEEE Journal of Selected Topics in Quantum Electronics 2(4), 943–950 (1996).
106. I. Y. Yanina, J. Schleusener, J. Lademann, V. V. Tuchin, and M. E. Darvin, "The effectiveness of glycerol solutions for optical clearing of the intact skin as measured by confocal Raman microspectroscopy," Optics and Spectroscopy 128, 759–765 (2020).
107. M. E. Darvin, C. S. Choe, J. Schleusener, and J. Lademann, "Non–invasive depth profiling of the stratum corneum in vivo using confocal Raman microscopy considering the non–homogeneous distribution of keratin," Biomedical Optics Express 10(6), 3092–3103 (2019).
108. I. Carneiro, S. Carvalho, R. Henrique, L. M. Oliveira, and V. V Tuchin, "A robust ex vivo method to evaluate the diffusion properties of agents in biological tissues," Journal of Biophotonics 12(4), e201800333 (2019).
109. J. A. Bouwstra, A. De Graaff, G. S. Gooris, J. Nijsse, J. W. Wiechers, and A. C. V. Aelst, "Water distribution and related morphology in human stratum corneum at different hydration levels," Journal of Investigative Dermatology 120(5), 750–758 (2003).
110. V. D. Genin, D. K. Tuchina, A. J. Sadeq, E. A. Genina, V. V. Tuchin, and A. N. Bashkatov, "Ex vivo investigation of glycerol diffusion in skin tissue," Journal of Biomedical Photonics & Engineering 2(1), 010303 (2016).
111. V. D. Genin, E. A. Genina, V. V. Tuchin, and A. N.Bashkatov, "Glycerol effects on optical, weight and geometrical properties of skin tissue," Journal of Innovative Optical Health Sciences 14(05), 2142006 (2021).
112. O. Nadiarnykh, P. J. Campagnola, "Retention of polarization signatures in SHG microscopy of scattering tissues through optical clearing," Optics Express 17(7), 5794–5806 (2009).
113. C. P. Neu, T. Novak, K. F. Gilliland, P. Marshall, and S. Calve, "Optical clearing in collagen–and proteoglycan–rich osteochondral tissues," Osteoarthritis and Cartilage 23(3), 405–413 (2015).
114. C. Zhang, W. Feng, Y. Zhao, T. Yu, P. Li, T. Xu, Q. Luo, and D. Zhu, "A large, switchable optical clearing skull window for cerebrovascular imaging," Theranostics 8(10), 2696–2708 (2018).
115. W. D. Meador, J. Zhou, M. Malinowski, T. Jazwiec, S. Calve, T. A. Timek, and M. K. Rausch, "The effects of a simple optical clearing protocol on the mechanics of collagenous soft tissue," Journal of Biomechanics 122, 110413 (2021).

Molecular Aggregation of Aluminum Phthalocyanine Chloride in Organic and Water-Organic Media

Inna V. Klimenko[1*], Tatiana Yu. Astakhova[1], Elena N. Timokhina[1], and Anton V. Lobanov[1,2]

[1] N.M. Emanuel Institute for Biochemical Physics Russian Academy of Sciences, 4 Kosygin str., Moscow 119334, Russia

[2] N.N. Semenov Federal Research Center for Chemical Physics, Russian Academy of Sciences, 4 Kosygin str., Moscow 119991, Russia

***e-mail:** inna@deom.chph.ras.ru

Abstract. The process of aluminum phthalocyanine chloride (AlClPc) aggregation in water and water-organic media was studied both by quantum mechanical theoretical calculations and experimental methods of optical absorption and fluorescence spectroscopy. The structures of AlClPc in the monomeric and dimerized (H- and J-aggregates) states in the gas phase and in both N,N-dimethylformamide (DMF) and DMF-water binary solution were calculated by the electron density functional theory (DFT) method. The absorption and fluorescence spectra of these structures were calculated in time-dependent electron DFT approximation. Comparing all data obtained, conclusions about the change in the aggregation state of AlClPc were drawn. Results demonstrate depending AlClPc photophysical parameters on its monomer/dimer ratio in solution, which is determined by concentration of the dye and water in the system. The experimental results obtained for water-organic medium indicate the existence of a critical water concentration (~ 7.8 %), at which the ratio of monomers and dimers (J-aggregates) of AlClPc changes dramatically. In AlClPc-DMF system the dye is completely in monomeric form. The results of the study make it possible to predict the aggregation behavior of AlClPc complexes in water-organic media, as well as to control and manage their aggregation behavior. © 2023 Journal of Biomedical Photonics & Engineering.

Keywords: aluminum phthalocyanine chloride; water-organic media; aggregation process; theoretical calculations; dimers; photophysical properties.

Paper #8120 received 27 Feb 2023; revised manuscript received 1 Jun 2023; accepted for publication 2 Jun 2023; published online 9 Jul 2023. doi: 10.18287/JBPE23.09.030301.

1 Introduction

Photodynamic therapy (PDT) is one of the most promising methods among the clinical treatments for cancer including surgery, radiation therapy, chemotherapy, and immunotherapy. PDT involves a combination of visible light and a photosensitizer (Ps), natural or artificially synthesized photoactive compound. Ps can selectively accumulate in target tissues and generate singlet oxygen or oxygen-containing free radicals when locally irradiated with the light of a certain wavelength, usually a red laser beam, corresponding to the maximum absorption of Ps. Singlet oxygen $^1O_2$ and other active forms of oxygen $O_2^{-\bullet}$, $OH^\bullet$, and H_2O_2, (cytotoxic reactive oxygen species, ROS) play a key role in photodynamic process. They are responsible for oxidative biological damage that destroys vital organelles of tumour cells and leads to cell death and, as a result, to necrosis, apoptosis, or autophagy of the target tissue [1–9].

Currently, significant efforts are focused on advancing PDT by improving drug delivery systems and developing new perfect photosensitizers. In this regard, phthalocyanines (Pc) discovered by Braun and Tcherniac [10] represent a dynamic research field and offer great opportunities due to their magnificent

photophysical and photochemical properties, structural versatility, and stability. All Pc are intensely coloured two-dimensional tetrapyrrolic macroheterocyclic compounds with particular electronic delocalization of the 18-π aromatic system. They display good absorption in the UV-Vis region, namely, the B-band region at 300–400 nm and the Q-band region at 600–700 nm (the so-called "therapeutic window" that guarantees maximum tissue penetration). They also have a long lifetime in the triplet state (0.1–1 ms) and a high quantum yield of singlet oxygen (Φ_Δ = 9.1) [11–19].

The synthetic Pc molecule, related to tetraazaporphyrins (porphyrazines), consists of four pyrrole subunits, which are linked by four nitrogen atoms, similar to the macrocycle of porphyrazines. It is disposed to be integrated with a metal atom (d^0- and d^{10}-configurations) in the central cavity to form metal phthalocyanine complexes (MePc) [20–24]. This central coordinated metal atom can be one of at least 70 different elements of the periodic table [25], and MePc were developed similarly to the biologically important class of porphyrins and can be synthesized through metal-template directed cyclotetramerization between a phthalocyanine precursor (phthalonitriles) and the corresponding metal salt [25].

When complexed with metal, the geometries as well as the electronic and other desirable properties of Pc can be improved. When the central metal atom is diamagnetic or a nontransition metal element, MePc are considered to be more efficient sensitizers owing to their high triplet state quantum yields and long triplet lifetimes [26, 27]. MePc are very interesting substances for biomedical analysis because of easy detection of their changed photophysical properties when treated with biologically significant compounds such as volatile organic compounds, for example, alcohol and aldehyde vapors [28]. Also, the type of central metal ions is a key factor affecting the catalytic activity of MePc [29–31].

The optical properties of MePc also depend on the type of a solvent. For example, the maximum absorption wavelength of MePc weakly correlates with the polarity of the solvent, but it is sensitive to the very structure of the solvent molecules [32]. It is known [33] that N,N-dimethylformamide (DMF), a polar aprotic solvent, interacts with the central metal cation of Pc macrocycle through the double-bonded oxygen atom that can explain high DMF solvation. Also, the highest solvation ability of DMF to Pc can be caused by its donor-acceptor properties [33]. The addition of water to the DMF solution changes the absorption spectrum of Pc. The aggregation of the metal complex also increases with the increase in the percentage of water in the system [34].

Moreover, DMF is a hepatotoxic agent with unique antibacterial and antiviral properties. It is frequently used in safe concentrations as a solvent for pharmceutical, biomedical, and chemical applications because of its unique solvency parameters, for example, when synthesizing sulfadiazine, cortisone, and vitamin B_6 [35, 36]. DMF-water solution is often used as a liquid medium for obtaining platform for drug delivery process [37–39] and can be used as a solvent (in small doses) when receiving drugs for antibacterial and photodynamic therapy.

It is very critical to have MePc molecules in monomeric (isolated) form for their effective functioning as photosensitizers for PDT. In this case, there is no self-quenching of triplet excited states, which leads to efficient triplet energy transfer to the oxygen molecule and triggering the mechanism of photodynamic action [40]. However, for medical diagnostics, it is extremely important to use MePc without any adverse phototoxic properties [40, 41].

Phthalocyanines, like other tetrapyrrolic compounds, have a strong tendency to stacking (self-aggregation) with the formation of dimers and other types of aggregates in water or water solutions, which reduce photodynamic activity of MePc. The degree of aggregation depends on various parameters such as Pc concentration, a central coordinated metal, a solvent type, and substituents in the side chain. The self-aggregation of Pc occurs due to π-π interactions between the aromatic systems of Pc; specific interactions between the metal ligand and solvent molecules are also possible [17, 42, 43]. Aggregation of MePc in water solutions can occur due to hydrogen bonds between the atoms of MePc and water molecules [16, 17, 42, 44].

Various methods are used to prevent the aggregation of MePc complexes in water/biological systems and bodily fluids [8, 24, 45–52]. The modification of the Pc macro ring by replacing peripheral and/or nonperipheral hydrogen atoms with various substituents (alkyl, aryl, alkoxy, and aryloxy), the synthesis of one-dimensional crystals of MePc nanowires to increase the dispersibility of Pc in water, the synthesis of phthalogen conjugates with carbohydrates and the formation of related MePc complexes with carbohydrates, immobilization of Pc on the surface of an inert solid support are among them. Various drug delivery systems are also used to transport Pc to targets, such as liposomal and micellar media, magnetic emulsion with nanostructured colloidal particles and biocompatible polymer nanoparticles, etc.

In order to reduce hydrophobicity and Pc aggregation in water and water solutions, the authors recently proposed to use a theranostic two-dimensional (2D) nano carbon material, oxygen-free graphene, as a part of hybrid systems in conjunction with phthalocyanine. The synthesis of hybrid structures based on oxygen-free graphene and MePc complex – aluminum phthalocyanine chloride (AlClPc, $C_{32}H_{16}AlClN_8$) was reported [17, 53]. It was found that the coordinating interaction of graphene with AlClPc prevents the aggregation of the latter and stabilizes it as a chemically active monomer. Moreover, AlClPc in combination with oxygen-free graphene exhibited a high PD effect.

Thus, the search for new MePc complexes with low aggregation in water and physiological solutions is of current interest. An effective search requires an understanding of the mechanisms of interchromoform interaction in water and water solutions. In this paper in the development of the topic and in order to evaluate the

possibility of changing the physicochemical properties of AlClPc, we carried out the theoretical and experimental studies of the AlClPc complex aggregation in DMF and DMF-water solution with different concentration of water. Aggregation was controlled experimentally by the optical absorption and fluorescence spectra. Quantum chemical methods were used to evaluate all possible AlClPc structures. The adsorption and fluorescence spectra of these structures were calculated in time-dependent electron Density Functional Theory (DFT) approximation. By comparing the experimental and theoretically calculated spectra, conclusions were drawn about the change in the aggregation state of AlClPc depending on the water concentration.

2 Materials and Methods

2.1 Theoretical Calculations; Methods

Quantum chemical calculations were performed with ORCA 4.2.1 package [54]. All structures, monomer in the ground and excited states and dimers in the ground state, were optimized with the DFT method based on the PBE functional [55] and def2-SVP basis set [56] in the gas phase ($\varepsilon = 1$) with empirical Grimme correction D3BJ [57]. All the optimizations were confirmed to be stationary points by the analysis of the number of imaginary frequencies, found – not found for the minima. All spectrum calculations were performed in PBE0 functional [58] with def2-TZVP [56] basis set in DMF and DMF/water mixture solvents taken into account in the Polarizable Continuum Model (CPCM) [59]. The UV-Vis spectra based on the ground states geometry were calculated in time-dependent density-functional theory (TDDFT) [60] without the Tamm-Dancoff approximation. Additionally, absorption spectra based on the excited state dynamics were calculated in the adiabatic Hessian approximation, where both the ground state and the excited state geometries and Hessians are calculated in advance.

2.2 Sample Preparation

A metal complex AlClPc *stock solution* (Acros Organics, USA) with a concentration of 1.18×10^{-3} mol/l was prepared by dissolution of an AlClPc dry sample (weight of 0.0152 g) in 20 ml of DMF (Reakhim, Russia, double-distilled). The resulting concentration was determined from the electronic absorption spectra. The purity and individuality of crystalline AlClPc were confirmed using MALDI mass spectrometry on a Thermo DSQ II device (USA). The *stock solution* was stored in the dark at 4 °C and, if necessary, diluted before the experiment: 0.02 ml *stock solution* of metal complex AlClPc per 8 ml DMF, then *base solution*.

To study AlClPc aggregation behavior in DMF depending on different concentration of AlClPc we diluted 0.02 ml of *stock solution* in 1 ÷ 15 ml of DMF. Also, to study AlClPc aggregation behavior depending on different concentration of water in solution, we placed 2 ml of AlClPc *base solution* in a K10 standard quartz cuvette with a path length of 1 cm (to perform immediately spectrophotometric), and then 0.01 ÷ 1 ml of DMF-water solution (the DMF concentration was C_{DMF} = 4.7 vol.%) was sequentially added to the cuvette with an interval of 0.01 ml, by titration.

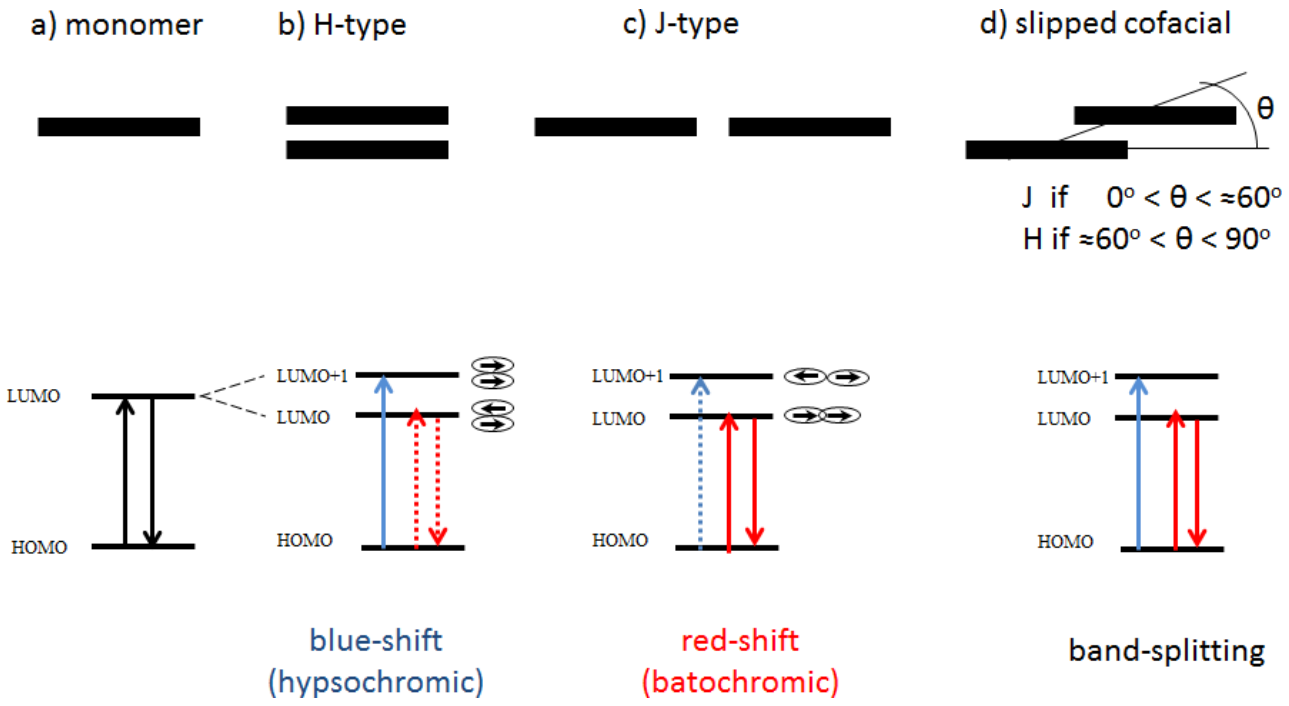


Fig. 1 Scheme of energy levels of MePc in monomer (a) and dimer (b–d) states with allowed (solid arrows) and prohibited (dotted arrows) transitions determined by parallel and antiparallel orientations of dipole transition moments.

2.3 Absorption and Fluorescence Spectroscopy

The UV-Vis absorption spectra were measured at room temperature in air using a TU-1901 UV-Vis spectrophotometer (Beijing Purkinje General Instrument Co. Ltd., China). The poorly resolved absorption spectra were analyzed by their decomposition into Gaussian components. Fluorescence measurements within 630−860 nm were performed with a Fluorat-02 Panorama spectrophotometer (Lumex, Russia). The excitation wavelength was 610 nm. All spectroscopy data were reduced to the initial value of the AlClPc-DMF solution volume.

3 Results and Discussion

3.1 The Classification of MePc Aggregates

According to the exciton coupling theory [61], MePc aggregates are classified as H-type, J-type and slipped cofacial structures depending on the mutual orientation of the molecules in MePc aggregates. The classification for dimers is illustrated in Fig. 1, where the molecules orientation and schematic energy levels are shown.

The long axis of an individual molecule in H-aggregates (Fig. 1(b)) is perpendicular to the axis of the aggregate ("face-to-face" stacked centrosymmetric structure). The transition between HOMO and LUMO levels is prohibited in H-type dimer due to the antiparallel orientations of dipole transition moments of individual molecules in dimer (see short arrows in ovals). That is why H-aggregate dimers show no detectable fluorescence. The lowest-energy allowed transition is between HOMO and LUMO + 1 levels. This band is blue-shifted and referred to as the H band ("H" for hypsochromic).

The long axis of an individual molecule in J-aggregates (Fig. 1(c)) is collinear to the axis of the aggregate ("head-to-tail" stacked). In contrast to H-aggregates, the transition between HOMO and LUMO levels is allowed. That is why J-aggregate dimers demonstrate fluorescence. This band is red-shifted and referred to as the J band ("J" is presumably for Jelley - one of the first researchers who investigate this red-shifted band).

Generally (Fig. 1(d)), the angle between the long axis of an individual molecule and the axis of the aggregate is between 0º and 90º (slipped cofacial structures). All transitions with different probabilities depending on the tilt angle θ are allowed in these dimers. There are both H- and J-bonds with different intensities in absorption spectra of slipped cofacial dimers. If θ is close to 90º, the H-band intensity is high and the J-bond intensity is low. If θ is close to 0º, the situation is vice versa. By convention, slipped cofacial structures refer to H-aggregates if θº≥ 60º, and slipped cofacial structures refer to J-aggregates if θ ≤ 60º.

Due to the structural features, H-aggregates of MePc are formed in many systems and they are not photoactive, while J-aggregates are formed much rarely and could be photoactive [62–65]. There are few works on red- and blue-shifted adsorption and red-shifted fluorescent spectra of Pc dimers [65–68].

3.2 Theoretical Calculations of AlClPc Monomer and Dimers Ground State

The ground state structures of possible types of dimers as well as those of monomer were calculated in gas-phase and DMF and DMF–water solution to elucidate the AlClPc aggregation in water and water-organic solutions.

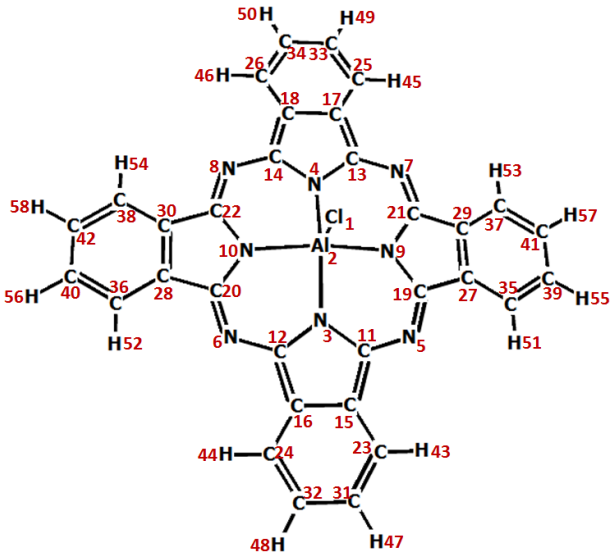
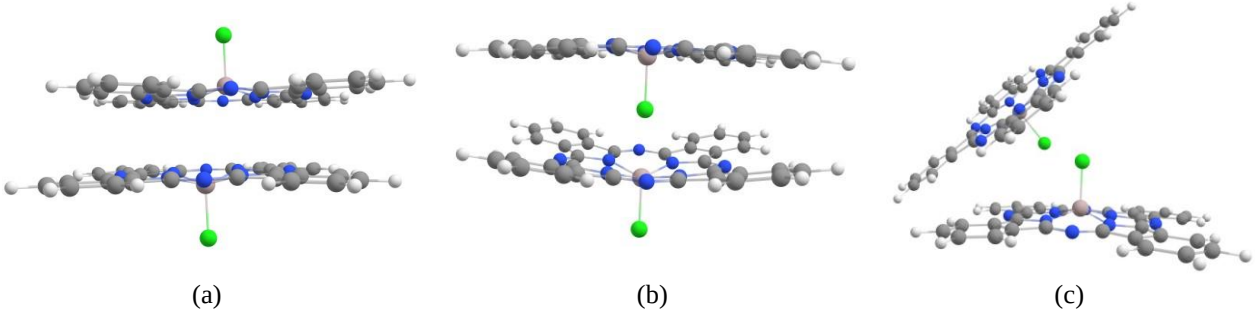


Fig. 2 Optimized structure of AlClPc monomer with atomic numbers.

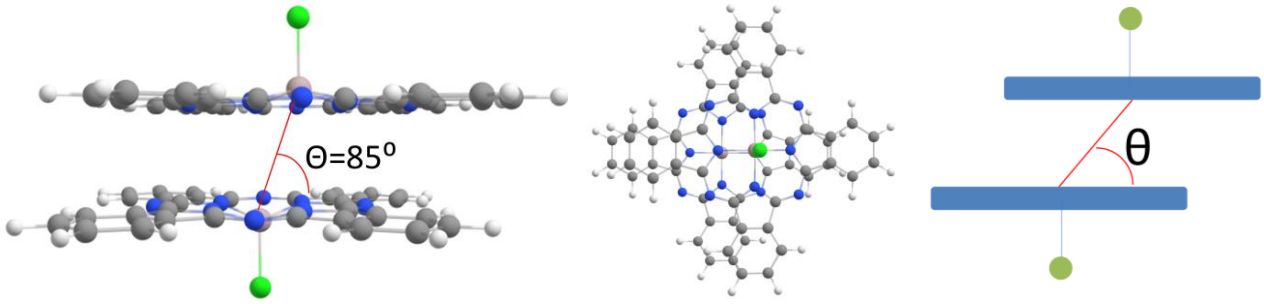


(a) (b) (c)

Fig. 3 Optimized geometries of AlClPc dimers with: (a) "back-to-back", (b) "back-to-face", and (c) "face-to-face" arrangements.

Table 1 AlClPc monomer structure parameters obtained by PBE/def2-SVP DFT calculations and X-ray diffraction data [69].

Parameter	DFT calculation	X-Ray	Parameter	DFT calculation	X-Ray
Bond lengths, Å					
Al_2–Cl_1	2.16	2.18	C_{15}–C_{16}	1.41	1.36
Al_2–N_3	2.00	1.98	C_{15}–C_{23}	1.40	1.46
N_3–C_{11}	1.39	1.44	C_{23}–C_{31}	1.40	1.41
C_{11}–C_{15}	1.46	1.37	C_{31}–C_{32}	1.41	1.41
N_5–C_{11}	1.33	1.36			
Bond angles, degree					
N_3–Al_2–Cl_1	103	103	C_{11}–C_{15}–C_{16}	106	109
C_{11}–N_3–Al_2	126	122	C_{16}–C_{15}–C_{23}	121	122
C_{11}–N_3–C_{12}	108	106	C_{15}–C_{23}–C_{31}	117	116
N_3–C_{11}–C_{15}	110	109	C_{23}–C_{31}–C_{32}	121	122
C_{11}–N_5–C_{19}	127	126			
Dihedral angles, degree					
Al_2–N_3–C_{11}–C_{15}	167	165	N_3–C_{11}–C_{12}–C_{16}	179	174
C_{11}–C_{15}–C_{16}–C_{24}	179	175	N_5–C_{11}–C_{19}–N_9	177	176



(a) (b) (c)

Fig. 4 Dimer of AlClPc with two molecules slightly dislocated: a) side view, b) top view, and c) scheme of slipped cofacial structures: $0 < \theta < 55°$ in J-aggregates and $55° < \theta < 90°$ in H-aggregates.

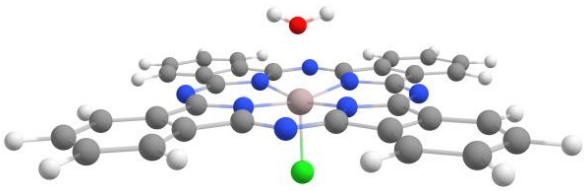
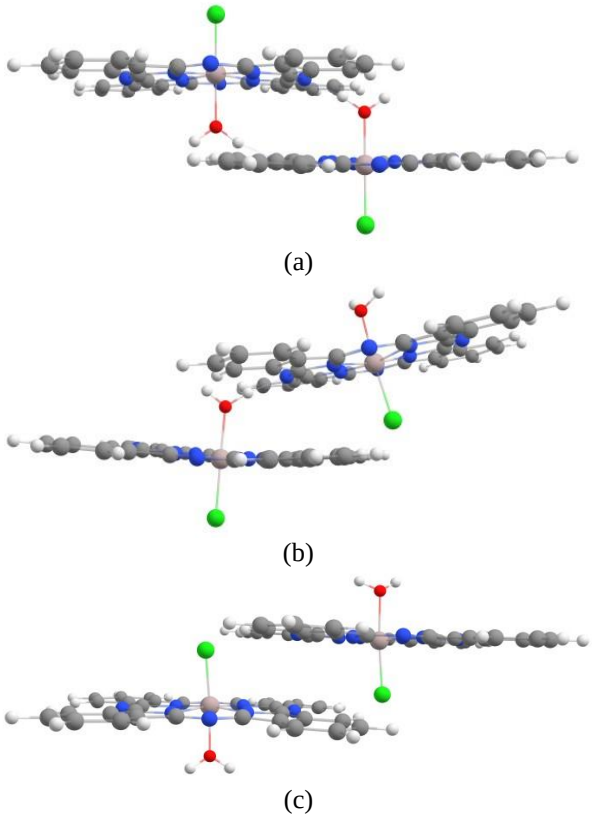


Fig. 5 Bounded AlClPc and H_2O molecules.

The AlClPc monomer with atomic numbering is shown in Fig. 2. The structure parameters of optimized monomer geometry are shown in Table 1, as well as X-ray diffraction literature data [69]. Table 1 demonstrates a good agreement between the calculated ground state AlClPc monomer geometry and the experimentally obtained [69] X-ray diffraction results. All geometries below are optimized in gas because of good reproduction of the experimental molecule parameters when calculating in the gas phase at an adequate cost of computer resources. It was shown that the spectra calculated on the geometry in DMF differ little from the spectra calculated on the gas-phase geometry.

Three different confirmations of dimer can be constructed for the AlClPc molecule, which have (a) “back-to-back”, (b) “back-to-face”, and (c) “face-to-face” arrangements, as illustrated in Fig. 3. Calculations show that “back-to-back” conformation is the most favorable. It is 19.7 and 20.6 kcal/mol lower than “back-to-face” and “face-to-face” conformations, respectively.

This AlClPc dimer is very similar to that of ZnPc [70]. The molecules in AlClPc dimer maintain the monomer geometry (Fig. 4), as in the ZnPc dimer. They are shifted relative to each other, and the aluminum is located above one of the nitrogens of the other molecule. As a result, a slipped cofacial aggregation is formed. The geometric parameters of each AlClPc in the dimer are similar to that in the monomer, and the intermolecular distance is *ca.* 3.7 Å. The energy of the dimer formation is *ca.* −40.7 kcal/mol, calculated as the difference between the dimer energy and twice energy of the monomer.



(a)

(b)

(c)

Fig. 6 Optimized geometries of bonded by two H_2O molecules AlClPc dimers with: (a) "back-to-back", (b) "back-to-face", and (c) "face-to-face" arrangements.

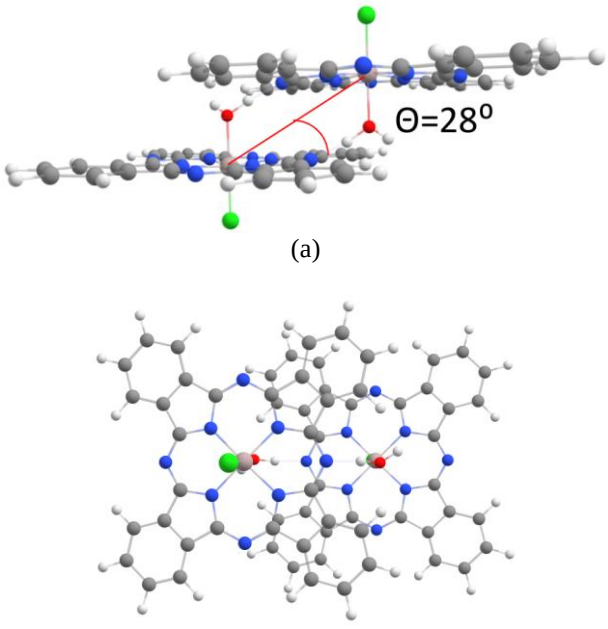
These results show that the lone nitrogen pair is involved in the formation of the AlClPc dimer, as in the case of the ZnPc dimer [70]. The stability of the dimer is due to the intermolecular coordination N → Al, since Al is partially positively charged in the AlClPc molecule. Thus, according to Kasha's exciton theory, the AlClPc dimer belongs to slipped coaficial structure with θ = 85º, i.e. AlClPc dimer can be referred to none-fluorescent H-aggregates [61]. Below, the AlClPc dimer is denoted by $[AlClPc]_2$.

In water-containing solvents, the AlClPc molecule easily binds to one H_2O molecule (Fig. 5) with the formation of a coordination bond between the Al atom of AlClPc and the O atom of the water molecule. The bond length is 2.23 Å and the hydration energy is −16.84 kcal/mol.

Hydrated AlClPc molecules can also form dimers with (a) "back-to-back", (b) "back-to-face", and (c) "face-to-face" arrangements, as illustrated in Fig. 6. Calculations show "back-to-back" arrangement in dimer with the lowest energy (Fig. 6(a)). It is stabilized by four bonds between two AlClPc molecules and two water molecules. Each water molecule has two bonds, one of them is a coordination bond between the O atom of the molecule and the Al atom of the AlClPc molecule, and one hydrogen bond is between the H atom of the molecule and the N atom of the other AlClPc molecule. Below, this AlClPc dimer is denoted by $[AlClPc\_H_2O]_2$. $[AlClPc\_H_2O]_2$ and belongs to slipped coaficial structure with θ = 28º, i.e. $[AlClPc\_H_2O]_2$ can be referred to short-fluorescent J-aggregates [61]. Side and top views of $[AlClPc\_H_2O]_2$ are shown in Fig. 7. The distance between AlClPc molecules in dimer is 3.15 Å.

3.3 Optical Absorption of AlClPc in DMF and DMF-Water Solution

The linear optical spectra of AlClPc in DMF and DMF-water solution in the excited state were analyzed to understand the types of interactions between AlClPc molecules in solutions. Generally, two strong optical absorption regions in the UV-Vis spectra of MePc are mainly caused by the π-electron transition on the conjugated system of Pc. The central metals have a significant effect on the position and intensity of the absorption maxima in the MePc UV-Vis spectra since the delocalization of the π-bond and d-orbitals of the metal in the MePc molecule is influenced by solvent molecules, which leads to a change in the shape and position of the B-band (or Soret band) and the Q-band [32]. According to Davydov's theory the Q-band splitting, the value is a characteristic of interaction energy between molecules with different site symmetries [71].



(a)

(b)

Fig. 7 Dimer of AlClPc, with the two molecules linked through two H_2O molecules: a) side view, b) top view.

The typical Q-band and B-band absorptions in the spectra for AlClPc in DMF and DMF-water solutions (Fig. 8) are in good agreement with those in Refs. [17, 32, 50, 62, 72]. In the absorption spectrum of AlClPc in DMF solution (Fig. 8, curve 1) there are two-principle π-π* transitions from the highest occupied molecular orbital (HOMO) to the lowest unoccupied molecular orbital (LUMO) of the metal complex: the B-band located at 300–450 nm with an absorption maximum at 349 nm, attributed to the a_{2u} (π) → e_g (π*)

transition, which is a characteristic of all MePc, and stronger Q-band located at 600–700 nm with an absorption maximum at λ_{QI} = 673 nm and a shoulder at λ_{QII} = 640 nm, which is a characteristic of all Pc and it is responsible for the colour of the compound. The latter absorption maximum at λ_{QI} = 673 nm is attributed to the $a_{1u}(\pi) \rightarrow e_g(\pi^*)$ transition, as well as its vibrational satellite of low intensity with an absorption maximum at λ_{QIII} = 607 nm, and it is a characteristic of the monomeric form of the AlClPc. At a high Pc concentration, the shoulder at ~ 640 nm transforms into a broader band, the intensity of which increases with the increase of the Pc concentration. The authors [73, 74] attribute this band to H-aggregates and explain a growth of the absorption at ~ 640 nm by dimerization / aggregation of the Pc at higher Pc concentrations. The absence of absorption in the long-wavelength region of the spectrum at λ = 710–850 nm (Fig 8, curve 1) indicates the absence of AlClPc J-aggregates in DMF.

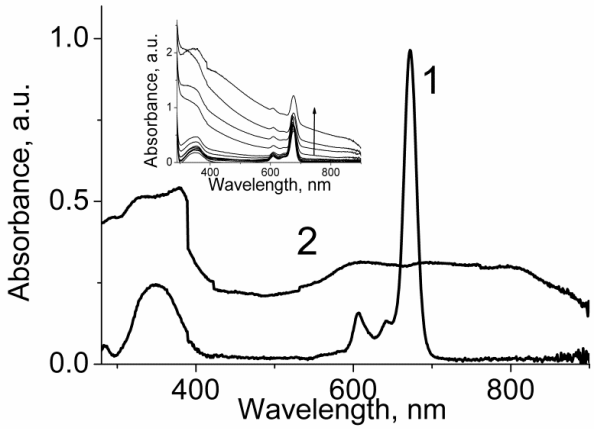


Fig. 8 UV-Vis spectra of AlClPc in DMF (1) and DMF-water mixture (C_{H2O} = 15 vol. %) (2). Inset: UV-Vis spectra of AlClPc in DMF-water solution with different concentration of water (C_{H2O} = 1.2 ÷ 11.1 vol. %); the arrow shows the increase in C_{H2O}.

As expected, the optical absorption of AlClPc in DMF-water solution (Fig. 8, curve 2) differs significantly from the same in DMF solution. There is a sharp decrease in the intensity of the Q-band, a significant broadening of the spectrum lines, and a shift of the absorption spectrum maximum to the short-wave length region. These changes in absorption spectra are related to aggregating behavior of AlClPc in the presence of water and a sharp decrease of AlClPc monomers, which leads to a reduce in quantum yield of singlet oxygen and a decrease in photodynamic activity of Pc [17, 33, 73]. Moreover, the formation of rather rare J-aggregates of AlClPc is observed, as evidenced by the presence of absorption in the optical region of λ = 700–850 nm and the appearance of small peaks in the region of λ = 705–780 nm (Fig. 8, curve 2). An insert describing the behavior of AlClPc in the presence of water indicates the aggregation capacity of AlClPc in binary DMF-water mixtures. With the increase of water concentration, the increase of scattering intensity is observed. At higher water amount in system (> 5 vol. %) the spectra show a complex multiple equilibrium between different types of AlClPc aggregates. The higher-order aggregates (J-type) are seen in a large number. It is known that scattering intensity is proportional to the size of aggregates [75]. So, we can state that aggregates increase in size with the increasing water concentration in system. Moreover, the presence of absorption at long wavelength region testifies a loss of symmetry in the AlClPc molecule due to the distortion of the MePc. This distortion of flat orientation is probably associated with the presence of oxygen in water and its interaction with Al.

3.4 Theoretical Calculations of AlClPc UV-Vis Absorption Spectra

The theoretical UV-Vis spectra were also calculated for monomer and both dimers in ground-state gas geometry for DMF and DMF-water in different proportions for better understanding of AlClPc aggregation and interpretation of the experimental spectra. It turned out that neither the positions of the peaks, nor the oscillator strengths are practically independent of the solvent. Moreover, the spectra are little sensitive to changes in the structural parameters. Also, the position of the peaks changes by no more than 0.5 nm at practically unchanged oscillator strengths when the optimized in DMF geometry is chosen instead of the optimized in gas.

Fig. 9 presents UV-Vis spectra of monomer and dimers in H-aggregate (see Fig. 4) and J-aggregate (see Fig. 7) forms normalized to the Q-band of monomer. Here, vertical lines present spectrum states and solid lines present the Gaussian broadening of the corresponding spectrum. The spectra were calculated in DMF for ground state geometries of corresponding structures, i.e. the spectra were calculated at T = 0 K without taking into account the electron-phonon interaction.

The peak at ~ 670 nm in the monomer spectrum corresponds to the Q-band related to the transition from the ground state to the first excited state. This is HOMO → LUMO transition (see orbitals in Fig. 10). The B-band (Soret) is presented by a series of peaks around ~ 330 nm.

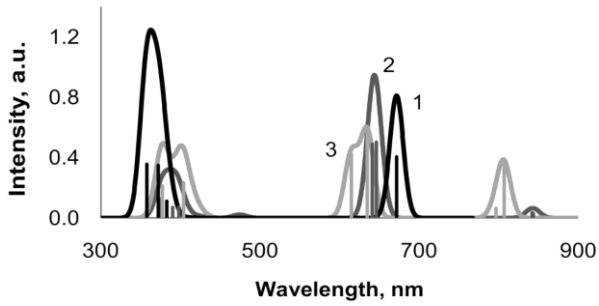
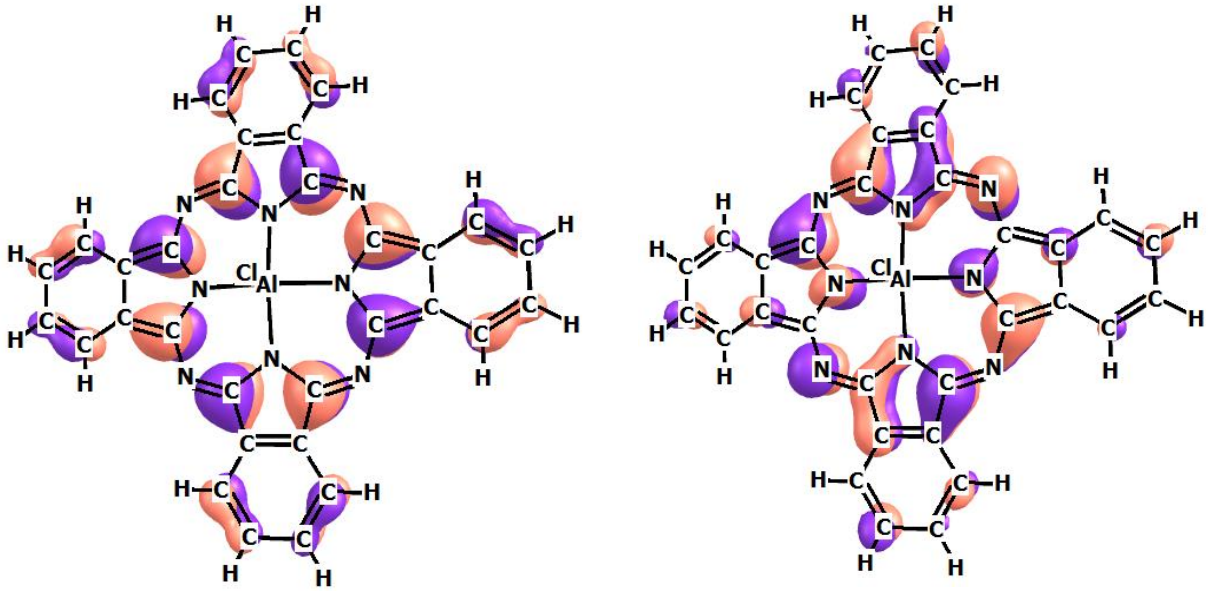


Fig. 9 Calculated absorption spectra of AlClPc monomer (1) and dimers in H-aggregate (2) and J-aggregate (3) forms in DMF.



(a) (b)

Fig. 10 HOMO (a) and LUMO (b) orbitals of AlClPc.

The UV-Vis spectrum of H-aggregates is characterized by two high peaks in the spectrum region at ~ 640 nm and two low peaks in the spectrum region at ~ 840 nm. Since θ in H-aggregates is slightly less than 90 (θ = 85º, see Fig. 4), there is a low-intensity J-band (~ 840 nm), in addition to the high-intensity H-band (~ 640 nm), in the UV-Vis spectrum. The peaks at ~ 640 nm are the characteristics of the dimer; they are hypsochromically shifted with respect to the peak of the monomer. The peak at λ = 641 nm is presented by HOMO → LUMO + 3 transition with small contribution from HOMO − 1 → LUMO transition, and the peak at λ = 646 nm is presented by HOMO – 1 → LUMO + 2 transition with small contribution from HOMO → LUMO + 1 transition. The peaks at ~ 840 nm (λ = 841 and 842 nm) are the characteristics of the dimer; they are bathochromically shifted with respect to the peak of the monomer. They are symmetrical to the peaks at ~ 640 nm but with the inversion in contribution of transitions. The Soret band of the H-aggregate is located around 380 nm.

The calculated UV-Vis spectrum of J-aggregates differs from that of H-aggregates as the AlClPc molecules in J-aggregate are linked by two H_2O molecules. Since θ in J-aggregates is far from 0 (θ = 28º, see Fig. 7), both H-band and J-band in the spectra have high intensities. A hypsochromic shift of the absorption spectrum (H-band) with the formation of two well-separated peaks at 615 and 635 nm is observed, where the peak at 615 nm is presented by HOMO – 1 → LUMO + 3, and the peak at 635 nm is presented by HOMO – 1 → LUMO transition with small contribution from HOMO → LUMO + 2 transition. In the long wavelength spectrum region, the bathochromic shift (J-band) is detected with the formation of two peaks at ~ 797 and ~ 807 nm, while the peak at ~ 765 nm is low intensive. They are symmetrical to the peaks at ~ 615–635 nm but with the inversion in contribution of transitions. The Soret band of the J-aggregate is located around 390 nm as that of H-aggregates.

All calculated peaks in the Cope region are wide and overlap each other, so it is rather difficult to separate them in experimental spectra. Moreover, the peak at ~ 640 nm can indicate both H- and J-aggregates, since the latter have a strongly pronounced hypsochromic peak.

The spectra in Fig. 9 are superimposed on each other. However, in reality, the ratio of peak heights differs due to different concentrations of the components in the solution. Usually the concentration of J-aggregates is small, and concentration of H-aggregates depends on AlClPc concentration. Therefore, the intensities of J-aggregate peaks at ~ 800 nm are small, and their peaks at ~ 630 nm are not visible against the background of the peaks of the H-aggregate. Taking into account the different concentrations of monomers and H- and J-aggregates, Fig. 9 fairly well reflects the general picture of the adsorption spectrum in DMF, where the concentration of monomers is the largest, a small part of dimers is in the form of H-aggregates, and there are no J-aggregates.

According to Fig. 9 we can assume that both AlClPc H-aggregates and monomers influence the position of peaks and their intensity in the region of ~ 610–640 nm of the experimental spectrum (Fig. 8, curve 1). However, it is rather difficult to separate their contributions into the total absorption spectrum because of their overlap. Nevertheless, the presence of H-aggregates is highly improbable in the DMF-water system (Fig. 8, curve 2), since it is energetically favorable for AlClPc molecules to form J-aggregates with the help of two water molecules. In this case, the greater the amount of water is

in the system, the more AlClPc molecules are in the form of J-aggregates.

Electron-phonon interaction should be taken into account for better description of adsorption and emission spectra. In order to predict absorption or emission rates, including all vibronic transitions, ideally one needs both the ground state and excited state geometries and Hessians (matrix of the second-order partial derivatives of the molecule energy-function). Optimization of the excited state requires much more computer costs than optimization of the ground state. Therefore, we limited ourselves to calculating the most intensive Q-band in the monomer, which is of the most important interest from a practical point of view.

Fig. 11 presents monomer experimental and calculated absorption spectra in the region of Q-band. The theoretical spectrum was calculated in DFT/TDDFT without the Tamm-Dancoff approximation (TDA) for the first excited state at T = 298 K. The spectrum was calculated by the Adiabatic Hessian (AH) method, where the Hessians of both the ground and excited states are calculated in advance.

The Fig. 11 demonstrates excellent agreement between experiment and calculation. In the AlClPc spectrum, as well as in the ZnPc spectrum [65], there are two lower bands related to vibronic transitions at ~ 610 nm (Q_{III}) and ~ 640 nm (Q_{II}). The excellent agreement between the experimental adsorption spectrum in the range of 550–750 nm and the Q-band calculated in the adiabatic approximation indicates the presence of almost only monomers in DMF at experimental AlClPc concentrations of $C_{AlClPc} = 2.9 \times 10^{-6}$ mol/l (Fig. 8, curve 1). Thus, the calculated data (Fig. 11) fully confirm the conclusion on the absence of both H- and J- AlClPc aggregates in the DMF solution drawn from the experimental data (Fig. 8, curve 1).

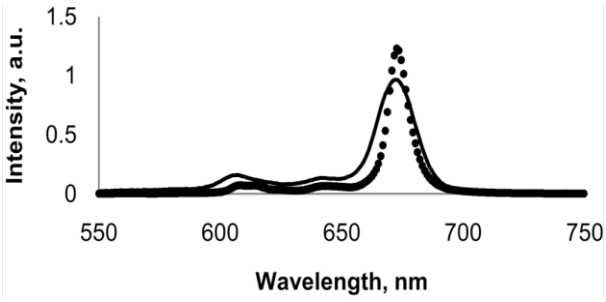


Fig. 11 Absorption spectrum of AlClPc monomer in the region of Q-band including the vibronic transitions: experiment (solid) and TD-DFT calculation (dots).

3.5 Fluorescence of AlClPc in DMF and DMF-Aqua Solution

Aggregation behavior of metal complex AlClPc in DMF was also studied by fluorescence spectroscopy. Fig. 12 shows the fluorescence spectra of AlClPc in DMF at different concentrations of the dye. As seen, AlClPc in DMF demonstrates high fluorescence intensity with excitation wavelength $\lambda_{ex} = 610$ nm. At high concentrations of AlClPc in DMF ($C_{AlClPc} = 2.3 \times 10^{-5}$ mol/l), the AlClPc fluorescence maximum is at ~ 687 nm. When the concentration of AlClPc in DMF decreases (from $C_{AlClPc} = 2.3 \times 10^{-5}$ mol/l to $C_{AlClPc} = 2.3 \times 10^{-6}$ mol/l), there is a blue shift in fluorescence maximums from 687 nm to 679 nm, which indicates that the concentration of Pc in DMF solution is an essential parameter.

Moreover, according to Ref. [65], it can be assumed that the change in the Pc concentration leads to an increase or suppression of fluorescence from different emission bands, and, possibly, the form of fluorescent curves detects various types of Pc aggregates in solution. For example, at higher concentrations of AlClPc in solution (~ 10^{-5} mol/l), pronounced shoulders around the main peak are the characteristics of aggregates, probably dimers, and at dye concentrations $C_{AlClPc} > 5 \times 10^{-6}$ mol/l dimers predominate. However, fluorescence dimers are very rare, and they are of J-type aggregate, so, it might be supposed that J-type dimers prevail in AlClPc-DMF solution with a $C_{AlClPc} > 5 \times 10^{-6}$ mol/l.

This conclusion is well consistent with the data obtained from the calculated optical absorption spectra (Fig. 9 and Fig. 11). Thus, this fact suggests that all experimentally obtained maxima on the absorption spectrum in the Q region can be safely attributed to bands characterizing the monomeric shape of the dye.

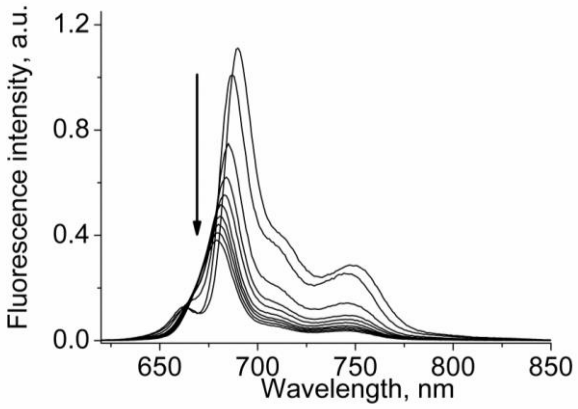


Fig. 12 The fluorescence spectra of AlClPc in DMF. $C_{AlClPc} = 2.3 \times 10^{-6}$ mol/l ÷ 2.3×10^{-5} mol/l. $\lambda_{ex} = 610$ nm. The arrow shows the decrease in AlClPc concentration.

At lower AlClPc concentrations in DMF solution ($< 5 \times 10^{-6}$ mol/l) a significant amount of the dye is in the monomeric form (Fig. 12). However, in our experiments, we did not reach the C_{AlClPc} at which the position of the fluorescence maximum remains unchanged, indicating that all AlClPc molecules are in monomeric form. Nevertheless, the position of the fluorescence maximum at $C_{AlClPc} < 3 \times 10^{-6}$ mol/l changes insignificantly, which indicates the predominance of the monomeric form of the dye in the DMF solution.

It is also known that the spectral position of all luminescence bands shifts to the short-wavelength region of the spectrum as the particle size decreases. A blue shift in fluorescence maximums with decreasing AlClPc

concentration also indicates the quantitative reduction of dimers and the predominance of monomers at low AlClPc concentrations in DMF solution.

The fluorescence spectra of AlClPc in DMF-water solution at different concentrations of aqua are shown in Fig. 13.

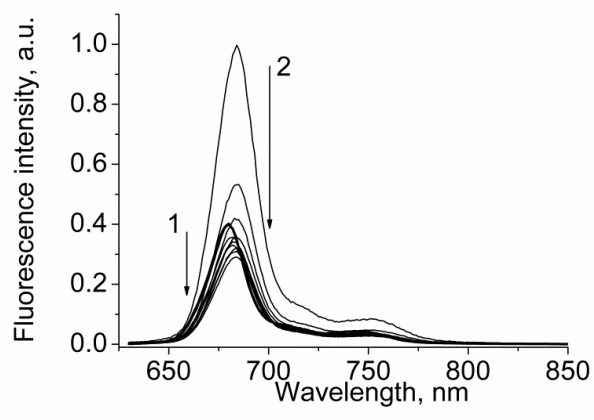


Fig. 13 The fluorescence spectra of AlClPc in DMF-water solution. C_{H20} = 0 ÷ 12.3 vol. %. λ_{ex} = 610 nm. The arrows show the increase in water concentration: (1) from 0 to 6.7 vol. %, (2) from 7.8 to 12.3 vol. %.

Unlike the data in Fig. 12, we observe a red shift of the fluorescence maximum AlClPc in DMF-water solution ($C_{AlClPc} = 2.9 \times 10^{-6}$ mol/l) with the increasing of water concentration in the system from 680 nm (C_{H2O} = 0 vol. %) to 684 nm (C_{H2O} = 5.6 vol. %) that indicates the aggregation process and the reduction of monomers in the system in this water concentration region (Fig. 13). Then, up to the water concentration in the system of C_{H2O} = 12.3 vol. %., the position of the fluorescent maximum does not change. Also, the shape of the fluorescence spectrum of AlClPc in a DMF-water solution differs from the shape of the dye spectrum in pure DMF.

We did not observe peak splitting at ~ 650–675 nm, as in Fig. 12, that indicates that the formation of dimers (aggregates) of the same nature occurs immediately, without the formation of intermediates. Also, we observed a drop in the luminescence intensity with an increase in the water concentration in the system from (C_{H2O} = 0 vol. %) to C_{H2O} = 7.8 vol. %. Then the intensity increases sharply, followed by a fall. Consequently, it might be supposed that there is a strong influence of the water concentration upon the aggregation state of the AlClPc, indicating, also, that there is a critical concentration of water when the ratio of monomers and dimers (J-aggregates) in the system changes dramatically.

When water is added to the system up to C_{H2O} = 6.7 vol. % the decrease in the fluorescence intensity and a shift in the fluorescence maximum towards long wavelengths testify to decreasing gradually the amount of AlClPc monomers and the simultaneous appearance of aggregates. It is hard to separate the input of monomers and aggregates to the general spectrum. However, since the fluorescence intensity sharply increases at C_{H2O} = 7.8 vol. %, it can be assumed that the amount of monomers in the system has sharply decreased due to AlClPc dimerization and formation of fluorescent J-aggregates.

The dependence of the monomeric AlClPc fraction on the water content was calculated by the method proposed in Refs. [73, 76, 77] based on the Gaussian decomposition of the data presented in Fig. 8 and taking into account the material balance equations $2C_m \leftrightarrow C_d$ and $C_0 = C_m + C_d$, where C_0, C_m and C_d are the total concentration of AlClPc and the concentration of monomers and dimers in the system, respectively. C_d and C_m in the mixed solution were determined from the equation for the total absorbance of the solution $D_0 = \varepsilon_0 \times C_0 = \varepsilon_m \times C_m + \varepsilon_d \times C_d$, where ε_0, ε_m, and ε_d are the observed molar extinction coefficient and molar extinction coefficients of monomers and dimers at a certain wavelength, respectively. The concentration of monomers C_m in the system with water was determined from the ratio $C_m = C_0 \times [(\varepsilon_0 - \varepsilon_d)/(\varepsilon_m - \varepsilon_d)]$. Thus, assuming that the proportion of monomers in the solution $f_m = C_m/C_o$, we obtained, that f_m decreases when water is added to the system and remains substantially unchanged up to C_{H2O} = 7.8 vol. %, with an average value of 90%. With a further increase in the water concentration there is a decrease in f_m (for example, at C_{H2O} = 11.2 vol. % the f_m = 0.7). The data obtained confirm the conclusion drawn from the fluorescence data analysis (Fig. 12, Fig. 13) and also indicate the presence of a critical water concentration in the system, at which the ratio of monomers and dimers changes dramatically.

3.6 Theoretical Calculations of AlClPc UV-Vis Fluorescence Spectrum

The calculated (T = 298 K) and experimental ($C_{AlClPc} = 2.9 \times 10^{-6}$ mol/l) fluorescence spectra are shown in Fig. 14. In contrast to the adsorption spectrum (Fig. 11), the calculated fluorescence spectrum does not show exact agreement with the experimental one. This is due to the features of the solvent continuum model, where the parameters are selected for better reproduction of the molecular ground state. Since the absorption spectrum is calculated as a vertical transition on the ground state geometry, it is quite well reproduced with an appropriate choice of functional and basis set.

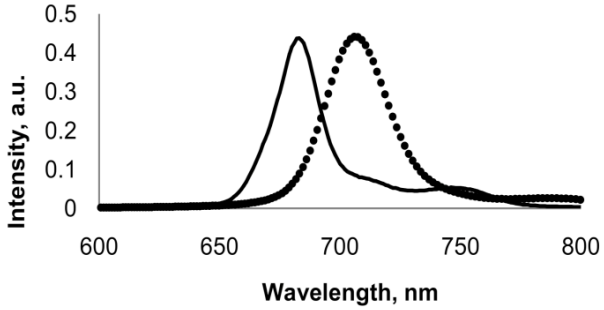


Fig. 14 Fluorescence spectrum of AlClPc monomer: experiment (solid) and TD-DFT calculation (dots).

The fluorescence spectrum is calculated on the geometry of the excited state. Since the continuum solvent model does not take into account the reorganization of the solvent under the transition from the ground state to the excited state. Moreover, the accuracy of the calculation of the fluorescence spectrum is worse than the accuracy of the calculation of the adsorption spectrum. Nevertheless, the calculated fluorescence spectrum reproduces the Stokes shift towards longer wavelengths. As the Stokes shift is primarily the result of vibrational relaxation and solvent reorganization, and the Pc molecule is a dipole surrounded by solvent molecules in a specific orientation, so the dipole moment of the molecule changes upon absorption of a photon and transition to an excited state. Part of the energy gained under the photon absorption is spent on rearranging the orientation of the solvent molecules. Therefore, the emitted photon has a lower energy than the absorbed one, and a shift towards longer wavelengths is observed in the fluorescence spectrum.

4 Conclusion

In this work, we studied the process of AlClPc aggregation in order to reveal differences in the behavior of the dye in organic and water-organic media.

Bearing in mind that AlClPc is being investigated as an effective Pc for PDT, the intensity of absorption in the infrared and visible regions and the ease of controlling the fluorescence maximum, achievable by changing the concentration of the dye in the solution are the important characteristics in the chemistry of Pc. All experimental and theoretical studies show the dependence the photophysical parameters of AlClPc on its aggregation properties and the monomer-dimer ratio in solutions, that are determined by the dye concentration in the medium.

It has been shown that in water-organic media the metal cation in the AlClPc molecule becomes six-coordinated, with two extraligands directed on opposite sides of the Pc macrocycle plane. Reduced solubilization capacity of the water-organic medium stimulates aggregation of MePc. Thus, along with the monomer, the spectra contain Pc dimers differing in structure. The higher the concentration of Pc in the solution and the greater the proportion of water in the water -DMF binary system, the higher the degree of Pc aggregation. Moreover, the simultaneous existence of AlClPc molecules in both forms (monomer/aggregates) is observed, as well as transitions between these states depending on the water and C_{AlClPc} concentrations in system. A critical concentration of water in system (~ 7.8 vol. %) when the ratio of monomers and dimers (J-aggregates) of AlClPc changes dramatically has been determined.

A different picture is observed when AlClPc is dissolved in pure DMF. In this case, Pc is completely in monomeric form. This solvatochromic effect also makes it possible to predict the aggregation behavior of AlClPc complexes in various media in hybrid materials, as well as to control and manage their aggregation behavior.

Acknowledgements

This research was supported by the IBCP RAS State Targets Project # 122041400110-4. We thank the Joint Supercomputer Center of the Russian Academy of Sciences (JSCC RAS) for providing computer resources for quantum calculations.

Disclosures

The authors declare no conflict of interest.

References

1. I. Rosenthal, “Phthalocyanines as photodynamic sensitizers,” Photochemistry and Photobiology 53, 859–870 (1991).
2. I. V. Klimenko, A. V. Lobanov, “Photosensitizing properties of supramolecular systems based on chlorin e6,” Journal of Biomedical Photonics & Engineering 2(4), 040310 (2016).
3. Z. Zhou, J. Song, L. Nie, and X. Chen, “Reactive oxygen species generating systems meeting challenges of photodynamic cancer therapy,” Chemical Society Reviews 45, 6597–6626 (2016).
4. L. Lin X. Song, X. Dong, and B. Li, “Nano-photosensitizers for enhanced photodynamic therapy,” Photodiagnosis and Photodynamic Therapy 36, 102597 (2021).
5. S. B. Brown, T. G. Truscott, “New light on cancer therapy,” Chemistry in Britain 29(11), 955–958 (1993).
6. R. Bonnett (Ed.), Chemical Aspects of Photodynamic Therapy, Gordon and Breach Science Publishers, Amsterdam (2000). ISBN 90-5699-248-1.
7. A. Ogunsipe, T. Nyokong, “Effects of central metal on the photophysical and photochemical properties of non-transition metal sulfophthalocyanine,” Journal of Porphyrins and Phthalocyanines 9(2), 121–129 (2005).
8. Z. A. Carneir, J. C. de Moraes, F. P. Rodrigues, R. G. de Lima, C. Curti, Z. N. da Rocha, M. Paulo, L. M. Bendhack, A. C. Tedesco, A. L. B. Formiga, and R. S. da Silva, “Photocytotoxic activity of a nitrosyl phthalocyanine ruthenium complex – A system capable of producing nitric oxide and singlet oxygen,” Journal of Inorganic Biochemistry 105(8), 1035–1043 (2011).
9. C. Jing, R. Wang, H. Ou, A. Li, Y. An, S. Guo, and L. Shi, “Axial modification inhibited H-aggregation of phthalocyanine in polymeric micelles for enhanced PDT efficacy,” Chemical Communications 54(32), 3985–3988 (2018).

10. A. Braun, J. Tcherniac, "Uber die Produckte der Einwirkung von Acetanhydrid auf Phthalamid," Berichte der deutschen chemischen Gesellschaft 40(2), 2709–2714 (1907).
11. H. S. Nalwa (Ed.), Supramolecular Photosensitive and Electroactive Materials, 1st ed., San Diego, USA (2001). ISBN: 9780080542119.
12. M. van Leeuwen, A. Beeby, I. Fernandes, and S. H. Ashworth, "The photochemistry and photophysics of a series of alpha octa(alkyl-substituted) silicon, zinc and palladium phthalocyanines," Photochemical & Photobiological Sciences 13, 62–69 (2014).
13. C. G. Claessens, U. Hahn, and T. Torres, "Phthalocyanines: From Outstanding Electronic Properties to Emerging Applications," The Chemical Record 8(2), 75–97(2008).
14. F. Cong, B. Ning, Y. Ji, X. Wang, F. Ke, Y. Liu, X. Cui, and B. Chen, "The facile synthesis and characterization of tetraimido-substituted zinc phthalocyanines," Dyes and Pigments 77(3), 686–690 (2008).
15. R. Medyouni, B. Hallouma, L. Mansour, S. Al-Quraishy, and N. Hamdi, "DBU-catalysed synthesis of metal-free phthalocyanines and metallophthalocyanines containing 2(3,4-dimethoxyphenyl)ethanol and 4-hydroxybenzaldehyde groups: characterisation, antimicrobial properties and aggregation behaviour," Journal of Chemical Research 41(5), 291–295 (2017).
16. T. M. Tsubone, G. Braga, B. H. Vilsinski, A. P. Gerola, N. Hioka, A. L. Tessaro, and W. Caetano, "Aggregation of Aluminum Phthalocyanine Hydroxide in Water/Ethanol Mixtures," Journal of the Brazilian Chemical Society 25(5), 890–897 (2014).
17. I. V. Klimenko, E. A. Trusova, A. N. Shchegolikhin, A. V. Lobanov, and L. V. Jurina, "Surface modification of graphene sheets with aluminum phthalocyanine complex," Fullerenes, Nanotubes and Carbon Nanostructures 30(1), 133–139 (2022).
18. J. M. Dąbrowski, L. G. Arnaut, "Photodynamic therapy (PDT) of cancer: from a local to a systemic treatment," Photochemical & Photobiological Sciences 14(10), 1765–1780 (2015).
19. K. Palewska, J. Sworakowski, and J. Lipiński, "Molecular aggregation in soluble phthalocyanines – chemical interactions vs. π-stacking," Optical Materials 34(10), 1717–1724 (2012).
20. I. R. Calori, A. C. Tedesco, "Lipid vesicles loading aluminum phthalocyanine chloride: Formulation properties and disaggregation upon intracellular delivery," Journal of Photochemistry and Photobiology B: Biology 160, 240–247 (2016).
21. M.-S. Liao, S. Scheiner, "Electronic Structure and Bonding in Metal Phthalocyanines, Metal = Fe, Co, Ni, Cu, Zn, Mg," The Journal of Chemical Physics 114(2), 9780−9791 (2001).
22. X. Lu, K. W. Hipps, X. D. Wang, and U. Mazur, "Scanning tunneling microscopy of metal phthalocyanines: d7 and d9 cases," Journal of the American Chemical Society 118(30), 7197−7202 (1996).
23. S. Feng, N. Luo, A. Tang, W. Chen, Y. Zhang, S. Huang, and W. Dou, "Phthalocyanine and metal phthalocyanines adsorbed on graphene: a density functional study," The Journal of Physical Chemistry C 123(27), 16614−16620 (2019).
24. J. Rak, P. Pouckova, J. Benes, and D. Vetvicka, "Drug delivery systems for phthalocyanines for photodynamic therapy," Anticancer Research 39(7), 3323–3339 (2019).
25. G. Swart, E. Fourie, and J. Swarts, "Octakis(dodecyl)phthalocyanines: Influence of Peripheral versus Non-Peripheral Substitution on Synthetic Routes, Spectroscopy and Electrochemical Behaviour," Molecules 27(5), 1529 (2022).
26. G. Gümrükçü, G. K. Karaoğlan, A. Erdoğmuş, A. Gül, and U. Avcıata, "Photophysical, Photochemical, and BQ Quenching Properties of Zinc Phthalocyanines with Fused or Interrupted Extended Conjugation," Journal of Chemistry 2014, 435834 (2014).
27. I. J. MacDonald, T. J. Dougherty, "Basic principles of photodynamic therapy," Journal of Porphyrins and Phthalocyanines 5(2), 105–129 (2001).
28. J. P. Mensing, C. Sriprachuabwong, A. Wisitsoraat, T. Kerdcharoen, and A. Tuantranont, "Phthalocyanine/graphene hybrid-materials for gas sensing in bio-medical applications," in the 4th 2011 Biomedical Engineering International Conference, 29–31 January 2012, Chiang Mai, Thailand, 190–193 (2012).
29. G. Zhang, Y. Zhang, A. Tan, Y. Yang, and M. Tian, "Effects of MN4- type coordination structure in metallophthalocyanine for bioInspired oxidative desulfurization performance," Molecules 27(3), 904 (2022).
30. M. Cavazzini, G. Pozzi, S. Quici, and I. Shepperson, "Fluorous biphasic oxidation of sulfides catalysed by (salen)manganese(III) complexes," Journal of Molecular Catalysis A: Chemical 204–205, 433–441 (2003).
31. M. J. Schultz, M. S. Sigman, "Recent advances in homogeneous transition metal-catalyzed aerobic alcohol oxidations," Tetrahedron 62(35), 8227–8241 (2006).
32. H. Cao, M. Gong, M. Wang, Q. Tang, L. Wang, and X. Zheng, "Steady/transient state spectral researches on the solvent-triggered and photo-induced novel properties of metal-coordinated phthalocyanines," RSC Advances 12(10), 5964–5970 (2022).
33. A. Jlali, C. Jablaoui, M. Lahouel, and B. Jamoussi, "New Zinc (II) Phthalocyanines Substituents: Synthesis, Characterization, Aggregation Behavior, Electronic and Antibacterial Properties," International Journal of Science and Research 5, 1750–1756 (2016).

34. N. B. Sul'timova, P. P. Levin, A. V. Lobanov, and A. M. Muzafarov, "Laser photolysis study of the triplet states of phthalocyanines on the surface of silica nanoparticles in aqueous solutions," High Energy Chemistry 47(3), 98–102 (2013).
35. K. Grodowska, A. Parczewski, "Organic solvents in the pharmaceutical industry," Acta Poloniae Pharmaceutica. Drug Research 67(1), 3–12 (2010).
36. E. I. Olivier, D. du Toit, and J. H. Hamman, "Development of an analytical method for the evaluation of N,N-dimethylformamide in dosage form design," Die Pharmazie-An International Journal of Pharmaceutical Sciences 62(10), 735–738 (2007).
37. E. A. Trusova, I. V. Klimenko, A. M. Afzal, A. N. Shchegolikhin, and L. V. Jurina, "Comparison of oxygen-free graphene sheets obtained in DMF and DMF-aqua media," New Journal of Chemistry 45(23), 10448–10458 (2021).
38. M. E. Alea-Reyes, M. Rodrigues, A. Serra, M. Mora, M. L. Sagrista, A. Gonzalez, S. Duran, M. Duch, J. A. Plaza, E. Valles, D. A. Russell, and L. Perez-Garcia, "Nanostructured materials for photodynamic therapy: synthesis, characterization and in vitro activity," RSC Advances 7(28), 16963–16976 (2017).
39. P. Vallecorsa, G. D. Venosa, M. B. Ballatore, D. Ferreyra, L. Mamone, D. Sáenz, G. Calvo, E. Durantini, and A. Casas, "Novel meso-substituted porphyrin derivatives and its potential use in photodynamic therapy of cancer," BMC Cancer 21, 547 (2021).
40. A. V. Lobanov, G. S. Dmitrieva, N. B. Sul'timova, and P. P. Levin, "Aggregation and Photophysical Properties of Phthalocyanines in Supramolecular Complexes," Russian Journal of Physical Chemistry B 8, 272–276 (2014).
41. N. A. Kuznetsova, N. S. Gretsova, V. M. Derkacheva, O. L. Kaliya, and E. A. Lukyanets, "Sulfonated phthalocyanines: aggregation and singlet oxygen quantum yield in aqueous solutions," Journal of Porphyrins and Phthalocyanines 7(03), 147–154 (2003).
42. C. C. Jayme, I. R. Calori, E. M. F. Cunha, and A. C. Tedesco, "Evaluation of aluminum phthalocyanine chloride and DNA interactions for the design of an advanced drug delivery system in photodynamic therapy," Spectrochimica Acta Part A: Molecular and Biomolecular Spectroscopy 201, 242–248 (2018).
43. N. S. Lebedeva, O. V. Petrova, A. I. Vyugin, V. E. Maizlish, and G. P. Shaposhnikov, "Peculiarities of solvation interaction of water-soluble metallophthalocyanines with ethanol," Thermochimica Acta 417(1), 127–132 (2004).
44. Q. Li, Z. Wang, Q. Liang, M. Zhou, S. Xu, Z. Li, and D. Sun, "Tetra-substituted cobalt (II) phthalocyanine/multi-walled carbon nanotubes as new efficient catalyst for the selective oxidation of styrene using tert-butyl hydroperoxide," Fullerenes, Nanotubes and Carbon Nanostructures 28(10), 799–807 (2020).
45. T. Nyokong, "Effects of substituents on the photochemical and photophysical properties of main group metal phthalocyanines," Coordination Chemistry Reviews 251(13-14), 1707−1722 (2007).
46. J. Janczak, "Water-involved hydrogen bonds in dimeric supramolecular structures of magnesium and zinc phthalocyaninato complexes," ACS Omega 4(2), 3673−3683 (2019).
47. H. K. Moon, M. Son, J. E. Park, S. M. Yoon, S. H. Lee, and H. C. Choi, "Significant increase in the water dispersibility of zinc phthalocyanine nanowires and applications in cancer phototherapy," NPG Asia Materials 4(4), e12 (2012).
48. F. L. Primo, M. M. A. Rodrigues, A. R. Simioni, M. V. L. B. Bentley, P. C. Morais, and A. C. Tedesco, "In vitro studies of cutaneous retention of magnetic nanoemulsion loaded with zinc phthalocyanine for synergic use in skin cancer treatment," Journal of Magnetism and Magnetic Materials 320(14), e211–e214 (2008).
49. O. I. Koifman, M. Hanack, S. A. Syrbu, and A. V. Lyubimtsev, "Phthalocyanine conjugates with carbohydrates: synthesis and aggregation in aqueous solutions," Russian Chemical Bulletin 62(4), 896–917 (2013).
50. M. A. Gradova, I. I. Ostashevskaya, O. V. Gradov, A. V. Lobanov, and V. B. Ivanov, "Photophysical properties and photochemical activity of metal phthalocyanines adsorbed on modified montmorillonite macroheterocycles," Macroheterocycles 11(4), 404–411 (2018).
51. E. P. O. Silva, E. D. Santos, C. S. Gonçalves, M. A. G. Cardoso, C. P. Soares, and M. Beltrame, "Zinc phthalocyanineconjugated with bovine serum albumin mediated photodynamic therapy of human larynx carcinoma," Laser Physics 26, 105601 (2016).
52. E. Güzel, A. Atsay, S. Nalbantoglu, N. Şaki, A. L. Dogan, A. Gül, and M. B. Koçak, "Synthesis, characterization and photodynamic activity of a new amphiphilic zinc phthalocyanine," Dyes and Pigments 97(1), 238–243 (2013).
53. I. V. Klimenko, A. V. Lobanov, E. A. Trusova, and A. N. Schegolikhin, "New hybrid oxygen-free graphene and phthalocyanine aluiminum structures: preparation and physicochemical properties," Russian Journal of Physical Chemistry B 13, 964–968 (2019).
54. F. Nees, F. Wennmohs, U. Becker, and C. Riplinger, "The ORCA quantum chemistry program package," The Journal of Chemical Physics 152(22), 224108 (2020).
55. J. P. Perde, K. Burke, and M. Ernzerhof, "Generalized gradient approximation made simple," Physical Review Letters 77(18), 3865–3868 (1996).
56. F. Weigend, R. Ahlrichs, "Balanced basis sets of split valence, triple zeta valence and quadruple zeta valence quality for H to Rn: Design and assessment of accuracy," Physical Chemistry Chemical Physics 7(18), 3297–3305 (2005).

57. S. Grimme, J. Antony, S. Ehrlich, and H. Krieg, "A consistent and accurate ab initio parametrization of density functional dispersion correction (DFT-D) for the 94 elements H-Pu," The Journal of Chemical Physics 132(15), 154104 (2010).
58. M. Ernzerhof, G. E. Scuseria, "Assessment of the Perdew-Burke-Ernzerhof exchange-correlation functional," The Journal of Chemical Physics 110(11), 5029–5036 (1999).
59. V. Barone, M. Cossi, "Quantum Calculation of Molecular Energies and Energy Gradients in Solution by a Conductor Solvent Model," The Journal of Physical Chemistry A 102(11), 1995–2001 (1998).
60. C. Adamo, D. Jacquemin, "The calculations of excited-state properties with time-dependent density functional theory," Chemical Society Reviews 42(3), 845–856 (2013).
61. M. Kasha, "Energy transfer mechanisms and the molecular exciton model for molecular aggregates," Radiation Research 20(1), 55–71 (1963).
62. A. V. Lobanov, N. B. Sul'timova, P. P. Levin, I. B. Meshkov, and M. Y. Melnikov, "Aluminum phthalocyanine on silica nanoparticles: aggregation and excited states," Macroheterocycles 8(3), 279–283 (2015).
63. K. Kameyama, M. Morisue, A. Satake, and Y. Kobuke, "Highly fluorescent self-coordinated phthalocyanine dimers," Angewandte Chemie International Edition 44(30), 4763–4766 (2005).
64. F. Würthner, T. E. Kaiser, and C. R. Saha-Möller, "J-Aggregates: From Serendipitous Discovery to Supramolecular Engineering of Functional Dye Materials," Angewandte Chemie International Edition 50(15), 3376–3410 (2011).
65. P. P. Pompa, G. Ciccarella, J. Spadavecchia, R. Cingolani, G. Vasapollo, and R. Rinaldi, "Spectroscopic investigation of inner filter effects by phthalocyanine solutions," Journal of Photochemistry and Photobiology A: Chemistry 163(1-2), 113–120 (2004).
66. S. FitzGerald, C. Farren, C. F. Stanley, A. Beeby, and M. R. Bryce, "Fluorescent phthalocyanine dimers—a steady state and flash photolysis study," Photochemical & Photobiological Sciences 1(8), 580–587 (2002).
67. A. Y. Tolbin, V. B. Sheinin, O. I. Koifman, and L. G. Tomilova, "Synthesis of stable dimeric phthalocyanine J-type complexes and investigation of their nucleophilic properties," Macroheterocycles 8(2), 150–155 (2015).
68. P. N. Vasilevsky, E. S. Davydova, D. I. Podshivalova, and M. S. Saveliev, "Nonlinear optical response of Phthalocyanine J-type dimeric complexes of Mg in DMF using pulsed femtosecond radiation," in 2021 IEEE Conference of Russian Young Researchers in Electrical and Electronic Engineering (ElConRus), 26–29 January 2021, Saint Petersburg, Moscow, Russia, 2902–2905 (2021).
69. T. Strenalyuk, S. Samdal, and H. V. Volden, "Molecular Structures of Chloro(phthalocyaninato)-aluminum(III) and -gallium(III) as determined by gas electron diffraction and quantum chemical calculations: quantum chemical calculations on fluoro(phthalocyaninato)-aluminum(III) and -gallium(III), chloro(tetrakis(1,2,5-thiadiazole)porphyrazinato)-aluminum(III) and -gallium(III) and comparison with their X-ray structures," The Journal of Physical Chemistry A 112(38), 9075–9082 (2008).
70. I. R. Calori, C. C. Jayme, L. T. Ueno, F. B. C. Machado, and A. C. Tedesco, "Theoretical and experimental studies concerning monomer/aggregates equilibrium of zinc phthalocyanine for future photodynamic action," Spectrochimica Acta Part A: Molecular and Biomolecular Spectroscopy 214, 513–521 (2019).
71. G. A. Kumar, J. Thomas, N. V. Unnikrishnan, V. P. N. Nampoori, and C. P. G. Vallabhan, "Optical properties of phthalocyanine molecules in cyano acrylate polymer matrix," Materials Research Bulletin 36(1–2), 1–8 (2001).
72. Z. Ou, J. Shen, and K. M. Kadish, "Electrochemistry of Aluminum Phthalocyanine: Solvent and Anion Effects on UV−Visible Spectra and Reduction Mechanisms," Inorganic Chemistry 45(23), 9569–9579 (2006).
73. A. W. Snow, "Phthalocyanine aggregation," in The Porphyrin Handbook: Phthalocyanines: Properties and Materials, K. M. Kadish, K. M. Smith, and R. Guilard (Eds.), Academic Press, San Diego, 129–176 (2003).
74. S. Dhami, D. Phillips, "Comparison of the photophysics of an aggregating and non-aggregating aluminium phthalocyanine system incorporated into unilamellar vesicles," Journal of Photochemistry and Photobiology A: Chemistry 100(1–3), 77–84 (1996).
75. J. Parkash, J. H. Robblee, J. Agnew, E. Gibbs, P. Collings, R. F. Pasternack, and J. C. de Paula, "Depolarized Resonance Light Scattering by Porphyrin and Chlorophyll a Aggregates," Biophysical Journal 74(4), 2089–2099 (1998).
76. D. A. Makarov, N. A. Kuznetsova, O. A. Yuzhakova, L. P. Savvina, O. L. Kaliya, E. A. Lukyanets, V. M. Negrimovskii, and M. G. Strakhovskaya, "Effects of the degree of substitution on the physicochemical properties and photodynamic activity of zinc and aluminum phthalocyanine polycations," Russian Journal of Physical Chemistry A 83, 1044–1050 (2009).
77. A. V Ziminov, V. K. Mal'tsev, A. A. Sherstyuk, Y. A. Vikent'eva, N. S. Seravin, and S. M. Ramsh, "Synthesis and aggregation of cationic zink and magnesium phthalocyanines containing 4-(3,5-dimethyl-1h-pyrazol-1-yl)phenoxy groups," Russian Journal of General Chemistry 88(8), 1648–1656 (2018).

Analysis of Medical Images Classification Methods: The Case of Neutrophil Nuclei

Anna V. Neupokoeva[1*], Semen A. Naydenov[2], and Elena V. Shevchenko[2]
[1] Samara State Medical University, 89 Chapaevskaya str., Samara 443099, Russian Federation
[2] Irkutsk State Medical University, 1 Krasnogo Vosstaniya str., Irkutsk 664003, Russian Federation

***e-mail:** annett_2005@inbox.ru

Abstract. A comparative analysis of methods for processing and classification of medical images was exemplified by neutrophil nuclei digital images. Special consideration was given to three methods: 1) measuring the fractal dimension of neutrophil nuclei to determine their functional state; 2) selecting the neutrophil nucleus contours and calculating their characteristics; 3) using a neural network to classify neutrophils according to the maturity degree. When using a neural network trained on the initial data, the classification accuracy was 60%, whereas after expanding the dataset by modifying the original images, the accuracy reached 85%, although the result was not stable. The combination of contours selection of the target objects in the image, the calculation of the numerical characteristics of these contours, and classification using deep learning methods achieves the accuracy of 72–73%, whereas the accuracy deviation does not exceed 5.6%. © 2023 Journal of Biomedical Photonics & Engineering.

Keywords: fractals; deep learning; neural networks; image processing; neutrophils.

Paper #8811 received 5 Mar 2023; revised manuscript received 27 May 2023; accepted for publication 10 Jun 2023; published online 9 Jul 2023. doi: 10.18287/JBPE23.09.030302.

1 Introduction

These days, there are two clearly pronounced and interrelated trends in medicine. On the one hand, development of diagnostic technology and increased number of available diagnostic studies lead to a rise in the amount of information on each patient's health. On the other hand, the workload for doctors increases, especially during mass morbidity, which drives the need for developing systems for automatic processing of diagnostic information. One of the most common areas in medicine is processing and classification of the images obtained from ultrasound examinations, computed tomography, X-rays, blood smears, or images of histological sections.

The current clinical practice makes wide use of White Blood Cell Differential Count – a percentage ratio of various leukocyte types, especially different neutrophil forms counted in a stained blood smear under a microscope.

Neutrophil granulocytes (neutrophil leukocytes, neutrophils) are the most numerous group of leukocytes. The reference values of their blood level vary from 48 to 78% of the total leukocyte number. The nucleus of a mature segmented neutrophil contains 3–5 segments connected by thin filaments. In blood, there are neutrophils of three types of maturity: metamyelocytes (juvenile neutrophils), band neutrophils and segmented neutrophils. Metamyelocytes and band neutrophils qualify as young cells. Under normal conditions, the metamyelocyte level does not exceed 0.5% and is characterized by a kidney bean shaped nucleus. Band neutrophils under normal conditions make up 1–6% of the total number of leukocytes having an unsegmented nucleus often of a horseshoe or S-shape. Increased percentage of metamyelocytes and band neutrophils may indicate the presence of an acute pyoinflammatory process or acute vast blood loss. This is caused by accelerated hemopoiesis process and by replacement of the lost cells with younger forms [1, 2].

Microscopic examination of blood smears in an ordinary hospital is very time-consuming due to a large number of patients. Various methods of image processing automation have been actively developed in recent years. Conventionally, they can be divided into two types using

This paper was presented on the Biophotonics Workshop of the XX All-Russian Youth Conference-Contest on Optics and Laser Physics, Dedicated to the 100th Anniversary of N.G. Basov, Samara, Russia, November 8–12, 2022.

different approaches. The first type involves the selection of certain numerical characteristics from the source image: the distribution of target objects by brightness, color, size, area, contour length, surface roughness, etc. The next classification [3–6] is based on the obtained numerical data using various methods: the k-nearest neighbors algorithm, the naive Bayes classifier method, the random forest method, and the support vector machine method.

Another approach involves submitting images as input data and using convolutional neural networks (CNN) for classification. Over the past few years, there has been an active growth in the use of neural networks for medical image recognition, for example, for screening diabetic retinopathy, classifying skin diseases and detecting metastases in lymph nodes [7–11]. There have also appeared studies in which both approaches are used for comparison and selecting the best method, or combined together to increase efficiency [12–14].

At the same time, most papers focus on the results of X-ray images or computed tomography since they contain a large amount of labeled data necessary for training a neural network [8, 10–12].

The papers [15–20] devoted to processing blood images solve the problems of erythrocyte classification [3, 4] in anemia or recognition and classification of the leukocyte types in diagnosing leukemia [15–21]. In the case of using neural networks, both publicly available image databases [16, 18] and original images [17, 19, 20] are used for their training. At the same time, it should be noted that training a neural network on a set from one source followed by presenting a set from another source for testing can significantly reduce classification accuracy [18].

Another problem is excessive complexity of standard neural network architectures when using small datasets, as well as the need to modify the architecture and to configure network parameters taking into account specific classification tasks [15, 16].

Refs. [15–21] address the task of leukocyte classification via solving two problems. The first is assigning the leukocyte in the image to a certain class and then counting the number of cells for each class (i.e. automating the quantitative processing of blood smears). The second is identifying the altered (atypical) forms of leukocytes and calculating the ratio between the normal and atypical forms in a blood smear to detect leukemia and specify its stage.

However, if the blood test is not related to detecting oncology, then the task of classifying one of the leukocytes types – neutrophils – by the maturity degree becomes more routine and more widely demanded.

Therefore, the purpose of this work is to compare different methods of classifying neutrophil images and to choose the optimal approach in terms of accuracy, the need for pre-processing of images and the degree of pre-processing automation.

2 Materials and Methods

The materials for this study were fixed and routine stained blood smears in patients of the Surgery Department of Irkutsk Research Center of Surgery and Traumatology (Russia). Blood was collected before and after surgery. The blood smears were stained by Romanowsky–Giemsa solution for 20 min.

The prepared smears were viewed and microphotographed by the Altami-163t microscope equipped with the Levenhuk C-Series digital camera with the resolution of 2048 × 1546 px. The cells were viewed at 1000× magnification. The total number of the neutrophils photos was 146 images: 30 images of metamyelocytes, 57 images of band neutrophils and 59 images of segmented neutrophils (Fig. 1).

All images were divided into three classes with the neutrophils classified according to the morphological characteristics of granulocyte germ cells given below [2]:

1) *metamyelocytes* (Fig. 1(a)) having the cell size from 10 to 16 μm, a bean-shaped or kidney-shaped core, the lilac shade core color. The cytoplasm is pale pink, grayish or light blue. Inside, the cell contains neutrophilic granularity evenly distributed throughout the cytoplasm;

2) *band neutrophils* (Fig. 1(b)) having the cell size from 9 to 12 μm. The nucleus is of curved band shape and of purple color. The chromatin has a crude structure. The cytoplasm is pink with a purple shade. Inside, it is characterized by neutrophil granularity, often unevenly spread over the cytoplasm.

3) *segmented neutrophils* (Fig. 1(c)) having the cell size from 9 to 12 μm. The nucleus is of irregular shape, polymorphic, segmented (with 2 to 5 lobes) and bright purple. Between the lobes there are thin connecting filaments. The cell cytoplasm is pink or pink purple with neutrophil granularity.

2.1 Calculation of Fractal Dimension

The fractal dimension was calculated with the covering method by a specially developed algorithm described in Ref. [22].

2.2 Selection of Contours and Calculation of Their Parameters

To highlight the contours in the photo, two functions were written in Python using the OpenCV library.

The image of a blood smear containing neutrophil was read in grayscale. Then the image was blurred: a filter replaces the central pixel to the median of all pixels in the core area. This type of blur is most effective at removing salt noise. The size of the original image was 1000 × 1000 px and the selected size of the blur core was 25 px. The next step was to binarize the image: all pixels below a certain threshold were changed to white and those above a certain threshold were changed to black. Binarization allows isolating the image of the neutrophil nucleus that looks much darker than the other cells on the stained smear, such as erythrocytes (Fig. 1).

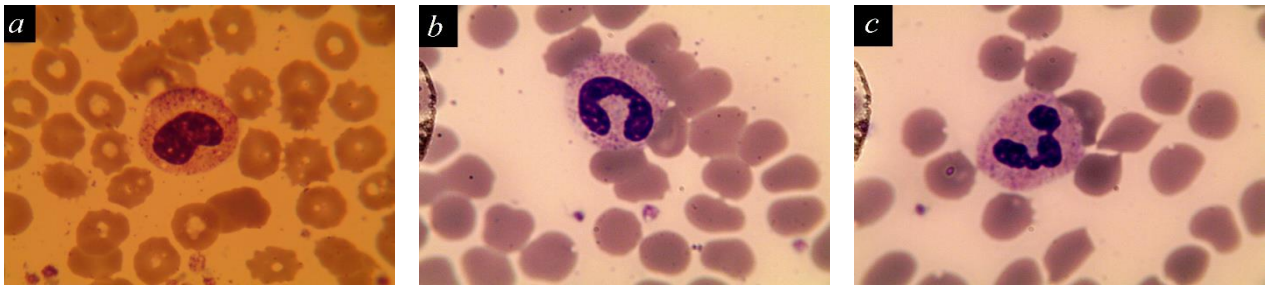


Fig. 1 Three degrees of neutrophil maturity: (a) metamyelocyte, (b) band neutrophil, and (c) segmented neutrophil.

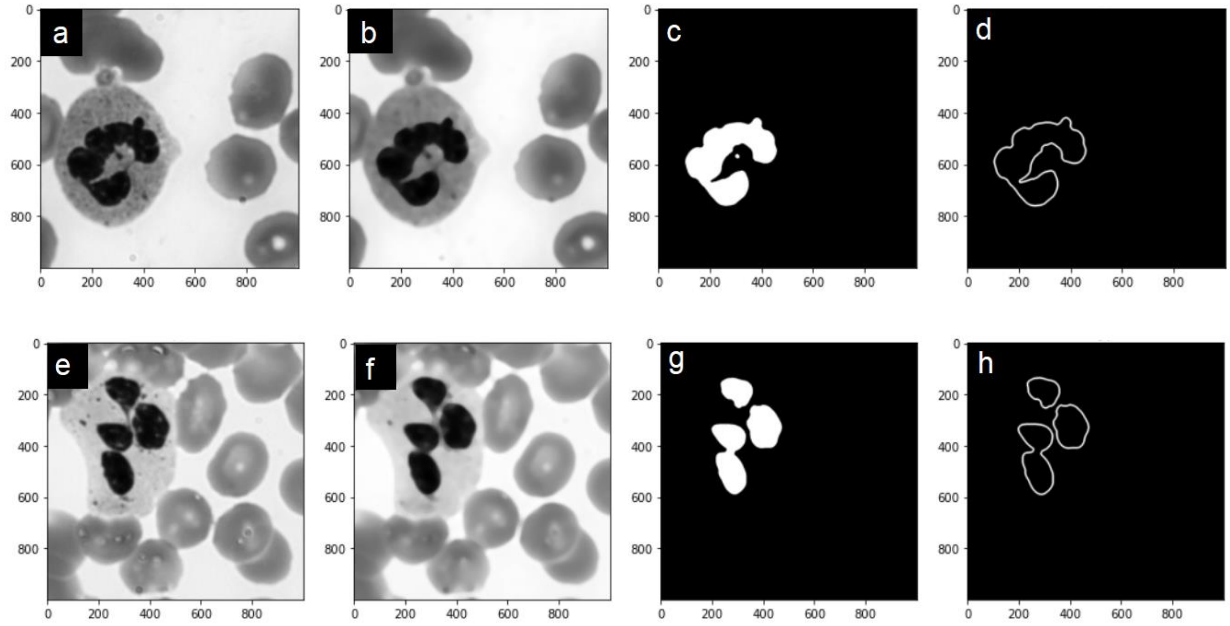


Fig. 2 Selection of a simple nucleus with one contour on the example of a band neutrophil (a, b, c, d) and a composite nucleus with several contours on the example of a segmented neutrophil (e, f, g, h): (a), (e) the original image, (b), (f) the image after blurring, (c), (g) the binary image, (d), (h) the selection of the core contour (it can be single (d) or composite (h)).

In the binary image, the contours were selected and sorted by area from the largest to the smallest. Then the lengths of two contours (the largest and the second largest) were calculated and compared sequentially. If the difference between the lengths exceeded 600 units, then only the largest contour was taken into account for calculation while the others were discarded. If the difference between the contour lengths was less than 600 units, the total length of the contours was considered. After that, the comparison procedure was repeated for the second and third circuits, then for the third and fourth, etc. At the same time, the program counted how many contours were taken into account for this image in the end.

The algorithm for calculating the contour length by summing the lengths of several contours was forcibly used to account for all segments of the nucleus of segmented neutrophils. For band neutrophils and metamyelocytes, this algorithm was automatically interrupted at the first step, since the image contained no objects comparable in size to the neutrophil nucleus in the image (Fig. 2).

As a result of applying the written function to all images of the same class, 6 lists were formed in accordance with the number of calculated parameters:

1) contour length (d),
2) contour area (S),
3) the number of contours taken into account for calculations (N),
4) the ratio of the total contour length to the number of contours taken into account (the perimeter of a single contour is d/N),
5) the contour form-factor that takes into account the degree of deviation of the contour from the spherical shape and was calculated by the following formula:

$$\text{form-factor} = \frac{4\pi S}{d^2} \cdot 100, \quad (1)$$

6) contour compactness calculated by the formula:

$$\text{compactness} = \frac{d^2}{S}. \quad (2)$$

Further classification was carried out according to several combinations of parameters. The most effective pairs were "contour form-factor – contour area" and "contour form-factor – the ratio of the total length of the contour to the number of contours taken into account in the calculation". Classification methods (the k-nearest neighbors method, the Bayes method and the linear regression method) were applied by means of the standard algorithms of the Sklearn library [23–25]. At the same time, the entire dataset was mixed randomly with 80% of the data used to build a classifier and 20% used to test its efficiency. Each method was applied 10 times, the dataset was mixed after each application. Next, the average accuracy (as a percentage) and the accuracy average square deviation were calculated.

2.3 Using a Neural Network for Classification

To classify neutrophils according to the degree of maturity, a convolutional neural network (CNN) was used.

Any neural network consists of the input layer, one or more hidden layers and the output layer. Convolutional neural networks have one or more blocks of convolutional layers designed to highlight the image characteristic features by performing a convolution operation over the entire image [26] followed as a rule by dimension reduction (pooling). Convolutional layers are followed by fully connected layers in which each neuron has a weighted connection with each neuron in the previous layer. The best-known networks that have shown themselves well in image recognition and classification, such as AlexNet, GoogLeNet, VGG, ResNet, have a large number of convolutional layers (5 for AlexNet and 19 for VGG19), as they are designed to recognize a large number of classes (e.g., 1000 classes in the ImageNet Large-Scale Visual Recognition Challenge). At the same time, it is well-known [11, 26] that under small datasets, as well as under a small number of classes, a large number of convolutional layers leads to overfit neural network, decreased classification accuracy and increased learning time.

Since the neural network architecture affects the image classification capabilities and computational complexity of this process, the network configuration should be optimized. The optimization task consists of several steps including selecting the activation function, determining the number of hidden layers and the number of neurons in each layer. The number of neural blocks (or filters) in the input and output layers depends on the input data of this model and the number of classes at the output. There are no specific recommendations for determining and selecting the optimal number of hidden layers and the number of neurons in them, so in practice these parameters are often chosen by trial and error [11, 17, 18, 27].

To determine the optimal neural network architecture, various neural networks with different numbers of neurons and hidden layers were experimentally tested. In our case, the CNN input layer should consist of three neurons (one neuron for each component of the RGB image), and the output layer also consists of three neurons, according to the number of classes that we define. Variants with one, two and three blocks of convolutional layers were tested. Each block consisted of two consecutive convolutional layers with a 3×3 convolution core, and the number of neurons in the subsequent layer was two times greater than in the previous one. The next layers were maxpooling (that reduces dimension) and data normalization (BatchNormalization). To avoid CNN overfitting, 20% of neurons were dropped out. The activation functions were ReLU.

To classify neutrophil images without preprocessing the best result was shown by a neural network whose architecture is presented in Fig. 3. The CNN was created by means of the Keras library functions of the Python programming language.

An image converted to 256 × 256 px format was fed to the network input. The neural network included three blocks of convolutional layers (each block was followed by a dimension reduction operation) and three fully connected layers containing 64, 32, and 3 neurons, respectively (Fig. 3).

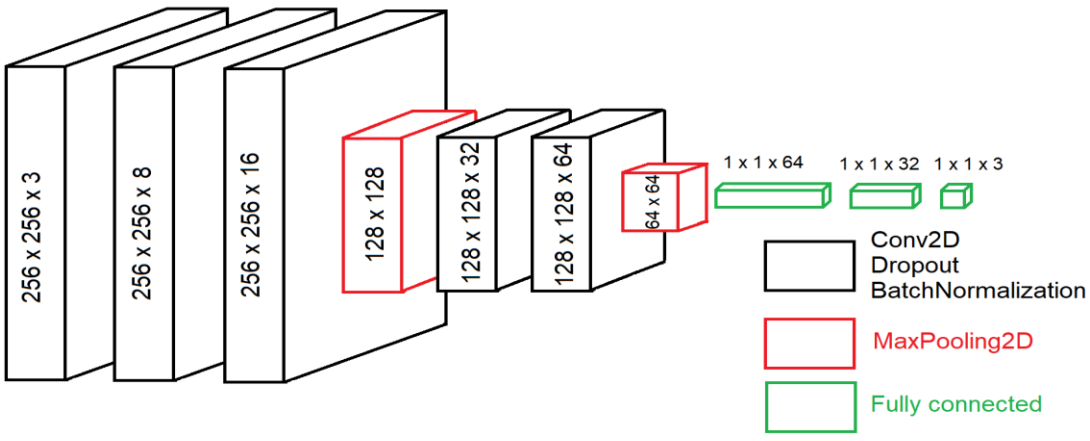


Fig. 3 Neural network architecture.

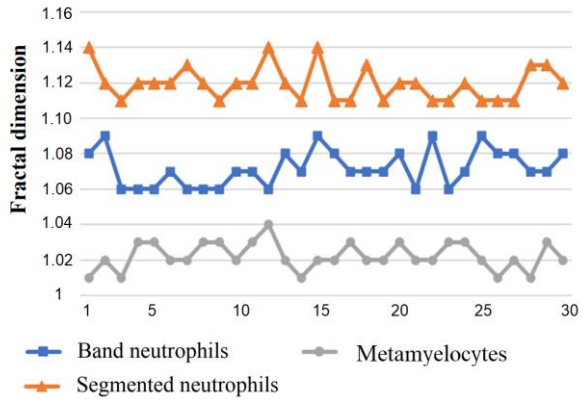


Fig. 4 Fractal dimension of neutrophils.

The whole set of images was divided into a part intended for training a neural network (80% or 117 images) and a part used for validation of learning outcomes (20% or 29 images). To assess the quality of the neural network classification, the standard parameters were used: accuracy and loss function. The training was carried out for 100 epochs.

3 Results

The calculation of the fractal dimension shows the absence of intersections for neutrophils belonging to three different classes according to their morphological features (Fig. 4): for the band neutrophils, the fractal dimension of the nucleus ranges from 1.06 to 1.08. For the segmented neutrophils, the fractal dimension of the nucleus ranges from 1.11 to 1.14. For the metamyelocytes, the fractal dimension of the nucleus ranges from ranges from 1.01 to 1.03. The confidence interval was calculated using the standard method for small samples, so the same number of images of each class was selected from the entire set of images containing 30 pieces each [22].

The obtained data were processed by calculating the Student coefficient for independent quantities. A comparison of the critical and empirical t-criteria showed the statistical significance of differences in the fractal dimension of the nuclei of the metamyelocytes as well as the segmented and band neutrophils [22].

Calculating the lengths, areas, and other parameters of the neutrophil nucleus contours described above is adequate for separating the metamyelocytes (contour length 872 ± 234, contour area (60.8 ± 13.2) × 10^3) from the two other classes (contour length 1356 ± 432 and 1470 ± 284, contour area (74.4 ± 12.8) × 10^3 and (62.6 ± 10.6) × 10^3). At the same time, it is impossible to separate the segmented and the band neutrophils by the length or the area of the core contour, since these parameters overlap for both classes. But when considering the number of contours to take into account, the total length of the contour metamyelocytes and band neutrophils for all images contain one contour, whereas the segmented ones contain from 1 to 4 (1.8 contours on average).

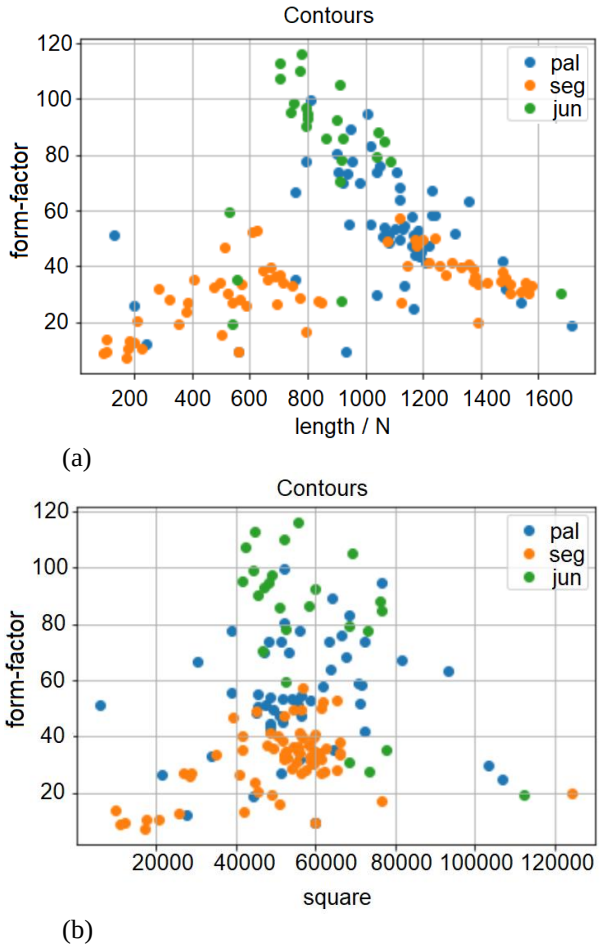


Fig. 5 The position of the objects in the form of points on the coordinate plane: (a) “contour form-factor is the ratio of the total length of the contour to the number of contours taken into account in the calculation”, (b) “contour form-factor is a contour area”. The metamyelocytes, the band and segmented neutrophils are marked with dots of different colors.

Therefore, two combinations of parameters were experimentally selected for automatic classification: “contour form-factor – contour area” and “contour form-factor – the ratio of the total length of the contour to the number of contours taken into account in the calculation”. Fig. 5 shows the position of all the studied objects in the form of points on the coordinate plane with the objects of different classes indicated by different colors.

The accuracy of classification by various methods based on the numerical contour data is presented in Table 1. The highest accuracy was shown by the Bayes method (73%) whereas the logistic regression method has a slightly lower accuracy (72%) but a more stable classification result.

The results for the neural networks applied for original image classification turned out to be unstable: the classification accuracy according to training data reached 93%, but the validation accuracy did not exceed 60% (Fig. 6a). Low classification accuracy can be attributed to a relatively small amount of training data.

Table 1 Classification accuracy (%) of neutrophil nuclei by various methods based on numerical contour parameters.

Contours parameters	Classification methods		
	k-nearest neighbors method	**linear regression method**	**Bayes method**
"contour form-factor – the ratio of the total length of the contour to the number of contours taken into account in the calculation"	69.1 ± 5.6	72.4 ± 5.0	73.6 ± 5.6
"contour form-factor – contour area"	52.4 ± 8.8	65.8 ± 5.6	71.9 ± 7.7

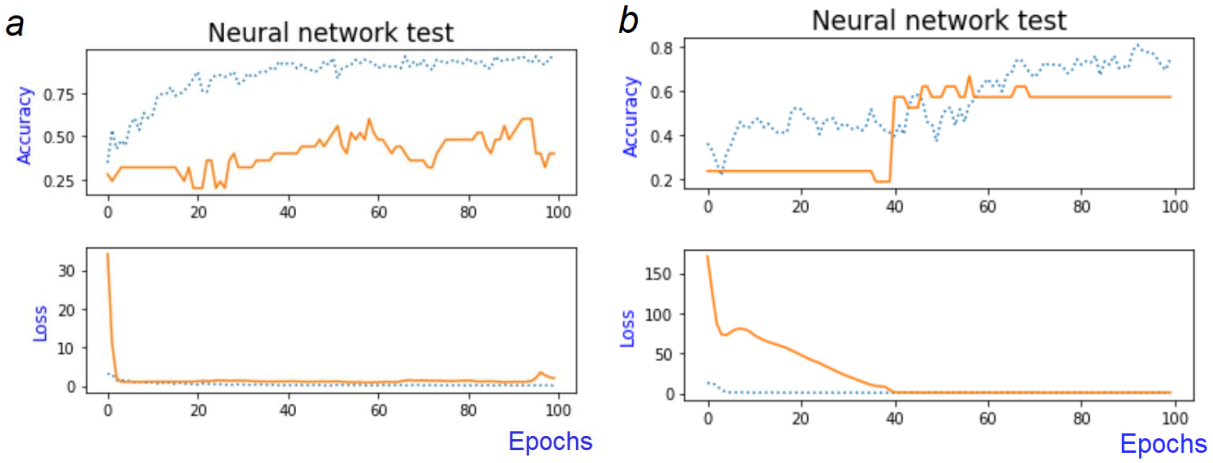


Fig. 6 Classification accuracy and loss function: (a) for source images, (b) for binary images. The blue dotted line is training, the solid orange line is validation.

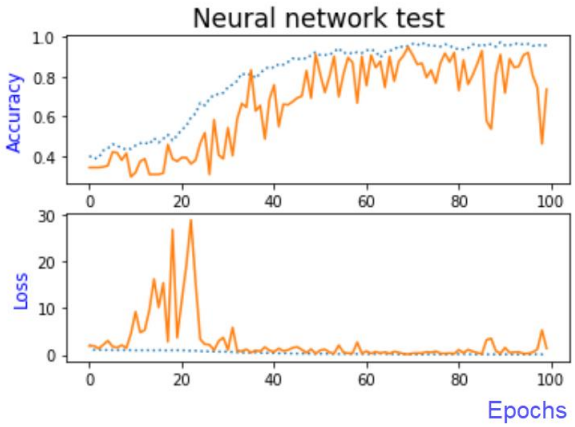


Fig. 7 Classification accuracy and loss function for classification by an extended set of non-processed images. The blue dotted line is training, the solid orange line is validation.

The use of neural networks to classify binary images has shown the classification accuracy of 75–85% for the training data while the validation accuracy did not exceed 65%, however their classification results are more stable than for the original images (Fig. 6(b)).

To increase classification accuracy, a larger dataset is needed. One of the ways to expand the training dataset is to add images obtained by rotating/shifting/compressing the original photos [20, 28].

In this study, we generated additional data by rotating images at a random angle up to 270 degrees, shifting them vertically and horizontally by 10% of the original size, and reflecting them horizontally. The amount of data for segmented and band neutrophils was increased 10 times while the increase for metamyelocytes was 20 times since the number of their images was initially smaller. Thus, the expanded dataset consisted of 1510 images (520 for the segmented, 500 for the bond neutrophils and 490 for the metamyelocytes). 1208 images were used to train the neural network, and 302 images were used for validation.

Neural network training on an expanded dataset took 100 epochs, while the accuracy of the training sample reached saturation by 70 epochs and reached 98%, although classification accuracy during validation remained unstable and the averaged magnitude was about 85% (Fig. 7).

The relatively low accuracy of classification of neutrophil images using a neural network is explained by a small number of images included into the training set. In contrast, non-binary classification of objects often demonstrates poor accuracy even with a training sample size of several thousand images. Thus, an attempt to divide the fundus images automatically into 5 classes – the absence of diabetic retinopathy and four stages of retinopathy presence – demonstrated only a 57% classification accuracy even for a set of more than 12,000 images [29]. The same paper reports that transition to binary classification increased the accuracy up to 80%.

Ref. [30], on the contrary, states that 3000 images are sufficient not only for a stable classification result but also to obtain an accuracy of 95–98% by dividing images into three classes. Both papers [29, 30] used open data from the Kaggle database. At the same time, in Refs. [31, 32], the original image sets required pre-processing of images or including additional parameters to improve the accuracy of classification.

Refs. [15, 16, 18] describe the classification of leukocytes by five types of neural networks with a much more complex architecture than the one we propose. Their high classification accuracy (97–98%) was achieved by training the network on a large dataset and, then, using an already trained network to classify leukocytes (a so-called "transfer learning" approach).

Ref. [33] used a set of images comparable to ours, while the goal was to segment the cells in the image and to divide them into three classes. The classification accuracy depended on the cell type and reached 56–61% for erythrocytes, 67–91% for lymphocytes, and 28–56% for platelets.

It should be noted that the classification accuracy we obtained by using a neural network of 60% for the initial set of images and 85% for the extended set is in good agreement with the literature data on solving similar problems [18, 19, 33], but the stability of the results is insufficient for practical use.

Therefore, in the case of a small initial image set, a more stable result is obtained by preprocessing images, which makes it possible to identify the numerical characteristics of the contours, and then to use them for classification. A similar approach was used in Ref. [17] to solve the classification problem, and in Ref. [34] for segmentation of cell images.

The algorithm of contour selection and calculation of their numerical parameters proposed in this paper has proven its validity and feasibility as one of the stages in automating the process of calculating fractal dimension. It should be noted that the algorithm identified the core contour incorrectly only in 16% of cases. As a rule, incorrect operation of the algorithm is attributed to a single binarization threshold for all images, although in some cases, red blood cells are the same dark color as the neutrophil nucleus, which leads to erroneous account for an additional contour. The opposite situation is observed, when the core is painted weakly and in this case, the selected contour is unnecessarily "cut off".

The presented results demonstrate that fractal analysis provides the best accuracy in the classification of neutrophils by maturity degree because this method most definitely takes into account the shape of the neutrophil nucleus rather than its size. A disadvantage of the method at the moment is incomplete automation at the contour selection stage which should be eliminated in the future. Moreover, dimensionality calculation was carried out using images taken with the same magnification and having the same resolution. The question of the stability of the results with other image acquisition parameters remains open. For example, Ref. [30] uses an algorithm similar to the one we described in this paper – image binarization, contour selection and fractal dimension calculation – and reveals that the results of fractal analysis depend on the degree of magnification of histological images.

The most stable classification result is observed for a combination of several numerical contour parameters and further classification using deep learning methods.

4 Conclusion

This study has shown the possibility of applying two different approaches to image analysis: image classification be means of a neural network and using images to isolate numerical features, which allows classification to be carried out with the help of deep learning methods.

Training a neural network on a limited amount of data has proven to be possible but classification accuracy of this technique is quite low. When expanding the dataset by modifying the original images, classification accuracy increases to an average of 85%, whereas the main disadvantage of this method is unstable results.

Selecting the contours of the image target object and calculating their numerical characteristics allow the classification accuracy to achieve 72–73%, while the accuracy deviation does not exceed 5.6%.

5 Disclosures

The authors have no relevant financial interest in this article and no conflict of interest to disclose.

References

1. J. Actor, Elsevier's Integrated Review Immunology and Microbiology, 2nd ed., Elsevier (2012). ISBN: 9780323074476.
2. D. Zucker-Franklin, M. F. Greaves, C. E. Grossi, and A. M. Marmont, "Neutrophils, Atlas of Blood Cells: Function and Pathology," Lea and Ferbiger, Philadelphia 1(2), (1988).
3. T. Go, H. Byeon, and S. J. Lee, "Label-free sensor for automatic identification of erythrocytes using digital in-line holographic microscopy and machine learning," Biosensors and Bioelectronics 103, 12–18 (2018).
4. Y. G. Kim, Y. Jo, Y. Cho, H. S. Min, and Park, "Learning-based screening of hematologic disorders using quantitative phase imaging of individual red blood cells," Biosensors and Bioelectronics 123, 69–76 (2019).

5. V. K. Ilyin, Z. O. Solovieva, M. A. Skedina, N. V. Verdenskaya, K. V. Volkova, and I. A. Ivanova, "Choice of an optimal set of signs and evaluation of the quality of microbial objects recognition by their images," Aerospace and Environmental Medicine 52(3), 73–79 (2018). [in Russian]
6. P. Wang, J. Wang, L. Wang M. Yin,Y. Li, and J. Wu, "Classification of pathogenic bacteria using near-infrared diffuse reflectance spectroscopy," Journal of Applied Spectroscopy 85(6), 1029–1036 (2018).
7. V. Gulshan, L. Peng, M. Coram, M. C. Stumpe, D. Wu, A. Narayanaswamy, S. Venugopalan, K. Widner, T. Madams; J. Cuadros, R. Kim, R. Raman, P. C. Nelson, J. L. Mega, and D. R. Webster, "Development and validation of a deep learning algorithm for detection of diabetic retinopathy in retinal fundus photographs," Journal of the American Medical Association 316(22), 2402–2410 (2016).
8. R. Yamashita, M. Nishio, R. K. G. Do, and K. Togashi, "Convolutional neural networks: an overview and application in radiology," Insights into Imaging 9, 611–629 (2018).
9. V. O. Vinokurov, Y. Khristoforova, O. Myakinin, I. Bratchenko, A. Moryatov, A. Machikhin, and V. Zakharov, "Neural network classifier of hyperspectral images of skin pathologies," Computer Optics 45(6), 879–886 (2021). [in Russian]
10. X. Yi, E. Walia, and P. Babyn, "Generative adversarial network in medical imaging: A review," Medical Image Analysis 58, 101552 (2019).
11. G. Litjens, T. Kooi, B. E. Bejnordi, A. A. A. Setio, F. Ciompi, M. Ghafoorian, Jeroen A.W.M. van der Laak, Bram van Ginneken, and C. I. Sánchez, "A survey on deep learning in medical image analysis," Medical Image Analysis 42, 60–88 (2017).
12. Yu. D. Agafonova, A. V. Gaidel, E. N. Surovtsev, and A. V. Kapishnikov, "Meningioma detection in MR images using convolutional neural network and computer vision methods," Journal of Biomedical Photonics and Engineering 6(3), 030301 (2020).
13. G. C. Mallika, A. Alsadoon, D. T. H. Pham, S. Abdullah, H. T. Mai, P. W. C. Prasad, and T. Q. V. Nguen, "A Novel Intelligent System for Detection of Type 2 Diabetes with Modified Loss Function and Regularization," Proceedings of the Institute for System Programming of the Russian Academy of Sciences, 33(2), 93–114 (2021). [In Russian]
14. A. E. Sulavko, P. S. Lozhnikov, A. G. Choban, D. G. Stadnikov, A. A. Nigrey, and D. P. Inivatov, "Evaluation of EEG identification potential using statistical approach and convolutional neural networks," Information and Control Systems (6), 37–49 (2020).
15. A. Meenakshi, J. A. Ruth, V. R. Kanagavalli, and R. Uma, "Automatic classification of white blood cells using deep features based convolutional neural network," Multimedia Tools and Applications 81(21), 30121–30142 (2022).
16. H. Kutlu, E. Avci, and F. Özyurt, "White blood cells detection and classification based on regional convolutional neural networks," Medical Hypotheses 135, 109472 (2020).
17. A. Bodzas, P. Kodytek, and J. Zidek, "Automated Detection of Acute Lymphoblastic Leukemia From Microscopic Images Based on Human Visual Perception," Frontiers in Bioengineering and Biotechnology 8,1005 (2020).
18. L. Vogado, R. Veras, K. Aires, F. Araújo, R. Silva, M. Ponti, and J. M. R.Tavares, "Diagnosis of leukaemia in blood slides based on a fine-tuned and highly generalisable deep learning model," Sensors 21(9), 2989 (2021).
19. C. Marzahl, M. Aubreville, and A. Maier, "Classification of leukemic B-Lymphoblast cells from blood smear microscopic images with an attention-based deep learning method and advanced augmentation techniques," in ISBI 2019 C-NMC Challenge: Classification in Cancer Cell Imaging, Lecture Notes in Bioengineering, A. Gupta, R. Gupta (Eds.), Springer, Singapore, 13–22 (2019).
20. M. S. Jarjees, S. S. M. Sheet, and B. T. Ahmed, "Leukocytes identification using augmentation and transfer learning based convolution neural network," Telkomnika (Telecommunication Computing Electronics and Control) 20(2), 314–320 (2022).
21. S. M. Abas, A. M. Abdulazeez, and D. Q. Zeebaree, "A YOLO and convolutional neural network for the detection and classification of leukocytes in leukemia," Indonesian Journal of Electrical Engineering and Computer Science 25(1), 200–213 (2022).
22. S. A. Naydenov, P. A. Naydenov, and E. V. Shevchenko, "Practical implementation analysis of the fractal dimension calculating algorithm for the medical images by the example of neutrophil nuclei," Journal of Biomedical Photonics and Engineering 6(1), 010304 (2020).
23. H. Brink, J. W. Richards, and M. Fetherolf, Real-World Machine Learning, Manning Publication, Shelter Island, New York (2016). ISBN 9781617291920.
24. C. M. Bishop, Pattern recognition and machine learning, Springer, New York (2006). ISBN: 9780387310732.
25. A. Smola, S. V. N. Vishwanathan, Introduction to Machine Learning, Cambridge University Press, United Kingdom (2008).
26. M. Nielsen, Neural Networks and Deep Learning, Determination Press, San Francisco, CA, USA (2015).
27. T. Falk, D. Mai, R. Bensch, Ö. Çiçek, A. Abdulkadir, Y. Marrakchi, A. Böhm, J. Deubner, Z. Jäckel, K. Seiwald, A. Dovzhenko, O. Tietz, C. D. Bosco, S. Walsh, D. Saltukoglu, T. L. Tay, M. Prinz, K. Palme, M. Simons, I. Diester, T. Brox and O. Ronneberger, "U-Net: deep learning for cell counting, detection, and morphometry," Nature Methods 16, 67–70 (2019).

28. T. A. Sumi, M. S. Hossain, and K. Andersson, "Automated Acute Lymphocytic Leukemia (ALL) Detection Using Microscopic Images: An Efficient CAD Approach," Chapter 5 in Proceedings of Trends in Electronics and Health Informatics: TEHI 2021. Lecture Notes in Networks and Systems 376, M. S. Kaiser, A. Bandyopadhyay, K. Ray, R. Singh, V. Nagar (Eds), 363–376 (2022).
29. T. H. Mamedov, D. V. Dzjuba, and A. N. Narkevich, "Application of convolutional neural networks for recognition of diabetic retinopathy," Siberian Medical Review 1, 83–87 (2022). [in Russian]
30. A. M. Ignatova, M. A. Zemlyanova, M. S. Stepankov, and Y. V. Kol'dibekova, "Using multifractal analysis to assess the morphology of lung tissues with and without pathology," Fundamental and Applied Aspects of Public Health Risk Analysis: Materials of the All-Russian Scientific and Practical Internet Conference of Young Scientists and Specialists of Rospotrebnadzor with International Participation, 10–14 October, 2022 Perm, Russia, 222–229 (2022). [in Russian]
31. V. K. Belyakov, E. P. Sukhenko, A. V. Zakharov, P. P. Koltsov, N. V. Kotovich, A. A. Kravchenko, A. S. Kutsaev, A. S. Osipov, and A. B. Kuznetsov, "On one method of blood cell classification and its software implementation," Software & Systems 4(108), 46–56 (2014). [in Russian]
32. S. N. Rjabceva, V. A. Kovalev, V. D. Malyshev, I. A. Siamionik, M. A. Derevyanko, R. A. Moskalenko, A. S. Dovbysh, T .R. Savchenko, and A. N. Romaniuk, "Development of an algorithm for searching for tumor areas based on the processing of full-slide histological images of breast cancer," Doklady BGUIR 18(8), 21–28 (2020).
33. J. Pfeil, A. Nechyporenko, M. Frohme, F. T. Hufert, and K. Schulze, "Examination of blood samples using deep learning and mobile microscopy," BMC Bioinformatics 23, 65 (2022).
34. A. Sharma, B. Buksh, "Intellectual acute lymphoblastic leukemia (ALL) detection model for diagnosis of blood cancer from microscopic images using hybrid convolutional neural network," International Journal of Engineering and Advanced Technology 8(6), 2972–2981 (2019).

Estimating of Fraction of Weakly Deformable Erythrocytes in a Blood Sample Based on the Method of Laser Ektacytometry and a Database of Simulated Diffraction Patterns

Vladislav D. Ustinov, Evgeniy G. Tsybrov*, and Sergey Y. Nikitin
M. V. Lomonosov Moscow State University, GSP-1 Leninskie Gory, Moscow 119991, Russia

***e-mail:** tsybrovevgeniy@yandex.ru

Abstract. The problem of measuring the fraction of weakly deformable erythrocytes in a blood sample by the laser diffractometry in a shear flow (ektacytometry) is considered. The algorithm for measuring this parameter is proposed, based on a comparison of experimentally observed diffraction patterns with ones calculated in the bimodal ensemble approximation, when only two types of erythrocytes are present in a blood sample – normal (deformable) and rigid (non-deformable) erythrocytes. The accuracy of the algorithm was estimated by the method of numerical experiment and the area of its applicability was determined. © 2023 Journal of Biomedical Photonics & Engineering.

Keywords: erythrocyte deformability; laser ektacytometry; data processing algorithms.

Paper #7216 received 21 Feb 2023; revised manuscript received 15 Jun 2023; accepted for publication 16 Jun 2023; published online 22 Jul 2023. doi: 10.18287/JBPE23.09.030303.

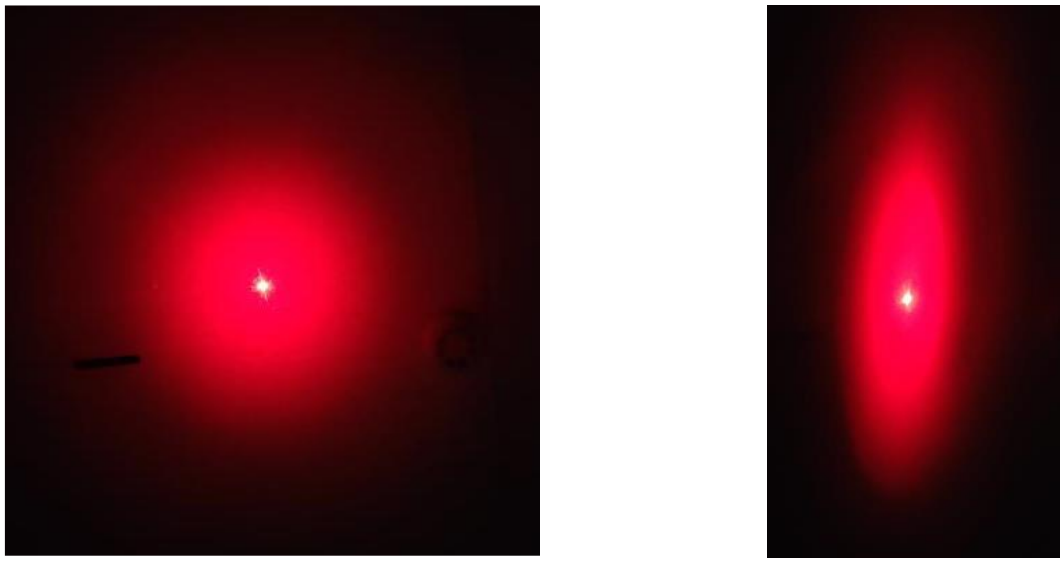
1 Introduction

One of the main rheological characteristics of blood is the deformability of erythrocytes, which is defined as a measure of the ability of blood cells to change their shape under the action of external forces [1–4].

Rapid measurements of the deformability characteristics of erythrocytes are possible based on the method of laser diffractometry in shear flow (ektacytometry) [5–9]. This method is based on the observation and analysis of diffraction patterns arising at the scattering of a laser beam by a suspension of erythrocytes in a given field of shear stresses. Currently, there are laser erythrocyte ektacytometers – Lorrca (Netherlands) and RheoScan (Republic of Korea) [10], which can be used to measure the average deformability of the erythrocytes. At the same time, the problem of measuring the distribution of erythrocytes in deformability [11–14] is great of significance, in particular, the problem of measuring the fraction of weakly deformable erythrocytes in a blood sample [15–19]. In this paper, we propose an algorithm for measuring the fraction of weakly deformable erythrocytes based on comparing the experimentally observed diffraction pattern with the pattern calculated in the bimodal ensemble approximation, when only two types of erythrocytes are present in a blood sample: normal (deformable) and rigid (non-deformable) erythrocytes.

2 Laser Ektacytometry of Erythrocytes

In a rotary ektacytometer, a diluted suspension of erythrocytes is poured into a narrow gap between the walls of two transparent coaxial cups, one of which is stationary and the other can be rotated with a given angular velocity. The rotation of the outer cup leads to arising a shear stress in the suspension, which elongate the erythrocytes in the direction of the shear flow. The suspension is illuminated with a laser beam, the image of the pattern of light scatter by erythrocytes is registrated and analyzed using a special algorithm. Examples of the diffraction patterns obtained for a normal blood sample are shown at the Fig. 1. At low shear stress, the diffraction pattern has circular symmetry (Fig. 1a). At high shear stress, the pattern is elongated (Fig. 1b), demonstrating the deformation of erythrocytes by viscous friction forces.



(a) (b)

Fig. 1 Diffraction patterns obtained by the laser erythrocyte ektacytometer for a normal blood sample at low (a) and high (b) shear stresses. The blood sample was taken from a healthy man at the age of 25 years.

3 Model of a Bimodal Ensemble of Erythrocytes

The simplest model of a blood sample containing cells with reduced deformability is the model of a bimodal ensemble of erythrocytes, which assumes the presence of only two types of cells in the blood - normal (deformable) erythrocytes and rigid (non-deformable) erythrocytes. Erythrocytes in shear flow acquire a shape close to ellipsoidal [11, 12]. For simplicity, we will model erythrocytes with flat elliptical disks. This makes it possible to describe the scattering of a laser beam by erythrocytes in an analytical form, and on this basis to build algorithms for processing laser ektacytometry data. An elliptical disk is characterized by the dimensions of its semi-axes a and b and the aspect ratio $s = a/b$. In the bimodal ensemble, there are two types of erythrocytes with semiaxes a_1, b_1 and a_2, b_2 and aspect ratios $s_1 = a_1/b_1$ and $s_2 = a_2/b_2$. Let us denote the fraction of the first type erythrocytes in a blood sample as p. Considering erythrocytes of the first type as rigid (non-deformable) cells, we set $s_1 = 1$. Erythrocytes of the second type are considered normal, for them $s_2 > 1$, and this value depends on the shear stress in the ektacytometer (or elongation of the cell at certain shear stress). In our calculations, we will change the parameter s_2 at a certain range, thus modeling ensembles of erythrocytes with differences in the degree of heterogeneity of the bimodal ensemble.

4 Diffraction Pattern

The diffraction pattern of laser beam scattering by an inhomogeneous ensemble of erythrocytes was calculated in Ref. [20, 21]. For a bimodal ensemble, it is described by the following Eq. [22]:

$$\tilde{I}(x,y) = \frac{p\cdot(a_1b_1)^2 G\left(\frac{k}{z}\sqrt{a_1^2x^2+b_1^2y^2}\right)+(1-p)\cdot(a_2b_2)^2 G\left(\frac{k}{z}\sqrt{a_2^2x^2+b_2^2y^2}\right)}{p\cdot(a_1b_1)^2+(1-p)\cdot(a_2b_2)^2}.$$

Here $\tilde{I}$ is the light intensity normalized to the intensity of the central maximum of the diffraction pattern, x, y are the Cartesian coordinates of a point on the observation screen, z is the distance from the measuring volume to the observation screen, $k = 2\pi/\lambda$ is the wavenumber, λ is the wavelength of the laser beam, p is the fraction of weakly deformable erythrocytes in a blood sample. The function $G(x)$ is defined by the following Eq.:

$$G(\mathrm{x}) = [2J_1(x)/x]^2,$$

where $J_1(x)$ is the first order Bessel function. The remaining parameters are expressed by the Eqs.:

$$a_1 = a_0 \cdot (1 + \varepsilon_1), \qquad b_1 = b_0 \cdot (1 - \varepsilon_1),$$

$$a_2 = a_0 \cdot (1 + \varepsilon_2), \qquad b_2 = b_0 \cdot (1 - \varepsilon_2),$$

$$M = (s_1 - s_2) \cdot \left(p - \frac{1}{2}\right),$$

$$s = M + \sqrt{M^2 + s_1 s_2},$$

$$\varepsilon_1 = \frac{s_1 - s}{s_1 + s}, \qquad \varepsilon_2 = \frac{s_2 - s}{s_2 + s},$$

$$b_0 = a_0/s.$$

Here a_0 and b_0 are the average sizes of the semi-axes of the elliptical disk.

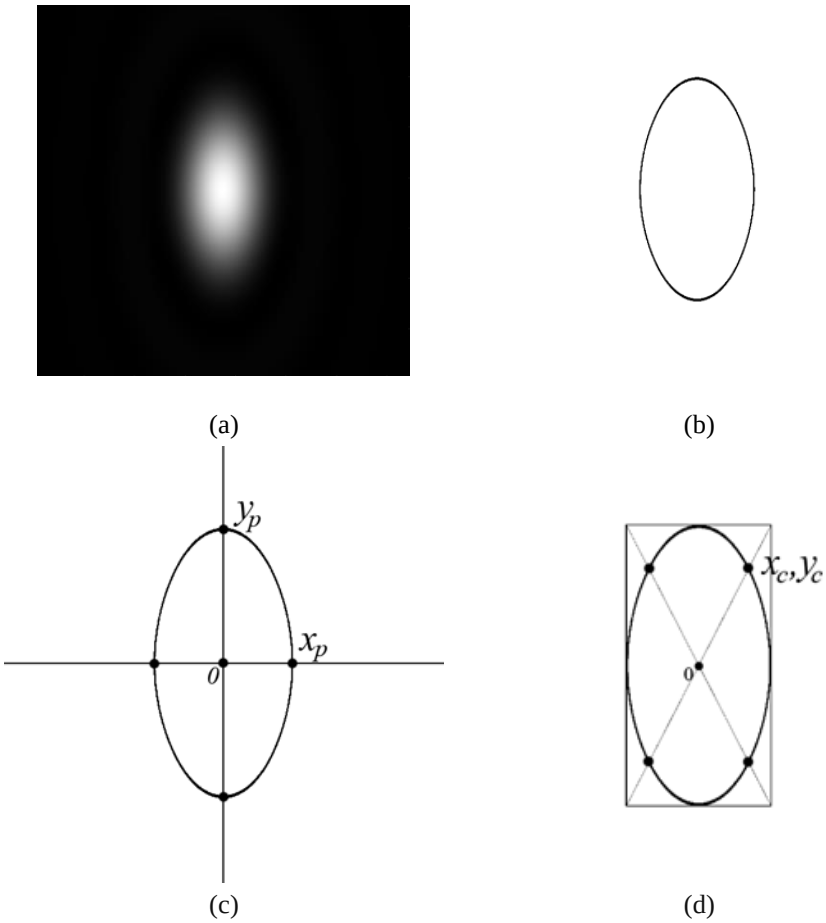


Fig. 2 Example of a diffraction pattern (a), isointensity line (b), its polar (c) and characteristic points (d). The diffraction pattern was constructed numerically for a bimodal ensemble of erythrocytes with parameters $s_1 = 1$, $s_2 = 2.02$, and $p = 0.062$. The isointensity line corresponds to the level $\tilde{I} = 0.05$. The parameters of the polar and characteristic points of this line are $D_e = 1.945$, $Q_e = 0.984$.

5 Iso-Intensity Line, Polar, and Characteristic Points

The analysis of the diffraction pattern is carried out on the basis of the concept of the isointensity line. This is the name of the set of points on the observation screen, the light intensity in which has a certain value $\tilde{I} = const$. The isointensity line equation has the form

$$\frac{p\cdot(a_1b_1)^2 G\left(\frac{k}{z}\sqrt{a_1^2x^2+b_1^2y^2}\right)+(1-p)\cdot(a_2b_2)^2 G\left(\frac{k}{z}\sqrt{a_2^2x^2+b_2^2y^2}\right)}{p\cdot(a_1b_1)^2+(1-p)\cdot(a_2b_2)^2} = \tilde{I}.$$

This Eq. implicitly defines the function $x = x(y)$ or $y = y(x)$, which describes the shape of the iso-intensity line. The form of this function can be found numerically. Let us introduce the concepts of polar and characteristic points of the isointensity line. Points of intersection of the iso-intensity line with the Cartesian coordinate axes (symmetry axes of the iso-intensity line) are called polar. The characteristic points are the points of intersection of the iso-intensity line with the diagonals of the rectangle enclosing this line. An example of a diffraction pattern, an isointensity line, as well as its polar and characteristic points (numerical simulation data) are shown in Fig. 2.

Due to the symmetry of the iso-intensity line, it suffices to consider the upper and right polar points and one characteristic point. Let us denote the coordinates of the upper polar point $x = 0, y = y_p$, the coordinates of the right polar point $x = x_p, y = 0$, the coordinates of the characteristic point $x = x_c, y = y_c$. Let us introduce the parameters [23]:

$$D = \frac{y_p}{x_p},$$

$$Q = \frac{1}{\sqrt{2}}\left(\frac{x_c}{x_p} + \frac{y_c}{y_p}\right).$$

As can be seen from Fig. 2,

$$y_c = x_c \frac{y_p}{x_p}.$$

Hence

$$y_c = x_c D,$$

$$Q = \sqrt{2}\frac{x_c}{x_p}.$$

Parameters D and Q can be measured experimentally using a laser erythrocyte ektacytometer or calculated theoretically based on a particular model. Our further task is to find the relationship between these parameters and the characteristics of the bimodal ensemble of erythrocytes p and s_2, and on this basis to develop an algorithm for measuring the fraction of weakly deformable erythrocytes p in a blood sample.

6 Database of Simulated Diffraction Patterns Building

The database of simulated diffraction patterns is a set of solutions of the direct scattering problem, when the known parameters of the ensemble of erythrocytes are used to find the characteristics of the diffraction pattern that occurs when a laser beam is scattered by blood samples with different initial distribution parameters. When constructing the database, we will consider the parameters of the erythrocyte ensemble s_1, s_2, p as well as the level of light intensity $\tilde{I}$ on the iso-intensity line chosen for measurements, to be known. We will calculate the geometric parameters of the iso-intensity line - the parameter of the polar points D and the parameter of the characteristic point Q. For a given value of the parameter $\tilde{I}$, the database is a function set of two variables $D = D(p, s_2)$ and $Q = Q(p, s_2)$ specified in table form. Calculations are made as follows.

Let us introduce the normalized coordinates of a point on the screen for observing the diffraction pattern U and V, defining them by the Eqs.:

$$x = \frac{z}{ka_0}U,$$

$$y = \frac{z}{kb_0}V.$$

In these coordinates, the isointensity line equation takes the form [24]

$$\frac{pe_1G\left(\sqrt{e_{1u}^2U^2+e_{1v}^2V^2}\right)+(1-p)e_2G\left(\sqrt{e_{2u}^2U^2+e_{2v}^2V^2}\right)}{pe_1+(1-p)e_2} = \tilde{I},$$

where

$$e_1 = (1-\varepsilon_1^2)^2, \qquad e_2 = (1-\varepsilon_2^2)^2,$$

$$e_{1u} = 1+\varepsilon_1, \qquad e_{2u} = 1+\varepsilon_2,$$

$$e_{1v} = 1-\varepsilon_1, \qquad e_{2v} = 1-\varepsilon_2.$$

Normalized coordinates of the upper polar point $U = 0$, $V = V_p$, right polar point $U = U_p$, $V = 0$, characteristic point $U = U_c$, $V = V_c$. Polar and characteristic point parameters

$$D = s\frac{V_p}{U_p},$$

$$Q = \sqrt{2}\frac{U_c}{U_p}.$$

The Eqs. for the coordinates U_p, V_p, U_c of the polar and characteristic points have the form

$$\frac{pe_1G(e_{1u}U_p)+(1-p)e_2G(e_{2u}U_p)}{pe_1+(1-p)e_2} = \tilde{I},$$

$$\frac{pe_1G(e_{1v}V_p)+(1-p)e_2G(e_{2v}V_p)}{pe_1+(1-p)e_2} = \tilde{I},$$

$$\frac{pe_1G\left(\frac{U_c}{U_p}\sqrt{e_{1u}^2U_p^2+e_{1v}^2V_p^2}\right)+(1-p)e_2G\left(\frac{U_c}{U_p}\sqrt{e_{2u}^2U_p^2+e_{2v}^2V_p^2}\right)}{pe_1+(1-p)e_2} = \tilde{I}.$$

By setting the parameters of the bimodal ensemble of erythrocytes s_1, s_2, p as well as the level of light intensity on the isointensity line $\tilde{I}$, these Eqs. can be used to calculate the parameters of the diffraction pattern D and Q of interest to us. In all cases, we assumed $s_1 = 1$, which corresponds to the presence in the ensemble erythrocytes are rigid (non-deformable) cells. As an example, Tables 1 and 2 show the fragment of the database obtained for $\tilde{I} = 0.05$. All numbers in Tables 1 and 2 are given with an accuracy of three decimal places.

Table 1 Parameter D values.

		p		
		0	**0.05**	**0.1**
s_2	**1.95**	1.948	1.891	1.831
	2.00	2.000	1.940	1.877
	2.05	2.049	1.987	1.919

Table 2 Parameter Q values.

		p		
		0	**0.05**	**0.1**
s_2	**1.95**	1.000	0.988	0.975
	2.00	1.000	0.987	0.974
	2.05	1.000	0.987	0.972

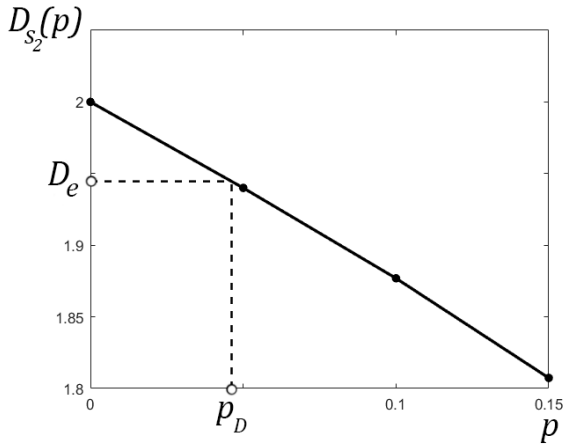
The volume of the database is indicated in Section 9.

7 Measurement Algorithm

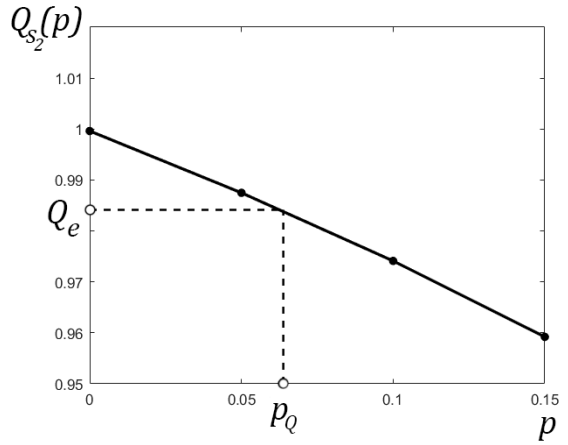
The task of ektacytometry is to find the characteristics of the ensemble of erythrocytes p and s_2 from the known parameters of the diffraction pattern D_e and Q_e. To do this, we need to solve the Eqs.:

$$D(p, s_2) = D_e,$$

$$Q(p, s_2) = Q_e.$$



(a)



(b)

Fig. 3 Graphs of the functions $D_{s2}(p)$ (a) and $Q_{s2}(p)$ (b) constructed for $s_2 = 2$ and и $\tilde{I} = 0.05$.

where the functions $D(p, s_2)$ and $Q(p, s_2)$ are defined as database tables. The problem is solved in the following way. With a fixed value of the parameter s_2, the values D and Q become functions of one variable, the parameter p. Let us denote these functions as $D_{s2}(p)$ and $Q_{s2}(p)$. An analysis of the tables shows that both of these functions are monotonically decreasing. They can be approximated with good accuracy by continuous piecewise linear functions. This allows each number s_2 from the database to be associated with a number p_D such that $D_{s2}(p_D) = D_e$ and a number p_Q such that $Q_{s2}(p_Q) = Q_e$. As an example, Fig. 3 shows the graphs of the functions $D_{s2}(p)$ and $Q_{s2}(p)$ constructed for $s_2 = 2$ and $\tilde{I} = 0.05$.

Repeating such calculations for different values of the number s_2, we obtain the functions $p_D(s_2)$ and $p_Q(s_2)$, given in the form of tables. In the region of parameter change of interest to us, one of these functions is monotonically increasing, and the second is monotonically decreasing. These functions can also be approximated with good accuracy by continuous piecewise linear functions. This makes it possible to find the number s_2, at which $p_D(s_2) = p_Q(s_2)$, and determine the corresponding value of the number p such that $p = p_D(s_2) = p_Q(s_2)$. As an example, Fig. 4 shows the graphs of the functions $p_Q(s_2)$ and $p_D(s_2)$ constructed for $\tilde{I} = 0.05$, $D_e = 1.945$ and $Q_e = 0.984$.

Mathematically, these procedures are expressed by the following Eqs.:

$$p_D(s_2) = \frac{(D_2 - D_e)p_{1D} + (D_e - D_1)p_{2D}}{D_2 - D_1}, \quad (1)$$

$$p_Q(s_2) = \frac{(Q_2 - Q_e)p_{1Q} + (Q_e - Q_1)p_{2Q}}{Q_2 - Q_1}, \quad (2)$$

$$p = \frac{p_Q(s_{22})p_D(s_{21}) - p_D(s_{22})p_Q(s_{21})}{p_Q(s_{22}) - p_Q(s_{21}) - p_D(s_{22}) + p_D(s_{21})}, \quad (3)$$

$$s_2 = \frac{[p_Q(s_{22}) - p_D(s_{22})]s_{21} + [p_D(s_{21}) - p_Q(s_{21})]s_{22}}{p_Q(s_{22}) - p_Q(s_{21}) - p_D(s_{22}) + p_D(s_{21})}. \quad (4)$$

Here numbers D_1, D_2 are neighboring numbers from row s_2 of the table of parameter D values such that

$$D_1 \le D_e \le D_2.$$

The numbers p_{1D}, p_{2D} are the values of the number p such that

$$D_{s2}(p_{1D}) = D_1,$$

$$D_{s2}(p_{2D}) = D_2.$$

The numbers Q_1, Q_2 are neighboring numbers from the row s_2 of the table of Q parameter values such that

$$Q_1 \le Q_e \le Q_2.$$

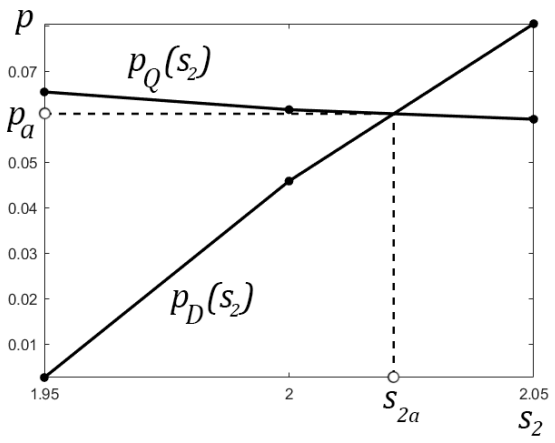


Fig. 4 Graphs of functions $p_D(s_2)$ and $p_Q(s_2)$ constructed for $\tilde{I} = 0.05$, $D_e = 1.945$, and $Q_e = 0.984$.

The numbers p_{1Q}, p_{2Q} are the values of the number p p such that

$$Q_{s2}(p_{1Q}) = Q_1,$$

$$Q_{s2}(p_{2Q}) = Q_2.$$

The numbers s_{21}, s_{22} are neighboring values of the number s_2 from the database such that the values $p_D(s_{21}) - p_Q(s_{21})$ and $p_D(s_{22}) - p_Q(s_{22})$ have different signs.

8 Verification of the Algorithm by Numerical Experiment

Let the bimodal ensemble of erythrocytes be characterized by the parameters

$$s_1 = 1, \qquad s_2 = 2.02, \qquad p = 0.062.$$

The pattern of laser beam scattering by such an ensemble is shown in Fig. 2a. Let us choose the iso-intensity line of the diffraction pattern at the level of relative light intensity

$$\tilde{I} = 0.05.$$

This line is shown in Fig. 2b, its polar and characteristic points are shown in Figs. 2c and 2d. The parameters of the polar and characteristic points of this line have the following numerical values

$$D_e = 1.945, \qquad Q_e = 0.984.$$

To solve the inverse scattering problem, we use the data given in Tables 1 and 2. From Table 1 for

$$s_2 = 1.95$$

using conditions

$$D_1 \le D_e \le D_2$$

we find

$$D_1 = 1.891, \qquad D_2 = 1.948,$$

and the values of the parameter p corresponding to these numbers

$$p_{1D} = 0.05, \qquad p_{2D} = 0.$$

Further, according to Eq. (1), we obtain

$$p_D(s_2 = 1.95) = 0.0026.$$

The procedure for finding this number is illustrated in Fig. 3a. Acting similarly, we find several private values of the functions $p_D(s_2)$ and $p_Q(s_2)$:

$$p_D(s_2 = 1.95) = 0.0026, \quad p_Q(s_2 = 1.95) = 0.0654,$$

$$p_D(s_2 = 2.00) = 0.0458, \quad p_Q(s_2 = 2.00) = 0.0615,$$

$$p_D(s_2 = 2.05) = 0.0804, \quad p_Q(s_2 = 2.05) = 0.0594.$$

It follows that the difference $p_D(s_2) - p_Q(s_2)$ changes sign when

$$s_{21} \le s_2 \le s_{22},$$

where

$$s_{21} = 2.00, \qquad s_{22} = 2.05.$$

The partial values of the functions $p_D(s_2)$ and $p_Q(s_2)$ at these points are found by Eqs. (1), (2) and we obtain

$$p_D(s_{21}) = 0.0458, \qquad p_D(s_{22}) = 0.0804,$$

$$p_Q(s_{21}) = 0.0615, \qquad p_Q(s_{22}) = 0.0594.$$

Finally, using Eqs. (3), (4), we calculate the required parameters of the ensemble of erythrocytes

$$p_a = 0.061, \qquad s_{2a} = 2.02.$$

Comparing these numbers with the initially given (true) values of these parameters

$$p = 0.062, \qquad s_2 = 2.02,$$

we conclude that in this case the parameter s_2 is determined exactly, and the parameter p is determined with an error of less than 2%. Thus, for typical experimental conditions, the accuracy of the database-based algorithm turns out to be very high.

9 Results

Calculations of parameters D and Q of diffraction patterns were performed for the following values of parameters of bimodal ensembles of erythrocytes:

$$s_1 = 1,$$

$1.9 \le s_2 \le 3$ with step $\Delta s_2 = 0.05$ (total 23 numbers s_2),

$0 \le p \le 0.5$ with step $\Delta p = 0.05$ (total 11 p numbers),

and levels of relative light intensity on the iso-intensity line

$$\tilde{I} = 0.03;\ 0.05;\ 0.07;\ 0.09;\ 0.15;\ 0.25;\ 0.4;\ 0.5.$$

In total, 1928 D numbers and 1928 Q numbers were found. These numbers form a database, i.e. a set of solutions to the direct problem of diffractometry.

The database algorithm check was made for the following parameter values:

$$s_1 = 1,$$

$$s_2 = 2.02;\ \ 2.92,$$

$$p = 0.0075;\ 0.015;\ 0.031;\ 0.062;\ 0.125;\ 0.25,$$

$$\tilde{I} = 0.03;\ 0.05;\ 0.07;\ 0.09;\ 0.15;\ 0.25;\ 0.4.$$

The accuracy of the algorithm and the area of its applicability are characterized by the data presented in Tables 3 and 4. These tables indicate the error in determining the fraction of weakly deformable erythrocytes in the bimodal ensemble, found by numerical simulation of diffraction patterns and their analysis using the database algorithm.

Table 3 Error in determining the fraction of weakly deformable erythrocytes in a bimodal ensemble (in percent) based on the database algorithm – numerical experiment (s_1 = 1, s_2 = 2.02).

		p				
		0.015	**0.031**	**0.062**	**0.125**	**0.25**
$\tilde{I}$	**0.03**	6.6	5.5	1.8	0.7	1.0
	0.05	0.7	9.1	1.4	0.5	0.8
	0.07	1.3	4.3	4.5	1.5	0.0
	0.09	13.7	2.6	1.5	4.0	2.4
	0.15	10.0	39.5	8.2	0.7	0.9

Table 4 Error in determining the fraction of weakly deformable erythrocytes in a bimodal ensemble (in percent) based on the database algorithm – numerical experiment (s_1 = 1, s_2 = 2.92).

		p				
		0.015	**0.031**	**0.062**	**0.125**	**0.25**
$\tilde{I}$	**0.03**	17.3	5.0	2.2	12.2	2.2
	0.05	0.6	8.7	1.0	1.0	0.1
	0.07	10.8	4.5	3.2	1.4	0.2
	0.09	23.3	7.6	1.6	0.5	0.4
	0.15	36.3	7.1	6.2	1.9	0.2

It can be seen from Tables 3 and 4 that the error in measuring the number p does not exceed 10% in the region of parameter values

$$0.03 \le \tilde{I} \le 0.09$$

and

$$0.03 \le p \le 0.25$$

which corresponds to the spread of erythrocytes in deformability

$$0.087 \le \mu' \le 0.23 \qquad \text{for } s_2 = 3,$$

$$0.058 \le \mu' \le 0.15 \qquad \text{for } s_2 = 2.$$

Here the parameter μ' is defined by the Eq.:

$$\mu' = \sqrt{p\varepsilon_1^2 + (1-p)\varepsilon_2^2}$$

and has the meaning of the standard deviation of the deformability of erythrocytes in a bimodal ensemble from its average value. For the levels of relative light intensity $\tilde{I} = 0.25$ and $\tilde{I} = 0.40$, the measurement error of parameter p using the database algorithm, as a rule, exceeds 10%. As for the measurement error of parameter s_2, it did not exceed 1% in all cases.

In real experiments, some assumptions of our theoretical model can be fulfilled only approximately. This concerns the shape of erythrocytes in a shear flow, their distribution in size and deformability, location and orientation in space, the assumption that there are no other light-scattering particles in the measuring volume, etc. If necessary, these circumstances can be taken into account in the theory, but this will lead to its significant complication. On the other hand, it is possible to bring the theory closer to the experiment by selecting the experimental conditions, such as the method of preparing blood samples, choosing the optimal shear stress and the coordinate system on the observation screen, etc. The final verification and assessment of the accuracy of the model can be carried out in experiments with specially prepared blood samples.

10 Conclusion

In this paper, we consider the problem of measuring the fraction of weakly deformable erythrocytes (FWDE) in a blood sample by laser diffractometry of erythrocytes in a shear flow (ektacytometry). The parameters of the diffraction pattern that are most sensitive to FWDE are revealed. These parameters are the coordinates of the polar and characteristic points of the isointensity line. An algorithm for measuring FWDE is proposed based on a comparison of experimentally observed diffraction patterns with patterns calculated in the bimodal ensemble approximation, when only two types of erythrocytes are present in a blood sample – normal (deformable) and rigid (non-deformable) erythrocytes. The accuracy of the algorithm was estimated by numerical experiment and the area of its applicability was determined both in relation to the allowable inhomogeneity of the ensemble of erythrocytes and in relation to the part of the diffraction pattern suitable for measurements. The calculations are made for typical experimental conditions, when the aspect ratio of the isointensity line chosen for measurements is $D = 2 \div 3$. It is shown that the measurement error of FWDE does not exceed 10% if the spread of erythrocytes in deformability is $\mu' = 6 \div 23$ %, and the light intensity on the isointensity line is $\tilde{I} = 3 \div 9$ % relative to the intensity of the central maximum of the diffraction pattern. For light intensity levels $\tilde{I} = 25 \div 40$ %, the measurement error of FWDE, as a rule, exceeds 10%. These data confirm the earlier conclusion that the most sensitive to the parameters of the ensemble of erythrocytes is that part of the diffraction pattern, where the light intensity is approximately an order of magnitude lower than the intensity of the central

diffraction maximum. The aspect ratio for the soft component of the ensemble of erythrocytes (parameter s_2) in all cases considered by us was found with an error not exceeding 1%.

Acknowledgments

This work was supported by the Russian Science Foundation (grants 18-71-00158 and 22-15-00120) and by the Ministry of Education and Science of the Russian Federation as part of the program of the Moscow Center for Fundamental and Applied Mathematics under the agreement № 075-15-2022-284 as well as by Interdisciplinary Scientific and Educational School of Moscow University "Photonic and Quantum Technologies. Digital Medicine".

Disclosures

The authors declare no conflict of interest.

References

1. E. Ch. Mokken, M. Kedaria, Ch. P. Henny, M. R. Hardeman, and A. W. Gelb, "The clinical importance of erythrocyte deformability, a hemorrheological parameter," Annals of Hematology 64, 113–122 (1992).
2. S. Shin, Y. Ku, M. S. Park, and J. S. Suh, "Deformability of red blood cells: A determinant of blood viscosity," Journal of Mechanical Science and Technology 19, 216–223 (2005).
3. O. K. Baskurt, M. Boynard, G. C. Cokelet, P. Connes, B. M. Cooke, S. Forconi, F. Liao, M. R. Hardeman, F. Jung, H. J. Meiselman, G. Nash, N. Nemeth, B. Neu, B. Sandhagen, S. Shin, G. Thurston, and J. L. Wautier, "New guidelines for hemorheological laboratory techniques," Clinical Hemorheology and Microcirculation 42(2), 75–97 (2009).
4. T. J. McMahon, "Red BloodCell Deformability, Vasoactive Mediators, and Adhesion," Frontiers in Physiology 10, 1417 (2019).
5. M. Bessis, N. Mohandas, "A diffractometric method for the measurement of cellular deformability," Blood Cells 1, 307–313 (1975).
6. N. Nemeth, F. Kiss, and K. Miszti–Blasius, "Interpretation of osmotic gradient ektacytometry (osmoscan) data: A comparative study for methodological standards," Scandinavian Journal of Clinical and Laboratory Investigation 75(3), 213–222 (2015).
7. A. Sadaf, K. G. Seu, E. Thaman, R. Fessler, D. G. Konstantinidis, H. A. Bonar, J. Korpik, R. E. Ware, P. T. McGann, C. T. Quinn, and T. A. Kalfa, "Automated Oxygen Gradient Ektacytometry: A Novel Biomarker in Sickle Cell Anemia," Frontiers in Physiology 12, 636609 (2021).
8. A. U. Zaidi, S. Buck, M. Gadgeel, M. Herrera–Martinez, A. Mohan, K. Johnson, S. Bagla, R. M. Johnson, and Y. Ravindranath, "Clinical Diagnosis of Red Cell Membrane Disorders: Comparison of Osmotic Gradient Ektacytometry and Eosin Maleimide (EMA) Fluorescence Test for Red Cell Band 3 (AE1, SLC4A1) Content for Clinical Diagnosis," Frontiers in Physiology 11, 636 (2020).
9. M. A. E. Rab, B. A. van Oirschot, J. Bos, T. H. Merkx, A. C. W. van Wesel, O. Abdulmalik, M. K. Safo, B. A. Versluijs, M. E. Houwing, M. H. Cnossen, J. Riedl, R. E. G. Schutgens, G. Pasterkamp, M. Bartels, E. J. van Beers, and R. van Wijk, "Rapid and reproducible characterization of sickling during automated deoxygenation in sickle cell disease patients," American Journal of Hematology 94(5), 575–584 (2019).
10. O. K. Baskurt, M. R. Hardeman, M. Uyuklu, P. Ulker, M. Cengiz, N. Nemeth, S. Shin, T. Alexy, and H. J. Meiselman, "Comparison of three commercially available ektacytometers with different shearing geometries," Biorheology 46(3), 251–264 (2009).
11. J. G. G. Dobbe, M. R. Hardeman, G. J. Streekstra, J. Starckee, C. Ince, and C. A. Grimbergen, "Analyzing red blood cell–deformability distributions," Blood Cells, Molecules, and Diseases 28(3), 373–384 (2002).
12. J. G. G. Dobbe, G. J. Streekstra, M. R. Hardeman, C. Ince, and C. A. Grimbergen, "Measurement of the Distribution of Red Blood Cell Deformability Using an Automated Rheoscope," Cytometry: The Journal of the International Society for Analytical Cytology 50(6), 313–325 (2002).
13. S. Yu. Nikitin, A. E. Lugovtsov, V. D. Ustinov, M. D. Lin, and A. V. Priezzhev, "Study of laser beam scattering by inhomogeneous ensemble of red blood cells in a shear flow," Journal of Innovative Optical Health Science 8(4), 1550031 (2015).
14. N. L. Parrow, P.-C. Violet, H. Tu, J. Nichols, C. A. Pittman, C. Fitzhugh, R. E. Fleming, N. Mohandas, J. F. Tisdale, and M. Levine, "Measuring Deformability and Red Cell Heterogeneity in Blood by Ektacytometry," Journal of Visualized Experiments (131), e56910 (2018).
15. J. Plasek, T. Marik, "Determination of undeformable erythrocytes in blood samples using laser light scattering," Applied Optics 21(23), 4335–4338 (1982).
16. G. J. Streekstra, J. G. G. Dobbe, and A. G. Hoekstra, "Quantification of the poorly deformable red blood cells using ektacytometry," Optics Express 18(13), 14173–14182 (2010).
17. Y. Man, R. An, K. Monchamp, Z. Sekyonda, E. Kucukal, C. Federici, W. J. Wulftange, U. Goreke, A. Bode, V. A. Sheehan, and U. A. Gurkan, "Occlusion Chip: A functional microcapillary occlusion assay complementary to

ektacytometry for detection of small–fraction red blood cells with abnormal deformability," Frontiers in Physiology 13, 954106 (2022).
18. Y. J. Kang, S. Serhrouchni, A. Makhro, A. Bogdanova, and S. S. Lee, "Simple Assessment of Red Blood Cell Deformability Using Blood Pressure in Capillary Channels for Effective Detection of Subpopulations in Red Blood Cells," American Chemical Society Omega 7(43), 38576–38588 (2022).
19. M. Grau, L. Kuck, T. Dietz, W. Bloch, and M. J. Simmonds, "Sub–Fractions of Red Blood Cells Respond Differently to Shear Exposure Following Superoxide Treatment," Biology 10(1), 47 (2021).
20. S. Yu. Nikitin, A. V. Priezzhev, and A. E. Lugovtsov, "Laser Diffraction by the Erythrocytes and Deformability Measurements," Chapter 6 in Advanced Optical Flow Cytometry: Methods and Disease Diagnoses, V. V. Tuchin (Ed.), 1st ed., John Wiley & Sons, 133–154 (2011). ISBN:9783527634286.
21. S. Yu. Nikitin, A.V. Priezzhev, and A. E. Lugovtsov, "Analysis of laser beam scattering by an ensemble of particles modeling red blood cells in ektacytometer," Journal of Quantitative Spectroscopy and Radiative Transfer 121, 1–8 (2013).
22. S. Yu. Nikitin, V. D. Ustinov, S. D. Shishkin, and M. S. Lebedeva, "Line curvature algorithm in laser ektacytometry of red blood cells," Quantum Electronics 50(9), 888–894 (2020).
23. S. Yu. Nikitin, V. D. Ustinov, "Characteristic point algorithm in laser ektacytometry of red blood cells," Quantum Electronics 48(1), 70–74 (2018).
24. S. Yu. Nikitin, V. D. Ustinov, and S. D. Shishkin, "Band point algorithms for measuring diffraction pattern parameters in laser ektacytometry of red blood cells," Quantum Electronics 51(4), 353–358 (2021).

High-Resolution Ultra-Spectral Imager for Advanced Imaging in Agriculture and Biomedical Applications

Maria M. Antony[#], C. S. Suchand Sandeep[*#], Hoong-Ta Lim, and Murukeshan Vadakke Matham[†]
Centre for Optical and Laser Engineering, School of Mechanical and Aerospace Engineering,
Nanyang Technological University, 50 Nanyang Avenue, 639798, Singapore
[#] These authors contributed equally to this work

e-mail: [*]ssuchand@ntu.edu.sg, [†]mmurukeshan@ntu.edu.sg

Abstract. Conventional imaging practices used for the inspection and monitoring of biological specimens employ RGB cameras with limited capabilities for early identification of diseases or abnormalities. In this work, we demonstrate and validate a quick, non-destructive, and precise inspection method utilizing an in-house developed push broom ultra-spectral imager. Precise image classification based on ultra-spectral signatures can provide fully automated machine vision capabilities, reducing inspection time, human errors, and man-hours. The proposed method has high spectral resolution ($\Delta\lambda < 1$ nm) with 756 spectral bands, improved detection sensitivity, and high spatial resolution, which could potentially enable early-stage detection and accurate classification of abnormalities or diseases. Two potential applications of the developed system in agriculture and biomedical fields are demonstrated. © 2023 Journal of Biomedical Photonics & Engineering.

Keywords: hyperspectral imaging; spectral mapping; machine vision; non-destructive testing; smart farming; datacube; spectral library.

Paper #8928 received 8 Mar 2023; revised manuscript received 31 May 2023; accepted for publication 31 May 2023; published online 27 Jul 2023. doi: 10.18287/JBPE23.09.030304.

1 Introduction

Automated detection of abnormalities and diseases is of utmost importance in modern agro-food and medical applications [1]. It has been reported that early detection of diseases reduces complications caused by human errors, delays, and inaccuracies [2]. Traditional techniques for inspecting and monitoring biological specimens are based on transmission, absorption, fluorescence, or electron microscopy, and have limited capabilities for automated disease identification at an early stage [3–8]. In general, these techniques only provide spatial information about the sample under study and are thus insufficient for automation. There are a few techniques that combine spectroscopy and imaging that can enable automated disease detection using imaging spectroscopes [4, 9, 10]. Imaging spectroscopes can provide information from multiple spectral bands and hence are excellent candidates for automated and early detection of diseases or abnormalities. Such imagers, also known as spectral imagers, are divided into three categories based on the number of spectral bands they can resolve: multispectral (a few spectral bands), hyperspectral (tens of spectral bands), and ultra-spectral (hundreds of spectral bands) [11, 12].

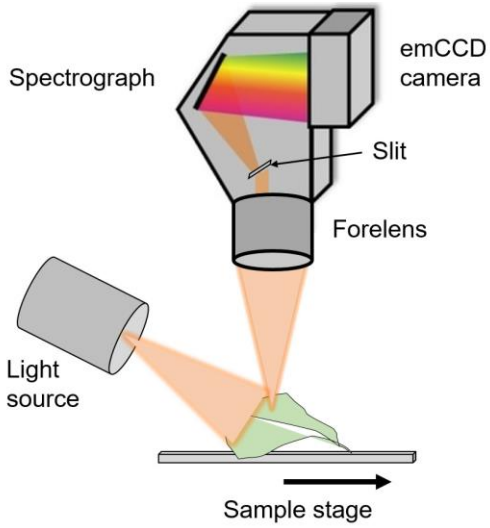


Fig. 1 Schematic diagram of the pushbroom ultra-spectral imaging system developed.

This paper was presented at the International Conference on Nanoscience and Photonics for Medical Applications – ICNPMA, December 28–30, 2022, Manipal, India.

These spectral imaging systems store images as datacubes, with the x and y dimensions containing spatial information about the sample and the z dimension containing spectral information.

Numerous works utilizing hyperspectral imaging technology have been reported in the last two decades, revolutionizing several application scenarios [13–18]. However, there have not been many reports on ultra-spectral imagers for agriculture and biomedical applications. Ultra-spectral imagers can record data from hundreds of spectral bands, increasing the spectral detection selectivity, particularly for molecular absorption and emissions, which can potentially improve automated abnormality and disease detection and classification capabilities. This paper discusses the bio and agro-food applications of an ultra-spectral imaging (USI) system that offers high spectral resolution, improved detection sensitivity, and high spatial resolution. This technique has several advantages over existing imaging methods used for bio and agro-food applications. For example, fluorescence microscopy, one of the gold standards used for biomedical and agricultural applications, needs the samples to be tagged with fluorescent markers, or are applicable only to samples that possess autofluorescence. Hence, fluorescence imaging would be invasive or has limited applicability. The proposed method on the other hand is non-invasive, does not require any kind of sample preparation, suitable for large area inspection, and in general is applicable to all types of samples. It is anticipated that biomedical and agricultural industries will benefit greatly from automated inspection using such systems.

2 Materials and Methods

A schematic diagram of the in-house developed USI system used for the investigations is shown in Fig. 1. The system works in the line scanning (pushbroom) spectral imaging configuration [14]. The sample is illuminated using a broadband light source (Edmund Optics, MI-150). The light reflected from the sample is collected by a fore lens on to a narrow silt, which is then dispersed by a spectrograph. The dispersed light from the spectrograph is imaged by an electron multiplying charge coupled device (emCCD) camera (Andor, LucaEM). The use of the emCCD improves the sensitivity of the system compared to traditional charge coupled device (CCD) or complementary metal oxide semiconductor device (CMOS) cameras. The emCCD camera's electron-multiplying gain and exposure time can be fine-tuned depending on the lighting condition to optimize the image quality. The spectrum from each sample point in the line of view of the USI system was spread along the detector camera's y-axis. The USI system was initially calibrated for wavelength mapping of the spatial positions on the detector using standard spectral lines. Calibration was performed by imaging a flat sample illuminated with a tunable laser source (NKT Photonics, SuperK Extreme EXR-15, SuperK Select 4xVIS/IR) at twelve calibration wavelengths. A second-order polynomial regression model given in Eq. (1) was used to calibrate the USI system.

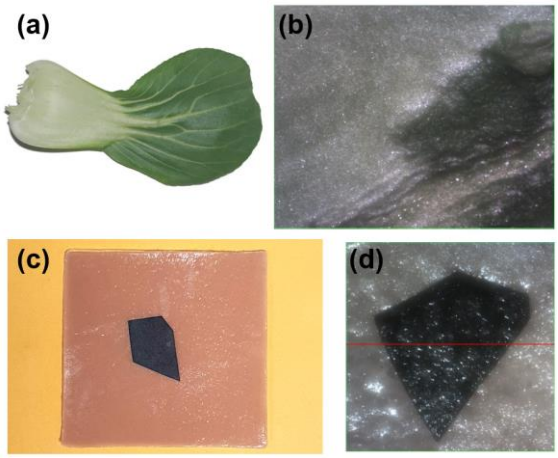


Fig. 2 Photographs of the samples investigated. (a) Chinese cabbage leaf, (b) enlarged view of the ROI showing a bruise on the leaf, (c) phantom tissue sample, and (d) enlarged view of the ROI on the phantom tissue under inspection showing the abnormal tissue region as black.

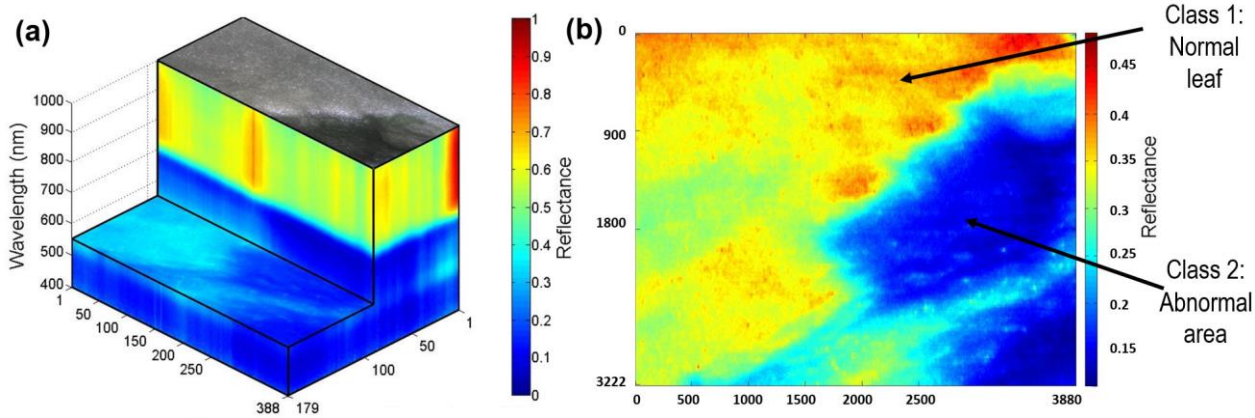


Fig. 3 (a) Datacube recorded from the Chinese cabbage sample. (b) Reflectance mapping at 550 nm showing clear distinction between normal and abnormal leaf areas. x &y axes represent the sample dimensions in μm.

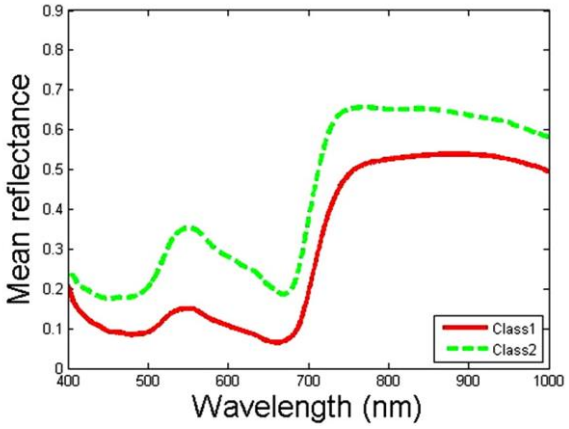


Fig. 4 Average reflectance spectra of the two sample classes in Chinese cabbage sample.

$$\lambda_{cal} = a \times C_y^2 + b \times C_y + c, \quad (1)$$

C_y represents the detector row, λ_{cal} denotes the calibrated wavelength, and a, b, c are constants. The values of these constants were obtained by numerically fitting the calibration data and were found to be, $a = 7.345 \times 10^{-5}$ nm, $b = 0.726$ nm, and $c = 331.871$ nm. The calibration is cross-verified by imaging the standard spectral line from a helium neon (He-Ne) laser.

During the measurements, the sample was mounted on an automated high-resolution 3-axis translation stage (Physik Instruments) and was scanned in micrometer steps to record the ultra-spectral image of the region of interest (ROI). The system's spectral range, 400–1000 nm, spans the visible to near-infrared wavelength band with a spectral resolution of ~ 1 nm over 756 spectral bands. The spatial resolution of the system was evaluated by imaging a USAF 1951 resolution test target and the system was able to resolve vertical and horizontal lines of Group 3 Element 5 of the test target, corresponding to a lateral resolution of 39.37 μm. The whole system was automated using an in-house developed LabVIEW® code. The datacube generation as well as all the data processing were done using custom written MATLAB® scripts.

Two representative bio samples, namely Chinese cabbage (Pak Choi) and a phantom tissue sample are chosen from agriculture and biomedical fields respectively, for the investigation using the USI system. A fresh leaf from a Chinese cabbage plant with a tiny bruise damage was used for the first set of investigations. The biophantom tissue sample was procured from Simulab Corporation and the abnormal area on the biophantom tissue was simulated by pasting a black tape on to the sample surface. Representative images of the samples used in the measurements are shown in Fig. 2.

3 Results and Discussion

The Chinese cabbage leaf sample with visible bruises was mounted on the translation stage and the images were recorded using the USI system in line scanning mode. The ultra-spectral datacube recorded and the reflectance mapping at 550 nm for the Chinese cabbage sample are shown in Fig. 3.

The reflectance mapping of the image at 550 nm shows a clear distinction between normal and abnormal regions as shown in Fig. 3(b). The average reflectance spectra extracted from the datacube for the two areas are shown in Fig. 4. The reflectance spectrum labelled class 1 represents the average reflectance spectrum captured from normal leaf area while the spectrum labelled class 2 represents the average reflectance spectrum captured from the abnormal area. The clear distinction between the two can be utilized for the automated quality inspection of Chinese cabbage crops.

The ultra-spectral datacube recorded for the biophantom tissue with simulated abnormal area is shown in Fig. 5(a). The wavelength mapping at 700 nm shows distinct changes for class 1 (normal tissue) and class 2 (abnormal tissue) as shown in Fig. 5(b).

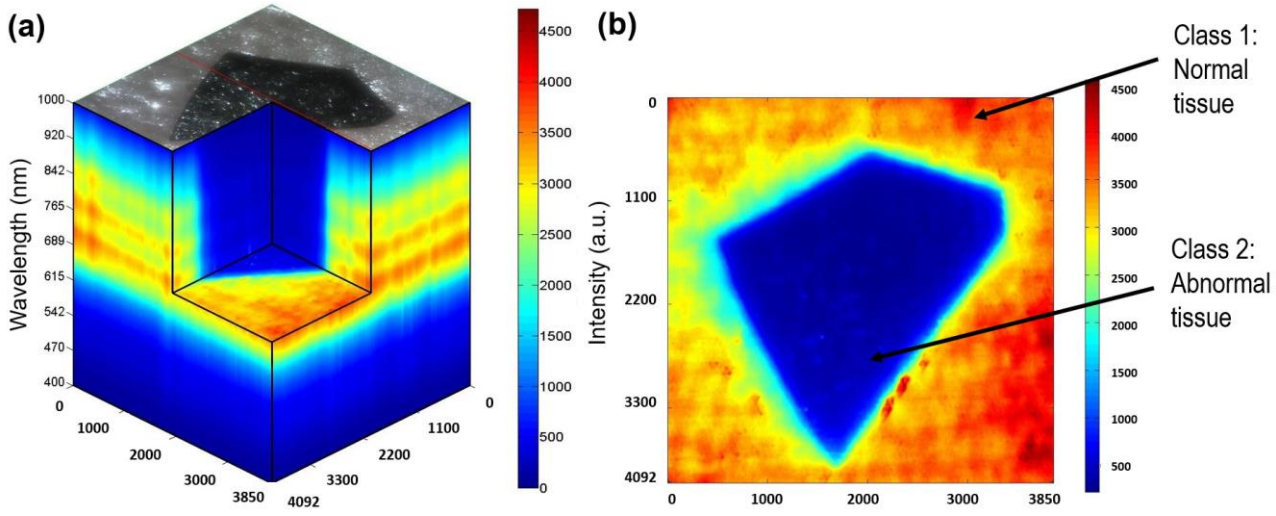


Fig. 5 (a) Datacube recorded from the biophantom tissue sample. (b) Wavelength mapping at 700 nm. x & y axes represent the sample dimensions in μm.

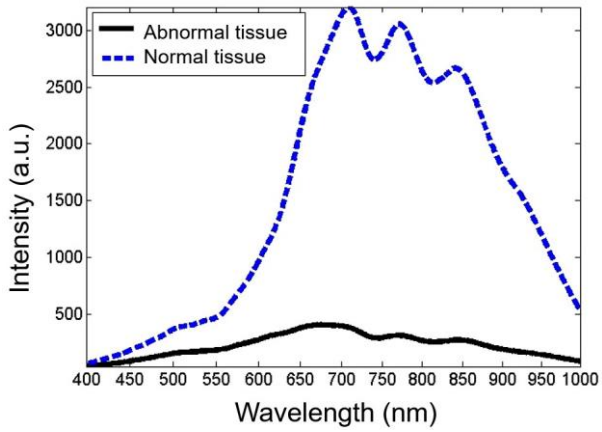


Fig. 6 Average reflectance spectra from the normal tissue (class 1) and abnormal tissue (class 2) regions in the biophantom tissue sample.

The average spectra extracted for the different sample classes (shown in Fig. 4 and Fig. 6) can be used for developing the spectral libraries required for automated classification. Detection using spectral imaging largely depends on robust reference libraries. The detection of pathological sites and diseases will be through the comparison of the spectral variations to the reference libraries using classification algorithms, deep learning, and specific indices. Several algorithms have been developed by various research groups for this purpose [19, 20]. Details of the algorithm utilized for the automated abnormality classification based on the spectral libraries created is shown in Fig. 7. Briefly, the USI datacubes recorded undergoes appropriate spectral pre-processing depending on the reference spectral libraries loaded to the algorithm. The dimensionality of the extracted spectral data is then reduced using specialized techniques such as independent component analysis (ICA), principal component analysis (PCA), or non-negative matrix factorization (NMF). Subsequently, selected mapping and further feature extraction from the data using techniques such as normalized difference index (NDI) can enable quick automated classification and detection using the algorithm shown in Fig. 7.

Distinct features are seen in the reflection spectra extracted from class 1 (normal tissue) and class 2 (abnormal tissue) areas of the sample as shown in Fig. 6, which can be utilized for the automated classification of the abnormalities in the phantom tissue sample.

To illustrate the viability and selectivity of the proposed algorithm, the classification of a Chinese cabbage plant was carried out. For this purpose, the well-known classification method, spectral angle mapper (SAM) was used. SAM is an automated method for evaluating the image spectra similarity with a known spectra or endmember from the reference spectral library. In this method, the spectra are treated as vectors and the spectral angle between them is calculated. Initially, the angle between each endmember vector and the vector defined by the pixel values for each pixel is calculated. This results in a raster layer for each endmember containing the spectral angle. The more closely a pixel resembles a particular endmember class, the smaller is the spectral angle. Based on the pre-defined tolerance level for the spectral angle, the classification is established. As the vector's direction is only considered in this algorithm for classification, this method is insensitive to illumination intensity [21]. Fig. 8(a) shows the RGB image of the Chinese cabbage plant inspected and Fig. 8(b) shows the classified image obtained by applying the SAM classification algorithm. The green shaded areas correspond to healthy/normal region while the red shaded areas represent abnormal region. This figure clearly illustrates the automated detection capability of the proposed algorithm. It is envisioned that such techniques and algorithms have immense potential for automation in biomedical and agro-food sectors.

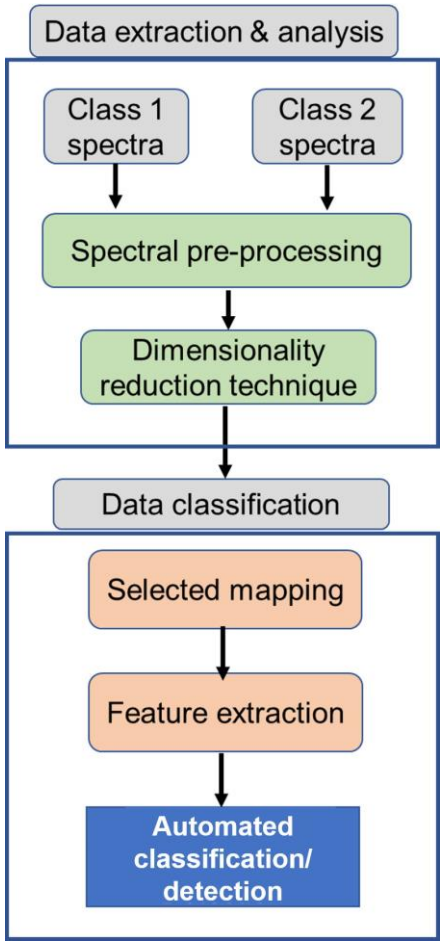


Fig. 7 Block diagram showing the algorithm for automated classification/detection based on reference spectral libraries created.

4 Conclusion and Future Work

A USI system with high spectral and spatial resolutions was developed and the applications of the developed system for agro and biomedical applications are demonstrated. An algorithm for the automated detection of abnormalities using the spectral signatures is detailed. Spectral libraries generated using the USI system is utilized for the automated classification of agro-food samples.

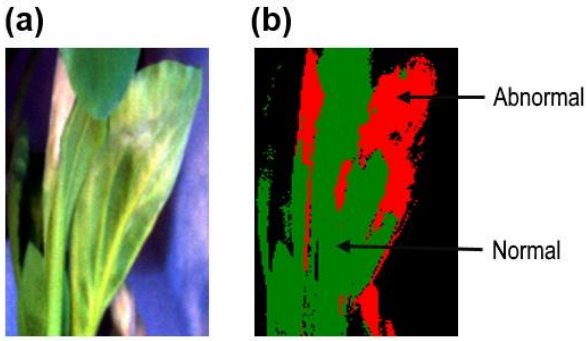


Fig. 8 SAM classified image of a Chinese cabbage plant showing automatically segmented normal and abnormal regions.

The proposed method offers possibilities for early-stage detection and classification of abnormalities or diseases. In addition, possible applications of the proposed technique for automated and early detection of diseases in biomedical domain could enable real-time result oriented solutions with detection, diagnosis and treatment approaches that can find potential applications in related diagnostic medical fields.

Acknowledgements

This research is supported by the National Research Foundation, Singapore and Singapore Food Agency, under its Singapore Food Story R&D Programme (Theme 1: Sustainable Urban Food Production) Grant Call (SFS_RND_SUFP_001_03). The authors also acknowledge financial support received through COLE-EDB funding at COLE, NTU.

Disclosures

The authors declare no conflict of interest.

References

1. J. Goecks, V. Jalili, L. M. Heiser, and J. W. Gray, "How Machine Learning Will Transform Biomedicine," Cell 181(1), 92–101 (2020).
2. E. S. Shenoy, E. S. Rosenthal, Y. P. Shao, S. Biswal, M. Ghanta, E. E. Ryan, D. Suslak, N. Swanson, V. M. Junior, D. C. Hooper, and M. B. Westover, "Real-Time, Automated Detection of Ventilator-Associated Events: Avoiding Missed Detections, Misclassifications, and False Detections Due to Human Error," Infection Control & Hospital Epidemiology 39(7), 826–833 (2018).
3. C. S. Suchand Sandeep, S. Sarangapani, X. J. Hong, T. Aung, M. Baskaran, and V. M. Murukeshan, "Optical sectioning and high resolution visualization of trabecular meshwork using Bessel beam assisted light sheet fluorescence microscopy," Journal of Biophotonics 12(12), e201900048 (2019).
4. T. Vo-Dinh, "A hyperspectral imaging system for in vivo optical diagnostics," IEEE Engineering in Medicine and Biology Magazine 23(5), 40–49 (2004).
5. J. James, V. M. Murukeshan, and L. S. Woh, "Integrated photoacoustic, ultrasound and fluorescence platform for diagnostic medical imaging-proof of concept study with a tissue mimicking phantom," Biomedical Optics Express 5(7), 2135–44 (2014).
6. S. B. Colak, M. B. Van der Mark, G. W. t Hooft, J. H. Hoogenraad, E. S. Van der Linden, and F. A. Kuijpers,"Clinical optical tomography and NIR spectroscopy for breast cancer detection," IEEE Journal of Selected Topics in Quantum Electronics 5(4), 1143–1158 (1999).
7. N. Sujatha, V. M. Murukeshan, L. S. Ong, and L. K. Seah, "An all fiber optic system modeling for the gastrointestinal endoscopy: design concepts and fluorescent analysis," Optics Communications 219(1–6), 71–79 (2003).
8. S. M. Perinchery, A. Shinde, C. Y. Fu, X. J. Jeesmond Hong, M. Baskaran, T. Aung, and V. M. Murukeshan, " High resolution iridocorneal angle imaging system by axicon lens assisted gonioscopy," Scientific Reports 6, 30844 (2016).
9. F. Strasser, M. Offterdinger, R. Piestun, and A. Jesacher, "Spectral image scanning microscopy," Biomedical Optics Express 10(5), 2513–2527 (2019).
10. A. F. Goetz, G. Vane, J. E. Solomon, and B. N. Rock, "Imaging spectrometry for Earth remote sensing," Science 228(4704), 1147–1153 (1985).
11. V. Kravets, P. Kondrashov, and A. Stern, "Compressive ultraspectral imaging using multiscale structured illumination," Applied Optics 58(22), F32–F39 (2019).
12. Y. Garini, I. T. Young, and G. McNamara, "Spectral imaging: principles and applications," Cytometry A 69(8), 735–47 (2006).
13. S. Mahesh, D. S. Jayas, J. Paliwal, and N. D. G. White, "Hyperspectral imaging to classify and monitor quality of agricultural materials," Journal of Stored Products Research 61, 17–26 (2015).
14. G. Lu, B. Fei, "Medical hyperspectral imaging: a review," Journal of Biomedical Optics 19(1), 010901 (2014).
15. H. T. Lim, V. M. Murukeshan, "A four-dimensional snapshot hyperspectral video-endoscope for bio-imaging applications," Scientific Reports 6, 24044 (2016).
16. H.-T. Lim, V. M. Murukeshan, "Hyperspectral photoacoustic spectroscopy of highly-absorbing samples for diagnostic ocular imaging applications," International Journal of Optomechatronics 11(1), 36–46 (2017).

17. M. M. Antony, C. S. Suchand Sandeep, and V. M. Murukeshan, "Hyperspectral z-scan: Measurement of spectrally resolved nonlinear optical properties," Spectrochimica Acta Part A: Molecular and Biomolecular Spectroscopy 261, 120005 (2021).
18. M. M. Antony, C. S. Sandeep, H. T. Lim, and M. V. Matham, "Hyperspectral Vision Based Probe for In Situ Corrosion Monitoring in Saline Environments," IEEE Transactions on Instrumentation and Measurement 71, 1–7 (2022).
19. S. Ortega, M. Halicek, H. Fabelo, G. M. Callico, and B. Fei, "Hyperspectral and multispectral imaging in digital and computational pathology: a systematic review [Invited]," Biomedical Optics Express 11(6), 3195–3233 (2020).
20. A. Lowe, N. Harrison, and A. P. French, "Hyperspectral image analysis techniques for the detection and classification of the early onset of plant disease and stress," Plant Methods 13, 80 (2017).
21. F. Van Der Meer, M. Vazquez-Torres, and P. M. Van Dijk, "Spectral characterization of ophiolite lithologies in the Troodos Ophiolite complex of Cyprus and its potential in prospecting for massive sulphide deposits," International Journal of Remote Sensin 18(6), 1245–1257 (1997).

C-MEMS Derived Glassy Carbon Glucose Sensor

Naresh Mandal[1] and Bidhan Pramanick[1,2*]

[1] School of Electrical Sciences, Indian Institute of Technology Goa, Ponda 403401, India

[2] Centre of Excellence in Particulates Colloids and Interfaces, Indian Institute of Technology Goa, Ponda 403401, India

***e-mail:** bidhan@iitgoa.ac.in

Abstract. Diabetes is one of the most severe health diseases in the world. More than 150 million people worldwide suffer from diabetes caused by an abnormal glucose concentration in their blood and tissues. The analysis of glucose levels in the body is significant, primarily due to diabetes mellitus. Therefore, accurately detecting blood glucose is crucial for diagnosing, treating, and managing diabetes. Diabetic patients can self-manage their condition by monitoring their glucose levels. The electrochemical glucose biosensor has several advantages, including recognizing glucose specifically, low price, ease of sensor manufacture, correctness, portability, and easy operation. We have developed glassy carbon electrodes (GCE) with conventional carbon-micro-electromechanical (C-MEMS) procedures for glucose sensing. SU-8 photoresist was used as the carbon precursor. The fabricated C-MEMS-derived GCE surface has been functionalized with chitosan and glucose oxidase. Glucose oxidase is a well-known enzyme for oxidizing glucose into gluconic acid and H_2O_2. This reaction kinetics has been recorded with increasing glucose concentration using electrochemical analysis. In summary, we have presented an electrochemical glucose biosensor in a single-step immobilization protocol of glucose oxidase on the glassy carbon electrode (GCE) surface and obtained satisfactory responses for 1 mM to 10 mM glucose solutions. © 2023 Journal of Biomedical Photonics & Engineering.

Keywords: C-MEMS; glassy carbon; biosensor; chitosan, glucose oxidase, impedance spectroscopy; electrochemical sensing; bio-functionalization.

Paper #6476 received 13 Feb 2023; revised manuscript received 20 May 2023; accepted for publication 21 May 2023; published online 1 Aug 2023. doi: 10.18287/JBPE23.09.030305.

1 Introduction

In the 21st century, diabetes has become a significant disease around the globe, with more than 439 million cases of Diabetes Mellitus (DM) estimated in 2030 [1]. According to WHO, 422 million people worldwide suffer from diabetes mellitus, which is predicted to be the seventh deadliest disease by 2030 [2]. Long-term suffering from DM causes cardiovascular diseases, kidney failure, blindness etc. The only way to cure DM is to control glycaemia levels. To control the glucose level in the blood, a diabetic patient needs to monitor the blood glucose level regularly. Therefore, it is a need for the hour to develop a novel, quick-response, low-cost biosensor for glucose sensing. Nano glucose sensors are usually made using an oxidoreductase to oxidize the glucose on the electrode surface. In general, glucose oxidase (GOx) is used for this purpose because it has excellent glucose selectivity, a high degree of stability, and a high activity level across a wide pH range [3]. According to this research, when GOx is used directly with bare electrode surfaces, it changes its structure, biological activity, and function [4]. The conventional finger-pricking method of measuring blood glucose levels causes pain, infection, and tissue damage [5]. The alternative way of finger pricking is without using blood samples in a non-invasive way [6], using bio fluids like tears, sweat, interstitial fluid (ISF), and saliva [7]. The non-invasive measurement techniques include the electromagnetic wave (EM) method, optical measuring and electrochemical sensing. M. Gourzi et al. developed a technique for measuring blood glucose from the skin using EM waves. However, this method is unreliable because measured glucose levels depend on temperature

This paper was presented at the International Conference on Nanoscience and Photonics for Medical Applications – ICNPMA, Manipal, India, December 28–30, 2022.

and cholesterol and ionize the biomolecules [8]. The mid-infrared spectroscopy is better than near-infrared spectroscopy [9]; in both methods, the pressure, temperature, and humidity severely affect the measured glucose value from the skin [10]. The temperature changes influence the measured value of glucose from the skin by optical coherence tomography (OCT) [11]. The specificity of the optical polarimetry technique of glucose measurement from the eye is very low because of eye movement, motion artifact and the optically active composition of aqueous humor [12].

A great deal of interest has been shown in enzyme immobilization technology concerning designing, fabricating, and applying biosensors. Various immobilization techniques are available, such as physical methods (absorption or entrapment) and chemical methods (for example, covalent bonds). Detecting trace components of biological, clinical, industrial and environmental systems can be carried out relatively simply, sensitively, and selectively using electrochemistry. When preparing biosensors, immobilization on the solid matrix is vital to maintaining enzyme function. It is essential that the structure and thickness of the materials used to immobilize enzymes do not reduce their functionality severely.

In the case of chitosan (CS), this polysaccharide biopolymer is formed by the partial deacetylation of chitin. The biocompatibility of chitosan makes it a desirable structural material for enzymatic immobilization and enhances biosensors' performance by retaining enzyme activity. Using chitosan for immobilizing enzymes and cells has been demonstrated as a functional, structural material. Several papers have reported using chitosan-modified biosensors, for example, the modified glucose biosensor built using a sol-gel/chitosan membrane [13, 14]. Adhesion and non-toxicity are good characteristics of this material. Additionally, its structure contains amino and hydroxyl groups, allowing easy chemical modification [15].

The electrochemical method of sensing glucose has immensely made the process easy due to its quick response, less sample use and reduced cost of testing. It is possible due to the advancement of low-cost fabrication techniques of sensors [16]. There are two methods of electrochemically sensing glucose from biofluids such as saliva, sweat, and tears: enzymatic and non-enzymatic. Clark and Lyons first evolved the concept of enzymatic bio-modified electrode sensor [17]. There have been numerous attempts to improve electron transfer from glucose oxidase (GOx) to electrode surfaces. As a result, there has been a growing interest in using semiconductors, carbon materials, such as carbon nanotubes, graphene, glassy carbon (GC) etc., and conductive polymers for achieving this goal. A fabricated platinum electrode was bio-modified in the layer-by-layer structure of single-walled carbon nanotube (SWNT), chitosan, and gold nanoparticles to measure glucose from saliva, obtaining a low detection limit of 0.1 mg/dl [18]. H. Yao et al. developed a contact lens sensor system to measure enzymatically tear glucose *in vitro* [19]. A study was carried out to measure glucose from ISF in tattoo based, noninvasive way [20]. Z. Temoçin implemented a sensor by modifying the surface of glassy carbon electrodes (GCE) with a blend nanofiber of poly (vinyl alcohol) and poly (ethylenemine), immobilized glucose oxidase (GOx). They obtained linear responses for blood glucose range, long storage stability, and high anti-interference for ascorbic and uric acid [21]. A GCE functionalized with high catalytic MnO_2 nanowires and coated with GOx showed high sensitivity [22]. Followed by modified GCE with MnO_2NPs and carbon nanofiber (CNF) nanocomposites, which showed higher performance in terms of sensitivity, selectivity, and response time [23]. The electron transfer rate was enhanced in a GCE modified by Co_3O_4 nanoparticles, multiwalled carbon nanotubes (MWCNTs) and immobilized GOx [24]. It was also experimentally verified that Ni/CoO-loaded carbon nanofiber deposited GCE showed a good catalytic effect on glucose [25]. To enhance the performance of glucose sensors, GCE was modified by polypyrrole, nafion functionalized Multiwalled carbon nanotubes (MWCNTs) nanocomposite, chitosan and glucose oxidase showed excellent catalytic activity [26]. GOx, encapsulated in liposome microreactors, was coated on a chitosan layer over GCE showing excellent repeatability and stability [27]. The non-covalently functionalization of MWCNTs and GOx was also deposited on GCE to detect glucose in milk [28]. The poly(p-phenylenediamine) (PPD) and Fe_3O_4 nanoparticles (Fe_3O_4 NPs) nanocomposites were developed as enzyme immobilizers on GCE. The modified electrode showed good affinity to glucose in clinical samples without interferences [29]. The GOx was immobilized on single-layer graphene doped with AuNPs over fabricated GCE. The sensor showed ultra-sensitive for low concentrations of glucose [30]. The 2D-RGO (Reduced graphene oxide) nanocomposites modified GCE, developed by G. Bharath et al., obtained higher electron transfer rate and sensitivity [31]. It has been demonstrated that palladium nanoparticle/chitosan-grafted graphene nanocomposites can be used as glucose biosensors [32]. To detect dopamine selectively, graphene/chitosan electrodes were developed [33]. In direct electrochemistry and glucose sensing, a glucose oxidase–graphene–chitosan electrode was developed [34].

Sol-gel techniques have been used to construct many of these very successful biosensors. However, according to our knowledge, the method for producing biosensors also has some disadvantages. For example, through the porous nature of the thin sol-gel matrix, the enzyme is slowly leached from the electrode surface. There are several issues with the biosensor, such as its slow response time, the procedures being more complicated, and a fragility that makes it difficult to use. It is important to note that during the sol-gel process, certain harsh conditions are exposed to the enzyme, namely partial denaturation by the catalyst (ether basic or acidic) or the solvent (usually methanol).

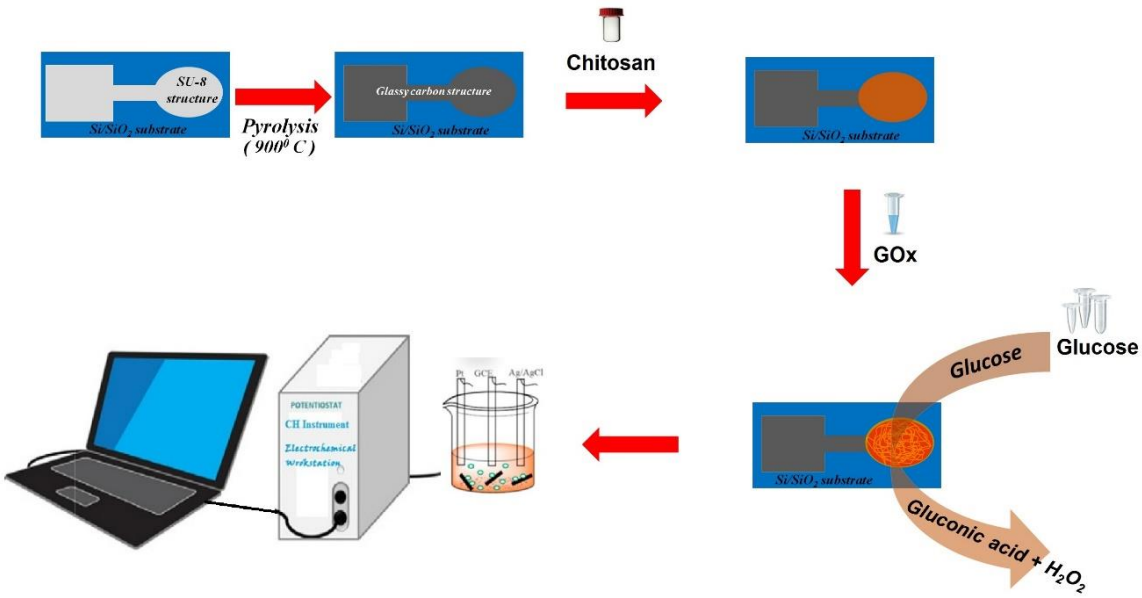


Fig. 1 General scheme of bio-modified glassy carbon electrode (GCE) sensor.

In this paper, a novel biosensor is presented to overcome these problems. We have developed a simple, cost-effective glucose biosensor based on the entrapment of glucose oxidase directly in chitosan on a GC electrode. Compared to the sol-gel/chitosan-modified Glucose Oxidase biosensor, this low-cost design simplifies the fabrication process to ensure a stable and sensitive biosensor. A significant advantage of such devices is that they offer faster, more straightforward methods of obtaining sequence-specific information than the traditional sol-gel techniques. An optimization study was conducted for the biosensor, and its analytical performance was evaluated. A schematic representation of the steps involved in the modification process of the glassy carbon electrode (GCE) for the glucose electrochemical sensing platform is shown in Fig. 1.

2 Materials and Methods

2.1 Reagents and Solutions Preparation

For bio-modifying GCE chitosan from shrimp shells, ≥ 75% (deacetylated) Glucose Oxidase from Aspergillus niger with an activity of 100000–250000 units/g was purchased from Sigma Aldrich. Phosphate buffer saline (PBS) contains NaCl, KCl, Sodium dihydrogen phosphate (Na2HPO4), and Potassium dihydrogen phosphate (KH2PO4), which were purchased from Sigma Aldrich. Standard glucose solution is prepared from D-(+)-Glucose ≥ 99.5% (GC) was purchased from Sigma Aldrich. Glacial acetic acid was purchased from Sigma Aldrich to prepare chitosan solution of chitosan in 0.1 M acetic acid. Milli-Q 0.5 water with a resistivity of 18 MΩ cm was taken from in house plant of IIT Goa for making PBS solutions and washing the electrodes. Chitosan solution has been prepared by dissolving (2 mg/mL) chitosan sample in 0.6 wt% glacial acetic acid at room temperature using magnetic stirring at 1000 rpm for 1 h. A glucose oxidase (GOx) concentration of 35 mg/mL has been prepared in 0.25 M PBS.

2.2 Fabrication of Electrodes

The conventional method of photolithography and pyrolysis was used to fabricate GCE (Fig. 2) on a 4-inch silicon wafer with a 1 µm thermally-oxidized SiO_2 layer (NOEL Technologies, Campbell, CA, USA). SU-8 negative photoresist was spin-coated at 3000 rpm for the 30 s and then soft-baked on a hotplate at 95 ºC for 3 min to get an even distribution of the layer on the substrate and evaporate the solvent. UV radiation was exposed on photoresist through a thin film photomask to a total energy of 120 mJ/cm^2 and baked again for 3.5 min at 95 °C to crosslink the exposed patterns. Then the samples were dipped in SU-8 PR developer solution for 2 min to dissolve the unexposed region [35]. The SU-8 structured pattern was pyrolyzed in an inert furnace to convert the SU-8 to glassy carbon (GC) structure. Initially, the SU-8 pattern was heated to 300 ºC at a determined temperature ramp rate of 5 ºC/min and kept at that temperature for 60 min for thermal stabilization. Then the temperature was increased to 900 ºC at a rate of 5 ºC/min, maintained the temperature for 1 h and cooled down the furnace at a rate of 10 ºC/min. Thus, the SU-8 sensor structure was pyrolyzed to GC structure [36].

2.3 Electrode Surface Modification

The chitosan solution 0.6 wt% in 0.1 M acetic acid was prepared by magnetic stirring at 1000 rpm for 1 h. The GCE electrode was cleaned in Milli-Q water, dried using N_2 gas flow, and coated with chitosan solution by pipetting. Then it was kept at room temperature for 1 h till drying. Afterwards, the chitosan-coated GCE was pipetted with 35 mg/ml GOx solution in 0.25 M PBS and preserved at 4 ºC temperature for 2 h before use (Fig. 3).

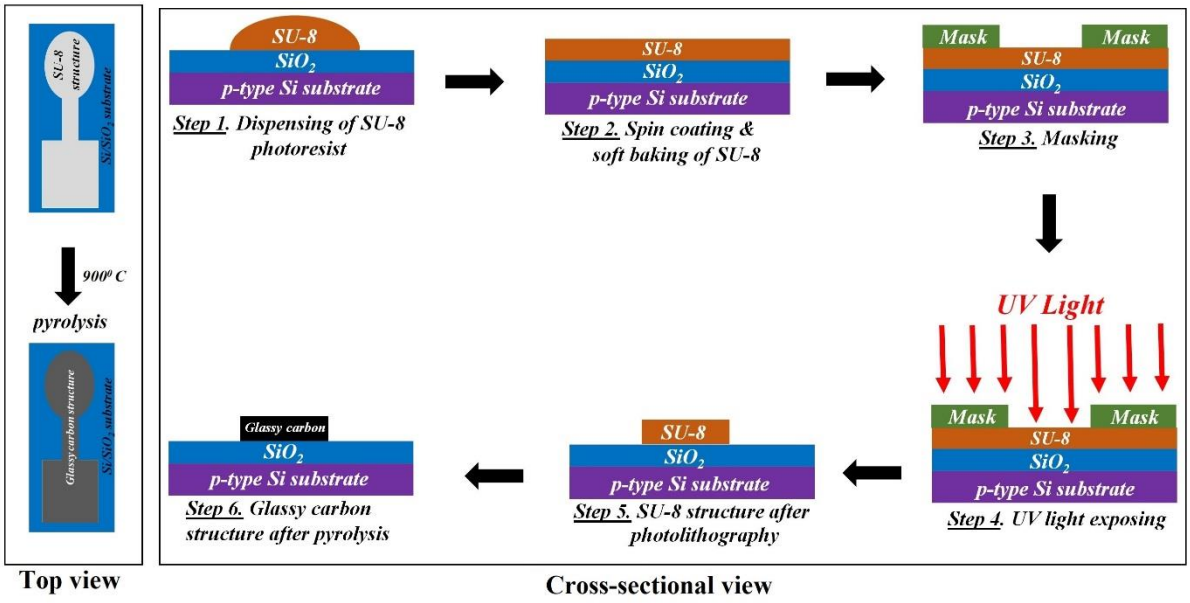


Fig. 2 Fabrication steps of GC electrode.

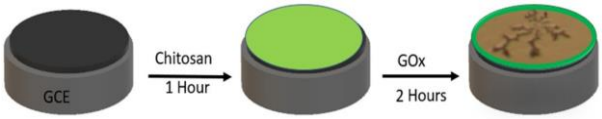


Fig. 3 Bio-modifying of GC electrode.

The bio-modified electrode was cleaned in PBS solution to remove unbound glucose oxidase enzyme before electrochemical testing. All electrochemical experiments were carried out using a potentiostat of CHI 760E electrochemical workstations. A three-electrode system of bio-modified GCE as the working electrode, Ag/AgCl as the reference electrode and Platinum wire as the counter electrode was used for electrochemical characterization.

2.4 Structural Characterization

The surface of the patterned SU-8 structure was shrunk due to pyrolysis. Scanning Electron Microscopy (SEM) (EVO, Zeiss, Germany) was used to characterize the surface morphology and to measure the shrinkage of the carbonized electrodes. The crystallinity of the fabricated carbon electrode was examined with Raman spectroscopy (inVia Qontor, Renishaw plc, UK) using a 514 nm Ar laser source. This work has been reported in the previously reported work [36].

2.5 FTIR Characterization

FTIR characterization has been performed using a SHIMADZU (IRAFFINITY 1S WL model) with a resolution of 4 cm^{-1} in the 400–4000 cm^{-1} region. This instrument is equipped with Specac attenuated total reflection (ATR) fitted with diamond crystal, scanned (transmittance *vs* wave numbers mode) at room temperature 25 ºC and humidity. Fourteen hundred scans have been taken for accuracy, and we reported the average value.

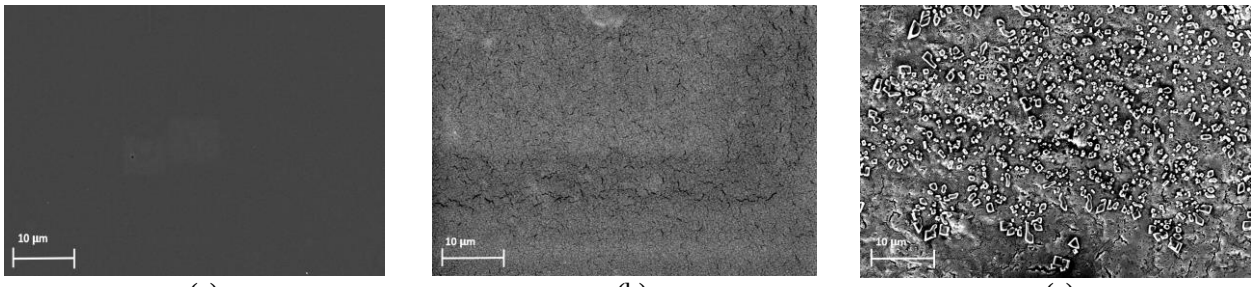
2.6 Electrochemical Characterization

Electrochemical impedance spectroscopy (EIS) is an efficient electrochemical measurement technique to analyse the behaviour of the surface-modified electrodes for a particular analyte [1]. The EIS data is usually fitted with an equivalent electrical circuit model to get the electrical fingerprint of the electrochemical behaviour of the sample. EIS was carried out for glucose concentrations 1 mM to 10 mM in 0.25 M PBS, applied ac signal perturbation 5 mV and frequency range from 100 Hz to 1 MHz. Cyclic voltammetry (CV) was carried out to observe the redox peak of bio-modified GCE for glucose concentrations 1 mM, 3 mM, 5 mM, and 8 mM for an applied potential range of –0.1 V to 0.6 V vs Ag/AgCl electrode at a scan rate of 100 mV/sec. We recorded Chronoamperometry reading for 1 mM, 3 mM, 5 mM, 8 mM, and 10 mM glucose concentrations to quantify the glucose concentration. All the experiments were carried out for glucose solutions in 0.25 M Phosphate buffer saline (PBS) of pH 7.4 and room temperature 25 ºC. All the readings were taken in triplets for each technique and the average has been plotted.

3 Results and Discussion

3.1 Morphologies of GCE, Chitosan, and Chitosan/ Glucose Oxidase / GCE

Micrographs of chitosan and chitosan/glucose oxidase have been characterized using SEM images, as shown in Fig. 4. Noticeably, Fig. 4(b) shows that the membrane of chitosan consists of a homogeneous arrangement, and its surface is flat and symmetrical.



(a) (b) (c)

Fig. 4 Scanning electron microscopy (SEM) photomicrograph (images captured at the magnification of 1.63 K X) showing the morphology of (a) glassy carbon electrode (GCE), (b) chitosan/GCE, and (c) chitosan/ glucose oxidase /GCE.

A bump structure is visible on the chitosan/glucose oxidase/GCE compared to the chitosan/GCE (Fig. 4b). The bumps are uniform in size and shape, suggesting glucose oxidase is immobilized in the chitosan/GCE surface (Fig. 4c).

3.2 Characterization of the Sensor Electrode by FTIR

First, 2 mg/mL chitosan solution was pipetted out on the GCE and kept at room temperature for 1 h. After the treatment, FTIR measurement was carried out to estimate the binding of GC with chitosan. After thoroughly drying the surface of the active area of GCE, 10 µL of glucose oxidase solution was pipetted out and allowed to dry for 2 h at room temperature. Again FTIR measurement has been recorded. For each of the electrochemical processes, FTIR plot of transmittance vs wave numbers have been recorded, which is depicted in Fig. 5(a) glassy carbon electrode (GCE), (b) GCE/chitosan, and (c) GCE/chitosan/ glucose oxidase.

GCE, the bare electrode, does not show many FTIR features that suggest the glassy carbon nature of the electrode (Fig. 5a). After adding chitosan (2 mg/mL) to the GCE, a broad peak appears around 3235 cm^{-1}, corresponding to O-H and N-H stretching frequency. The broadness of the peak is due to substantial hydrogen bonding. The peaks around 2915 and 2872 cm^{-1} are due to C-H stretching frequency. Carbonyl stretching frequencies around 1631 and 1549 cm^{-1} are characteristics of amide bonds of chitosan (N-acetyl groups). The most substantial peak at 1061–1023 cm^{-1} is attributed to C-O stretching frequencies of polysaccharides (Fig. 5b). On adding glucose oxidase to the chitosan-modified GCE, the peak intensities are reduced substantially, suggesting surface modification. A broad peak around O-H and N-H stretching frequency regions (~ 3250 cm^{-1}) was observed. The amide peaks around 1680–1643 cm^{-1} and 1543–1502 cm^{-1} were also observed. The prominent peak at 1067 due to C-O stretching was observed for glucose oxidase-modified electrodes (Fig. 5c). Comparing the FTIR of surface-modified electrodes, it is evident that the surface was modified initially by chitosan and subsequently with glucose oxidase. No new peaks were observed as chitosan, and glucose oxidase interaction is primarily hydrogen bonding.

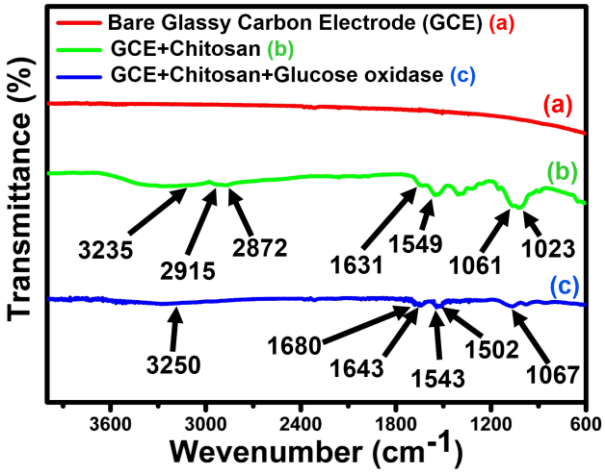


Fig. 5 FTIR spectrum of (a) glassy carbon electrode (GCE), (b) GCE/chitosan, and (c) GCE/chitosan/glucose oxidase.

3.3 Electrochemical Characterization Results

Electrochemical characterization of GCE has been carried out using 0.25 M Phosphate buffer saline (PBS) of pH 7.4 and room temperature 25 ºC. A conventional three-electrode system (CHI Electrochemical work analyzer (CH 760E)) has been employed for all Electrochemical measurements. In this system, we have used the carbon electrode as the working electrode, a platinum wire as the counter electrode and an Ag/AgCl as a reference electrode. The Eqs. below show that glucose oxidase reacts with glucose when oxygen is used as an electron acceptor.

$$Enzyme(oxidized)+\beta\text{-}d\text{-}glucose \rightarrow Enzyme(reduces)+d\text{-}gluconic\ acid, \quad (1)$$

$$Enzyme(reduced)+O_2 \rightarrow Enzyme(oxidized)+H_2O_2. \quad (2)$$

In the presence of an applied potential of +0.5 V, the following reaction occurs when H_2O_2 is brought closer to the surface of the anode.

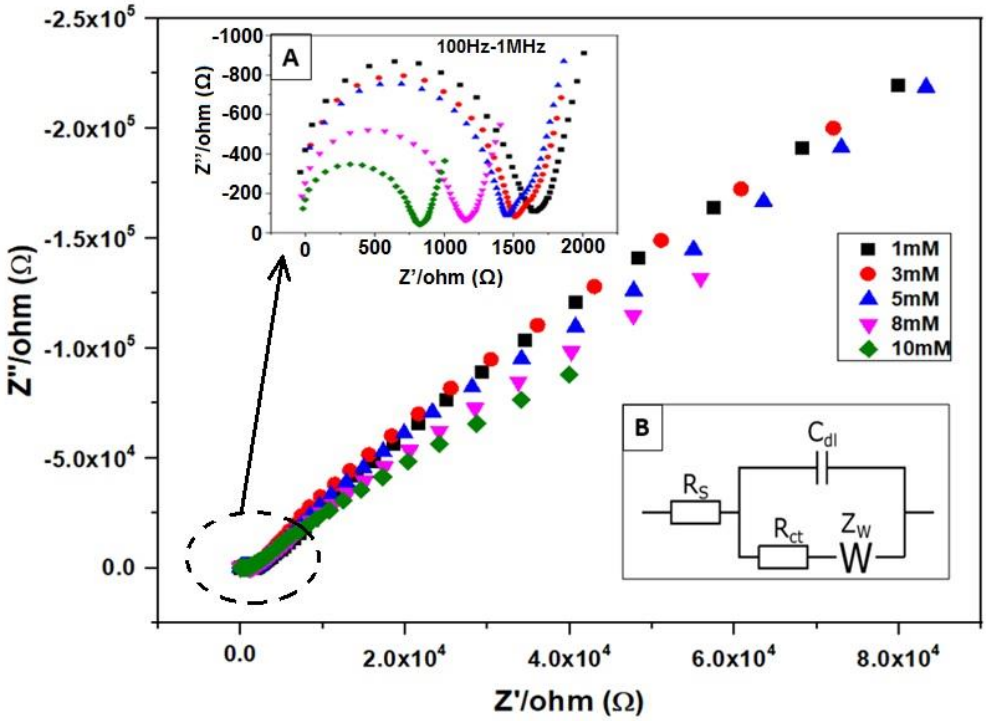


Fig. 6 EIS response of biomodified GCE for 1 mM–10 mM glucose concentrations, (A) zoom view of Nyquist plot for higher frequency ranges 100 Hz–1 MHz and (B) Randle's equivalent circuit model.

$$H_2O_2 \rightarrow {}^{\bullet}O_2 + 2H^+ + 2e^-. \quad (3)$$

When the H_2O_2 redox reaction occurs near the carbon electrode sensor surface, the resulting current increases as glucose concentration increases.

3.3.1 Electrochemical Impedance Spectroscopy (EIS) Measurements

During EIS (Electrochemical Impedance Spectroscopy) measurements, a 3-electrode configuration and a PC interfaced a conventional three-electrode system (CHI Electrochemical work analyzer (CH 760E)) was used with an applied sinusoidal signal of 5 mV amplitude in the frequency range of 100 Hz to 1 MHz. The Nyquist impedance plots have been recorded after the GCE has been exposed to 0.25 M Phosphate buffer saline (PBS) of pH 7.4 and room temperature 25 ºC. The Nyquist plots of the EIS data in Fig. 6A showed that with the increase in glucose concentration, the radius of the semi-circle was reduced, indicating the decrease in R_{ct} in Randle's circuit model Fig 6B.

The current through the electrode consists of faradaic current and double-layer capacitor charging current. Therefore, the electrical equivalent model can be defined as solution resistance (R_s) in series with the parallel combination of double-layer capacitance and in series with charge transfer resistance (R_{ct}) and warbag resistance (Z_w), responsible for mass transfer [37]. The warbag resistance (Z_w) is associated with diffusion, migration and convocation of charges towards the electrode [38]. The double layer capacitance (C_{dl}) is easily formed on GCE due to the porous surface [39]. The value of C_{dl} depends on the ionic concentration, pH, temperature, type of ions, oxide layers, and roughness of the electrode [40]. The impedance magnitude is decreased with the increase in glucose concentration, as the reactant will be more for higher concentrations. The concentrations measured in this study ranged from 1 mM to 10 mM, indicating that the whole process was controlled by the enzyme's catalytic kinetics. Increasing glucose concentration resulted in more hydrogen peroxide(H_2O_2) being released from enzyme base reactions and under air saturation conditions; as hydrogen peroxide (H_2O_2) concentration increases at the GC electrode surface, the oxidation current increases.

3.3.2 Cyclic Voltammetry (CV) Measurements

Cyclic voltammetry (CV) is a versatile electrochemical technique to study the redox kinetics on electrode surfaces with bio analytes. Cyclic voltammetry (CV) measurements of the GCE sensor have been performed in 0.25 M Phosphate buffer saline (PBS) of pH 7.4 at room temperature 25 ºC. For Cyclic voltammetry (CV) measurements, a three-electrode system has been used in a similar manner. Using this system, we used the GCE sensor as a working electrode, the platinum wire as a counter electrode, and the Ag/AgCl as a reference electrode. Cyclic voltammetry (CV) was carried out with an electrode potential range of −0.1 V to 0.6V vs Ag/AgCl electrode at a scan rate of 100 mV/sec.

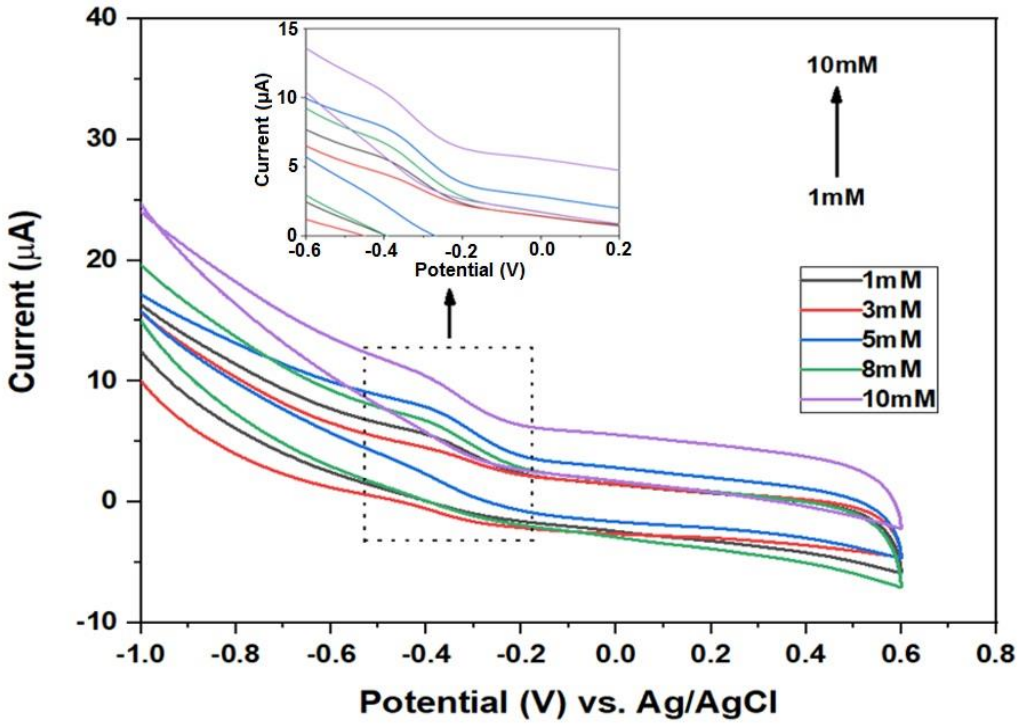


Fig. 7 Cyclic voltammogram of biomodified GCE for glucose concentrations 1 mM, 3 mM, 5 mM, 8 mM, and 10 mM.

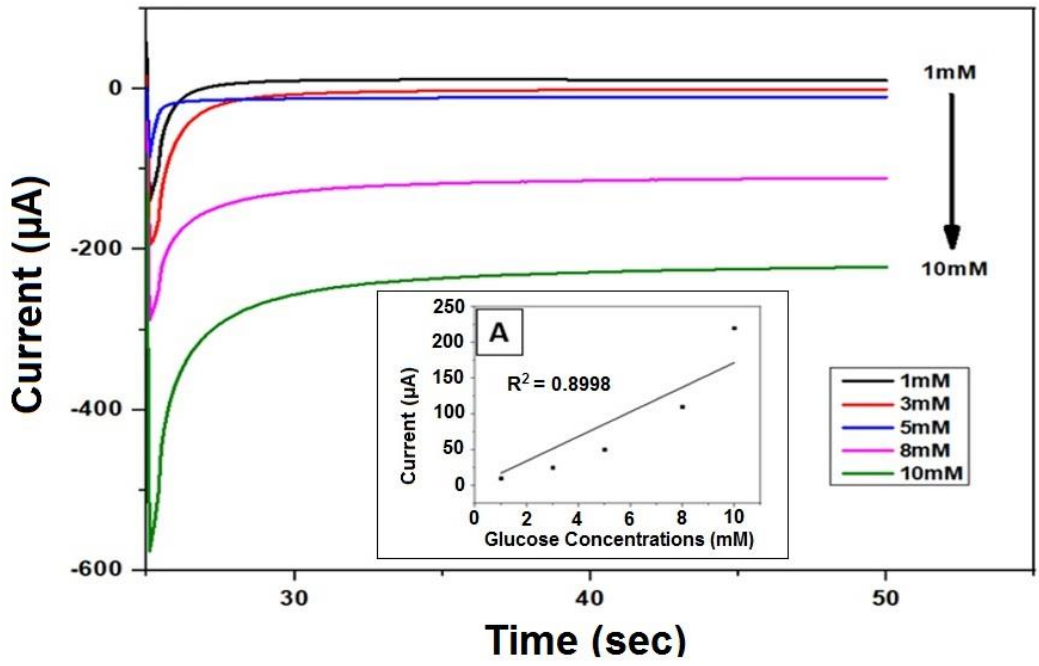
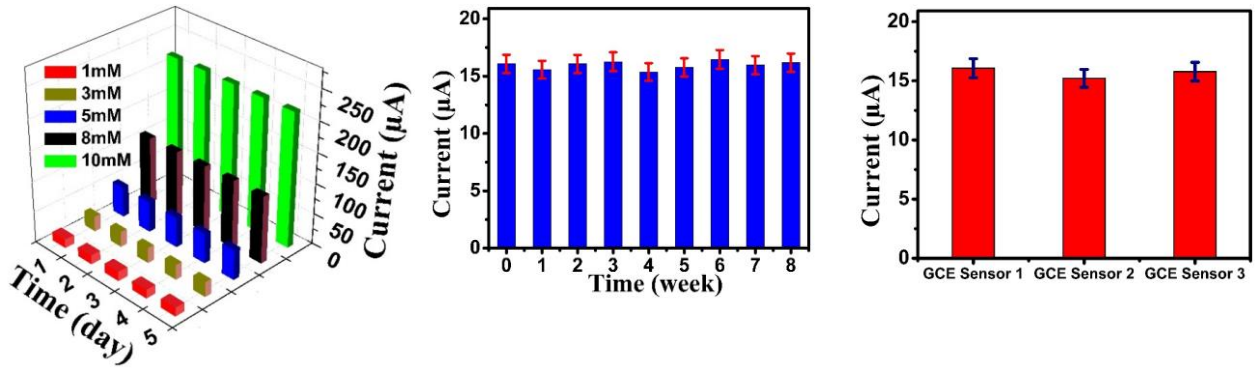


Fig. 8 Chronoamperometry response of bio-modified GCE. (A) The current change of different concentrations of glucose solution and the associated fitting curve.

The redox reaction on the top surface of the electrode occurs at a specific potential. It is related to the surface area, rate constant, interface with solution, pH of the solution, and temperature [41]. The peak current of CV responses was increased with the increase in glucose concentrations. The peak current is validated by Randles-Sevick Eqs. (4), peak current is directly proportional to the concentrations [42].

$$I_P = (2.69 \times 10^5) n^{\frac{3}{2}} A D^{\frac{1}{2}} C v^{\frac{1}{2}}. \quad (4)$$

Here, C is the concentration, and other symbols have standard meanings. From the CV response, it is obtained that maximum oxidation occurs at 0.5 V. The change of peak current of CV response with the change of concentration is shown in Fig. 7.



(a) (b) (c)

Fig. 9 (a) Variations of chronoamperometry measurements conducted for the glucose concentrations of 1, 3, 5, 8 and 10 mM for successive five days. (b) The measured current variation as a function of storage time for glucose concentration of 1 mM. (c) The reproducibility testing of three GEC sensors.

3.3.3 Chronoamperometery Measurements

The Michaelis-Menten constant is mainly utilized for the biological activity of immobilized glucose oxidase, and the Michaelis-Menten Eq. (5) can be used to calculate it.

$$I = I_{MAX} - K_s\left(\frac{I}{C}\right), \quad (5)$$

where I represents the steady-state catalytic current, I_{MAX} represents the maximum current (under saturated substrate conditions), C denotes the glucose concentration, and K_s represents the Michaelis-Menten constant of the system. As shown in Fig. 8, the glucose biosensor shows a typical current-time curve under optimized experimental settings. Chronoamperometery current was recorded for 1 mM–10 mM glucose solution by applying dc voltage 0.5 V. Fig. 8A shows that amperometric current increases with the increase of glucose concentration. The sensitivity obtained by linearizing the stable amperometric current with $R^2 = 0.8966$ curve is 17 μA/mM. It was observed that when 0.5 V was applied, an amperometric response was well-defined, stable, and fast. There was a direct relationship between glucose concentration and the currents produced in the solution when glucose was added. It took about 10 s for the current value to reach a steady state. This study evaluated 1 mM to 10 mM, which demonstrated that the enzyme's catalytic kinetics governed the whole system.

3.3.4 Stability and Reproducibility Test of the Bio-Modified GCE Sensor

Stability is a crucial factor when evaluating the effectiveness of an electrochemical biosensor. The stability of the GCE was assessed using two different methods. First, the GCE was employed to measure glucose levels over five consecutive days, and the resulting chronoamperometric current responses were recorded to determine the stability. The measurements were taken using 1, 3, 5, 8, and 10 mM glucose concentrations at pH 7.4. Followed by the measures, the GCE was stored in a refrigerator at 4.0 °C. The current values in Fig. 9(a) demonstrate that the GCE exhibited excellent stability in accurately measuring various glucose concentrations throughout the five days.

Ensuring long-term stability in enzyme-based biosensors is a challenging task due to the inherent instability of enzymes. Therefore, the GCE was stored in a refrigerator for 56 days to evaluate its stability further. In the stability test, chronoamperometric current measurements were taken at specific time intervals using glucose solutions with a consistent concentration of 1 mM. Fig. 9(b) illustrates the current values obtained from these measurements over the storage period. It was observed that there was a maximum decrease of 4% and an increase of 3% compared to the initial value. These findings indicate that the GCE exhibits exceptional long-term stability, which can be attributed to the adequate protection of the GOx enzyme through the single-step immobilization process.

The reproducibility of the analytic signal is a crucial requirement for biosensors. Three separate GCE sensors were prepared and utilized to detect glucose in 1 mM glucose solutions to assess its stability. The chronoamperometric current was recorded for each sensor with 1 mM glucose solution. The reproducibility of the different glucose sensors was determined and presented in Fig. 9(c). By calculating the relative standard deviation of glucose concentrations through consecutive measurements, it was found to be 5%. This result indicates that the bio-modified GCE sensors yielded glucose analysis outcomes with relatively low variability, demonstrating a high level of reproducibility.

4 Conclusions

The research on the development of blood glucose measurement in a non-invasive way has received enormous attention in the past two decades as this has become an utmost priority to monitor patients' blood glucose levels regularly. This work presents a thorough study of the available glucose measurement techniques

and their limitations, followed by the development of a glassy carbon glucose sensor. GCE has been fabricated by a conventional photolithography process and carbonization of SU-8 negative photoresist by pyrolysis. The GCE was functionalized by chitosan and glucose oxidase to detect glucose. Glucose oxidase converts glucose into gluconic acid and H_2O_2, and this reaction kinetics has been measured with an increasing glucose concentration of 1 mM to 10 mM glucose solutions. We have obtained a sensitivity of 17 µA/mM. We have presented and discussed the electrochemical glucose biosensor in this manuscript, which lies in a single-step immobilization protocol of glucose oxidase on the glassy carbon electrode (GCE) surface.

Acknowledgements

The authors would like to thank the technical staff of MEC and MEMS lab, Dept. of E&ECE, IIT Kharagpur, India, for their support in the fabrication of the carbon electrodes. The authors also would like to thank Dr. Raja Mitra, SCMS, IIT Goa, for his help analyzing FTIR results. The FTIR analysis support from IIT Goa is acknowledged. The authors would like to thank IIT Goa for its financial support.

Disclosures

The authors declare no conflict of interest.

References

1. J. E. Shaw, R. A. Sicree, and P. Z. Zimmet, "Global estimates of the preva lence of diabetes for 2010 and 2030," Diabetes Research and Clinical Practice 87(1), 4–14 (2010).
2. P. López-Soriano, P. Noguera, M. T. Gorris, R. Puchades, Á. Maquieira, E. Marco-Noales, and M. M. López, "Lateral flow immunoassay for on-site detection of Xanthomonas arboricola pv. pruni in symptomatic field samples," PLOS ONE 12(4), e0176201 (2017).
3. S. Ferri, K. Kojima, and K. Sode, "Review of glucose oxidases and glucose dehydrogenases: A Bird's eye view of glucose sensing enzymes," Journal of Diabetes Science and Technology 5(5), 1068–1076 (2011).
4. K.-J. Huang, L. Wang, J. Li, T. Gan, and Y.-M. Liu, "Glassy carbon electrode modified with glucose oxidase–graphene–nano-copper composite film for glucose sensing," Measurement 46(1), 378–383 (2013).
5. J. Chung, H. So, Choi, and T. K. S. Wong, "Recent advances in noninvasive glucose monitoring," Medical Devices: Evidence and Research 5, 45–52 (2012).
6. O. S. Khalil, "Noninvasive glucose measurement technologies: An update from 1999 to the dawn of the New Millennium," Diabetes Technology and Therapeutics 6(5), 660–697 (2004).
7. J. Heikenfeld, A. Jajack, B. Feldman, S. W. Granger, S. Gaitonde, G. Begtrup, and B. A. Katchman, "Accessing analytes in biofluids for peripheral biochemical monitoring," Nature Biotechnology 37, 407–419 (2019).
8. M. Gourzi, A. Rouane, R. Guelaz, M. S. Alavi, M. B. McHugh, M. Nadi, and P. Roth, "Noninvasive glycaemia blood measurements by electromagnetic sensor: Study in static and dynamic blood circulation," Journal of Medical Engineering & Technolog 29(1), 22–26 (2005).
9. A. J. Berger, T.-W. Koo, I. Itzkan, G. Horowitz, and M. S. Feld, "Multicomponent blood analysis by near-infrared Raman spectroscopy," Applied Optics 38(13), 2916–2926 (1999).
10. J. Kottmann, U. Grob, J. Rey, and M. Sigrist, "Mid-Infrared fiber-coupled photoacoustic sensor for biomedical applications," Sensors 13(1), 535–549 (2013).
11. K. V. Larin, M. S. Eledrisi, M. Motamedi, and R. O. Esenaliev, "Noninvasive blood glucose monitoring with optical coherence tomography," Diabetes Care 25(12), 2263–2267 (2002).
12. B. H. Malik, G. L. Coté, "Real-time, closed-loop dual-wavelength optical polarimetry for glucose monitoring," Journal of Biomedical Optics 15(1), 017002 (2010).
13. X. Chen, J. Jia, and S. Dong, "Organically modified sol-gel/chitosan composite based glucose biosensor," Electroanalysis 15(7), 608–612 (2003).
14. X. Yang, L. Hua, H. Gong, and S. N. Tan, "Covalent immobilization of an enzyme (glucose oxidase) onto a carbon sol–gel silicate composite surface as a biosensing platform," Analytica Chimica Acta 478(1), 67–75 (2003).
15. J. Choi, K.-J. Kim, B. Kim, H. Lee, and S. Kim, "Covalent functionalization of epitaxial graphene by Azidotrimethylsilane," The Journal of Physical Chemistry C 113(22), 9433–9435 (2009).
16. B. Pramanick, N. Mandal, D. Mondal, C. RoyChaudhuri, and S. Chakraborty, "C-MEMS derived glassy carbon electrodes-based sensitive electrochemical biosensors," IEEE Sensors Journal 20(21), 12472–12478 (2020).
17. L. C. Clark, C. Lyons, "Electrode systems for continuous monitoring in cardiovascular surgery," Annals of the New York Academy of Sciences 102(1), 29–45 (1962).
18. W. Zhang, Y. Du, and M. L. Wang, "Noninvasive glucose monitoring using saliva nano-biosensor," Sensing and Bio-Sensing Research 4, 23–29 (2015).
19. H. Yao, Y. Liao, A. R. Lingley, A. Afanasiev, I. Lähdesmäki, B. P. Otis, and B. A. Parviz, "A contact lens with integrated telecommunication circuit and sensors for wireless and continuous tear glucose monitoring," Journal of Micromechanics and Microengineering 22(7), 075007 (2012).

20. A. J. Bandodkar, W. Jia, C. Yardımcı, X. Wang, J. Ramirez, and J. Wang, "Tattoo-based noninvasive glucose monitoring: A proof-of-concept study," Analytical Chemistry 87(1), 394–398 (2015).
21. Z. Temoçin, "Designing of a stable and selective glucose biosensor by glucose oxidase immobilization on glassy carbon electrode sensitive to H_2O_2 via nanofiber interface," Journal of Applied Electrochemistry 51(2), 283–293 (2021).
22. L. Zhang, S.-M. Yuan, L.-M. Yang, Z. Fang, and G.-C. Zhao, "An enzymatic glucose biosensor based on a glassy carbon electrode modified with manganese dioxide nanowires," Microchimica Acta 180, 627–633 (2013).
23. L. Zhang, Q. Chen, X. Han, and Q. Zhang, "MNO2 nanoparticles and Carbon Nanofibers Nanocomposites with high sensing performance toward glucose," Journal of Cluster Science 29(6), 1089–1098 (2018).
24. C. Kaçar, B. Dalkiran, P. E. Erden, and E. Kiliç, "An amperometric hydrogen peroxide biosensor based on Co3O4 nanoparticles and multiwalled carbon nanotube modified Glassy Carbon Electrode," Applied Surface Science 311, 139–146 (2014).
25. Q. Mei, R. Fu, Y. Ding, L. li, A. Wang, D. Duan, and D. Ye, "Electrospinning of highly dispersed ni/COO carbon nanofiber and its application in glucose electrochemical sensor," Journal of Electroanalytical Chemistry 847, 113075 (2019).
26. B. K. Shrestha, R. Ahmad, H. M. Mousa, I.-G. Kim, J. I. Kim, M. P. Neupane, C. H. Park, and C. S. Kim, "High-performance glucose biosensor based on chitosan-glucose oxidase immobilized polypyrrole/Nafion/functionalized multiwalled carbon nanotubes bio-nanohybrid film," Journal of Colloid and Interface Science 482, 39–47 (2016).
27. H. Guan, D. Gong, Y. Song, B. Han, and N. Zhang, "Biosensor composed of integrated glucose oxidase with liposome microreactors/chitosan nanocomposite for amperometric glucose sensing," Colloids and Surfaces A: Physicochemical and Engineering Aspects 574, 260–267 (2019).
28. P. A. Gallay, M. D. Rubianes, F. A. Gutierrez, and G. A. Rivas, "Avidin and glucose oxidase-non-covalently functionalized multiwalled carbon nanotubes: A new analytical tool for building a bienzymatic glucose biosensor," Electroanalysis 31(10), 1888–1894 (2019).
29. M. Baghayeri, "Glucose sensing by a glassy carbon electrode modified with glucose oxidase and a magnetic polymeric nanocomposite," RSC Advances 5(24), 18267–18274 (2015).
30. Y. Yuan, Y. Wang, H. Wang, and S. Hou, "Gold nanoparticles decorated on single layer graphene applied for electrochemical ultrasensitive glucose biosensor," Journal of Electroanalytical Chemistry 855, 113495 (2019).
31. G. Bharath, R. Madhu, S.-M. Chen, V. Veeramani, A. Balamurugan, D. Mangalaraj, C. Viswanathan, and N. Ponpandian, "Enzymatic electrochemical glucose biosensors by Mesoporous 1D hydroxyapatite-on-2d reduced graphene oxide," Journal of Materials Chemistry B 3(7), 1360–1370 (2015).
32. Q. Zeng, J.-S. Cheng, X.-F. Liu, H.-T. Bai, and J.-H. Jiang, "Palladium nanoparticle/Chitosan-grafted graphene nanocomposites for construction of a glucose biosensor," Biosensors and Bioelectronics 26(8), 3456–3463 (2011).
33. Y. Wang, Y. Li, L. Tang, J. Lu, and J. Li, "Application of graphene-modified electrode for selective detection of dopamine," Electrochemistry Communications 11(4), 889–892 (2009).
34. X. Kang, J. Wang, H. Wu, I. A. Aksay, J. Liu, and Y. Lin, "Glucose oxidase–graphene–Chitosan modified electrode for direct electrochemistry and glucose sensing," Biosensors and Bioelectronics 25(4), 901–905 (2009).
35. C. Wang, G. Jia, L. H. Taherabadi, and M. J. Madou, "A novel method for the fabrication of high-aspect ratio C-MEMS structures," Journal of Microelectromechanical Systems 14(2), 348–358 (2005).
36. B. Pramanick, M. Vazquez-Pinon, A. Torres-Castro, S. O. Martinez-Chapaa, and M. Madou, "Effect of pyrolysis process parameters on electrical, physical, chemical and electrochemical properties of SU-8-derived carbon structures fabricated using the C-MEMS process," Materials Today: Proceedings 5(3), 9669–9682 (2018).
37. J. Huang, "Diffusion impedance of electroactive materials, electrolytic solutions and porous electrodes: Warburg impedance and beyond," Electrochimica Acta 281, 170–188 (2018).
38. I. Lelidis, G. Barbero, "Role of the displacement current on Warburg-type behavior," Physical Review E 95(5), 052604 (2017).
39. J. Huang, "Generalization of porous electrode theory for Noninteger Dimensional Space," The Journal of Physical Chemistry C 122(1), 557–565 (2018).
40. H. Li, C. Zhao, X. Wang, J. Meng, Y. Zou, S. Noreen, L. Zhao, Z. Liu, H. Ouyang, P. Tan, M. Yu, Y. Fan, Z. L. Wang, and Z. Li, "Fully bioabsorbable capacitor as an energy storage unit for Implantable Medical Electronics," Advanced Science 6(6), 1801625 (2019).
41. M. Mazaheri, A. Simchi, and H. Aashuri, "Enzymatic biosensing by covalent conjugation of enzymes to 3D-networks of graphene nanosheets on arrays of vertically aligned gold nanorods: Application to voltammetric glucose sensing," Microchimica Acta 185, 178 (2018).
42. N. Elgrishi, K. J. Rountree, B. D. McCarthy, E. S. Rountree, T. T. Eisenhart, and J. L. Dempsey, "A practical beginner's guide to cyclic voltammetry," Journal of Chemical Education 95(2), 197–206 (2018).

Lossy Mode Resonance Based Fiber Optic Sensor for the Detection of Acetone Concentration

Asokan Prasanth[1], Varadharajan Kanchana Harini[1], Mohan Velumani[2], Subramaniyam Narasimman[1], and Zachariah C. Alex[1*]

[1] School of Electronics Engineering, Vellore Institute of Technology, Vellore 632014, India

[2] Department of CSE – Cyber Security & IOT, Sri Ramachandra Faculty of Engineering and Technology, Sri Ramachandra Institute of Higher Education and Research, Chennai 600116, India

***e-mail:** zcalex@gmail.com

Abstract. Diabetic ketoacidosis (DKA) is a serious complication arising due to the shortage of insulin that allows blood sugar into cells to be used as energy. As a result, the liver begins to break down fat for energy, thus producing acids called ketones. The severity of DKA influences the number of ketones produced in the human body. Therefore, the acetone level in the human body samples has the potential to be used as a biomarker towards the analysis of diabetic levels. The present work reports the development of a Lossy Mode Resonance (LMR) based fiber optic sensor to detect acetone concentration in liquids. A sensing region was developed by coating Aluminium doped Zinc Oxide (AZO) over the unclad core region using sputtering technique. The structural, morphological, and optical properties of the AZO coating were analyzed using X-ray Diffraction (XRD), Scanning Electron Microscope (SEM), and an ellipsometer device. The sensor probe used to measure the acetone concentration ranging from 10 µl/ml to 800 µl/ml recorded resonance wavelength shifts in LMR1, LMR2, and LMR3 of 38 nm, 19 nm, and 9 nm, respectively. The wavelength shift was larger for LMR1 than for the other peaks with a sensor response of 4.73% and a sensitivity of 0.3 nm/(µl/ml). © 2023 Journal of Biomedical Photonics & Engineering.

Keywords: optical sensor; lossy mode resonance; acetone, diabetes.

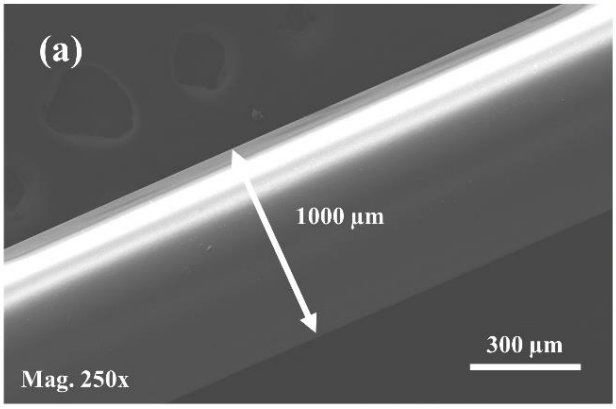
Paper #8176 received 28 Feb 2023; revised manuscript received 7 May 2023; accepted for publication 7 May 2023; published online 7 Aug 2023. doi: 10.18287/JBPE23.09.030306.

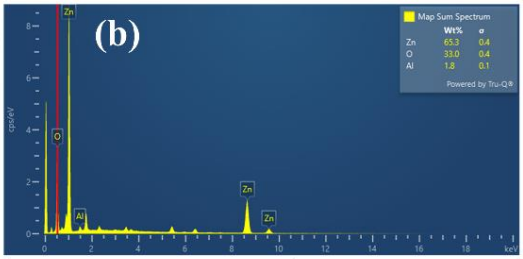
1 Introduction

Diabetic ketoacidosis (DKA) is a chronic condition that frequently affects people with type 1 diabetes. DKA occurs when the body cannot effectively utilize blood sugar (glucose) for energy because of insufficient insulin production. Because the cells cannot use blood sugar as the energy source, they consume fat instead. The decomposition of fat results in the production of blood byproducts known as ketones [1]. Acetone is one of the ketone bodies, and its elevated level during diabetic ketoacidosis (above 80 mg/dL or 4.4 mmol/l (1mg/dL = 0.055 mmol/L) i.e., 1.0191 µl/ml (1 ml of acetone weighs 0.7855 g)) indicates a metabolic disorder. Therefore, it is essential to monitor the acetone concentration in diabetics to determine the severity of DKA. The laboratory diagnostics for DKA includes blood glucose assays, serum electrolyte determinations, blood urea nitrogen (BUN) evaluation, urine ketone concentration, and arterial blood gas (ABG) measurements [2]. Among these, the detection of urinary ketone levels is one of the non-invasive techniques that is painless and comfortable [3]. Due to their potential for accurate disease diagnosis and treatment, analytical methods employing non-invasive nanotechnology-based techniques have gained popularity. In the present investigation, we have developed an LMR-based optical fiber sensor that can potentially replace the intrusive and unpleasant standard blood tests.

Standard methods such as gas chromatography and mass spectrometry that are available for the detection of acetone are often cumbersome and take up a great deal of space. Further, the sampling procedure is complicated and time-consuming. Another type of detector, namely the flame and light ionization reacts negatively to oxygen-containing organic substances [4].

This paper was presented at the International Conference on Nanoscience and Photonics for Medical Applications – ICNPMA, Manipal, India, December 28–30, 2022.





Element	Wt %
Zn	65.3
O	33.0
Al	1.8

Fig. 1 (a) SEM image of AZO coated probe and (b) EDS spectrum of AZO.

In addition to these methods, chemiresistive-based sensors are used to measure the acetone concentration [5]. However, the requirement for a high working temperature for such sensors poses a major disadvantage. Hence, the detection of acetone requires a sensor that is basic, sensitive, and capable of operating at room temperature.

In this scenario, fiber optic sensors with rapid response time, small size, multiplexing sensing capability, versatility, and immunity to electromagnetic interference, can serve as alternative to the aforementioned sensing methods. Several interrogation techniques, including evanescent waves [6], Surface Plasmon Resonance (SPR) [7], and Localized Surface Plasmon Resonance (LSPR) [8], have been used to build optical fiber sensors. According to the reports, the evanescent wave technique is one of the most cost-effective methods for determining the quantity of water in ethyl alcohol [9]. However, the evanescent mode optical fiber is dependent on intensity modulation, and hence, variations in the intensity of the light source can affect the output of the sensor. In such cases, the SPR approach could be employed to detect liquid sample Volatile Organic Compounds (VOCs) with higher sensitivity than the evanescent mode technique [10]. Nevertheless, the SPR-based fiber optic sensor with higher sensitivity and quicker response time is often difficult to fabricate [11] as it necessitates the use of noble metals and transverse magnetic polarized light. Therefore, for the purpose of acetone detection, we propose the development of an LMR-based sensor that offers numerous advantages, such as polarization independence, ease of fabrication, and cost-effective sensing layer [12]. LMR can only be produced when the real component of the permittivity of the supporting material is positive, greater in magnitude than its own imaginary component, and greater than that of the real components of the optical fiber core and the surrounding medium. Metal oxides such as zinc oxide (ZnO) [13] and indium tin oxide (ITO) [14] are widely used as LMR supporting materials for refractive index measurements. Despite the fact that the refractive index of the supporting material has a substantial effect on the sensitivity of LMR sensors, the performance of the sensor [15] is optimized by selecting materials of suitable thickness. For the present study, Aluminum-doped zinc oxide (AZO) with exceptional electrical conductivity, high transparency, and outstanding chemical and thermal stability was chosen as the LMR supporting material.

The present study aims to develop LMR-based sensor for the detection of acetone concentrations below a specific limit. The proposed sensor device was evaluated for acetone in the concentration range of 10 µl/ml to 800 µl/ml, and the corresponding resonance wavelength shift was measured. To the best of the authors knowledge, this is the first experimental report on an LMR-based acetone sensor. The efficacy of the sensor probe was determined by evaluating its sensing characteristics, namely its sensitivity and sensor response.

2 Preparation of Sensor Probe

The sensor probe was fabricated using clad modification technique, which involves removing 2 cm of the clad and replacing it with an AZO layer using Radio Frequency (RF) magnetron sputtering technique.

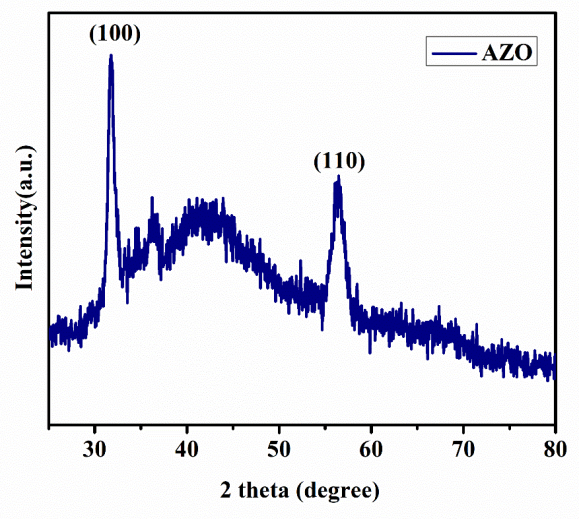


Fig. 2 XRD pattern of AZO coated thin film.

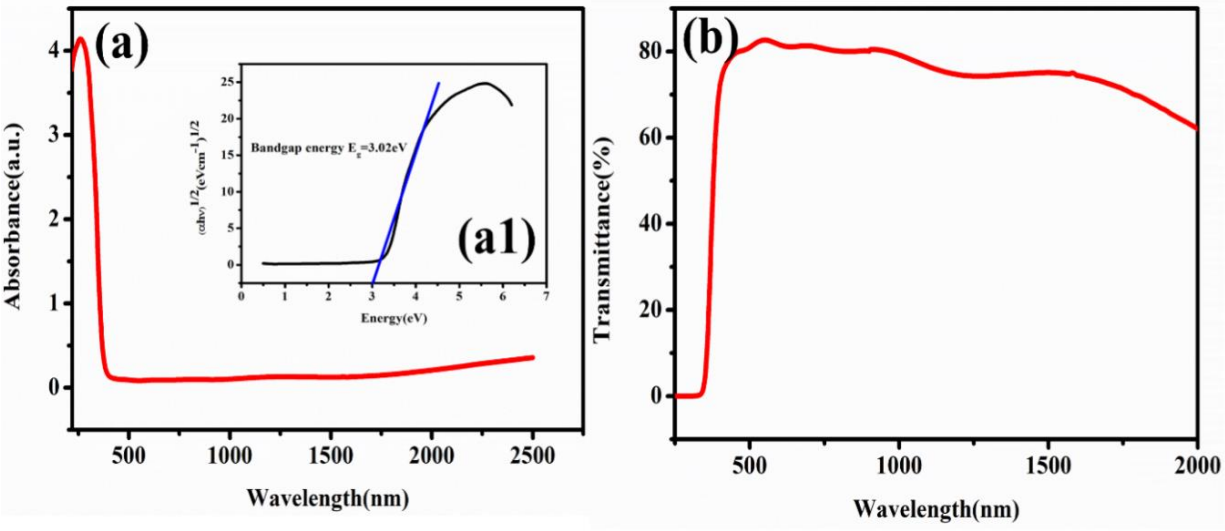


Fig. 3 (a) Absorption and (b) transmission spectra of AZO thin film.

For the preparation of the sensor probe, plastic-clad silica core (PCS) optical fiber (0.39 NA) with a 1000 μm core diameter (FMT1000, Thorlabs) was utilized. The index of refraction of the plastic-clad is 1.406, while that of the optical fiber core is 1.453. Using chemical etching method, the plastic-clad portion of the optical fiber was removed by immersing it for 5 min in an HF bath. The unclad portion of the optical fiber was fixed inside the RF Magnetron deposition chamber and the 99.99% pure AZO target (98% ZnO, 2% Al) was inserted 7 cm away from the fiber. AZO was coated for 25 min with a steady flow of 10 SCCM of Argon (Ar) and 5 SCCM of Oxygen (O_2) at pressures of 3×10^{-5} mbar (Base) and 25×10^{-3} mbar (Deposition), respectively over the interior of the fiber. During deposition, the optical fiber within the chamber was continuously rotated using a DC-motor-driven rotating system to ensure uniform coating thickness.

3 Characterization of the Sensing Layer

3.1 SEM & EDS Analysis

SEM measurements were carried out to determine the uniformity of the coating. The SEM images shown in Fig. 1 revealed uniform coating of the top surface of the optical fiber with AZO layer. The EDAX analysis confirmed the presence of aluminium (Al), zinc (Zn), and oxygen (O) molecules.

3.2 X-ray Diffraction

The crystalline properties of the prepared AZO layer were investigated using X-ray diffraction studies. The XRD pattern in Fig. 2 showed two major peaks at angles of 31.7° and 56.5° that can be attributed to the (100) and (110) diffraction planes.

3.3 UV-Vis Spectroscopy

UV-Vis spectroscopy was used to analyze the optical properties of the AZO layer. A sharp absorption edge at ~265 nm as shown in Fig. 3 was observed. The optical bandgap energy (E_g) of the AZO thin film was calculated using Tauc's equation given by Eq. (1).

$$\alpha h\nu^{1/2} = A(h\nu - E_g), \quad (1)$$

where A is a proportionality constant, $h\nu$ is the incident photon energy, α is the absorption coefficient, and E_g is the optical bandgap. The inset of Fig. 3(a) shows the plot of $\alpha h\nu$ vs $h\nu$ from which the optical bandgap of the AZO thin film was determined to be 3.02 eV. Further, the measured optical transmission of the AZO coated layer showed a maximum transmission of ~80% as seen from Fig. 3(b). The optical constants (n and k) of the thin films were determined using an ellipsometer (J. A. Woollam, Alpha-SE). Fig. 4 shows the dispersion characteristics of the AZO thin film obtained using the Lorentz model. The real parts of the refractive indices of the modified clads (AZO thin films) were higher than their imaginary parts. This confirmed that AZO is a supportive material for LMR sensing [16].

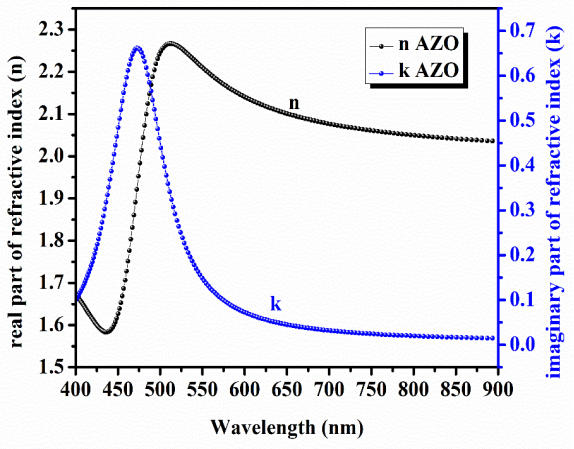


Fig. 4 Dispersion characteristics of AZO thin film.

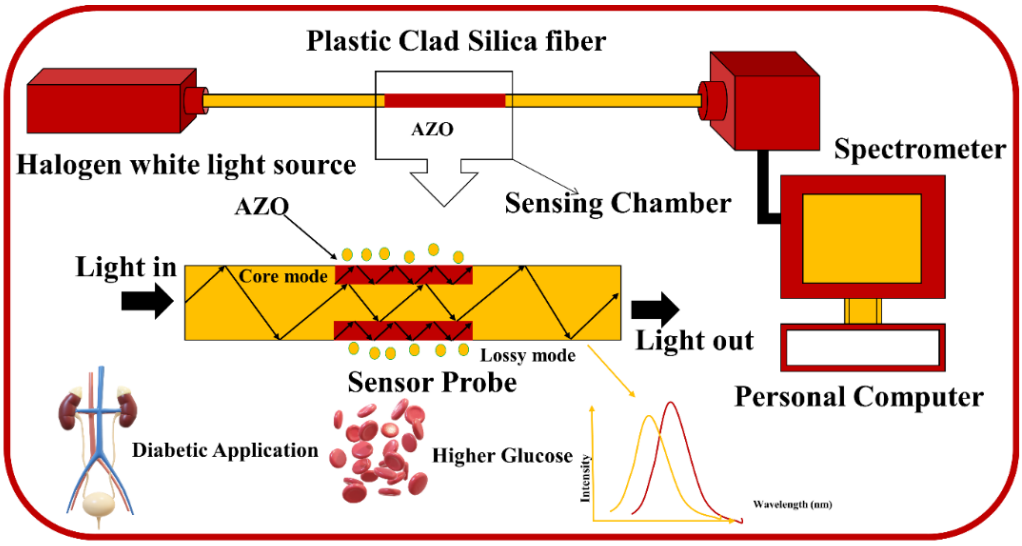


Fig. 5 Schematic representation of the experimental setup of AZO coated LMR based acetone sensor.

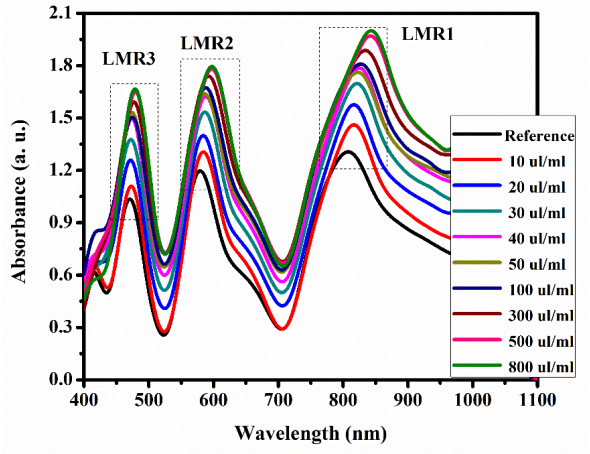


Fig. 6 Wavelength shift spectra of AZO coated LMR based acetone sensor.

4 Experimental Analysis

The schematic representation of the experimental setup of the fiber optic-based sensor for the detection of acetone is shown in Fig. 5. One end of the optical probe is connected to a broadband halogen white light source (200–2200 nm), while the other end is connected to a spectrometer (200–1100 nm). Acetone samples of different concentrations were prepared by diluting it with distilled water. The corresponding resonance wavelength shift for each concentration was measured.

4.1 Spectral Response of the Sensor Probe (SP)

Fig. 6 represents the LMR absorbance spectra of the SP for different concentrations of acetone (0–800 µl/ml) in water. Three maximum LMR peaks were observed at 806 nm (LMR1), 579 nm (LMR2), and 470 nm (LMR3) for 0% of acetone (water).

Each of these maxima correspond to a new mode referred to as a 'lossy mode' that passes the 'cut-off' condition and is governed by a 250 nm layer thickness. At a wavelength of 806 nm, the first mode is near to the cutoff condition, and the spectrum generates LMR1. As the wavelength decreases, a second mode overcomes the condition and passes through the coating. This is displayed in the spectrum as LMR2 at 579 nm. Similarly, the condition for guiding a third mode (LMR3) in the coating arises at a wavelength of 470 nm. Interestingly, it has been observed that with increase in the thickness of the AZO coating, a wider range of lossy modes can be guided through it. As the concentration of acetone increases, the change in the Surrounding Medium Refractive Index (SMRI) impacts the LMR resonance peaks. Since LMR sensors are extremely sensitive to SMRI, a minor change in the refractive index has a significant impact on the shift of the resonance wavelength as shown in Fig. 7.

The LMR resonance wavelength increases as the concentration of acetone rises, as shown in Fig. 7(a), (b), and (c). With a change in acetone concentration from the reference to 800 µl/ml, the resonance wavelength of LMR1 shifts from 806.3 nm to 844.5 nm, while the resonance wavelength of LMR2 changes from 579.7 nm to 597.7 nm. For the same range of acetone concentrations, the LMR3 resonance wavelength goes from 470.3 nm to 479 nm. From the observation, it has been inferred that an increase in the refractive index of the surrounding medium causes an increase in the resonance wavelength (i.e., redshift) up to an acetone concentration of 800 µl/ml. LMR1 shows a maximum wavelength shift of 38 nm as compared to LMR2 and LMR3 with wavelength shifts of 19 nm and 9 nm, respectively for acetone concentration ranging from reference to 800 µl/ml.

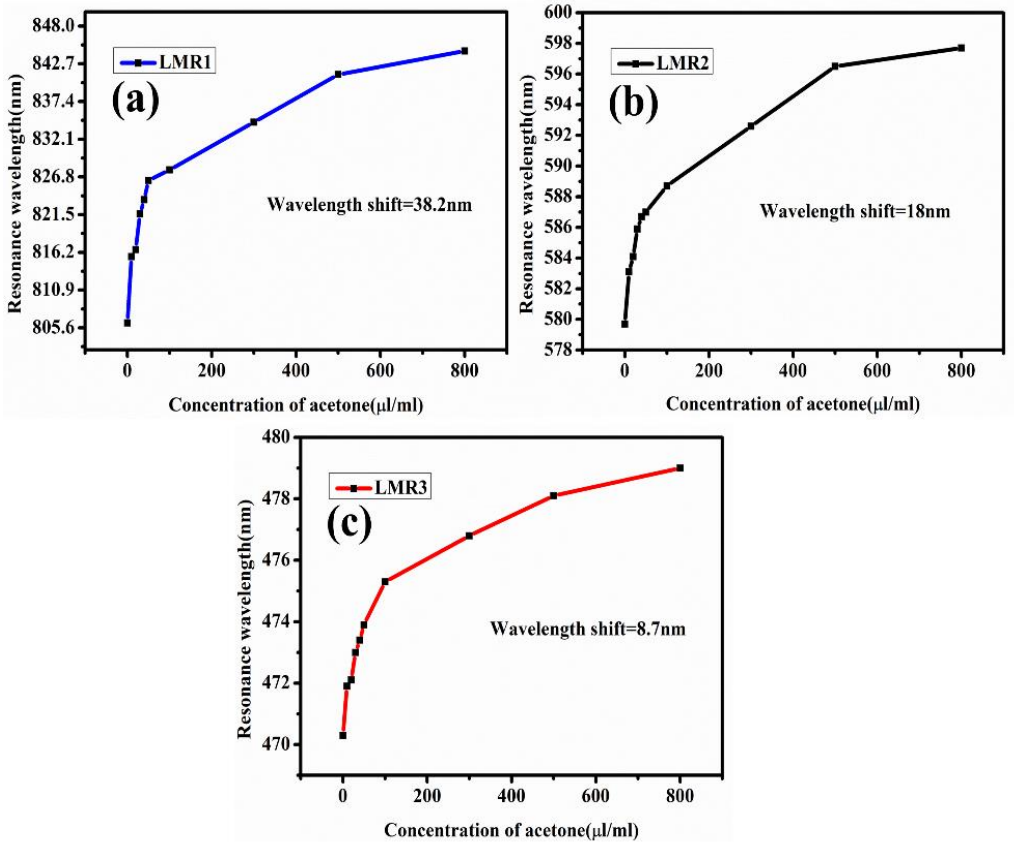


Fig. 7 Variation of resonance wavelength of AZO coated sensor probe (a) LMR1, (b) LMR2, and (c) LMR3.

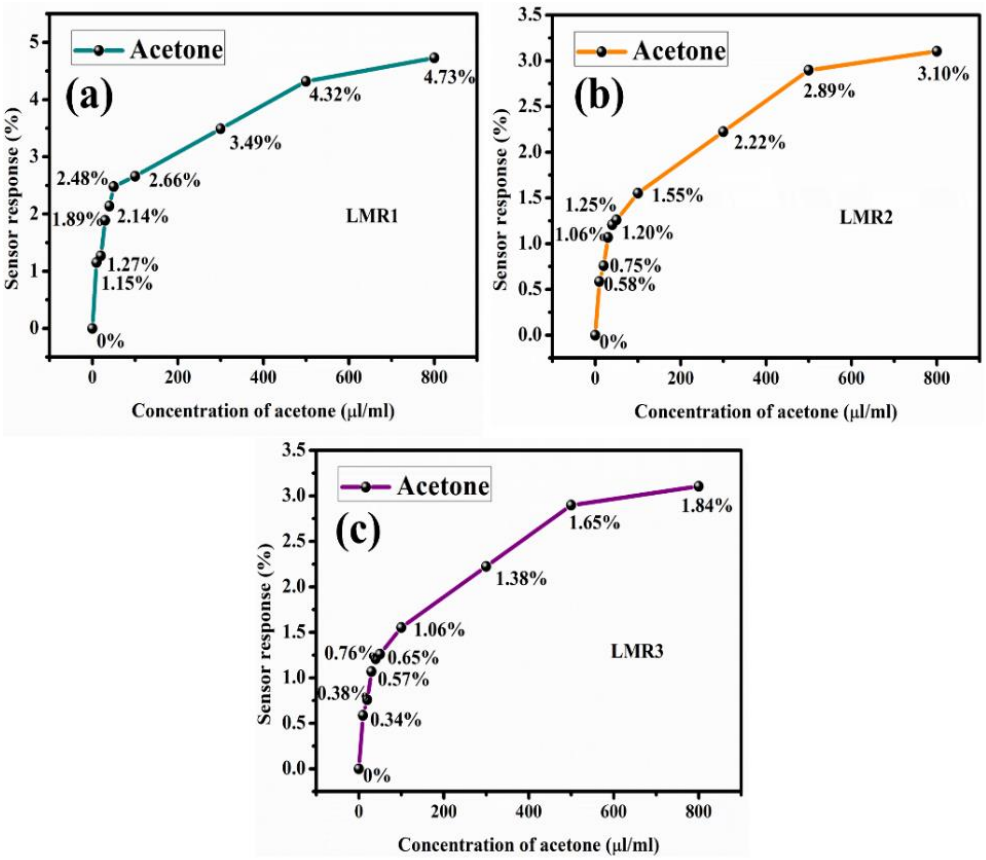


Fig. 8 Change insensor response of prepared AZO coated sensor probe (a) LMR1, (b) LMR2, and (c) LMR3.

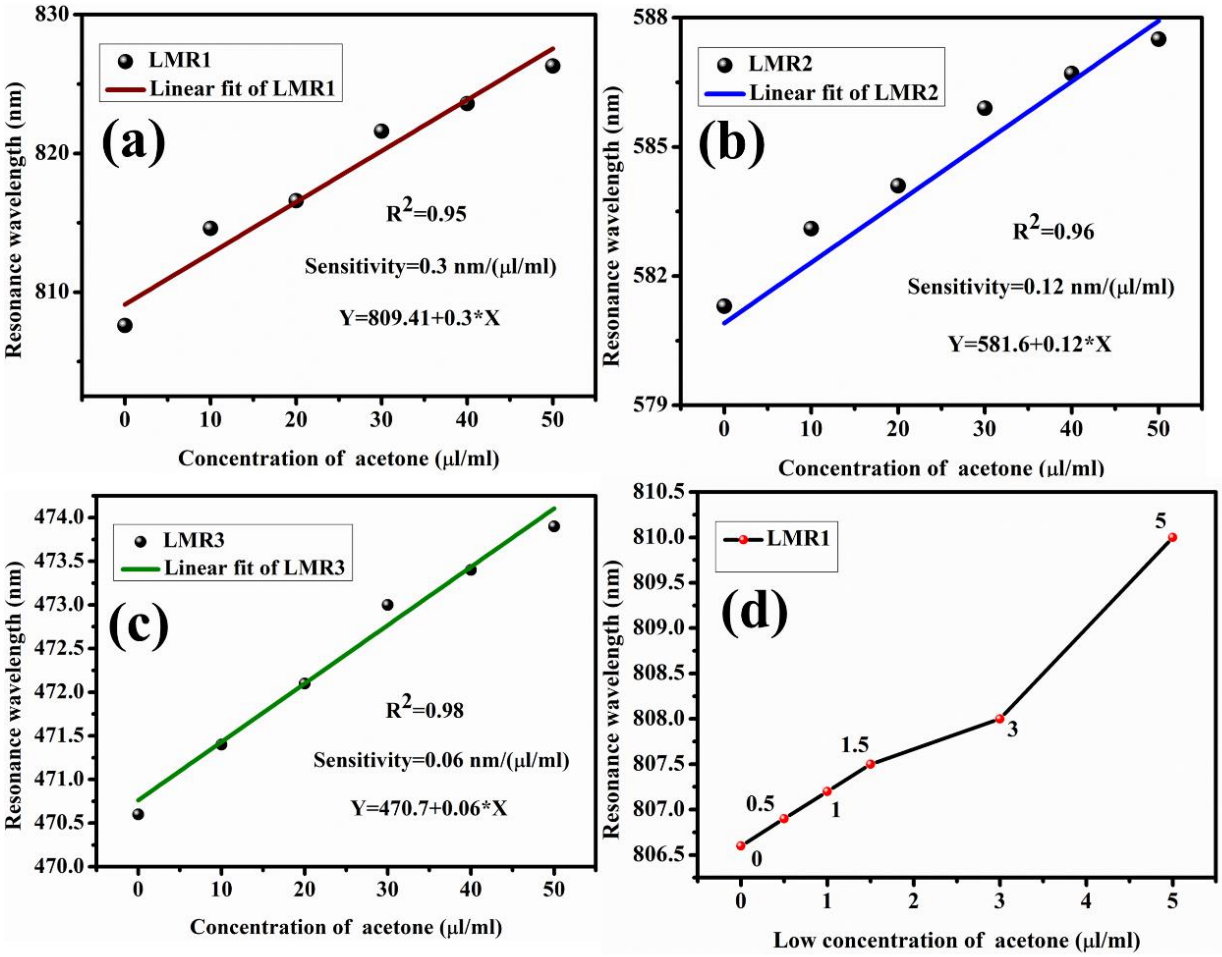


Fig. 9 Sensitivity plots of acetone sensor for (a) LMR1, (b) LMR2, (c) LMR3, and (d) change in resonance wavlength for lower concentrations (LMR1).

5 Sensor Response

The sensor response is defined as the relative change in the resonance wavelength in the presence of acetone over the resonance wavelength of the reference. It is determined using Eq. (2) given below [17].

$$\text{Sensor response (\%)} = \frac{S_w - S_a}{S_w} \times 100\ \%, \qquad (2)$$

where S_w is the resonance wavelength of the initial concentration of acetone and S_a is the resonance wavelength at different acetone concentration.

Fig. 8 shows the sensor response for varying acetone concentrations, from reference to 800 µl/ml. The sensor response for LMR1 was enhanced from 0% to 4.73% as the amount of acetone goes up from reference to 800 µl/ml. In the same way, the sensor response for LMR2 was enhanced by 3.10% while that for LMR3 was enhanced by 1.84%. Further, an improved sensor response was observed at elevated concentration of acetone and comparatively, the sensor response at LMR1was higher than that at LMR2 and LMR3.

6 Sensitivity

The sensitivity of the proposed acetone sensor is defined as the change in resonance wavelength per change in acetone concentration as expressed by Eq. (3) [18].

$$S_n = \Delta\lambda_{res}/\Delta C_a\,, \qquad (3)$$

where $\Delta\lambda_{res}$ is the resonance wavelength shift and ΔC_a is the difference in concentration of acetone.

The sensitivity of AZO coated LMR probe towards acetone detection was determined from the plot of resonance wavelength vs. acetone concentration shown in Fig. 9 (a–c). The sensitivities were found to be 0.3 µl/ml, 0.12 µl/ml, and 0.06 µl/ml, respectively, for LMR1, LMR2, and LMR3. The shift in resonance wavelength per volume percentage of acetone was significantly greater for LMR1 because higher wavelength resonances are more sensitive to the surrounding medium's refractive index than lower wavelength resonances. Further, the sensor could also detect concentration of acetone as low as 0.5 µl/ml as shown in Fig. 9(d).

7 Summary and Conclusion

A lossy mode resonance (LMR)-based optical fiber sensor for acetone detection in liquid samples under diabetic ketoacidosis was developed. RF Magnetron sputtering was used to deposit the AZO sensing layer over the unclad core of the optical fiber to fabricate the LMR-based optical fiber sensor probe. Using the characterization techniques such as SEM, XRD, UV-Vis spectroscopy, and ellipsometry, the uniformity, crystalline structure, and thickness of the AZO sensing layer were determined. Different concentrations of acetone ranging from 10 µl/ml to 800 µl/ml were used to examine the LMR wavelength shift using a sensor instrument. The sensor probe's absorption spectrum revealed three LMR peaks namely, LMR1, LMR2, and LMR3 when it was immersed in 0% acetone (DI water). With increase in the concentration of acetone from 10 µl/ml to 800 µl/ml, the resonance wavelengths for each of the three LMR peaks exhibited shifts. The maximum shifts in resonance wavelengths for LMR1, LMR2, and LMR3 were 38 nm, 19 nm, and 9 nm, respectively. The observations further indicate that LMR shifts with acetone concentration was higher at longer wavelengths (LMR1 > LMR2 and LMR3). The maximal sensor response of the LMR1 probe was 4.73% with a sensitivity of 0.3 nm/(µl/ml).

Acknowledgement

The authors express their sincere thanks to acknowledge DST- FIST and MHRD SPARC for providing financial support through projects [SR/FST/ETI-015/2011] and [S.P.A.R.C./2018-2019/P461/SL] for carrying out the present investigation.

Disclosures

The authors declare no conflict of interest.

References

1. H. S. Lee, J. S. Hwang, "Cerebral infarction associated with transient visual loss in child with diabetic ketoacidosis," Diabetic Medicine 28(5), 516–518 (2011).
2. "Diabetic ketoacidosis," Pediatric Care Online (2016).
3. M. J. Sulway, J. M. Malins, "Acetone in diabetic ketoacidosis," The Lancet 296(7676), 736–740 (1970).
4. M. J. Egoville, E. S. DellaMonica, "Gas chromatographic determination of water in acetone," Journal of Chromatography A 212(1), 121–125 (1981).
5. Z. Xie, M. V. R. Raju, A. C. Stewart, M. H. Nantz, and X.-A. Fu, "Imparting sensitivity and selectivity to a gold nanoparticle chemiresistor through thiol monolayer functionalization for sensing acetone," RSC Advances 8(62), 35618–35624 (2018).
6. A. Prasanth, S. Getachew, T. Shewa, M. Velumani, S. R. Meher, and Z. C. Alex, "A bilayer SnO2/MoS2-coated evanescent wave fiber optic sensor for acetone detection—an experimental study," Biosensors 12(9), 734 (2022).
7. S. Sen, F. C. Onder, R. Capan, M. Ay, and C. O. Erdogan, "Humidity effect on real-time response of tetranitro-oxacalix[4]arene-based surface plasmon resonance (SPR) acetone sensor at room temperature," Optik 272, 170303 (2023).
8. L. L. Liu, C. Y. He, S. P. Morgan, R. Correia, and S. Korposh, "A fiber-optic localized surface plasmon resonance (LSPR) sensor anchored with Metal Organic Framework (HKUST-1) film for acetone sensing," Proceedings of SPIE 11199, 111990Z (2019).
9. F. B. Xiong, D. Sisler, "Determination of low-level water content in ethanol by fiber-optic evanescent absorption sensor," Optics Communications 283(7), 1326–1330 (2010).
10. A. K. Pathak, V. Bhardwaj, R. K. Gangwar, and V. K. Singh, "SPR based cone tapered fiber optic chemical sensor for the detection of low water in ethanol," AIP Conference Proceedings 1728, 020017 (2016).
11. M. A. Jalil, M. A. Abas, "Detection of acetone using surface plasmon resonance," International Journal for Research in Applied Science and Engineering Technology 11(1), 1–4 (2023).
12. H. Chen, Q. Huang, and J. Shen, "Lossy mode resonance induced by cladding mode in long-period fibre grating," Optik 196, 162992 (2019).
13. K. Swargiary, P. Metem, C. Kulatumyotin, S. Thaneerat, N. Ajchareeyasoontorn, P. Jitpratak, T. Bora, W. S. Mohammed, J. Dutta, and C. Viphavakit, "ZnO nanorods coated single-mode–multimode–single-mode optical fiber sensor for VOC biomarker detection," Sensors 22(16), 6273 (2022).
14. M. Janik, M. Janczuk-Richter, D. Burnat, T. Gabler, J. Niedziółka-Jönsson, M. Koba, P. Sezemsky, V. Stranak, and M. Śmietana, "Dopamine sensing with electrochemically-enhanced ITO-coated lossy-mode resonance optical fiber sensor," Optical Fiber Sensors Conference 2020 Special Edition, Th4.18 (2021). ISBN: 978-1-55752-307-5.
15. A. Ozcariz, "Development of copper oxide thin film for lossy mode resonance-based optical fiber sensor," Proceedings 13(2), 893 (2018).
16. N. Paliwal, J. John, "Sensitivity enhancement of aluminium doped zinc oxide (AZO) coated lossy mode resonance (LMR) fiber optic sensors using additional layer of oxides," in Frontiers in Optics 2014, 19–23 October 2014, Tucson, Arizona, United States, JTu3A.40 (2014). ISBN: 1-55752-286-3.

17. A. Prasanth, S. R. Meher, and Z. C. Alex, "Metal oxide thin films coated evanescent wave based fiber optic VOC sensor," Sensors and Actuators A: Physical 338, 113459 (2022).
18. A. Prasanth, S. R. Meher, and Z. C. Alex, "Experimental analysis of SnO2 coated LMR based fiber optic sensor for ethanol detection," Optical Fiber Technology 65, 102618 (2021).

The Role of Sm^{3+} Energy Transfer on White Emission of $La_{1.98}Dy_{0.02}MgTiO_6$ Double Perovskite Nano-Phosphors for Endoscopy and Laparoscopy LEDs

Vannadil Puthiyaveetil Veena, Cherlan Kottianmadathil Shilpa, Seere Valappil Jasira, and Kavukuzhi Meerasahib Nissamudeen*

School of Pure and Applied Physics, Kannur University, Payyanur, Kannur district, Kerala 670327, India

***e-mail:** nisamkm@kannuruniv.ac.in

Abstract. Decent lighting is a major requisite in Laparoscopic and Endoscopic examinations, as the illumination is below the edge value, the image becomes distorted resulting inaccurate outcome. Double perovskites with flexible formulas and structures, lithic chemical-physical properties, and suitable optical bandgap, are the most suited candidates for such illumination devices. Novel perovskite nano-phosphor $La_{1.97}Dy_{0.02}Sm_{0.01}MgTiO_6$ ace among the group with violet-blue-yellow-red emission, which gives luminescence 3-fold than conventional lighting sources, owing to $Dy^{3+}\rightarrow Sm^{3+}$ energy transfer mechanism with efficiency 53%. The Commission Internationale de I'Elcairage (CIE) chromaticity coordinates are (0.322, 0.324) with color temperature 5835K, neighboring to ideal white light, which is threshold in picking the exact light source for endoscopic and laparoscopic applications. So, a meticulous optimization on broad white emission of $La_{1.97}Dy_{0.02}Sm_{0.01}MgTiO_6$ to the neutral point for biomedical application is an inevitability. © 2023 Journal of Biomedical Photonics & Engineering.

Keywords: perovskite nano-phosphors, endoscopy, white light emitting diodes.

Paper #7649 received 22 Feb 2023; revised manuscript received 4 Jul 2023; accepted for publication 8 Jul 2023; published online 14 Aug 2023. doi: 10.18287/JBPE23.09.030307.

1 Introduction

The advent of a fast-growing field, nanotechnology has made a great leap in energy, environment, and healthcare zones. Nanoscience and nanotechnology deal with the control of matter on an atomic or molecular scale. This knowledge fostered human life much simpler and easier. At this point, nano-medicines, nano-devices, and nano-probes have revolved around a healthy environment for balanced health requirements. The use cases range from drug delivery to tissue engineering, biosensors, and diagnostics. Human health and total well-being are central to economic growth [1]. So, the early detection and treatment of infirmity are crucial for human prosperity, which can be achieved through precise instrumentation setups. Biomedical engineering is advancing copiously in improving the healthcare sector with high-resolution real-time image recording devices that could improve disease detection and treatment probability. As the patient experiences minimal suffering and undergoes fast recovery, minimal invasive surgery (MIS) by means of endoscopes and laparoscopes, aids human well-being to a prodigious extent. The light source plays a vital role at this time in disease identification and examination. That is, good illumination is a major requisite in MIS treatment, as the intensity level is below the threshold value, the image gets distorted [2]. That is, the endoscopic examination involves real-time internal tissue imaging using a device equipped with a CCD camera attached to a high-brightness ideal light source. As the internal tissues are away from our line of sight, this device is inserted through the mouth, inside the body through the esophagus, duodenum, and stomach. Once it reaches the target site, using the CCD camera, the tissue is subjected to imaging and inspection (Fig. 1) [3]. The practicing xenon arc lamps grieve plasma oscillations and thermal runaway, leading to instability. At the same time, the UV radiations given out by them are prone to skin and cause damages to eye structure [4].

This paper was presented at the International Conference on Nanoscience and Photonics for Medical Applications – ICNPMA, December 28–30, 2022, Manipal, India.

Table 1 Comparison of properties of conventional xenon arc lamp and white LED (wLED).

Conventional Xenon arc lamp	wLEDs
Suffer plasma oscillations and thermal runaway	Minimal energy consumption, high efficiency, good brightness, longer operation time
The UV radiations are prone to skin and causes injury to eye structure	Eco-friendly in nature
Costly and require replacement after every 500 h run	Lifetime about 50,000 h
Violet spectral region is present	Violet spectral region is absent
Wide range emission	Fabricated by combining red-green-blue LEDs or by coating yellow phosphor on blue LED

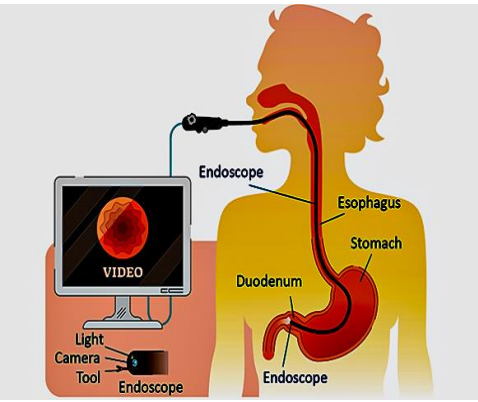


Fig. 1 Endoscopy procedure.

These lamps are expensive and involve a replacement after every 500 h of usage (Table 1). Recently, a white LED (wLED) source with a lifetime of about 50,000 h is swapping traditional arc lamps. However, the chief bottleneck lies is the lack of violet spectral region, which is inevitable in determining diseases [3, 5] like lesions, patterns of colonic mucosa, and adenoma (polyp) tumors [6].

The lighting sector is striving hard to replace conventional imaging sources of the health sector with an environmentally friendly, abiding, flexible, energy-saving, efficient, and miniature arrangement, that could improve the eminence of real-time recorded data. The double perovskite nano phosphors are among the group that is gaining ample attention in luminescence nanoscience research, owing to their wide applications in domestic, industrial, commercial, and health sectors [7–10]. The fourth-generation illumination technology, phosphor-converted white light emitting devices (wLED), that convert excitation energy to ideal visible white light flags this demand. Topical rummages suggest that the perovskite structure has been found to have very low toxicity and is truly biocompatible with human cells.

The potential double perovskite host matrix La_2MgTiO_6 ($A_2BB^{|}O_6$) is attaining much research fascination at this instant due to its unique luminescence properties when doped with apt rare earth ions [7, 11]. Dysprosium ions are doped in the crystal lattice of La_2MgTiO_6 perovskite nano-phosphors, co-activated by Samarium ions. The photoluminescence spectra reveal that the $La_{1.97}Dy_{0.02}Sm_{0.01}MgTiO_6$ emanate violet-blue-yellow-red emission peaks at 388 nm, 480 nm, 574 nm, and 670 nm corresponding to $^4F_{7/2} \rightarrow {}^6H_{15/2}$, $^4F_{9/2} \rightarrow {}^6H_{15/2}$, $^4F_{9/2} \rightarrow {}^6H_{13/2}$ and $^4F_{9/2} \rightarrow {}^6H_{11/2}$ transitions respectively [8–10]. This violet emission, which is generally absent in existing white LEDs, is of great importance in the health sector, mainly in identifying infirmities like polyps. The Commission Internationale de I'Elcairage (CIE) chromaticity of $La_{1.97}Dy_{0.02}Sm_{0.01}MgTiO_6$ is very close to ideal white light with luminescence intensity two times higher than that of commercially available wLED YAG:Ce^{3+}. So, an ideal white emitting source with violet spectral component is a necessity to boost the health sector.

2 Materials and Methods

Perovskite nano-phosphor $La_{1.97}Dy_{0.02}Sm_{0.01}MgTiO_6$ is prepared by combustion method. Quantitative ratios of analytical grade La_2O_3, MgO, TiO_2, Dy_2O_3 and Sm_2O_3 are constantly heated and stirred in 8 M HNO_3, unless it reduces to 40%. 1:2 ratio of citric acid is added as the fuel. When it makes a gel form, the mix is transferred to a corundum crucible and ignited in a muffle furnace at 1223 K for 4 h. After gradual cooling, the perovskite is powdered well, without any lumps. Using Rigaku, Smartlab X-ray diffractometer, the crystal structure and phase is investigated. The powder morphology, crystallinity, and shape were examined by field emission scanning electron microscopy (FE-SEM, ZEISS) and transmission electron microscopy (TEM, JEM-2100 Plus). The Flurolog, Horiba photoluminescence spectrometer is castoff for emission studies.

3 Results and Discussion

The X-ray diffraction (XRD) pattern of synthesized $La_{1.97}Dy_{0.02}Sm_{0.01}MgTiO_6$ perovskite nano-phosphor is indexed with standard ICDD card – 86852 and found to crystallize in orthorhombic crystal structure with space group *pbnm* (Fig. 2). The A site of the perovskite is occupied by La^{3+}, Dy^{3+} and Sm^{3+} ions. The B, $B^{|}$ sites are occupied by Mg^{2+} and Ti^{4+} respectively. Dy^{3+} and Sm^{3+} doping makes no noticeable changes in the La_2MgTiO_6 crystal frame.

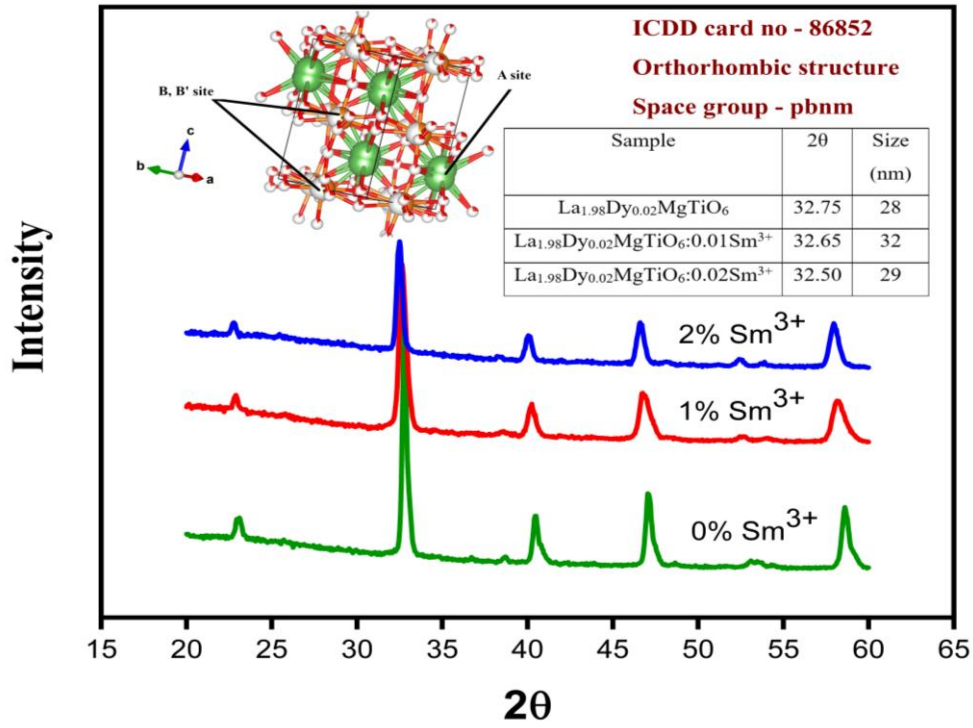
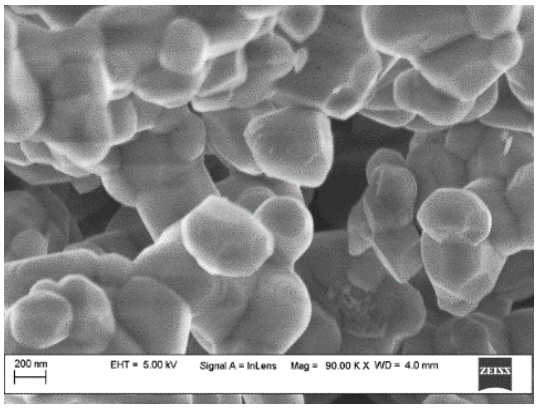
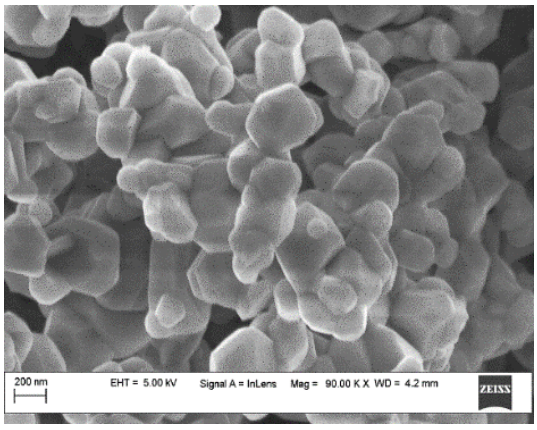


Fig. 2 XRD pattern of $La_{1.97}Dy_{0.02}Sm_{0.01}MgTiO_6$.



(a)



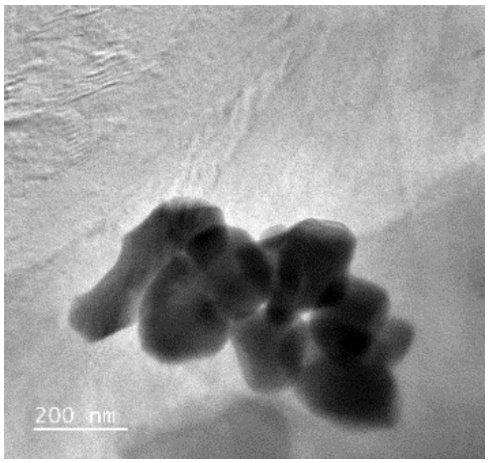
(b)

Fig. 3 FE-SEM images before Sm^{3+} co-doping (a) and after Sm^{3+} co-doping (b).

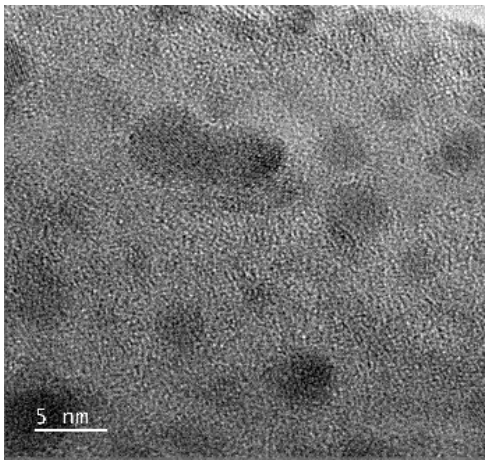
Due to the similar ionic radius, Dy^{3+} and Sm^{3+} are infixed in the La^{3+} crystal lattice. No additional peaks are observed, which ensure that Dy^{3+} and Sm^{3+} ions are well lodged in the host lattice from the XRD data, the particle size is calculated using Debye Scherrer Eq.:

$$D = \frac{k\lambda}{\beta cos\theta}, \quad (1)$$

where $k = 0.99$ is the shape factor, θ is the diffraction angle, λ is the wavelength of X-ray, and β is the full width at half maximum of the major peak (FWHM) [11], δ the dislocation density of $La_{1.97}Dy_{0.02}Sm_{0.01}MgTiO_6$ is calculated as $\delta = \frac{1}{D^2} = 0.00096$ nm^{-2}, which is negligible and is congruent with XRD pattern. The lattice strain (ε) is of the order of 0.003×10^{-3}, which can also be neglected [8]. The major peaks are sharp and pointed with broader noticeable FWHM, indicating the formation of nano-powders with crystalline environment [12]. The decrease in crystallinity with doping is due to lattice distortion [13], depending on the relative ionic radii of dopant and host site. Since the radii percentage difference of Dy^{3+} and Sm^{3+} is 5% (x<<35%), the deformation is minimum and thus acceptable. The crystal size, structure and morphology are confirmed using FE-SEM and TEM (Figs. 3, 4). It is evident that the perovskite phosphors are nano-sized crystalline particles that agglomerate to form a cauliflower like structure. Following the XRD and SEM and TEM images, it is evident that the crystallinity of the samples decreases with increase in Sm^{3+} concentration. It can be attributed to the increase in deformation of the crystal lattice due to the external doping.



(a)



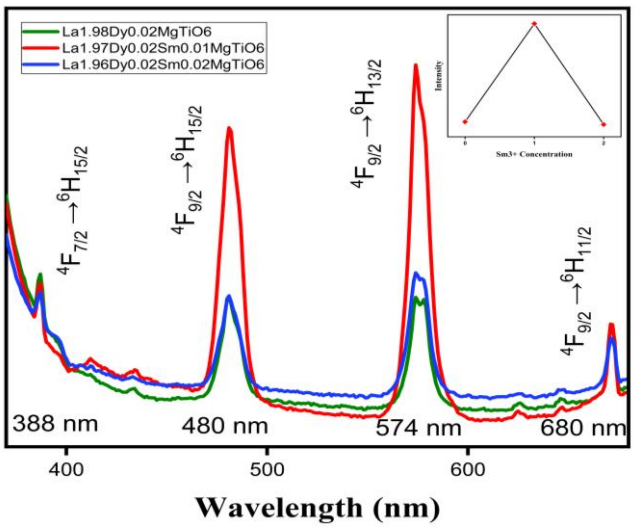
(b)

Fig. 4 TEM images after Sm^{3+} co-doping (a) 200 nm and (b) 5 nm resolution.

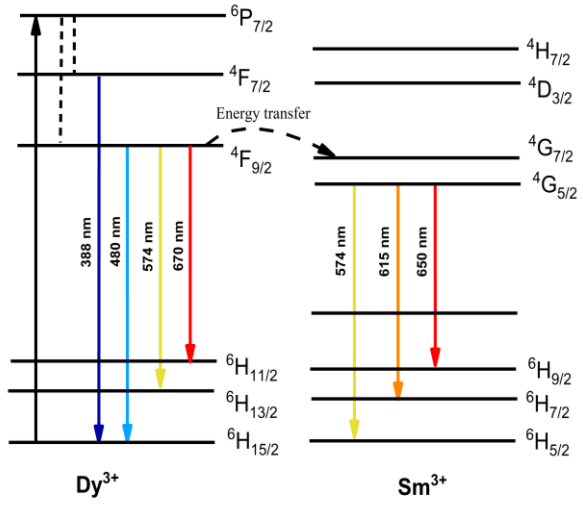
The photoluminescence (PL) studies are carried out using spectrophotometer Flurolog, monitored under 351 nm excitation (Fig. 5a). The emission spectra show four prominent peaks violet, blue, yellow, and red owing to different energy transition levels of Dy^{3+} ion. That is, emission peaks at 388 nm (violet), 480 nm (blue), 574 nm (yellow), and 670 nm (red) agreeing to $^4F_{7/2} \rightarrow {}^6H_{15/2}$, $^4F_{9/2} \rightarrow {}^6H_{15/2}$, $^4F_{9/2} \rightarrow {}^6H_{13/2}$ and $^4F_{9/2} \rightarrow {}^6H_{11/2}$ transitions [8–10] (Fig. 5b). The lower wavelengths (388 nm and 480 nm) are vulnerable to crystal environment whereas, the higher wavelengths (574 nm and 670 nm) are independent to crystal atmosphere [14–17]. An intense yellow emission is highly favored for white light emitting diodes, which is well observed in $La_{1.97}Dy_{0.02}Sm_{0.01}MgTiO_6$ nano-phosphors. Owing to the overlap between the excitation band of $Sm^{3+}$and emission band of Dy^{3+}, efficient energy transfer occurs between them, resulting the merging of Sm^{3+} ions enhancing the luminescence intensity. As the $^4G_{5/2}$ level of Sm^{3+} possesses orange-red luminescence with a higher lifetime, Sm^{3+} co-activation enhances the luminescence performance of Dy^{3+} triggered perovskites matrices to a noticeable extent. Sm^{3+} concentration is varied in each set (x = 0%, 1%, 2%) and is optimized for 1%, above which concentration quenching is observed [8, 17–18]. The intense peaks are showing ruptures due to crystal field splitting, showing the noble luminescence intensity. The increase in luminescence intensity can also be attributed to the $Dy^{3+} \rightarrow Sm^{3+}$ energy transfer mechanism. The maximum energy transfer efficiency is calculated to be 53% for 1% Sm^{3+} co-activation, using the relation Energy transfer efficiency,

$$\eta = 1 - \frac{I_{Dy}}{I_{Dy \rightarrow Sm}} = 53\%, \qquad (2)$$

where I_{Dy} is the luminescence intensity in Dy^{3+} doped samples and $I_{Dy \rightarrow Sm}$ is the luminescence intensity of Dy^{3+} doped samples with Sm^{3+} co-activation [19, 20]. The peak at 388nm, which is normally absent in conventional wLED, is of great importance in endoscope devices.



(a)

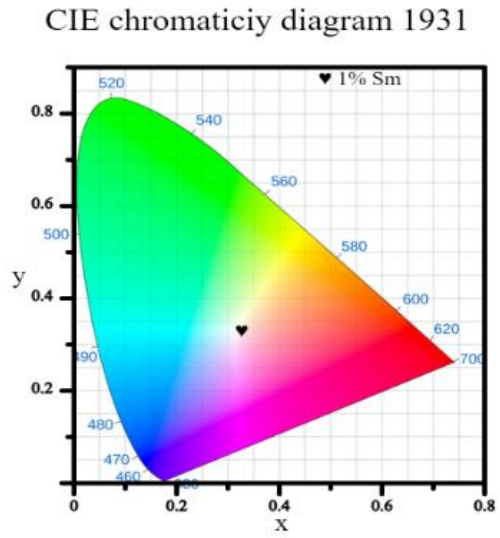


(b)

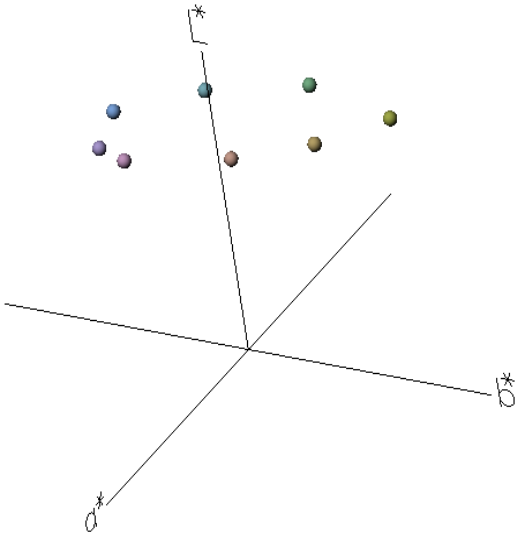
Fig. 5 (a) Photoluminescence spectra of Sm^{3+} activated samples. (b) $Dy^{3+} \rightarrow Sm^{3+}$ energy transfer mechanism.

Table 2 CIEL*a*b* parameters.

Color	L*	a*	b*	h*	C*	ΔE*
R1	62.0300	12.8136	12.9732	45.3545	18.2343	5.1956
R2	61.3044	−0.4141	30.1181	90.7877	30.1209	1.7179
R3	61.8845	−15.5404	44.0787	109.4206	46.7379	4.2023
R4	60.1403	−25.3198	13.8408	151.3372	28.8558	7.9601
R5	61.6243	−13.2351	−10.2461	217.7457	16.7377	4.9815
R6	60.3764	0.2935	−29.9818	270.5608	29.9832	2.4535
R7	60.6236	16.4615	−24.6955	303.6865	29.6791	3.0057
R8	62.2842	21.9746	−13.7657	327.9354	25.9302	5.4903



(a)



(b)

Fig. 6 (a) CIE chromaticity diagram, (b) CIEL*a*b* colour space.

This spectral region due to $^4F_{7/2} \rightarrow {}^6H_{15/2}$ electronic transition is acute in determining conditions like lesions, patterns of colonic mucosa, and adenoma (polyp) tumors [3, 5–6]. Presence of this violet region makes $La_{1.97}Dy_{0.02}Sm_{0.01}MgTiO_6$ a potential candidate for endoscope LEDs. Moreover, the CIE chromaticity diagram (Fig. 6.a) show color coordinates X = 0.322 and Y = 0.324, is in the neighborhood of ideal white light. The calculated color temperature (CCT) of $La_{1.97}Dy_{0.02}Sm_{0.01}MgTiO_6$ is 5835 K, which is very close to natural sunlight (5900 K). The CCT value, which is a measure of how yellow or blue the emitted light is. That is, CCT above 6500 K is take 'warm' whereas below 4000 K is 'cold' [8]. The color purity is 3.1%, estimated by

$$\text{Color Purity} = \sqrt{\frac{(x-x_i)^2+(y-y_i)^2}{(x-x_d)^2+(y-y_d)^2}} \times 100\%, \qquad (3)$$

where (x, y), (x_i, y_i) and (x_d, y_d) are the co-ordinates of sample, white light and dominant wavelength. The CIEL*a*b* color space diagram with L*a*b* parameters are shown below (Fig. 6b and Table 2). The L* represent the color coordinate of the sample on black-white (0 to 100) axis, a* on green-red axis (−60 to +60) and b* on blue-yellow (−60 to +60) axis. The difference in color is calculated by

$$\Delta E = (\Delta L^{*2} + \Delta a^{*2} + \Delta b^{*2})^{1/2}, \qquad (4)$$

where ΔL*, Δa*, and Δb*are the respective deviation of test with reference positions [21]. The cylindrical coordinates C^* (saturation) and h^* (hue angle or arctang) calculated by

$$h^* = \frac{a^*}{b^*}, \qquad (5)$$

$$C^* = (a^{*2} + b^{*2})^{1/2}. \qquad (6)$$

The L* value is near white light and ΔE* value is small, giving a fruitful output. So, from the CIE diagram and CIEL*a*b* color space parameters, it is clearly evident that $La_{1.97}Dy_{0.02}Sm_{0.01}MgTiO_6$ phosphor emit light identical to neutral daylight. That is, when the phosphor probe illuminates internal tissues, they resemble daylight exposure. Thus, the real-time recorded images appear precise and accurate. This in turn enhance the early detection and prevention of diseases. So $La_{1.97}Dy_{0.02}Sm_{0.01}MgTiO_6$ perovskite nano-phosphors brings out a new era of endoscope LEDs, which can improve human health sector, augment total well-being and develop holistic growth.

4 Conclusion

Biomedical engineering is striving hard to replace conventional imaging light sources with an environmentally friendly, flexible, energy-saving, efficient, and miniature arrangement, that could improve the accuracy of real-time recorded data. Double perovskites with variable formulas, flexible properties, and suitable optical bandgap, are the most suited candidates for such illumination devices. Sm^{3+} activated (x= 0%, 1%, 2%) $La_{1.98}Dy_{0.02}MgTiO_6$ is synthesized by combustion method. The crystal structure, morphology, size and phase are established by XRD, SEM, and TEM. With reference to concentration quenching, the co-doping concentration is optimized as 1%. PL studies show that the phosphor emits violet-blue-yellow-red wavelengths, with intensity 3-fold than conventional lighting sources, owing to $Dy^{3+}\rightarrow Sm^{3+}$ energy transfer mechanism of 53%. The CIE coordinates are (0.322, 0.324) with CCT being 5835 K, neighboring ideal white light; confirmed by CIEL**a***b** color space parameters. So, a meticulous optimization on broad white emission of $La_{1.97}Dy_{0.02}Sm_{0.01}MgTiO_6$ to the neutral point for biomedical application yield an accurate light source for endoscopic and laparoscopic applications.

Disclosures

The authors declare no conflict of interest.

Acknowledgment

Sincerely thanking Kannur University for providing all the necessary facilities during the course of the work.

References

1. K. Jorgenson, A. Alekseyko, and V. Giedraitis, "Energy consumption, human well-being and economic development in central and eastern European nations: A cautionary tale of sustainability," Energy Policy 66, 419–427 (2014).
2. S. D. Perli, N. Ahmed, and D. Katabi, "PixNet: Interference-free wireless links using LCD-camera pairs," Proceedings of the Sixteenth Annual International Conference on Mobile Computing and Networking, 137–148 (2010).
3. M. Pal Uttam, "Use of LED's in Endoscopy and Laparoscopy," LED inside of TRENDFORCE, 2014 (accessed 15 September 2022). [https://www.ledinside.com/knowledge/2014/2/use_of_leds_in_endoscopy_and_laparoscopy].
4. I. V. Ivanov, T. Mappes, P. Schaupp, C. Lappe, and S. Wahl, "Ultraviolet radiation oxidative stress affects eye health," Journal of Biophotonics 11(7), e201700377 (2018).
5. N. T. Clancy, R. Li, K. Rogers, P. Driscoll, P. Excel, R. Yandle, G. Hanna, N. Copner, and D. S. Elson, "Development and evaluation of a light-emitting diode endoscopic light source," Proceedings of SPIE 8214, 82140R (2012).
6. D. G. Adler, B. Chand, J. D. Conway, D. L. Diehl, S. V. Kantsevoy, R. S. Kwon, P. Mamula, S. A. Rodriguez, R. J. Shah, L. M. W. K. Song, and W. M. Tierney, "Capsule endoscopy of the colon," Gastrointestinal Endoscopy 68(4), 621–623 (2008).
7. V. P. Veena, C. K. Shilpa, S. V. Jasira, and K. M. Nissamudeen, "Modern era of double perovskite nano-phosphors: La2MgTiO6, Gd2MgTiO6 and Y2MgTiO6 – a brief review," Zeitschrift für Naturforschung A 77(10), 1003–1013 (2022).
8. V. P. Veena, C. K. Shilpa, S. V. Jasira, K. Vini, and K. M. Nissamudeen, "Adroit low-temperature synthesis and origin of blue–yellow–red emission in activated La2-xDyxMgTiO6 novel perovskite phosphor for WLED," Journal of Materials Science: Materials in Electronics 34, 870 (2023).
9. V. P. Veena, N. Akshaya, C. K. Shilpa, S. V. Jasira, and K. M. Nissamudeen, "The upshot of Li+ co-doping on white emission of La1.98Dy0.02MgTiO6 double perovskite nano phosphors," Materials Today: Proceedings (2023).
10. V. P. Veena, C. K. Shilpa, S. V. Jasira, and K. M. Nissamudeen, "Anti-Counterfeiting and Multifunctional Applications of Near White Emitting La1.99mgtio6:0.01dy Perovskite Nano Phosphors," Social Science Research Network (2023).
11. B. Bondzior, D. Stefańska, T. H. Q. Vũ, N. Miniajluk-Gaweł, and P. J. Dereń, "Red luminescence with controlled rise time in La2MgTiO6: Eu3+," Journal of Alloys and Compounds 852, 157074 (2021).
12. K. Vini, K. M. Nissamudeen, "Facile Combustion Synthesis of (Y, Pr) 2O3 Red Phosphor: Study of Luminescence Dependence on Dopant Concentration and Enhancement by the Effect of Co-dopant," Zeitschrift für Naturforschung A 75(4), 357–371 (2020).
13. M. Pal, U. Pal, J. M. G. Y. Jiménez, and F. Pérez-Rodríguez, "Effects of crystallization and dopant concentration on the emission behavior of TiO2: Eu nanophosphors," Nanoscale Research Letters 7, 1 (2012).
14. G. Tiwari, N. Brahme, R. Sharma, D. P. Bisen, S. K. Sao, and S. Tigga, "Luminescence properties of dysprosium doped di-calcium di-aluminium silicate phosphors," Optical Materials 58, 234–242 (2016).
15. W. Li, G. Fang, Y. Wang, Z. You, J. Li, Z. Zhu, C. Tu, Y. Xu, and W. Jie, "Luminescent properties of Dy3+ activated LaMgAl11O19 yellow emitting phosphors for application in white-LEDs," Vacuum 188, 110215 (2021).
16. I. P. Sahu, P. Chandrakar, R. N. Baghel, D. P. Bisen, N. Brahme, and R. K. Tamrakar, "Luminescence properties of dysprosium doped calcium magnesium silicate phosphor by solid state reaction method," Journal of Alloys and Compounds 649, 1329–1338 (2015).

17. I. P. Sahu, D. P. Bisen, N. Brahme, R. K. Tamrakar, and R. Shrivastava, "Luminescence studies of dysprosium doped strontium aluminate white light emitting phosphor by combustion route," Journal of Materials Science: Materials in Electronics 26, 8824–8839 (2015).
18. W. Yan, J. Li, W. Zhang, X. Gao, and P. Zhang, "Warm-white luminescence of Dy3+ and Sm3+ co-doped NaSrPO4 phosphors through energy transfer between rare earth ions," Journal of Materials Science: Materials in Electronics 32, 16648–16661 (2021).
19. H. Pamuluri, M. Rathaiah, K. Linganna, C. K. Jayasankar, V. Lavin, and V. Venkatramu, "Role of Dy3+ → Sm3+ energy transfer in the tuning of warm to cold white light emission in Dy3+/Sm3+ co-doped Lu3Ga5O12 nano-garnets," New Journal of Chemistry 42(2), 1260–1270 (2018).
20. M. Yu, X. Xu, W. Zhang, X. Chen, P. Zhang, and Y. Huang, "The effect of Sm3+ co-doping on the luminescence properties of Ca2.85Li0.15(PO4)1.85(SO4)0.15: Dy3+ white-emitting phosphors," Journal of Alloys and Compounds 817, 152761 (2020).
21. M. M. Gonzalez-Pena, M. D. Hale, "Colour in thermally modified wood of beech, Norway spruce and Scots pine. Part 1: Colour evolution and colour changes," 63(4), 385–393 (2009).

Terahertz Spectroscopy of Mouse Blood Serum in the Dynamics of Experimental Glioblastoma

Olga P. Cherkasova[1,2,3]*, Maria R. Konnikova[3,4,5], Maksim M. Nazarov[6], Denis A. Vrazhnov[5,7], Yury V. Kistenev[5,7], and Alexander P. Shkurinov[3,4,5]

[1] Institute of Automation and Electrometry, Siberian Branch of RAS, 1 Academician Koptyug Ave., Novosibirsk 630090, Russia

[2] Institute of Laser Physics of SB RAS, 15B Academician Lavrentyev Ave., Novosibirsk 630090, Russia

[3] Institute on Laser and Information Technologies, Branch of the Federal Scientific Research Centre "Crystallography and Photonics" of RAS, 1 Svyatoozerskaya str., Shatura 140700, Russia

[4] Faculty of Physics, Lomonosov Moscow State University, 1 Leninskiye Gory, Moscow 119991, Russia

[5] Laboratory of Laser Molecular Imaging and Machine Learning, Tomsk State University, 36 Lenin Ave., Tomsk 634050, Russia

[6] National Research Centre "Kurchatov Institute", 1 Akademika Kurchatova pl., Moscow 123182, Russia

[7] V.E. Zuev Institute of Atmospheric Optics SB RAS, 1 Academician Zuev Square, Tomsk 634055, Russia

***e-mail:** o.p.cherkasova@gmail.com

Abstract. In this study terahertz (THz) absorption spectra of mouse blood serum in the dynamics of experimental U87 glioblastoma were investigated. Decrease of THz absorption with glioma growth was demonstrated. A two-component Debye model was used to analyze the experimental data. Analysis of the complex dielectric permittivity parameters of blood serum indicates an increase in the proportion of bound water in the samples in the dynamics of tumor growth. © 2023 Journal of Biomedical Photonics & Engineering.

Keywords: terahertz time domain spectroscopy; mouse blood serum; U87 glioblastoma; Debye model.

Paper #8990 received 3 Apr 2023; accepted for publication 21 Jun 2023; published online 15 Aug 2023. doi: 10.18287/JBPE23.09.030308.

1 Introduction

Glioblastoma, a type of glioma, tumors developing in the glial tissue of brain, represents almost half of all malignant tumors of the central nervous system [1] and is among the most rapidly progressing cancers with the worst prognosis of survival [2]. One reason for this is late diagnosis and treatment [3]. Therefore, it is relevant and important for the early detection of glioblastoma and the development of non-invasive and minimally invasive methods to monitor the effectiveness of treatment. The study of oncological molecular markers, their causes and pathways of formation, is a major direction in the diagnosis and therapy of malignant tumors [4]. Conventional methods such as chromatography and mass spectrometry [5–7], as well as nuclear magnetic resonance [8, 9], due to complex sample preparation, long testing time and inability to provide timely intraoperative analysis cannot provide fully reliable information. Early diagnosis of glioblastoma can be achieved by analyzing body fluids [10, 11], including the use of more technological and simple spectroscopic methods [12, 13].

Terahertz (THz) pulse spectroscopy, which has a number of features determining its application in creating new methods of medical diagnostics, has received intensive development [14–16]. The ability to directly measure the refractive index, absorption coefficient and dielectric function spectrum of the studied sample is a distinctive feature of this method [17, 18]. This makes it possible to obtain a detailed spectral characterization of the analyzed sample in a single measurement, giving the prospect of developing noninvasive rapid diagnostics on this basis [19]. Previously, THz spectroscopy methods have been used to study the features of THz images of mouse and rat brain tissue, freshly dissected [20, 21] and encased in paraffin blocks, in the dynamics of glioma development [22–28]. It was shown that the main contrast source in THz frequency range is water content, which increased with increasing tumor size and degree of malignancy [22, 27]. Other sources of contrast were increased cell density [22] and lipid content [26],

appearance of necrosis zones [28]. In these works, blood was not considered as an object of investigation. Meanwhile, blood composition significantly changes during the development of pathologies in organs and tissues of the body [29, 30], which can be used to create minimally invasive diagnostic methods [31, 32].

In this work we investigated THz absorption spectra of mouse blood serum in the dynamics of experimental U87 glioblastoma development. Currently, glioblastoma models with continuous cell lines such as U87 derived from primary human tumor cells transplanted intracranially into the mouse brain are most common [33, 34]. Using glioblastoma models in animals makes it possible to follow tumor development and blood composition changes in dynamics.

2 Materials and Methods

2.1 Terahertz Time Domain Spectroscopy (THz-TDS)

Mouse serum samples were measured on a pulsed THz spectrometer, which is described in detail in previous articles [35–37]. A femtosecond laser (Spectra Physics Tsunami) with wavelength λ = 800 nm, pulse duration τ = 80 fs, and modulation frequency f = 80 MHz was used as pumping. The THz generator was a multidipole photoconductive antenna (iPCA-21-05-1000-800-h, Batop, Germany), the detector was a 300 μm ZnTe crystal. Photoconductive antenna emission power was in the range of 70÷75 mW, bias supply voltage was 15 V. Spectral range for reliable measurements was from 0.6 to 1.8 THz, with small attenuation of the passed radiation. The range was determined by the signal-to-noise ratio, which reached 10^2 or 20 dB across the field in the absence of sample. The experimental samples were placed in a demountable liquid cuvette (Bruker, USA) with two identical polystyrene windows. The refractive index of windows was 1.5 at 0.6–1.8 THz. The thickness of the liquid layer given by PTFE spacer was 180 ± 5 μm, which provided a transmittance value in the range 0.05–0.50, depending on the sample type. The lowest transmittance coefficient corresponded to the transmittance of distilled water at high frequencies. Measurements were performed at temperature of 21 ± 1 ºC and 35% relative humidity. The cuvette was installed in THz beam tangle with a diameter of 300 ± 15 μm. The time shape of pulse that passed through the cuvette was recorded. To exclude the statistical error associated with changes in the laser power during the experiment, the transmission measurements of empty cuvette, cuvette with water and sample were carried out alternately. A time sampling of 25 ps from 1024 points with a signal accumulation time in each point of 300 ms was used. To increase the reliability of measurements, three independent measurements were averaged for each serum sample. The measurement error was calculated as the standard deviation from the group mean. The time shapes of group-averaged THz pulses while passing through air (without a cuvette), an empty cuvette, and a cuvette filled with water and serum are shown in Fig. 1.

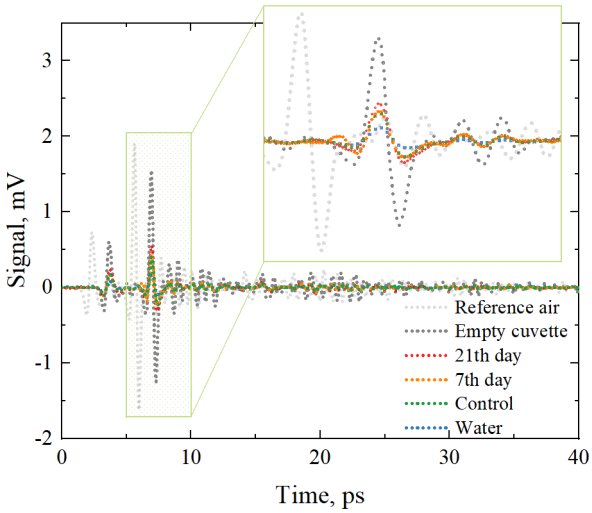


Fig. 1 Time shapes of group-averaged THz pulses: without cuvette (gray line), passed through empty cuvette (dark gray line), cuvette filled with water (blue line), serum of control mice (green line), after 7 (yellow line) and 21 days (red line) after injection of U87 glioblastoma cells.

Fourier transform of measured temporal shape of THz pulse gives complex spectrum $E(\omega)$ of radiation, i.e. amplitude $|E(\omega)|$ and phase $\arg(E(\omega))$ of spectrum, where E is electric component of electromagnetic wave field, $\omega = 2\pi f$, f is frequency. The transmittance spectrum of sample was calculated as follows:

$$T(\omega) = \frac{E(\omega)}{E_0(\omega)}, \quad (1)$$

where $E_0(\omega)$ is the reference spectrum of the THz pulse passing through an empty cuvette, $E(\omega)$ is the transmission of the cuvette with distilled water or blood serum.

The absorption coefficient and refractive index spectra were calculated using the methods described in detail in previous papers [14, 15, 31, 32, 35, 37, 38]; the sample absorption coefficient was calculated as follows:

$$\alpha(\omega) = \frac{-ln|T(\omega)|}{d} + \frac{ln(1-R_a^2)}{d}, \quad (2)$$

where d is sample thickness, $R_a = \frac{n_a-1}{n_a+1}$ is reflection coefficient for real part of refractive index averaged over all frequencies, $n_a = 1 + \Delta t \frac{c}{d}$ is averaged refractive index, Δt is pulse delay in passing through the sample. The refractive index was calculated as follows:

$$n(\omega) = \frac{-\arg(T(\omega)) \cdot c}{\omega \cdot d} + 1. \quad (3)$$

In this case, the complex permittivity has the form:

$$\varepsilon(\omega) = \left((n(\omega) - i\alpha(\omega) \cdot \frac{c}{\omega}) + 1 \right)^2. \quad (4)$$

2.2 Samples

The model of orthotopic xenotransplantation of U87 human glioblastoma cells into immunodeficient SCID mice was used [39]. A 5 µl cell suspension (500,000 U87 MG cells per animal) was injected in the subcortical brain structure through a hole in the animal's cranium. A 5 µl culture medium was introduced to animals from the control group according to a similar scheme. Tumor size was measured in vivo on a horizontal tomograph with a magnetic field strength of 11.7 Tesla (Biospec 117/16, Bruker, USA) [40]. After that, animals of experimental and corresponding control groups were removed from the experiment by decapitation on days 7 and 21 after injection. Blood was collected in separate tubes, centrifuged and serum was frozen at −80 °C until the day of analysis. There were 10 mice in each group. The study was carried out in accordance with the EU Directive 2010/63/EU and the ARRIVE 2.0 guidelines, and approved by the Inter-Institutional Commission on Biological Ethics at the Institute of Cytology and Genetics, Siberian Branch of the Russian Academy of Sciences (Permission #78, 16 April 2021).

3 Results and Discussion

Tumor size increases significantly in the dynamics of U87 glioblastoma development. Thus, the tumor size is 2.6 ± 0.4 mm^3 on day 7, and already 89.6 ± 11.5 mm^3 on day 21 of the experiment. The THz response of blood serum also changes significantly, which is expressed in decrease of absorption coefficient at the last stage of the experiment (Fig. 2, a).

The high water content in blood serum determines the nature of its dielectric response in THz frequency range [15, 41]. Water can be in free or bound to the surrounding molecules. The reason for changes in the THz response of blood serum is the transition of water from free to bound state and back [15, 41]. The THz spectrum of water is characterized by the absence of well-defined spectral features in the frequency range of 0.1–3.0 THz. A similar type of spectra was obtained previously by us and some authors when studying of human blood [42], serum of rats with experimental liver cancer [31], diabetes [43, 44], as well as blood plasma from patients with thyroid disease [32]. The absorption spectra of control mice serum and on the 7th day of experiment are indistinguishable within the limits of error and have a smaller amplitude compared to the absorption spectrum of water. It is known that metabolic changes associated specifically with brain injury and the development of an inflammation reaction are observed in the first week after the introduction of culture medium or tumor cells into the brain [45]. Then blood composition changes associated with tumor development become dominant [46]. The absorption coefficient of blood serum of mice on the 21st day of the experiment is significantly lower than the absorption coefficient of the other spectra in the entire range under study. At the same time, with increasing frequency, there is a greater degree of differentiation of absorption spectra for all samples. No significant differences in the refractive index spectra were observed (see Fig. 2, b).

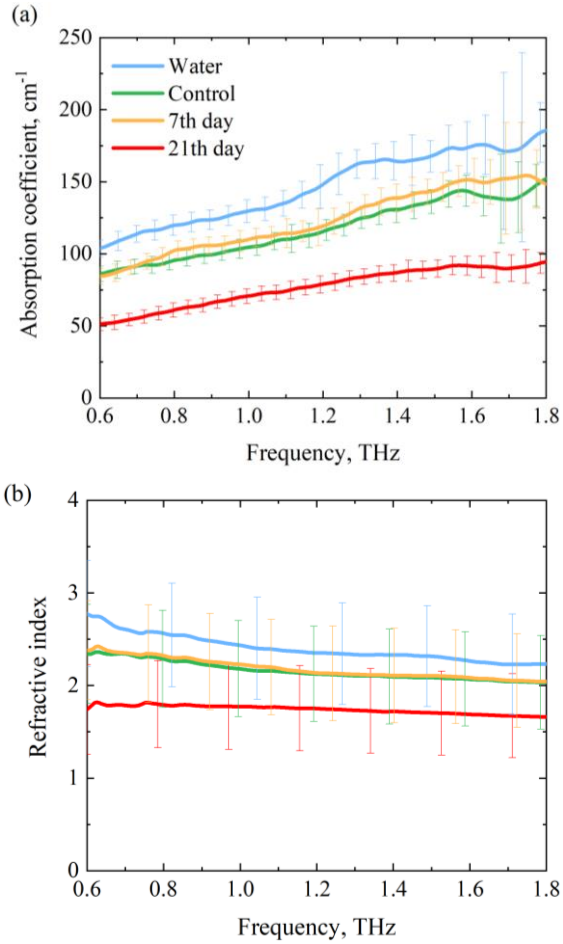


Fig. 2 Absorption coefficient (a) and refractive index (b) of water (blue line), blood serum of control mice (green line), and at 7 (yellow line) and 21 days (red line) after injection of U87 glioblastoma cells.

Based on comparison of experimentally obtained dielectric permittivity spectra with the model dielectric function of water ε(ω), which can be described by the two-component Debye model and the Lorentz term [15, 31, 37, 47–50], we analyzed the observed differences in THz spectra:

$$\varepsilon(\omega) = \varepsilon_\infty + \frac{\Delta\varepsilon_1}{1+i2\pi f\tau_1} + \frac{\Delta\varepsilon_2}{1+i2\pi f\tau_2} + \frac{A_1}{\omega_{01}^2-(2\pi f)^2+i2\pi f\gamma_{01}}, \quad (5)$$

where τ_1 and τ_2 are relaxation time of first ("slow") and second ("fast") Debye terms, $\Delta\varepsilon_i$ is contributions to dielectric permittivity of first and second Debye terms, A_1 is amplitude, ω_{01} is resonance frequency, γ_{01} is half-

width from the Lorentz term and ε_∞ is dielectric permittivity of water at high frequencies.

The following model parameters for water were obtained: $\Delta\varepsilon_1 = 74 \pm 9$, τ_1=9.47 ± 0.5 ps, $\Delta\varepsilon_2 = 1.67 \pm 0.03$, τ_2=0.24 ± 0.01 ps, A_1=31 THz^2, $\omega_{01} = 5.3$ THz, $\gamma_0 = 7$ THz, $\varepsilon_\infty = 2.3 \pm 0.2$. For frequency range of 0.05–2.5 THz at a temperature of 20–22 °C the given set of values is optimal. Comparison of the experimental imaginary Im(ε) and real Re(ε) parts of dielectric permittivity with model spectra for water are shown by blue line and dotted line in Fig. 3, respectively.

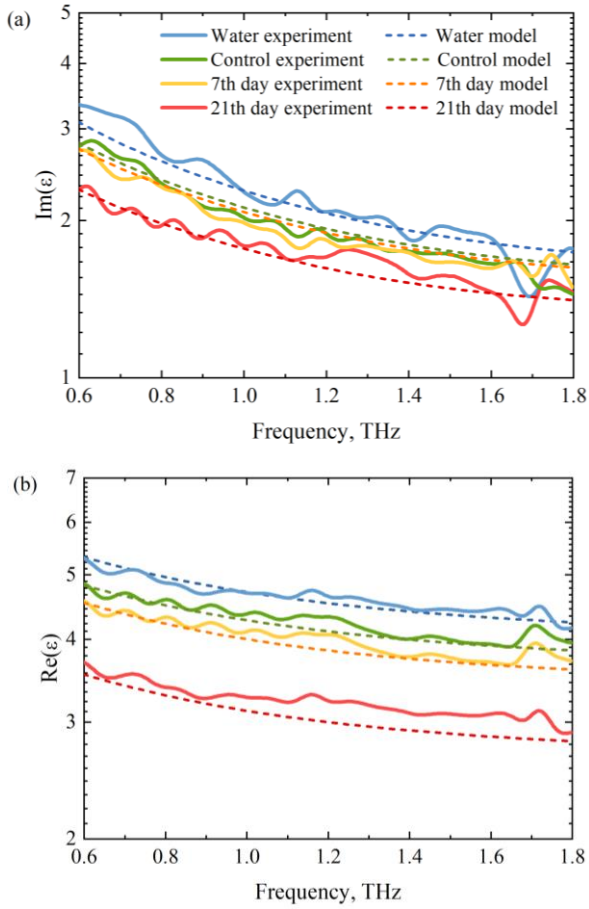


Fig. 3 Imaginary Im(ε) (a) and real Re(ε) (b) parts of dielectric permittivity for experimental data presented in Fig. 1 and their model curves: for water (blue line), blood serum of control mice (green line), and after 7 (yellow line) and 21 days (red line) after injection of U87 glioblastoma cells.

Earlier we demonstrated for the THz range that any aqueous solution of biomolecules, including blood serum, can be described with sufficient accuracy mainly by changes in the amplitude $\Delta\varepsilon_1$ and the relaxation time τ_1 of the first Debye term [31, 37, 43, 47–49]. This approach is valid also for a model spectrum of serum dielectric permittivity in the dynamics of glioma development. By changing $\Delta\varepsilon_1$ and τ_1, all other terms of the model (5) have fixed values corresponding to water parameters in the chosen frequency range. Results of comparison of experimental and model dielectric permittivity spectra are shown in Fig. 3. The parameters of Debye model $\Delta\varepsilon_1$ and τ_1 for all investigated samples are given in Table 1.

Table 1 Parameters $\Delta\varepsilon_1$ and τ_1 of studied samples.

Sample/Parameter	$\Delta\varepsilon_1$	τ_1 (ps)
Distilled water	74.9 ± 4.1	9.28 ± 0.51
Blood serum of control mice	74.3 ± 4.9	9.56 ± 0.31
Blood serum of mice after 7 days	68.2 ± 5.1	10.42 ± 0.32
Blood serum of mice after 21 days	57.9 ± 5.4	11.80 ± 0.29

It should be noted that for frequencies above 0.1 THz we cannot separate the contribution of the decrease $\Delta\varepsilon_1$ or increase τ_1 to the model spectrum. Only the change in the ratio $\Delta\varepsilon_1/\tau_1$ can be clearly discerned [47]. We have previously shown a 1.2-fold decrease in the ratio compared to water for blood plasma of rat with experimental diabetes, which is associated with a high level of glucose in the blood plasma [43]. It was also shown that as both glucose concentration and protein concentration increase in solutions, the proportion of water bound to biomolecules increases, which has a lower value of $\Delta\varepsilon_1$ and a high value of relaxation time τ_1 as compared to water molecules not bound by hydrogen bonds [47, 49].

Table 1 shows that in the dynamics of U87 glioblastoma there is a decrease in $\Delta\varepsilon_1$ and an increase in τ_1, which leads to a decrease in the ratio $\Delta\varepsilon_1/\tau_1$. As noted above, on day 21 of the experiment, there is a more than 34-fold increase in tumor size compared to 7 days after the introduction of glioblastoma U87 cells. This leads to a significant change in blood serum composition [46]. The decrease of $\Delta\varepsilon_1$ contribution to dielectric permittivity of samples in the dynamics of tumor growth is related to the decrease of free water fraction with simultaneous increase of bound water fraction. The increase of relaxation time τ_1 in the dynamics of tumor growth indicates a "slowing down" of the process of water molecules reorientation in the hydrogen bonding network. Thus, a change in blood serum composition in the dynamics of glioma development leads to a change in complex dielectric permittivity parameters.

4 Conclusion

The THz absorption spectra of mouse blood serum in frequency range 0.6–1.8 THz in the dynamics of experimental U87 glioblastoma were studied. It is shown that the absorption coefficients of healthy mouse serum and on the 7th day of experiment do not differ. The absorption coefficient of mouse serum on 21st day of the experiment is significantly lower compared to water and serum of other experimental groups. This difference in THz response is explained by changes in blood composition at different stages of U87 glioblastoma

development. Analysis of complex dielectric permittivity parameters of blood serum in the dynamics of glioblastoma development in mice indicates an increase in proportion of bound water with tumor growth.

Acknowledgements

This work was performed partly within the State Assignment of IA&E SB RAS, ILP SB RAS and FSRC "Crystallography and Photonics" RAS. This work has been supported by the Interdisciplinary Scientific and Educational School of Moscow University "Photonic and Quantum Technologies. Digital Medicine" for part of the results analysis. The research was carried out partly with the support of the Tomsk State University Development Program (Priority-2030). The work of D. V. and Yu. K. was supported by the Ministry of Science and Higher Education of the Russian Federation (budget funds for the V. E. Zuev Institute of Atmospheric Optics of the Siberian Branch of the Russian Academy of Sciences).

Disclosures

The authors declare no conflict of interest.

References

1. Q. T. Ostrom, G. Cioffi, K. Waite, C. Kruchko, and J. C. Barnholtz-Sloan, "CBTRUS Statistical Report: Primary Brain and Other Central Nervous System Tumors Diagnosed in the United States in 2014–2018," Neuro-Oncology, 23(Supplement S3), iii1–iii105 (2021).
2. T. Tykocki, M. Eltayeb, "Ten-year survival in glioblastoma. A systematic review," Journal of Clinical Neuroscience 54, 7–13 (2018).
3. M. Hishii, T. Matsumoto, and H. Arai, "Diagnosis and Treatment of Early-Stage Glioblastoma," Asian Journal of Neurosurgery 14(2), 589–592 (2019).
4. L. Wang, X. Liu, and Q. Yang, "Application of Metabolomics in Cancer Research: As a Powerful Tool to Screen Biomarker for Diagnosis, Monitoring and Prognosis of Cancer," Biomarkers Journal 4(3), 12 (2018).
5. V. Poinsignon, L. Mercier, K. Nakabayashi, M. D. David, A. Lalli, V. Penard- Lacronique, C. Quivoron, V. Saada, S. D. Botton, S. Broutin, and A. Paci, "Quantitation of isocitrate dehydrogenase (IDH)-induced D and L enantiomers of 2-hydroxyglutaric acid in biological fluids by a fully validated liquid tandem mass spectrometry method, suitable for clinical applications," Journal of Chromatography B 1022, 290–297 (2016).
6. M. Touat, A. Duran-Peña, A. Alentorn, L. Lacroix, C. Massard, and A. Idbaih, "Emerging circulating biomarkers in glioblastoma: promises and challenges," Expert Reviews 15(10), 1311–1323 (2015).
7. E. Miyauchi, T. Furuta, S. Ohtsuki, M. Tachikawa, Y. Uchida, H. Sabit, W. Obuchi, T. Baba, M. Watanabe, T. Terasaki, and M. Nakada, "Identification of blood biomarkers in glioblastoma by SWATH mass spectrometry and quantitative targeted absolute proteomics," PLoS ONE 13(3), e0193799 (2018).
8. E. Baranovičová, T. Galanda, M. Galanda, J. Hatok, B. Kolarovszki, R. Richterová, and P. Račay, "Metabolomic profiling of blood plasma in patients with primary brain tumours: Basal plasma metabolites correlated with tumour grade and plasma biomarker analysis predicts feasibility of the successful statistical discrimination from healthy subjects – a preliminary study," IUBMB Life 71(12), 1994–2002 (2019).
9. J. E. Lee, S. S. Jeun, S. H. Kim, C. Y. Yoo, H.-M. Baek, and S. H. Yang, "Metabolic profiling of human gliomas assessed with NMR," Journal of Clinical Neuroscience 68, 275–280 (2019).
10. J. M. Figueroa, "Detection of glioblastoma in biofluids," Journal of Neurosurgery 129(2), 334–340 (2018).
11. O. Cherkasova, Y. Peng, M. Konnikova, Y. Kistenev, C. Shi, D. Vrazhnov, O. Shevelev, E. Zavjalov, S. Kuznetsov, and A. Shkurinov, "Diagnosis of Glioma Molecular Markers by Terahertz Technologies," Photonics 8(1), 22 (2021).
12. H. J. Butler, P. M. Brennan, J. M. Cameron, D. Finlayson, M. G. Hegarty, M. D. Jenkinson, D. S. Palmer, B. R. Smith, and M. J. Baker, "Development of high-throughput ATR-FTIR technology for rapid triage of brain cancer," Nature Communications 10, 4501 (2019).
13. A. G. Theakstone, P. M. Brennan, M. D. Jenkinson, S. J. Mills, K. Syed, C. Rinaldi, Y. Xu, R. Goodacre, H. J. Butler, D. S. Palmer, B. R. Smith, and M. J. Baker, "Rapid Spectroscopic Liquid Biopsy for the Universal Detection of Brain Tumours," Cancers 13(15), 3851 (2021).
14. G. R. Musina, P. V. Nikitin, N. V. Chernomyrdin, I. N. Dolganova, A. A. Gavdush, G. A. Komandin, D. S. Ponomarev, A. A. Potapov, I. V. Reshetov, V. V. Tuchin, and K. I. Zaytsev, "Prospects of terahertz technology in diagnosis of human brain tumors – a review," Journal of Biomedical Photonics & Engineering 6(2), 020201 (2020).
15. O. A. Smolyanskaya, N. V. Chernomyrdin, A. A. Konovko, K. I. Zaytsev, I. A. Ozheredov, O. P. Cherkasova, M. M. Nazarov, J.-P. Guillet, S. A. Kozlov, Yu. V. Kistenev, J.-L. Coutaz, P. Mounaix, V. L. Vaks, J.-H. Son, H. Cheon, V. P. Wallace, Yu. Feldman, I. Popov, and V. V. Tuchin, "Terahertz biophotonics as a tool for studies of dielectric and spectral properties of biological tissues and liquids," Progress in Quantum Electronics 62, 1–77 (2018).
16. K. I. Zaytsev, I. N. Dolganova, N. V. Chernomyrdin, G. M. Katyba, A. A. Gavdush, O. P. Cherkasova, G. A. Komandin, M. A. Shchedrina, A. N. Khodan, D. S. Ponomarev, I. V. Reshetov, V. E. Karasik, M. Skorobogatiy, V.N. Kurlov, and V. V. Tuchin, "The progress and perspectives of terahertz technology for diagnosis of neoplasms: A review," Journal of Optics 22(1), 013001 (2020).

17. K. P. Cheung, D. H. Auston, "A novel technique for measuring far-infrared absorption and dispersion," Infrared Physics 26(1), 23–27 (1986).
18. D. Grischkowsky, S. Keiding, M. van Exter, and Ch. Fattinger, "Far-infrared time-domain spectroscopy with terahertz beams of dielectrics and semiconductors," Journal of the Optical Society of America B 7(10), 2006–2015 (1990).
19. O. Cherkasova, M. Nazarov, and A. Shkurinov, "Noninvasive blood glucose monitoring in the terahertz frequency range," Optical and Quantum Electronics 48(3), 217 (2016).
20. A. Gavdush, N. Chernomyrdin, K. Malakhov, S.-I. Beshplav, I. Dolganova, A. Kosyrkova, P. Nikitin, G. Musina, G. Katyba, I. Reshetov, O. Cherkasova, G. Komandin, V. Karasik, A. Potapov, V. Tuchin, and K. Zaytsev, "Terahertz spectroscopy of gelatin-embedded human brain gliomas of different grades: a road toward intraoperative THz diagnosis," Journal of Biomedical Optics 24(2), 027001 (2019).
21. A. A. Gavdush, N. V. Chernomyrdin, G. A. Komandin, I. N. Dolganova, P. V. Nikitin, G. R. Musina, G. M. Katyba, A. S. Kucheryavenko, I. V. Reshetov, A. A. Potapov, V. V. Tuchin, and K. I. Zaytsev, "Terahertz dielectric spectroscopy of human brain gliomas and intact tissues ex vivo: double-Debye and double-overdamped-oscillator models of dielectric response," Biomedical Optics Express 12(1), 69–83 (2020).
22. S. J. Oh, S.-H. Kim, Y. B. Ji, K. Jeong, Y. Park, J. Yang, D. W. Park, S. K. Noh, S.-G. Kang, Y.-M. Huh, J.-H. Son, and J.-S. Suh, "Study of freshly excised brain tissues using terahertz imaging," Biomedical Optics Express 5(8), 2837–2842 (2014).
23. K. Meng, T.-N. Chen, T. Chen, L.-G. Zhu, Q. Liu, Z. Li, F. Li, S.-C. Zhong, Z.-R. Li, H. Feng, and J.-H. Zhao, "Terahertz pulsed spectroscopy of paraffin-embedded brain glioma," Journal of Biomedical Optics 19(7), 077001 (2014).
24. S. Yamaguchi, Y. Fukushi, O. Kubota, T. Itsuji, T. Ouchi, and S. Yamamoto, "Brain tumor imaging of rat fresh tissue using terahertz spectroscopy," Scientific Reports 6, 30124 (2016).
25. L. Wu, D. Xu, Y. Wang, B. Liao, Z. Jiang, L. Zhao, Z. Sun, N. Wu, T. Chen, H. Feng, and J. Yao, "Study of in vivo brain glioma in a mouse model using continuous-wave terahertz reflection imaging," Biomedical Optics Express 10(8), 3953–3962 (2019).
26. Y. B. Ji, S. J. Oh, S.-G. Kang, J. Heo, S.-H. Kim, Y. Choi, S. Song, H. Y. Son, S. H. Kim, J. H. Lee, S. J. Haam, Y. M. Huh, J. H. Chang, C. Joo, and J.-S. Suh, "Terahertz reflectometry imaging for low and high grade gliomas," Scientific Reports 6, 36040 (2016).
27. L. Wu, Y. Wang, B. Liao, L. Zhao, K. Chen, M. Ge, H. Li, T. Chen, H. Feng, D. Xu, and J. Yao, "Temperature dependent terahertz spectroscopy and imaging of orthotopic brain gliomas in mouse models," Biomedical Optics Express 13(1), 93–104 (2022).
28. A. S. Kucheryavenko, N. V. Chernomyrdin, A. A. Gavdush, A. I. Alekseeva, P. V. Nikitin, I. N. Dolganova, P. A. Karalkin, A. S. Khalansky, I. E. Spektor, M. Skorobogatiy, V. V. Tuchin, and K. I. Zaytsev, "Terahertz dielectric spectroscopy and solid immersion microscopy of ex vivo glioma model 101.8: brain tissue heterogeneity," Biomedical Optics Express 12(8), 5272–5289 (2021).
29. A. G. Kamkin, A. A. Kamensky (Eds.), Fundamental and Clinical Physiology, Training manual, The Academy Moscow (2004). ISBN: 5-7695-1675-5.
30. O. P. Cherkasova, M. M. Nazarov, and A. P. Shkurinov, "Study of blood and its components by terahertz pulsed spectroscopy," EPJ Web of Conferences 195, 10003 (2018).
31. M. M. Nazarov, O. P. Cherkasova, E. N. Lazareva, A. B. Bucharskaya, N. A. Navolokin, V. V. Tuchin, and A. P. Shkurinov, "A complex study of the peculiarities of blood serum absorption of rats with experimental liver cancer," Optics and Spectroscopy 126(6), 721–729 (2019).
32. M. R. Konnikova, O. P. Cherkasova, M. M. Nazarov, D. A. Vrazhnov, Yu. V. Kistenev, S. E. Titov, E. V. Kopeikina, S. P. Shevchenko, and A. P. Shkurinov, "Malignant and benign thyroid nodule differentiation through the analysis of blood plasma with terahertz spectroscopy," Biomedical Optics Express 12(2), 1020–1035 (2021).
33. J. A. Koutcher, X. Hu, S. Xu, T. P. Gade, N. Leeds, X. J. Zhou, D. Zagzag, and E. S. Holland, "MRI of Mouse Models for Gliomas Shows Similarities to Humans and Can Be Used to Identify Mice for Preclinical Trials," Neoplasia 4(6), 480–485 (2002).
34. E. L. Zavjalov, I. A. Razumov, L. A. Gerlinskaya, and A. V. Romashchenko, "In vivo MRI Visualization of U87 Glioblastoma Development Dynamics in the Model of Orthotopic Xenotransplantation to the SCID Mouse," Russian Journal of Genetics: Applied Research 6, 448–453 (2016).
35. M. M. Nazarov, A. P. Shkurinov, E. A. Kuleshov, and V. V. Tuchin, "Terahertz time-domain spectroscopy of biological tissues," Quantum Electronics 38(7), 647 (2008).
36. O. P. Cherkasova, M. M. Nazarov, A. P. Shkurinov, and V. I. Fedorov, "Terahertz spectroscopy of biological molecules," Radiophysics and Quantum Electronics 52(7), 518–523 (2009).
37. M. M. Nazarov, O. P. Cherkasova, and A. P. Shkurinov, "A Comprehensive Study of Albumin Solutions in the Extended Terahertz Frequency Range," Journal of Infrared, Millimeter, and Terahertz Waves 39, 840–853 (2018).

38. M. R. Konnikova, O. P. Cherkasova, T. A. Geints, E. S. Dizer, A. A. Man'kova, I. S. Vasilievskii, A. A. Butylin, Yu. V. Kistenev, V. V. Tuchin, and A. P. Shkurinov, "Study of adsorption of the SARS-CoV-2 virus spike protein by vibrational spectroscopy using terahertz metamaterials," Quantum Electronics 52(1), 2 (2022).
39. D. Vrazhnov, A. Knyazkova, M. Konnikova, O. Shevelev, I. Razumov, E. Zavjalov, Y. Kistenev, A. Shkurinov, and O. Cherkasova, "Analysis of Mouse Blood Serum in the Dynamics of U87 Glioblastoma by Terahertz Spectroscopy and Machine Learning," Applied Sciences 12(20), 10533 (2022).
40. O. B. Shevelev, A. A. Seryapina, E. L. Zavjalov, L. A. Gerlinskaya, T. N. Goryachkovskaya, N. M. Slynko, L. V. Kuibida, S. E. Peltek, A. L. Markel, and M. P. Moshkin, "Hypotensive and neurometabolic effects of intragastric Reishi (Ganoderma lucidum) administration in hypertensive ISIAH rat strain," Phytomedicine 41, 1–6 (2018).
41. M. Nazarov, A. Shkurinov, V. V. Tuchin, and X.-C. Zhang, Handbook of Photonics for Biomedical Science. Series in Medical Physics and Biomedical Engineering, V. V. Tuchin (Ed.), 1st ed., CRC Press, Boca Raton (2010). ISBN: 9780429131271.
42. T.-F. Tseng, B. You, H.-C. Gao, T.-D. Wang, and C.-K. Sun, "Pilot clinical study to investigate the human whole blood spectrum characteristics in the sub-THz region," Optics Express 23(7), 9440–9451 (2015).
43. O. P. Cherkasova, M. M. Nazarov, A. A. Angeluts, and A. P. Shkurinov, "Analysis of blood plasma at terahertz frequencies," Optics and Spectroscopy 120, 50–57 (2016).
44. O. P. Cherkasova, M. M. Nazarov, I. N. Smirnova, A. A. Angeluts, and A. P. Shkurinov, "Application of time-domain THz spectroscopy for studying blood plasma of rats with experimental diabetes," Physics of Wave Phenomena 22, 185–188 (2014).
45. Y. Wang, G. Wang, D. Xu, B. Jiang, M. Ge, L. Wu, C. Yang, N. Mu, S. Wang, C. Chang, T. Chen, H. Feng, and J. Yao, "Terahertz spectroscopic diagnosis of early blast-induced traumatic brain injury in rats," Biomedical Optics Express 11(8), 4085–4098 (2020).
46. D. Vrazhnov, A. Mankova, E. Stupak, Y. Kistenev, A. Shkurinov, and O. Cherkasova, "Discovering Glioma Tissue through Its Biomarkers' Detection in Blood by Raman Spectroscopy and Machine Learning," Pharmaceutics 15(1), 203 (2023).
47. M. M. Nazarov, O. P. Cherkasova, and A. P. Shkurinov, "Study of the dielectric function of aqueous solutions of glucose and albumin by THz time-domain spectroscopy," Quantum Electronics 46 (6), 488 (2016).
48. O. Cherkasova, M. Nazarov, and A. Shkurinov, "Properties of aqueous solutions in THz frequency range," Journal of Physics: Conference Series 793(1), 012005 (2017).
49. O. P. Cherkasova, M. M. Nazarov, M. R. Konnikova, and A. P. Shkurinov, "THz Spectroscopy of Bound Water in Glucose: Direct Measurements from Crystalline to Dissolved State," Journal of Infrared, Millimeter, and Terahertz Waves 41, 1057–1068 (2020).
50. H. Yada, M. Nagai, and K. Tanaka, "Origin of the fast relaxation component of water and heavy water revealed by terahertz time-domain attenuated total reflection spectroscopy," Chemical Physics Letters 464 (4–6), 166–170 (2009).

Fabrication of Polyvinyl Alcohol Doped CuO Thin Films for Improved Amperometric-Non Enzymatic Hydrogen Peroxide Sensing

Navashree Nagarajan and Parthasarathy Panchatcharam*
Department of Electronics and Communication Engineering, CMR Institute of Technology, Bengaluru 560037, India

***e-mail:** arjunsarathii@gmail.com

Abstract. Nanotechnology is an emerging field in science and technology that primarily focus on nanoparticles ranging from 1–100 nm in diameter, which exhibit distinctive properties owing to their small size and large surface area. Among them, copper oxide nanostructures, are major metal oxide nanoparticles, widely used in various fields especially in the development of biosensors due to their unique structural characteristics and biological effects. In this work, copper oxide nanoparticles were synthesized using a simple chemical reduction method and characterized using XRD to study the morphological and structural properties. Those nanoparticles were doped with PVA by sol-gel process and the electrode was fabricated using the spin coating technique on the precleaned glass slide. CV studies showed that the CuO NPs electrode was effective in detecting hydrogen peroxide with high selectivity even in the presence of other substances. A high-level sensitivity of 0.002 $mA{\cdot}mM^{-1}cm^{-2}$ and a 0.5 mM to 1.5 mM quick linear response was accomplished due to the large specific surface areas and efficient electron transport in the corresponding reactions, making this electrode a very promising candidate for efficient and accurate non-enzymatic detection of hydrogen peroxide (H_2O_2). © 2023 Journal of Biomedical Photonics & Engineering.

Keywords: copper oxide nanoparticles; hydrogen peroxide; polyvinyl alcohol; electrochemical sensor; amperometric detection.

Paper #7782 received 24 Feb 2023; revised manuscript received 28 Jun 2023; accepted for publication 8 Jul 2023; published online 23 Aug 2023. doi: 10.18287/JBPE23.09.030309.

1 Introduction

Hydrogen peroxide (H_2O_2) plays a crucial role as a mediator in biological systems, where it contributes to the regulation of cell growth. It is involved in various cellular processes, including cell signaling, immune activation, and apoptosis. This is primarily attributed to the reactivity of H_2O_2 with other oxygen species present in the system [1]. It has numerous applications in diverse fields, such as controlling microbes, bleaching textiles and paper, cosmetics, food processing, pharmaceuticals, and environmental practices. In addition, H_2O_2 has many applications, including treating wastewater, oxidizing cellulose, enhancing rocket fuels, recycling waste paper, detoxifying organic pollutants, and manufacturing various chemicals and plastics that could potentially contaminate the environment. It is also crucial for various enzymatic reactions in the body, and the H_2O_2 layer serves as the initial defense mechanism against different pathogens [2]. However, excess H_2O_2 leakage in biological organisms can be harmful, causing gastrointestinal tract damage, skin and stomach irritation, and protein degradation. Specifically, excessive amounts of H_2O_2 in the body have been linked to several diseases, including fragmentation of DNA, diabetes, membrane damage, cardiovascular issues, cancer, Parkinson's, Alzheimer's, neurodegeneration, tissue damage, and aging problems [3]. It is also utilized as an oxidant in various fields, including environmental monitoring, food safety, and medical applications. These conditions make

This paper was presented at the International Conference on Nanoscience and Photonics for Medical Applications – ICNPMA, Manipal, India, December 28–30, 2022.

it crucial for the determination of hydrogen peroxide [4]. Various techniques have been developed to detect H_2O_2, including colorimetry, photoelectrochemical, light detection, titration, chromatography, and electrochemical methods. However, chromatography and titration methods are not suitable for in vitro and in vivo detection of H_2O_2. Similarly, light detection and chemiluminescent techniques are inconvenient for H_2O_2 detection because of the differences in excitation methods and the interference of H_2O_2 with chemical compounds during fluorescence measurements. As a result, the electrochemical method has gained popularity in recent years due to its simplicity, accuracy, speed, affordability, and user-friendliness [5]. Extensive research has been conducted on enzyme-based electrochemical biosensors, primarily due to their high sensitivity and excellent selectivity [6]. However, these biosensors suffer from a significant drawback due to a lack of stability and poor reproducibility caused by the inherent fragility of enzymes, which can be easily damaged during biosensor fabrication and testing. Consequently, recent studies have focused on enzyme-free electrochemical biosensors that offer advantages such as high sensitivity, rapid response, affordability, and good stability [7]. Numerous materials have been investigated for enzyme-free electrochemical biosensors, including transition metal nanoparticles, carbon nanotubes, semiconducting metal oxides, graphene, ordered mesoporous carbon, and their composites. These materials possess large specific surface areas and enhanced catalytic activities, enabling sensitive and rapid detection of hydrogen peroxide. Among them, copper oxide stands out as an excellent material due to its remarkable redox properties, non-toxicity, high stability, and conductivity [8]. Conducting polymers have also been employed as modifiers in the fabrication of electrochemical sensors due to their exceptional stability, good conductivity, and ability to maintain stability on the electrode surface [9, 10]. In the present study, we developed enzyme-free H_2O_2 electrochemical biosensing materials using CuO nanoparticles synthesized through a simple reduction method, which were then doped into polyvinyl alcohol polymer to create a thin film. Our findings demonstrate that the CuO nanostructure enhances the electrochemical performance for H_2O_2 detection, primarily due to its large specific surface area and efficient electron charge transfer properties.

2 Experimental Section

2.1 Materials

All the chemicals such as Copper (II) sulphate pentahydrate ($CuSO_4 \cdot 5H_2O$), Sodium hydroxide (NaOH), Ascorbic acid, Polyvinyl Alcohol, (PVA, average molecular weight of 85000), and Distilled water were purchased of analytical grade from Kesari Scientific chemicals (Chennai). Nonionic detergent and deionized water were used to clean all glassware and oven-dried before use.

2.2 Copper Oxide Nanoparticle Synthesis

To synthesize the copper oxide nanoparticles, a simple chemical reduction method was employed. The procedure involved the gradual addition of 25 ml of a 10 mM $CuSO_4 \cdot 5H_2O$ solution, drop by drop, into 50 ml of a 20 mM NaOH solution with vigorous stirring. Subsequently, 25 ml of a 10 mM ascorbic acid solution was added dropwise while continuously stirring the mixture for 1 hour at room temperature. As a result of the reduction facilitated by sodium hydroxide and ascorbic acid, the solution underwent a color change and formed a yellow precipitate containing copper oxide nanoparticles. The particles were then separated by filtration and subjected to thorough washing with distilled water and acetone. Finally, the washed nanoparticles were left to dry naturally at room temperature for 24 h. Distilled water served as the solvent for the preparation of the solution used in the synthesis process [11].

2.3 PVA Doping with Sol-Gel Technique

To incorporate the copper oxide nanoparticles into the polymer matrix, a sol-gel process was employed. The first step involved preparing a 5% solution of polyvinyl alcohol (PVA) by stirring it for 3 h at 60 °C and subsequently allowing it to cool down to room temperature. Once the PVA solution was prepared, the previously synthesized CuO nanoparticles were added to it. During this addition, a magnetic stirrer was used to ensure rapid and continuous stirring, preventing the nanoparticles from aggregating or clumping together. This process resulted in the formation of a CuO nanoparticle sol that was effectively incorporated within the PVA matrix. Fig. 1 represents the complete flow for the preparation of copper oxide nanoparticle sol.

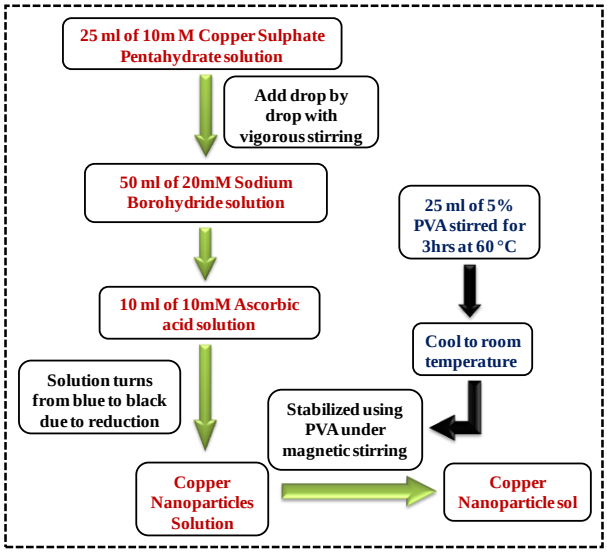


Fig. 1 Flowchart for Copper oxide nanoparticle doped PVA Sol preparation.

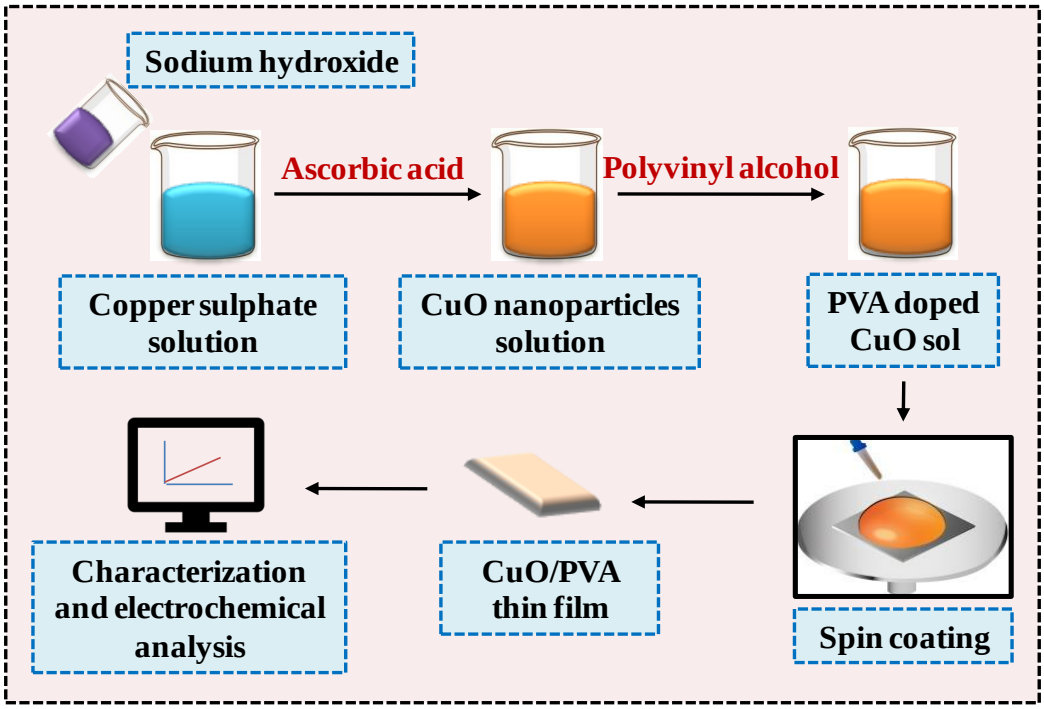


Fig. 2 Schematic representation for preparation of CuO NPs/PVA thin film.

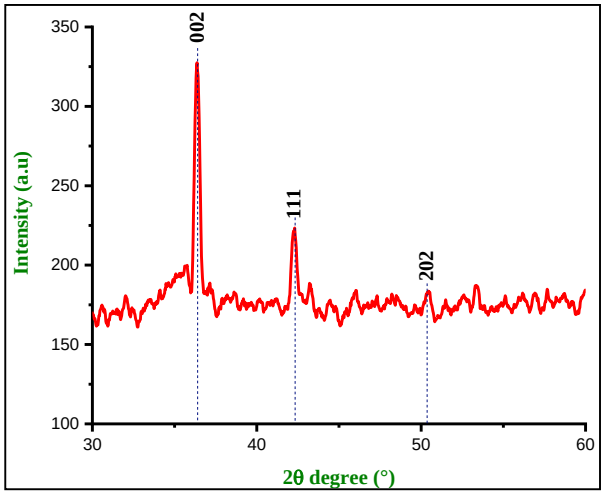


Fig. 3 X-ray diffraction pattern for CuO NPs/PVA thin film.

2.4 Electrode Fabrication

The CuO NPs thin films were deposited onto glass substrates via a sol-gel/spin coating process. The glass slides were pre-treated with alumina slurry and washed with deionized water and acetone. The CuO NPs sol was deposited onto the glass slides using a spin coater at 2500 rpm for 30 s, followed by drying and annealing at different temperatures (100–400 °C) for 5 min. Fig. 2 represents the complete flow for the preparation of thin film CuO NPs working electrode.

3 Result and Discussion

The structural properties of the coated films were determined using a Phillips X'Pert Pro X-ray diffractometer with Cu Kα1 radiation (1.5406). The electrochemical measurements, specifically the cyclic voltammetry (CV) curve and the CV VS H_2O_2 concentration, were performed in a three-electrode cell system at room temperature. The platinum was used as the counter electrode, Ag/AgCl saturated with potassium chloride was used as the reference electrode, and the newly developed thin film CuO NPs/PVA slide acted as the working electrode, with a diameter of 3mm. The Wireless potentiostat was used for the electrochemical measurements.

3.1 Materials Characterization

The crystal structure was identified with the aid of XRD analysis, which allowed for the detection of diffraction peaks in the copper oxide. The diffraction peaks at 2θ = 36.36°, 42.18°, and 50.91° (JCPDS 45-0937) were attributed to the (002), (111), and (202) crystallographic planes of the CuO monoclinic crystal structure, as shown in Fig. 3. These diffraction peaks were found to be responsible for the characteristic pattern of the copper oxide, confirming the crystalline nature of the copper nanostructures that were present in PVP.

The mean size of the nanoparticles was determined using the Scherrer formula based on the high-resolution X-ray diffraction peaks. The Scherrer formula is a mathematical equation that relates the size of crystalline domains to the width of X-ray diffraction peaks. It can be expressed as follows in Eq. (1):

$$\tau = \frac{K\lambda}{\beta cos\theta} \quad (1)$$

In Eq. (1), τ represents the mean size of the ordered (crystalline) domains, K is a dimensionless shape factor (approximately unity), λ is the X-ray wavelength, β is the line broadening at half the maximum intensity (full width at half maximum, FWHM, in radians) represented as 2θ, and θ is the Bragg angle. By performing the calculations using the Scherrer formula, the average size of the nanoparticles was determined to be approximately 19.72 nm.

3.2 Electrochemical Analysis of H_2O_2

3.2.1 Mechanism of Interaction

Despite the distinct morphological properties of copper oxide (CuO), it is capable of forming a compound with the polymer polyvinyl alcohol (PVA). Fig. 4 illustrates that the hydroxyl group present in PVA interacts with the oxygen atoms of CuO nanoparticles, leading to the formation of CuO-doped PVA through hydrogen bonding. This interaction between the polymer and nanoparticles allows for their integration at a molecular level. However, when a reactive species such as hydrogen peroxide (H_2O_2) comes into contact with the surface of CuO, it serves as a redox carrier and facilitates a chemical reduction process. This interaction with H_2O_2 can lead to changes in the properties or behavior of the CuO nanoparticles, potentially impacting their functionality or reactivity in certain applications. This electroreduction generates free electrons, corresponding to the concentration of H_2O_2.

When hydrogen peroxide (H_2O_2) molecules come into contact with the electrode surface, they undergo a reaction where they release $2H^+ + 2e^-$ ions. This process is accompanied by the production of an electric current when a potential is applied to the electrode. Fig. 5 depicts a schematic representation of this electrochemical process. By measuring the resulting current value, it is possible to estimate the quantity or concentration of H_2O_2 present in the sample.

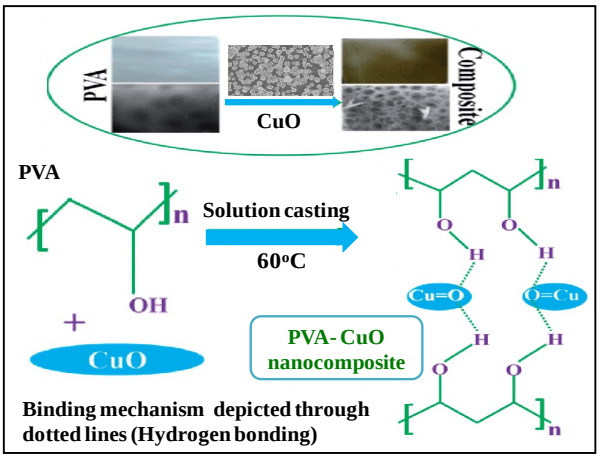


Fig. 4 Reaction mechanism between CuO and PVA [12].

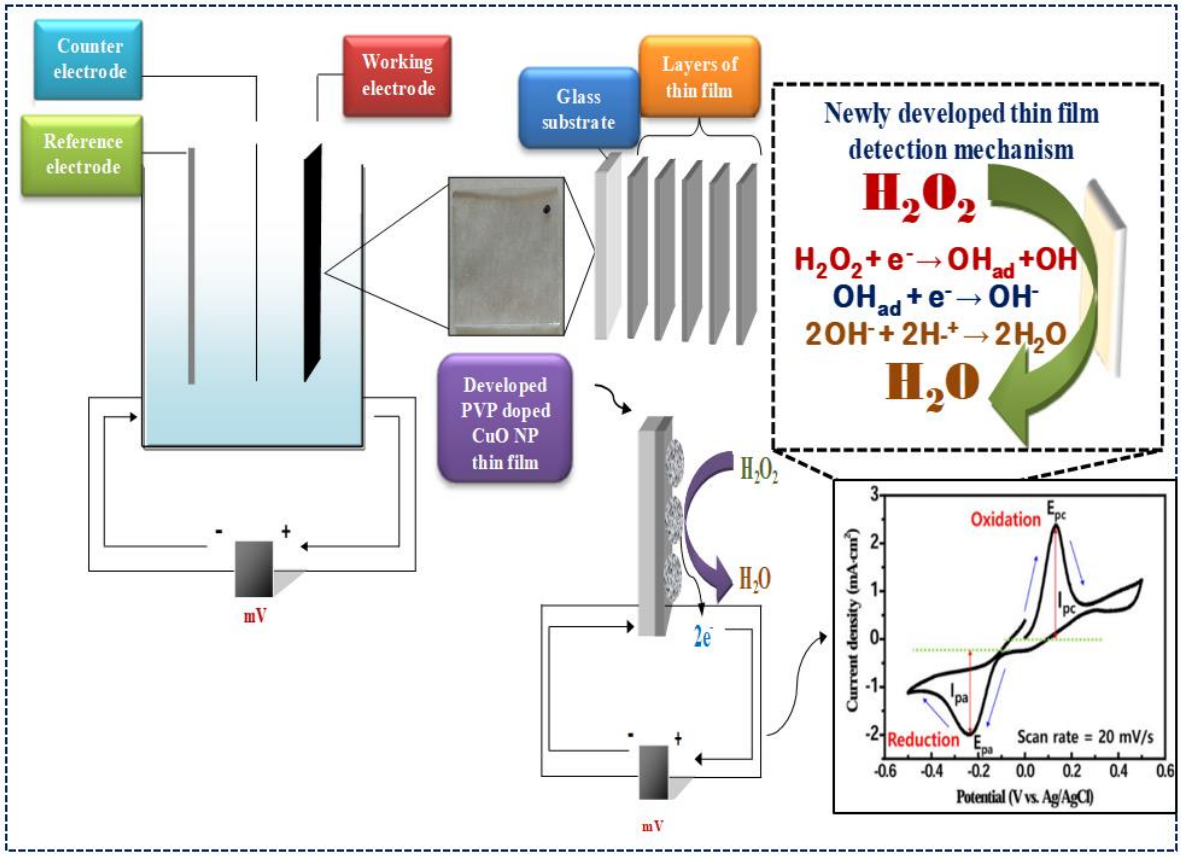


Fig. 5 Schematic representation of the working mechanism of developed CuO NPs/PVA thin film.

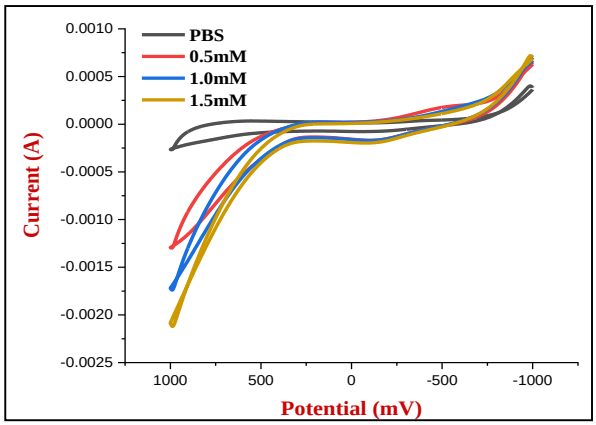


Fig. 6 Cyclic Voltammogram of H_2O_2 in CuO NPs/PVA thin film electrode at different concentrations with 500 mV/sec scan rate.

This mechanism forms the basis for the development of electrochemical sensors specifically designed for the detection and quantification of H_2O_2. These sensors utilize the electrochemical response generated by the interaction between H_2O_2 and the electrode surface to provide a means of detecting and measuring H_2O_2 levels in various applications.

3.2.2 *Different Concentration*

Cyclic Voltammetric measurements were performed on a CuO-doped PVA thin film working electrode in 10 mM PBS (pH 7.4) with 0.5 mM to 1.5 mM H_2O_2. The newly generated CuO NPs doped PVA thin film electrode displayed a significant response in reduction current. Prior to this, the CV results were obtained for the PBS solution without H_2O_2 for comparison. The cathodic peak observed between −0.4 to 0.2 V confirmed the electrocatalytic behavior of the thin film in H_2O_2 electroreduction. Fig. 6 displays the CVs of a CuO thin film electrode for varying concentrations of H_2O_2 in 10 mM PBS (pH 7.4) with a 500 mV/sec scan rate. The results reveal that the catalytic reduction current increased with increasing H_2O_2 concentrations (0.5−1.5 mM), indicating that the sensor is suitable for quantitative analysis.

3.2.3 *Different Scan Rate*

Fig. 7 illustrates the cyclic voltammograms (CVs) obtained from a CuO-doped PVA thin film electrode in 10 mM phosphate-buffered saline (PBS) with a pH of 7.4 and 1.0 mM hydrogen peroxide (H_2O_2) at 500 mV/sec scan rate. The cathodic reduction current of H_2O_2 exhibits a linear correlation with the square root of the scan rate. This suggests that the electron transfer reaction at the thin film electrode surface is diffusion-controlled. In other words, the rate of the electron transfer reaction is limited by the diffusion of H_2O_2 to the electrode surface. As the scan rate increases, the diffusion layer thickness decreases, allowing more H_2O_2 molecules to access the electrode surface, leading to a higher reduction current. This linear relationship between the reduction current and the square root of the scan rate agrees with the Randles-Sevcik equation, which describes the behavior of electrochemical systems under diffusion-controlled conditions. The Randles-Sevcik equation is an empirical relationship used in electrochemistry to describe the behavior of a reversible redox reaction at an electrode surface. It relates the peak current of a cyclic voltammogram to the concentration of the electroactive species, the scan rate, and the electrochemical properties of the system.

The Eq. (2) is expressed as:

$$i_p = (2.69 \times 10^5) n_2^3 AC(Dv)_2^1, \qquad (2)$$

where i_p is the peak current (in A), n is the number of electrons involved in the redox reaction, A is the electrode surface area (in cm^2), D is the diffusion coefficient of the electroactive species (in $cm^{2/s}$), C is the concentration of the electroactive species (in mol/cm^3), and v is the scan rate (in V/s).

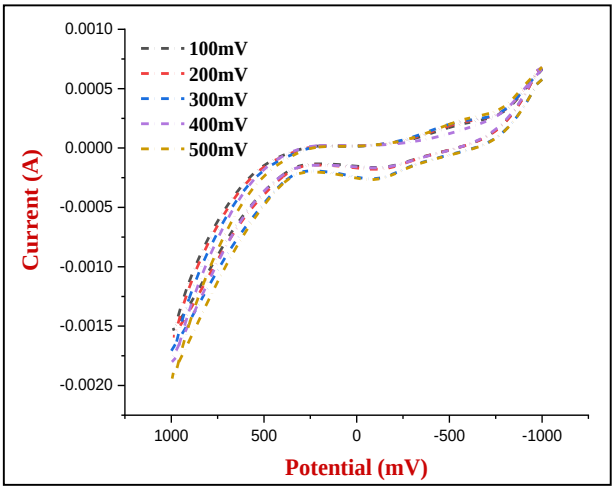


Fig. 7 Cyclic Voltammogram of H_2O_2 at different scan rates with 1.0 mM concentration.

3.2.4 *Effect of Annealing Temperature*

To investigate the impact of annealing temperature on the performance of the CuO-doped PVA thin film electrode, a series of thin films were prepared and subjected to annealing at different temperatures ranging from 100 °C to 400 °C. The cyclic voltammograms of these films were recorded and subjected to analysis. The outcomes, as shown in Fig. 8, indicate that an increase in annealing temperature resulted in a corresponding increase in current within the current-voltage response curve. This observation can be attributed to the heightened reactivity between CuO nanoparticles and H_2O_2 molecules, facilitated by the greater surface area of the CuO agglomerates formed at higher annealing temperatures. The enhanced reactivity leads to increased current generation during the electrochemical reaction. These findings are consistent with prior research [13−15], which has demonstrated the influence of annealing on the structural and morphological properties of thin films,

subsequently affecting their electrochemical behavior. By optimizing the annealing temperature, it becomes possible to customize the performance of the thin film electrode to meet specific application requirements. These results have significant implications for the advancement of electrochemical sensors that aim to achieve sensitive and selective detection of H_2O_2.

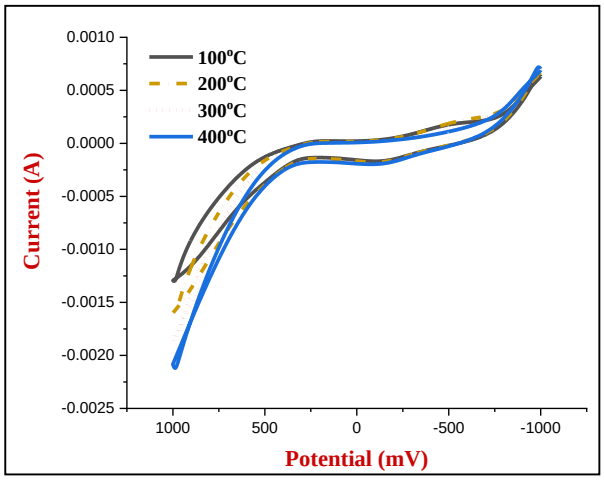


Fig. 8 Cyclic Voltammogram of H_2O_2 with CuO NPs/PVA thin films annealed at various temperatures.

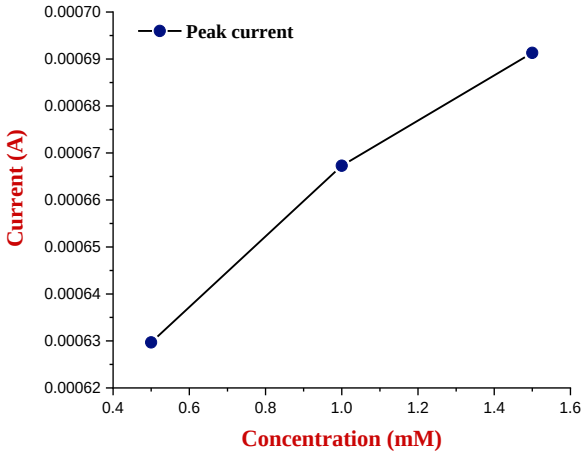


Fig. 9 Peak current density VS H_2O_2 concentration.

Table 1 Parameters for intercept and R-Square calculation.

Equation	y = a + b × x
Plot	B
Weight	No Weighting
Intercept	6.01167E−4 ± 8.48109E−6
Slope	6.16E−5 ± 7.85196E−6
Residual Sum of Squares	3.08267E−11
Pearson's r	0.99197
R-Square (COD)	0.98401

3.2.5 *Sensitivity and Detection Limit*

To assess the analytical effectiveness of a CuO-doped PVA thin film, a series of amperometric tests were carried out using known concentrations of H_2O_2 in a 10 mM PBS (pH 7.4) solution. The scan rate of 500 mV/sec was utilized, and standard solutions of H_2O_2 were added in successive amounts to generate a calibration curve. The linear range of the calibration curve was found to be 0.5 mM to 1.5 mM, and the corresponding peak current was determined. The resulting peak current for each concentration of H_2O_2 was plotted in Fig. 9. The relative sensitivity of the proposed sensor was found to be approximately 0.002 $mA{\cdot}mM^{-1}cm^{-2}$. The limit of detection (LOD) was calculated using the 3S/k approach [16] and was determined to be 0.78 mM. Overall, the results demonstrate that the CuO NPs/PVA thin film provides great performance in detecting H_2O_2 and acts as a prominent sensor for this application.

3.2.6 *Stability and Reproducibility*

Another requirement that a sensor must meet is long-term storage stability, which has been examined for theCuO-doped PVA thin film produced and tested in mM H_2O_2. The modified electrode was stored at room temperature when not in use. Results showed that after two weeks of storage, the electrode retained 96% of its initial reaction, as previously reported, and after a month, it could still sustain 98% of its original current. No reaction was detected over a longer period, indicating the high durability and stability of the newly developed electrode.

The reproducibility of the electrode was evaluated by measuring responses to 1.0 mM H_2O_2 solution for 20 successive measurements, which demonstrated peak currents at ±0.067 mA, as shown in Fig. 10. These results confirm the electrode's long-term stability, durability, and reproducibility.

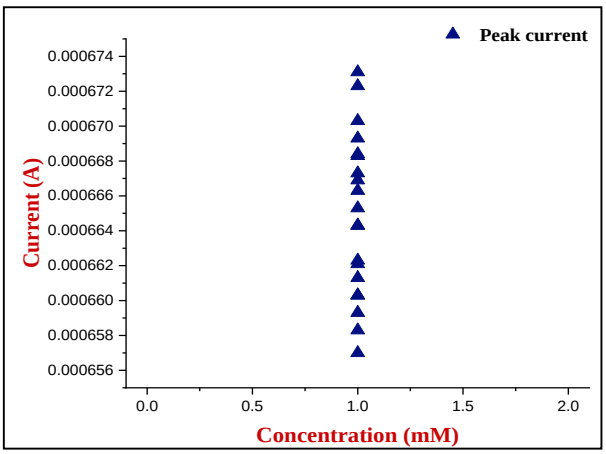


Fig. 10 Peak current VS 1.0 mM H_2O_2 concentration for 20 successive measurements.

4 Conclusion

In summary, a CuO nanostructure-based thin film was successfully synthesized using a reduction method without any additives, and it was incorporated into PVA for the detection of H_2O_2. The electrochemical properties of this material were thoroughly investigated. The analysis revealed that the morphology of the CuO nanostructures primarily depended on the initial amount of $CuSO_4$. The resulting CuO nanoparticle-doped PVA thin film demonstrated effective non-enzymatic detection of H_2O_2. The modified glass electrode with cubic CuO nanoparticles displayed outstanding catalytic performance towards H_2O_2, exhibiting high sensitivity ($0.002\ mA{\cdot}mM^{-1}cm^{-2}$), rapid response, relatively low detection limit, good stability, and favorable selectivity. Consequently, this electrode holds great promise for sensing applications due to its advantageous features and ease of production.

Acknowledgment

This work is supported by DST-SERB, New Delhi, Project File number: EEQ/2021/000467EEQ.

Disclosures

The authors declare no conflict of interest.

References

1. M. Shafa, I. Ahmad, S. Hussain, M. Asif, Yi Pan, R. Zairov, A. A. Alothman, M. Ouladsmane, Z. Ullah, N. Ullah, C. Lai, and U. Jabeen, "Ag-Cu nanoalloys: An electrochemical sensor for H2O2 detection," Surfaces and Interfaces 36, 102616 (2023).
2. N. Amini, B. Rashidzadeh, N. Amanollahi, A. Maleki, J. K. Yang, and S. M. Lee, "Application of an electrochemical sensor using copper oxide nanoparticles/polyalizarin yellow R nanocomposite for hydrogen peroxide," Environmental Science and Pollution Research 28, 38809–38816 (2021).
3. G. He, F. Gao, W. Li, P. Li, X. Zhang, H. Yin, B. Yang, Y. Liu, and S. Zhang, "Electrochemical sensing of H_2O_2 released from living cells based on AuPd alloy-modified PDA nanotubes," Analytical Methods 11(12), 1651–1656 (2019).
4. J. S. Kumar, S. Ghosh, N. C. Murmu, N. Mandal, and T. Kuila, "Electrochemical detection of H_2O_2 using copper oxide-reduced graphene oxide heterostructure," Journal of Nanoscience and Nanotechnology 19(8), 5295–5302 (2019).
5. P. Parthasarathy, "Synthesis and UV detection characteristics of TiO_2 thin film prepared through sol gel route," IOP Conference Series: Materials Science and Engineering 360, 012056 (2018).
6. P. Parthasarathy, S. Vivekanandan, "Investigation on uric acid biosensor model for enzyme layer thickness for the application of arthritis disease diagnosis," Health Information Science and Systems 6, 5 (2018).
7. P. Panchatcharam, "Synthesis and Characterization of CoO-ZnO-Based Nanocomposites for Gas-Sensing Applications," Chapter 5 in Multilayer Thin Films - Versatile Applications for Materials Engineering, S. Basu (Ed.), IntechOpen, London, UK (2020). ISBN: 978-1-83968-463-0.
8. A. A. Mathew, P. Parthasarathy, and S. Vivekanandan, "Development of Copper Nanoparticles from E-waste for Biomedical Applications," in Advances in Automation, Signal Processing, Instrumentation, and Control Select Proceedings of i-CASIC 2020. Lecture Notes in Electrical Engineering, V. L. N. Komanapalli, N Sivakumaran, and S Hampannavar (Eds.), Springer, Singapore, 703–715 (2021).
9. P. Gao, D. Liu, "Facile synthesis of copper oxide nanostructures and their application in non-enzymatic hydrogen peroxide sensing," Sensors and Actuators B: Chemical 208, 346–354 (2015).
10. P. Parthasarathy, S. Vivekanandan, "A comprehensive review on thin film-based nano-biosensor for uric acid determination: arthritis diagnosis," World Review of Science, Technology and Sustainable Development 14, 52–71 (2018).
11. M. A. Bhosale, S. C. Karekar, and B. M. Bhanage, "Room temperature synthesis of copper oxide nanoparticles: morphological evaluation and their catalytic applications for degradation of dyes and C–N bond formation reaction," ChemistrySelect 1(19), 6297–6307 (2016).
12. K. K. Dey, P. Kumar, R. R. Yadav, A. Dhar, and A. K. Srivastava, "CuO nanoellipsoids for superior physicochemical response of biodegradable PVA," RSC Advances 4, 10123–10132 (2014).
13. A. Muthumariappan, K. Sakthivel, S. M. Chen, T.-W. Chen, M. Govindasamy, and B.-S. Lou, "Effects of annealing temperature on crystal structure and glucose sensing properties of cuprous oxide," Sensors and Actuators B: Chemical 266, 655–663 (2018).
14. P. Parthasarathy, S. Vivekanandan, "Biocompatible TiO_2-CeO_2 nano-composite synthesis, characterization and analysis on electrochemical performance for uric acid determination," Ain Shams Engineering Journal 11, 777–785 (2020).
15. P. Parthasarathy, S. Vivekanandan, "Structural, optical and electrochemical response studies of TiO_2–ZrO_2 nanocomposite for uric acid detection," in 2019 Innovations in Power and Advanced Computing Technologies, Vellore, India, 1–6 (2019).

16. E. Gričar, K. Kalcher, B. Genorio, and M. Kolar, "Highly Sensitive Amperometric Detection of Hydrogen Peroxide in Saliva Based on N-Doped Graphene Nanoribbons and MnO_2 Modified Carbon Paste Electrodes," Sensors 21(24), 8301 (2021).

Concentration Dependent Thermal Diffusivity of Mn_3O_4 Nanoparticles Using Dual Beam Thermal Lens Technique

Jayaprasad K. V.*, Titu Thomas, Manu Vaishakh, and Sheenu Thomas
International School of Photonics, Cochin University of Science and Technology, Cochin 682022, India

***e-mail:** jayaprasad14@cusat.ac.in

Abstract. Concentration dependent thermal diffusivity measurement of Mn_3O_4 nanoparticles dispersed in ethylene glycol has been studied using dual beam mode mismatched thermal lens technique. The results reveal that the thermal diffusivity of the nanofluid depends on the concentration of Mn_3O_4 nanoparticles. The thermal diffusivity values were found to be greater than that of ethylene glycol for all sample concentrations. The samples with this high value of thermal diffusivity can be used as coolant for thermoelectric devices. The non-radiative decay process induced by defect states in the material, size and shape of nanoparticles etc. are the factors that control the thermal diffusivity of the nanoparticles dispersed in a solvent. The variation in thermal diffusivity of the Mn_3O_4 nanofluid is explained on the basis of changes in absorption and emission spectra with sample concentration. It is found that thermal diffusivity is inversely related with the emission intensity.
© 2023 Journal of Biomedical Photonics & Engineering.

Keywords: Mn_3O_4 nanoparticles; thermal diffusivity; coolant.

Paper #7784 received 25 Feb 2023; revised manuscript received 15 Jul 2023; accepted for publication 17 Jul 2023; published online 28 Aug 2023. doi: 10.18287/JBPE23.09.030310.

1 Introduction

Metal oxide nanoparticles are extremely exciting semiconducting materials which has wide range of application as energy storage material [1], semiconductor [2], insulator [3], catalyst [4], etc. Among the various metal oxide nanoparticles, Mn_3O_4 (trimanganese tetraoxide, hausmannite) is one of the most stable manganese oxides having spinel structure and special electronic configuration [5]. Compared to other forms of manganese oxide crystals, Mn_3O_4 has the advantage of low cost, non-toxicity and environmentally friendliness which find applications in various fields like biosensor, water treatment, cancer treatment, drug delivery, etc. [6–8].

The suitability of a material in various thermoelectric applications such as coolant, thermal insulators is determined by the thermal conductivity of the material. The various models proposed for the determination of thermal conductivity are Maxwell model, Hamilton-Crosser model, Yu-Choi model, Xue model, Strauss-Pober model, etc. [9–13]. In many of the proposed models, the experimental values are seen to be much deviated from the theoretical values. The measurement of thermal diffusivity (D) helps to determine thermal conductivity (k) as they are related by $D = \frac{k}{\rho C_P}$ where where ρ is the fluid density and C_p is the specific heat capacity [14]. Thermal diffusivity is the ability of a material to respond to change in thermal environment. Material with large thermal diffusivity takes less time to reach a new equilibrium condition whereas those with smaller thermal diffusivity will react slowly to change in temperature. The concentration dependent thermal diffusivity behaviour of materials is particularly important in the nanoscale region as the large surface area of the nanoparticles particularly enhances the heat transfer capacity. In addition, these particles do not settle in fluid as compared to micro sized particles.

Several techniques such as laser flash, hot-wire, photoacoustic, thermal-wave cavity, temperature oscillation, etc. have been developed to measure the thermal diffusivity of materials [15–19]. The laser flash technique is a standard technique for the determination of thermal diffusivity of solid samples. However, the necessity of accurate sample geometric requirements is the main limitation of this technique [15]. The need for precise recording of the temperature rise of the wire is the limiting factor of hot wire method [16]. Sufficient photoacoustic signal can be obtained in photoacoustic

This paper was presented at the International Conference on Nanoscience and Photonics for Medical Applications – ICNPMA, Manipal, India, December 28–30, 2022.

method only if the thickness of the sample is of the order of few tenth of millimetres [17]. In thermal wave cavity technique, measurement of thermal wavelength should be done at low modulation frequencies. Sensor sensitivity, noise, etc. limit the use of lower modulation frequencies in this technique [18]. The thermocouples should be located in isothermal planes in temperature oscillation technique to minimize the measurement uncertainty [19]. Compared to the above mentioned methods for thermal diffusivity measurement, thermal-lens (TL) technique is an accurate and sensitive method for thermal diffusivity measurement. The determination of dn/dt in this method includes information regarding thermal expansion coefficient, refractive index, polarizability of the material [20–25]. The basic principle in this technique involves the modification in the refractive index of a liquid by the passage of laser beam and it is a direct indication of non-radiative relaxation process. In the present work, we have studied the concentration dependent thermal nonlinearity of the Mn_3O_4 nanoparticles using dual beam thermal lens technique.

2 Theory

When laser beam passes through a sample, the atoms gets excited to higher energy levels from where they come back to lower energy levels by two ways. One way is by emitting light of higher wavelength than the absorbed light and is called radiative relaxation. Other way is to dissipate the absorbed energy as heat called the non-radiative relaxation. The non-radiative relaxation process causes heating of the material. If the beam is Gaussian, maximum heating will be along the beam axis resulting in temperature and refractive index variation in the sample. The refractive index gradient is produced perpendicular to the axis of the beam depending on temperature gradient. The expansion of liquids on heating causes the refractive index gradient to be negative resulting in the formation of concave lens in the sample [26].

In thermal lens technique, the generated lensing effect by the pump beam is analysed by the passage of another beam called probe beam through the sample. The variation in the intensity of probe beam as a function of time is given by Ref. [27]:

$$I(t) = I_0 \cdot \cdot \left[1 - \frac{\theta}{2} tan^{-1}\left(\frac{2mV}{((1+2m)^2+V^2)\frac{t_c}{2t}+1+2m+V^2}\right)\right]^2, \quad (1)$$

$$m = \left(\frac{\omega_{1p}}{\omega_e}\right)^2, \quad (2)$$

$$V = V' + \frac{Z_c}{Z_2}(V'^2 + 1), \quad (3)$$

$$V' = \frac{Z_1}{Z_c}, \quad (4)$$

$$Z_c = \frac{\pi \omega_{0p}{}^2}{\lambda_p}, \quad (5)$$

$$\omega_{1p} = \omega_{0p}{}^2(1 + V'^2), \quad (6)$$

$$\omega_e = \frac{f\lambda_e}{D}, \quad (7)$$

where ω_e and ω_{0p} are the beam waist of the pump and probe beam respectively, ω_{1p} is the radius of probe beam in the sample, Z_1, Z_2, Z_c are the distance between beam waist of the pump and probe beam, distance of the detector from the sample and rayleigh range of the probe beam respectively, f is the focal length of the lens, and D is the spot size of the laser beam.

The parameters θ and t_c can be estimated by theoretically fitting Eq. (1) to the experimental data, t_c is the characteristic thermal time constant associated with thermal diffusion in the sample. From the value of t_c, thermal diffusivity D can be calculated using

$$D = \frac{\omega_e{}^2}{4t_c}. \quad (8)$$

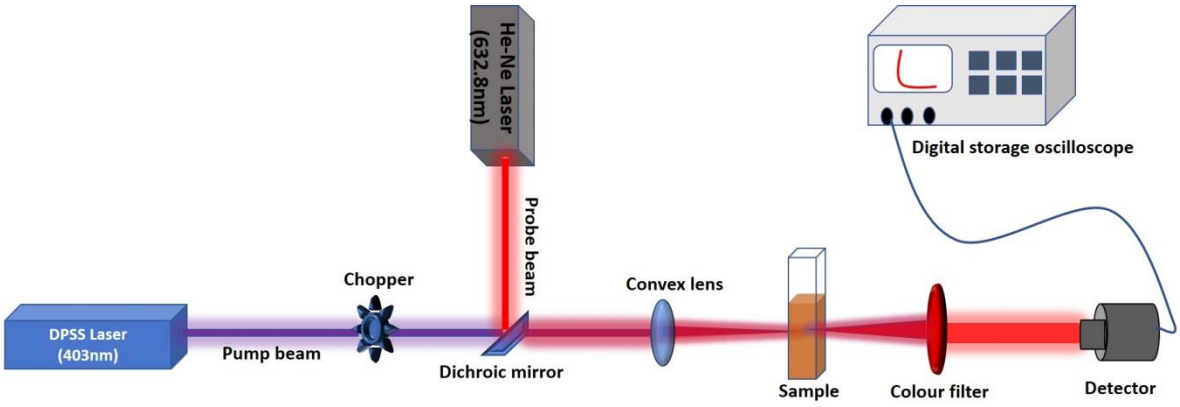


Fig. 1 Dual beam thermal lens setup.

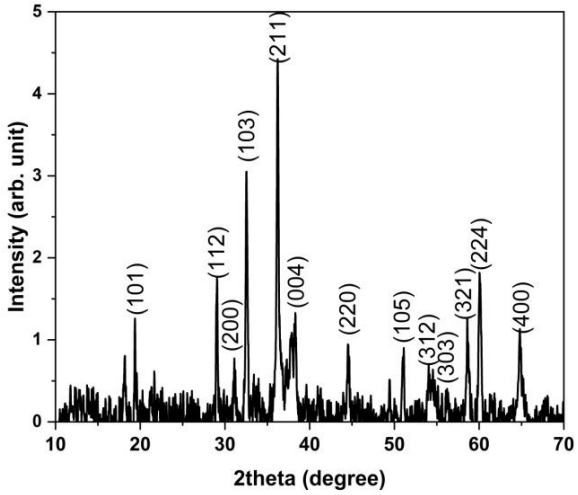


Fig. 2 XRD pattern of synthesized Mn_3O_4 nanoparticles.

3 Preparation of Mn_3O_4 Nanoparticles

Potassium permanganate ($KMnO_4$) and L-cysteine are the precursors used for the preparation of Mn_3O_4 nanoparticles. 0.5 gm of $KMnO_4$ was dissolved in 60 mL of distilled water under constant stirring and 0.2 gm of L-cysteine was introduced into the above solution. After stirring at 60 ºC for 1 h, a brown precipitate was formed. The precipitate was collected and washed several times with distilled water in order to remove excess impurities. Finally, the residue is dried at 70 ºC for 12 h in a hot air oven [28].

4 Experimentation

The schematic diagram of the thermal lens setup is shown in Fig. 1. The sample is pumped using a Diode pumped Solid State laser (VORTRAN Stradus TM 405) operating at 403 nm with a maximum power of 100 mW. The detection of thermal lens signal is achieved by making use of a 4 mW CW He-Ne laser (JDS Uniphase) at 632.8 nm wavelength. Both pump and probe beams are aligned in a collinear configuration. The chopping frequency is fixed at 3 Hz for all measurements. As the unmodulated probe beam passes through the irradiated region, a diverging lens effect and thermal blooming occurs. The change in probe beam intensity is measured using a photo detector-DSO system.

The structure of Mn_3O_4 nanoparticles was investigated by Bruker AXS D8 Advances X-ray diffraction (XRD) technique using Cu K_α radiation ($\lambda = 1.54056\ A^0$). The morphology of the nanoparticles was analysed using JEOL JEM-2100 transmission electron microscopy (TEM). Absorption and emission spectra were measured using JASCO V-770UV-vis-NIR spectrophotometer and Carry Eclipse Varian spectrophotometer respectively.

5 Results and Discussion

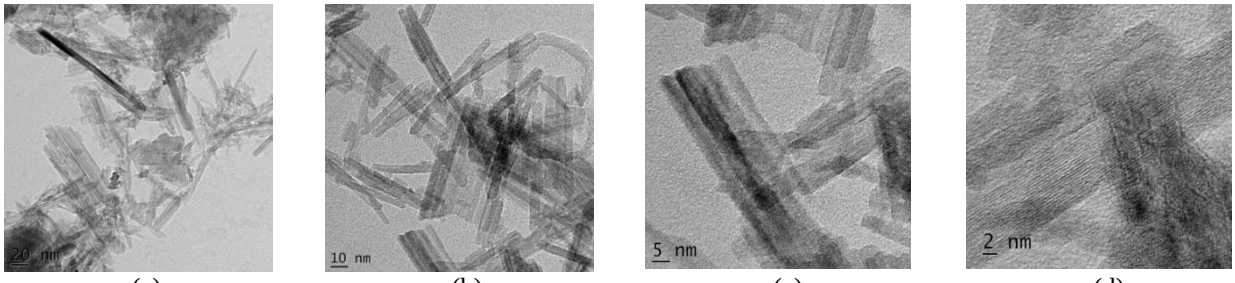
Fig. 2 shows the XRD pattern of the synthesized Mn_3O_4 nanoparticles. The formation of tetragonal Mn_3O_4 nanoparticles (hausmannite) was confirmed by indexing diffraction planes (101), (112), (200), (103), (211), (004), (220), (204), (105), (312), (303), (321), (224), (400), (305) and (413) (JCPDS file number 01-080-0382). No additional peaks of other phases had been detected in the XRD, indicating high purity and good crystallinity of Mn_3O_4 nanoparticles. The morphology of the synthesized nanoparticles analysed using TEM is shown in Fig. 3 which indicates the formation of Mn_3O_4 nanorods.

The optical absorption spectrum of Mn_3O_4 dispersed in ethylene glycol is shown in Fig. 4(a) and the emission spectrum is shown in Fig. 4(b). The electronic absorption spectrum of Mn_3O_4 is broad. Defects in the crystal structure create defect states to which electrons in the valance band can be excited to the conduction band [29]. The emissions peaks in the visible light region are due to the electronic transitions from the defects states in the crystal.

The calculated values of thermal diffusivity and the corresponding t_c for all the samples are tabulated in Table 1.

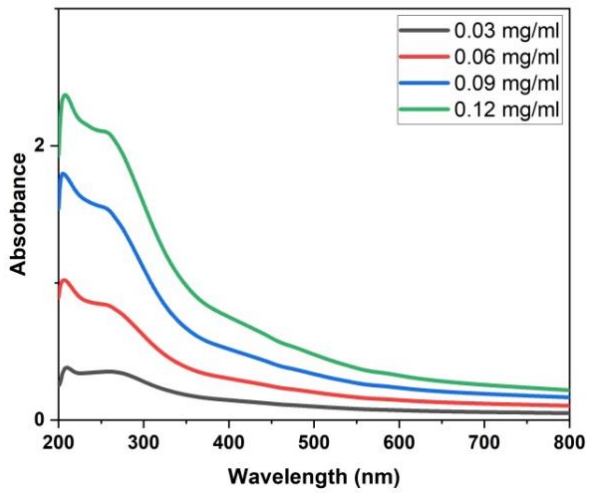
Table 1 Thermal diffusivity of samples for 403 nm excitation.

Sample concentration, (mg/ml)	***t*$_c$, (s)**	***D*, ($\times 10^{-7}$ m^2/s)**
0.03	0.0046	7.88
0.06	0.0113	3.24
0.09	0.0156	2.37
0.12	0.0217	1.70
0.18	0.0042	8.77
0.21	0.0022	16.5

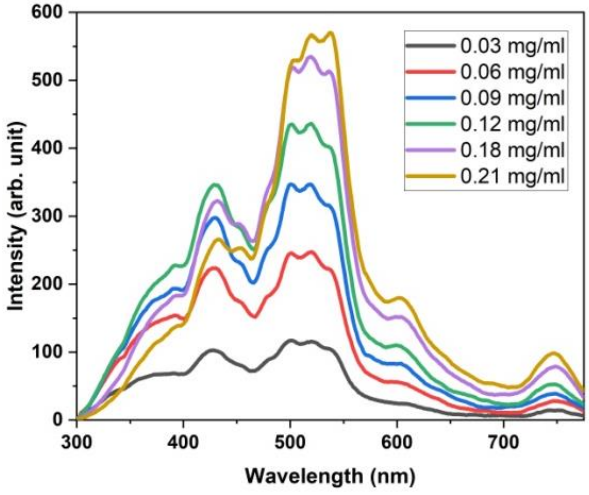


(a) (b) (c) (d)

Fig. 3 TEM images of the synthesized Mn_3O_4 nanoparticles with scale bars: (a) 20 nm, (b) 10 nm, (c) 5 nm, and (d) 2 nm.



(a)



(b)

Fig. 4 (a) Absorption spectra and (b) emission spectra of the Mn_3O_4 nanoparticles.

Thermal diffusivity as a function of sample concentration is shown in Fig. 5. The thermal diffusivity decreases with increase in sample concentration and reaches a minimum value at 0.12 mg/ml. After the optimum concentration, thermal diffusivity increases with increase in sample concentration. For all concentrations, the thermal diffusivity of nanofluid is higher than that of base fluid. The reported value of thermal diffusivity of ethylene glycol is 0.938×10^{-7} m^2/s [30–32]. Thus the addition of Mn_3O_4 nanoparticles significantly enhances the thermal diffusivity of base fluid and it can be varied by adjusting the concentration of nanoparticles. The thermal response of the sample with concentration 0.03 mg/ml, 0.09 mg/ml, and 0.12 mg/ml is shown in Fig. 6. The dotted curve shows the experimental data and solid curve shows the experimental fit.

The incorporation of nanoparticles into a liquid results in the formation of nanolayers which increases the phonon scattering and thereby enhancing the thermal diffusivity. The increase in concentration increases the number of particles per unit volume thereby increasing the interaction between the particles and reducing the heat exchange between particles and surrounding medium. This causes the thermal diffusivity to decrease with increase in sample concentration [33–35]. The reduction in factors such as dispersion stability, Brownian velocity, convection velocity, etc. are the other factors contributing to the decrease in thermal diffusivity with increase sample concentration [36].

Thermal diffusivity is inversely related to specific heat capacity. The specific heat capacity of nanofluid is lower than that of base fluid as solids possesses lower specific heat capacity as compared to fluids [37]. Specific heat capacity is inversely related to sample concentration. The enhancement in thermal conductivity and reduction in specific heat capacity contribute to the enhancement of thermal diffusivity with sample concentration [38]. All the above mentioned factors dominate the factors decreasing the thermal diffusivity of the sample and cause the thermal diffusivity to increase after the optimum concentration.

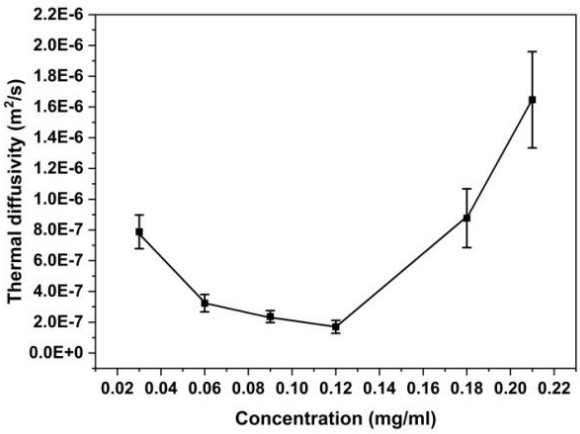


Fig. 5 Thermal diffusivity of Mn_3O_4 nanofluid with various concentrations.

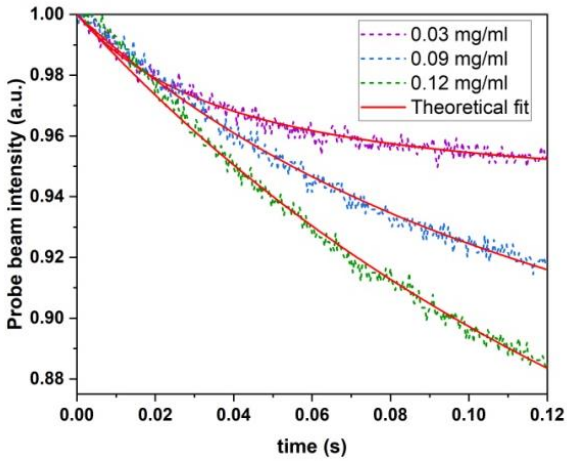


Fig. 6 Thermal response of Mn_3O_4 nanofluid.

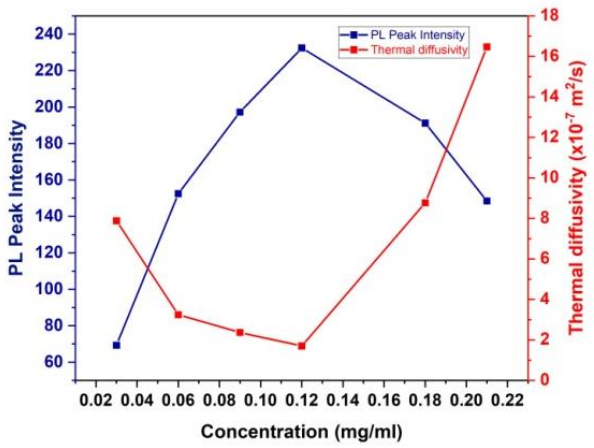


Fig. 7 Thermal diffusivity and PL intensity as a function of concentration.

The variation of thermal diffusivity and emission peak around 430 nm in the emission spectrum with sample concentration is shown in Fig. 7. It is a general fact that thermal diffusivity decreases with increase in emission intensity. This is due to the release of most of the absorbed energy in the form of radiative emission which reduces the non-radiative relaxation [36, 39]. Even though the dominant emission peak in the emission spectrum is around 530 nm, the relationship between thermal diffusivity and emission intensity is followed in the emission peak around 430 nm, the peak close to the excitation wavelength.

Thermophoretic motion, Brownian motion and osmophoretic motion are the most important mechanisms that affect the thermal conductivity of nanofluids [40]. The osmophoretic movement caused by the concentration difference is the main factor that controls the thermal diffusivity of samples at lower concentrations. Here, a decrease in the thermal diffusivity below 0.12 mg/ml results mainly from osmophoretic motion. After reaching an equilibrium state, Brownian motion plays an important role and increases the thermal diffusivity above 0.12 mg/ml [41].

6 Conclusion

The thermal diffusivity of Mn_3O_4 nanoparticles is measured using dual beam mode mismatched thermal lens technique. The thermal diffusivity is found to decrease with increase in sample concentration up to an optimum concentration and again increases with sample concentration. The correlation between the concentration and thermal diffusivity reveals that samples with desired thermal diffusivity for various applications can be obtained by adjusting the nanoparticles concentration. The obtained thermal diffusivity is higher than the thermal diffusivity of base fluid for all concentration. So the prepared nanoparticles can be used as coolant for thermoelectric devices.

Acknowledgments

Authors acknowledge Cochin University of Science and Technology for the financial support.

Disclosures

The authors declare no conflict of interest.

References

1. A. Dey, S. Hadavale, M. A. S. Khan, P. More, P. K. Khanna, A. K. Sikder, and S. Chattopadhyay, "Polymer based graphene/titanium dioxide nanocomposite (GTNC): an emerging and efficient thermoelectric material," Dalton Transactions 44(44), 19248–19255 (2015).
2. D. Finkelstein-Shapiro, P. Tarakeshwar, T. Rajh, and V. Mujica, "Photoinduced Kinetics of SERS in Bioinorganic Hybrid Systems. A Case Study: Dopamine− TiO2," The Journal of Physical Chemistry B 114(45), 14642–14645 (2010).
3. E. A. Cherney, "Silicone rubber dielectrics modified by inorganic fillers for outdoor high voltage insulation applications," IEEE Transactions on Dielectrics and Electrical Insulation 12(6), 1108–1115 (2005).
4. J. Li, G. Lu, G. Wu, D. Mao, Y. Guo, Y. Wang, and Y. Guo, "Effect of TiO2 crystal structure on the catalytic performance of Co3O 4/TiO2 catalyst for low-temperature CO oxidation," Catalysis Science & Technology 4(5), 1268–1275 (2014).
5. R. Bussamara, W. W. M. Melo, J. D. Scholten, P. Migowski, G. Marin, M. J. M. Zapata, G. Machado, S. R. Teixeira, M. A. Novak, and J. Dupont, "Controlled synthesis of Mn3O4 nanoparticles in ionic liquids," Dalton Transactions 42(40), 14473–14479 (2013).
6. S. Kumar, R. Kaur, R. Rajput, and M. Singh, "Bio pharmaceutics classification system (BCS) class IV drug nanoparticles: Quantum leap to improve their therapeutic index," Advanced Pharmaceutical Bulletin 8(4), 617 (2018).
7. L. Li, K. H. Seng, H. Liu, I. P. Nevirkovets, and Z. Guo, "Synthesis of Mn3O4-anchored graphene sheet nanocomposites via a facile, fast microwave hydrothermal method and their supercapacitive behavior," Electrochimica Acta 87, 801–808 (2013).

8. W.-N. Li, J. Yuan, X.-F. Shen, S. Gomez-Mower, L.-P. Xu, S. Sithambaram, M. Aindow, and S. L. Suib, "Hydrothermal synthesis of structure-and shape-controlled manganese oxide octahedral molecular sieve nanomaterials," Advanced Functional Materials 16(9), 1247–1253 (2006).
9. S. M. S. Murshed, C. A. N. de Castro, "Superior thermal features of carbon nanotubes-based nanofluids–A review," Renewable and Sustainable Energy Reviews 37, 155–167 (2014).
10. W. H. Azmi, K. V. Sharma, R. Mamat, G. Najafi, and M. S. Mohamad, "The enhancement of effective thermal conductivity and effective dynamic viscosity of nanofluids–A review," Renewable and Sustainable Energy Reviews 53, 1046–1058 (2016).
11. X.-Q. Wang, A. S. Mujumdar, "Heat transfer characteristics of nanofluids: a review," International Journal of Thermal Sciences 46(1), 1–19 (2007).
12. N. Sizochenko, M. Syzochenko, A. Gajewicz, J. Leszczynski, and T. Puzyn, "Predicting physical properties of nanofluids by computational modeling," The Journal of Physical Chemistry C 121(3), 1910–1917 (2017).
13. M. I. Pryazhnikov, A. V. Minakov, V. Ya. Rudyak, and D. V. Guzei, "Thermal conductivity measurements of nanofluids," International Journal of Heat and Mass Transfer 104, 1275–1282 (2017).
14. M. L. Baesso, J. Shen, and R. D. Snook, "Mode-mismatched thermal lens determination of temperature coefficient of optical path length in soda lime glass at different wavelengths," Journal of Applied Physics 75(8), 3732–3737 (1994).
15. F. Cernuschi, A. Figari, and L. Fabbri, "Thermal wave interferometry for measuring the thermal diffusivity of thin slabs," Journal of Materials Science 35, 5891–5897 (2000).
16. Y. Nagasaka, A. Nagashima, "Simultaneous measurement of the thermal conductivity and the thermal diffusivity of liquids by the transient hot-wire method," Review of Scientific Instruments 52(2), 229–232 (1981).
17. P. Charpentier, F. Lepoutre, and L. Bertrand, "Photoacoustic measurements of thermal diffusivity description of the "drum effect"," Journal of Applied Physics 53(1), 608–614 (1982).
18. J. A. Balderas-Lopez, A. Mandelis, "Simple, accurate, and precise measurements of thermal diffusivity in liquids using a thermal-wave cavity," Review of Scientific Instruments 72(6), 2649–2652 (2001).
19. W. Czarnetzki, W. Roetzel, "Temperature oscillation techniques for simultaneous measurement of thermal diffusivity and conductivity," International Journal of Thermophysics 16, 413–422 (1995).
20. J. H. Rohling, J. Mura, J. R. D. Pereira, A. J. Palangana, A. N. Medina, A. C. Bento, M. L. Baesso, and L. C. M. Miranda, "Thermal lens temperature scanning for quantitative measurements in complex fluids," Brazilian Journal of Physics 32(2b), 575–583 (2002).
21. A. Marcano, H. Cabrera, M. Guerra, R. A. Cruz, C. Jacinto, and T. Catunda, "Optimizing and calibrating a mode-mismatched thermal lens experiment for low absorption measurement," Journal of the Optical Society of America B 23(7), 1408–1413 (2006).
22. M. Franko, C. D. Tran, "Analytical thermal lens instrumentation," Review of Scientific Instruments 67(1), 1–18 (1996).
23. J. P. Gordon, R. C. C. Leite, R. S. Moore, S. P. S. Porto, and J. R. Whinnery, "Long-transient effects in lasers with inserted liquid samples," Journal of Applied Physics 36(1), 3–8 (1965).
24. M. A. Proskurnin, D. S. Volkov, T. A. Gor'kova, S. N. Bendrysheva, A. P. Smirnova, and D. A. Nedosekin, "Advances in thermal lens spectrometry," Journal of Analytical Chemistry 70, 249–276 (2015).
25. R. Silva, M. A. C. de Araújo, P. Jali, S. G. C. Moreira, P. Alcantara, Jr., and P. C. de Oliveira, "Thermal lens spectrometry: Optimizing amplitude and shortening the transient time," AIP Advances 1(2), 022154 (2011).
26. L. Thomas, J. John, N. A. George, and A. Kurian, "Silver nanoparticle assisted urine sugar determination using thermal lens spectroscopy," Measurement Science and Technology 25(11), 115701 (2014).
27. J. Shen, D. L. Roger, and R. D. Snook, "A model for cw laser induced mode-mismatched dual-beam thermal lens spectrometry," Chemical Physics 165(2–3), 385–396 (1992).
28. S. Prasanth, D. R. Raj, R. K. Thomas, T. V. Vineeshkumar, and C. Sudarsanakumar, "A systematic investigation on the interaction of l-cysteine functionalised Mn3O4 nanoparticles with lysozyme," RSC Advances 6(107), 105010–105020 (2016).
29. M. Perachiselvi, M. S. Bagavathy, J. J. Samraj, E. Pushpalaksmi, and G. Annadurai, "Synthesis and Characterization of Mn3O4 Nanoparticles for Biological Studies," Applied Ecology and Environmental Sciences 8(5), 273–277 (2020).
30. J. A. Balderas-Lopez, A. Mandelis, and J. A. Garcia, "Thermal-wave resonator cavity design and measurements of the thermal diffusivity of liquids," Review of Scientific Instruments 71(7), 2933–2937 (2000).
31. S. Delenclos, M. Chirtoc, A. H. Sahraoui, C. Kolinsky, and J. M. Buisine, "Assessment of calibration procedures for accurate determination of thermal parameters of liquids and their temperature dependence using the photopyroelectric method," Review of Scientific Instruments 73(7), 2773–2780 (2002).
32. L. Huang, L.-S. Liu, "Simultaneous determination of thermal conductivity and thermal diffusivity of food and agricultural materials using a transient plane-source method," Journal of Food Engineering 95(1), 179–185 (2009).

33. R. Herrera-Aquino, J. L. Jiménez-Pérez, D. C. Altamirano-Juárez, G. López-Gamboa, Z. N. Correa-Pacheco, and R. Carbajal-Valdéz, "Green synthesis of silver nanoparticles contained in centrifuged citrus oil and their thermal diffusivity study by using thermal lens technique," International Journal of Thermophysics 40, 3 (2019).
34. N. S. Basheer, B. R. Kumar, A. Kurian, and S. D. George, "Thermal conductivity measurement of organic solvents incorporated with silver nanoparticle using photothermal techniques," in IOP Conference Series: Materials Science and Engineering 73(1), 012039 (2015).
35. M. Ramya, T. K. Nideep, M. M. Varier, V. P. N. Nampoori, and M. Kailasnath, "Concentration dependent thermo-optic properties of yellow emissive ZnO quantum dots," Materials Research Express 6(12), 126208 (2019).
36. T. K. Nideep, M. Ramya, V. P. N. Nampoori, and M. Kailasnath, "The size dependent thermal diffusivity of water soluble CdTe quantum dots using dual beam thermal lens spectroscopy," Physica E: Low-dimensional Systems and Nanostructures 116, 113724 (2020).
37. V. M. Lenart, N. G. C. Astrath, R. F. Turchiello, G. F. Goya, and S. L. Gómez, "Thermal diffusivity of ferrofluids as a function of particle size determined using the mode-mismatched dual-beam thermal lens technique," Journal of Applied Physics 123(8), 085107 (2018).
38. J. John, L. Thomas, B. R. Kumar, A. Kurian, and S. D. George, "Shape dependent heat transport through green synthesized gold nanofluids," Journal of Physics D: Applied Physics 48(33), 335301 (2015).
39. V. Anupama, S. Udayan, P. N. Musfir, V. P. N. Nampoori, and S. Thomas, "Enhancement of defect states assisted thermal diffusivity in solution-processed GeSeSb chalcogenide glass matrix on silver incorporation," Journal of Non-Crystalline Solids 503–504, 151–157 (2019).
40. J. Koo, C. Kleinstreuer, "Impact analysis of nanoparticle motion mechanisms on the thermal conductivity of nanofluids," International Communications in Heat and Mass Transfer 32(9), 1111–1118 (2005).
41. M. Joseph, B. Anugop, K. R. Vijesh, Vipin Balan, V. P. N. Nampoori, and M. Kailasnath, "Morphology and concentration-dependent thermal diffusivity of biofunctionalized zinc oxide nanostructures using dual-beam thermal lens technique," Materials Letters 323, 132599 (2022).

Silver Anchored α-MnO_2 Nanorods Based SERS Substrates for Salivary Thiocyanate Detection and Application in Oral Cancer Diagnosis

Navami Sunil, Rajesh Unnathpadi, and Biji Pullithadathil*
Nanosensor Laboratory, PSG institute of Advanced Studies, Coimbatore 641004, India

***e-mail:** pbm@psgias.ac.in

Abstract. Salivary sensors are ideal non-invasive diagnostic platforms for cancer detection owing to the existence of many proteins and metabolites that can reflect individual's health status. Elevated levels of thiocyanate (SCN^-) in smokers' saliva may be a potential biomarker indicating increased oral cancer risk due to the nitrosation process. Herein, we report a highly sensitive, label-free, ultrasensitive surface-enhanced Raman spectroscopy (SERS) detection of salivary thiocyanate using silver anchored α-MnO_2 nanorods based SERS substrates for the early detection of oral cancer. The structural and morphological characterization of the synthesised Ag/ α-MnO_2 nanorods have been performed using XRD, FTIR, and TEM analysis. The intensity of SERS peak at around 2170 cm^{-1}, originating from the −C≡N stretching mode, indicated the concentrations of SCN^- ions. The SERS spectra of SCN^- was recorded at concentrations ranging from 1 to 6 mM, which was utilised to differentiate between smokers and non-smokers and hence to predict the risk of oral cancer. © 2023 Journal of Biomedical Photonics & Engineering.

Keywords: salivary sensors; non-invasive diagnosis; oral cancer; surface enhanced Raman spectroscopy; thiocyanate.

Paper #7203 received 21 Feb 2023; revised manuscript received 19 Apr 2023; accepted for publication 24 Jun 2023; published online 31 Aug 2023. doi: 10.18287/JBPE23.09.030311.

1 Introduction

Oral and oropharyngeal cancers are a diverse group of tumours that originate in the buccal mucosa, hard and soft palate, tongue, and oropharyngeal sub-sites such as the tonsils, posterior pharyngeal wall and tongue base. Oral cancer is the world's sixth most common cancer and is a major concern in Southeast Asia, owing to the prevalence of oral habits such as betel quid chewing, smoking, and alcohol consumption [1]. Tobacco use is linked to a variety of changes in the oral mucous membrane, ranging from benign and reversible lesions such as smoker's mouth to cancerous lesions from the palate to oral cancer. Saliva-based tests have several advantages, including ease of use, cost savings, non-invasiveness, and the ability to repeat sampling.

Thiocyanate (SCN) is a naturally occurring component of bodily fluids such as serum, saliva, urine, and tears which enters the human body through the consumption of Brassica vegetables, milk, and cheese. Thiocyanate, a significant cyanide metabolic by-product, is a key indicator of smoke inhalation along with carbon monoxide, nicotine, and cotinine. Its main sources in the human body are diet and tobacco and is secreted in saliva and has a half-life of 10−14 days [2]. Tobacco is known to suppress the immune system and is a well-known cause of adult periodontitis, leukoplakia and oral submucous fibrosis which have the potential for malignant transformation [3]. It is clear that smoking and oral cancer have a clear dose-response relationship. In normal non-smokers, salivary SCN^- concentrations range from 0.5 to 2 mM, with an average of 1 mM. Heavy smokers, on the other hand, may have salivary concentrations as high as 6 mM [4]. This elevated level of SCN in smokers' saliva may be responsible for the increased cancer risk of smokers due to the nitrosation process [5].

Although non-invasive quantitative assessment of the chemical compositions of saliva are possible through many methods such as ELISA, micro-satellite analysis,

This paper was presented at the International Conference on Nanoscience and Photonics for Medical Applications – ICNPMA, Manipal, India, December 28–30, 2022.

and high performance liquid chromatography (HPLC), mass spectrometry (MS) and can potentially detect these bio molecular changes, these highly specific techniques in molecular detection are typically labour-intensive procedures that require long analysis time. Raman spectroscopy-based spectral analysis of bio-fluids for disease diagnosis and screening may represent a potentially viable avenue for cancer diagnosis and is emerging as a potentially useful clinical adjunct, capable of identifying and differentiating the subtle changes in tissue biochemistry associated with oral disease and cancer progression in a label-free and non-invasive manner [6]. Recently, semiconductor nanostructures have been discovered to have the potential to improve SERS. Many studies have shown that synthesised semiconductor-noble metal nanocomposites have significant Raman enhancement effects [7]. Manganese oxide (MnO_2) has been extensively studied as a common metal oxide due to its low cost, natural abundance, diverse morphologies, and low toxicity. These advantages allow it to be used in a variety of applications such as catalysis, ion exchange, molecular adsorption, biosensors, and energy storage. MnO_2 can be formed into particles, rods, wires, tubes, sheets, and 3D porous nanostructures, with porous MnO_2 frameworks being a significant research area due to their superiority to bulk counterparts in many aspects.

In this investigation, we report a simple method for fabricating α-MnO_2 nanorods using hydrothermal method, followed by functionalization with Ag nanoparticles (AgNPs) using wet chemical method. α-MnO_2 nanorods can provide both smooth surfaces for homogeneous silver aggregation and sharp edges for the formation of hot spots. Because of the generation of homogeneous multiple hot spots and the propagation of SPRs, reliable and stable SERS signals can be expected after the arrangement of silver NPs on nanorods. The developed Ag@MnO_2 based SERS substrates are used for the detection of thiocyanate further extending its application to oral cancer diagnosis.

2 Experimental Details

2.1 Materials and Methods

Pottassium permanganate ($KMnO_4$, 99.5%, SRL) Polyvinyl pyrrolidone (PVP, average molecular weight = 360,000), Nitric acid (HNO_3, Merck), Silver Nitrate ($AgNO_3$, Merck), Sodium borohydride ($NaBH_4$, Merck), Ethylene glycol (EG, Merck), Pottassium thiocyanate (Isotherm) were used for the synthesis of Ag/α-MnO_2 NRs. All reagents were of analytical grade and directly used without any further purification.

2.2 Synthesis of α-MnO_2 Nanorods

α-MnO_2 nanorods were synthesised using the hydrothermal method [8–10] as described below. 6.7 g of $KMnO_4$ was first dissolved in 50 mL of de-ionized water and the mixture was stirred for 10 min. Following that, 4.2 mL of HNO_3 was dropped into the desired mixture and vigorously stirred for an hour. The resulting mixture was then transferred to a 50 mL Teflon-lined stainless-steel autoclave and kept at 120 °C in the furnace for 12 h. Following the reaction, the obtained brown product was washed several times with DI water and centrifuged. Finally, the as-synthesized product was dried overnight in an oven at a constant temperature of 80 °C before being characterised. For the synthesis of silver decorated α-MnO_2 NRs, 100 mL of ethylene glycol was treated with 400 mg of α-MnO_2 nanowires and 130 mg of PVP (polyvinyl pyrrolidone).

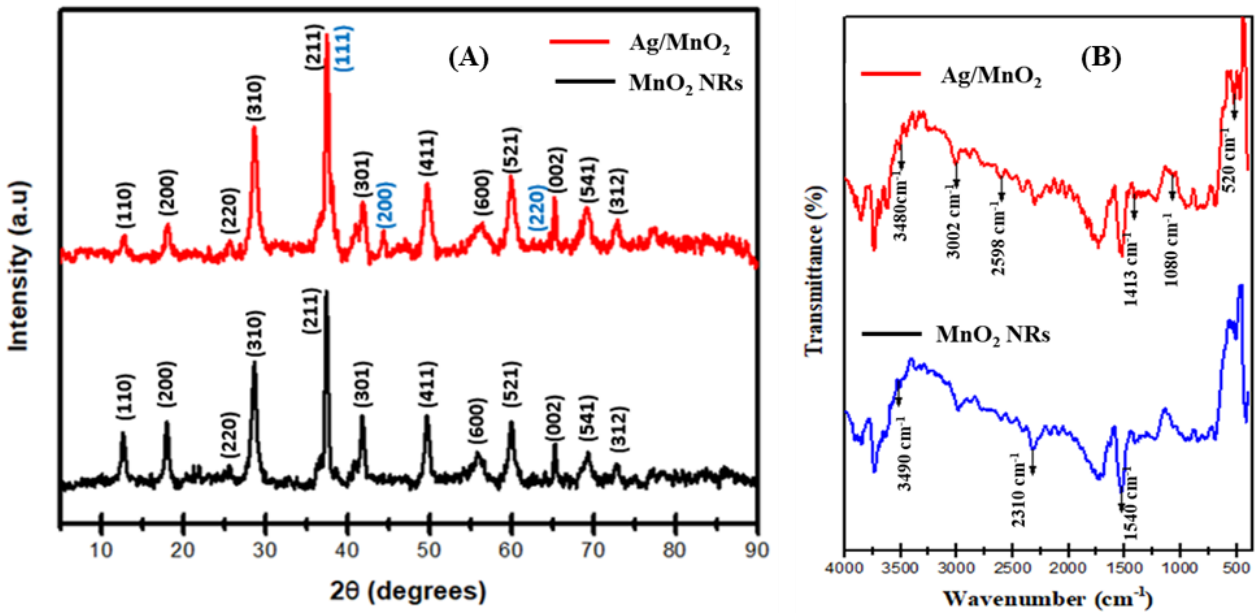


Fig. 1 (A) XRD patterns and (B) FTIR spectra of α-MnO_2 NRs and Ag anchored α-MnO_2 NRs.

The suspension was transferred to a 250 mL round-bottom flask and vigorously stirred at 90 °C for 20 min. The reaction flask was then filled with $NaBH_4$ (1.0 mmol) and 2 mL of 0.1 M $AgNO_3$ solutions. This mixture was stirred for another 12 h to produce Ag@MnO_2, which was washed three times with ethanol and water followed by successive rounds of centrifugation supernatant removal. Finally, the product was vacuum dried.

2.3 Saliva Sample Collection

Human saliva (female, 20–30 years) was collected between 9:00 am to 10:00 am to avoid the interference from the food. Prior to the sample collection, the mouth was washed thrice with pure water. A non-stimulated collecting procedure was used in which the saliva was spit directly into a disposable cup. The sample was then transferred to a 2 mL centrifuge tube and centrifuged at 12,000 rpm for 15 min at 4 °C to remove the oral mucous epithelium cells and food debris and stored at 4 °C until analysis.

Different concentrations of the thiocyanate ranging from 1 mM to 6 mM were prepared. Then, 0.5 mL of the saliva was mixed with 0.5 mL of different concentrations of the thiocyanate solutions and 5 uL of the as prepared spiked sample is drop cased on the surface of the SERS substrate, dried and analysed.

2.4 Preparation of SERS Substrate

The glass slides were thoroughly cleaned with ethanol and ultrasonic oscillation for 30 min. After drying, the synthesized Ag@MnO_2 was drop-casted on cleaned glass slides and dried to produce the SERS substrate. Different concentrations of thiocyanate were prepared. The known concentration of thiocyanate solution was dropped on the surface of the prepared SERS substrate, dried before SERS measurements for SCN^- detection. Finally, SERS signals were collected at random locations. To evaluate the ability of Ag@MnO_2 NRs to detect SCN^- in the human saliva, the saliva sample was spiked with different concentrations of the thiocyanate ranging from 1 mM to 6 mM. 20 uL of the saliva containing spiked SCN^- was then dropped on the developed Ag@MnO_2 based SERS substrates and dried prior to SERS analysis.

2.5 Characterization Techniques

The structural and morphological characterization of Ag@MnO_2 NRs was carried out using transmission electron microscopy (JEM-2010, 200 kV, JEOL, Japan) integrated with EDAX. X-ray diffraction (XRD) measurements were acquired using a PANalytical X-pert diffractometer (Malvern) with Cu Kα radiation (λ = 1.54 Å) as the source. SERS spectra was acquired using confocal Raman microscope (WITec alpha300 RA, Ulm, Germany) equipped with 532 nm laser.

3 Results and Discussion

3.1 Characterization of Ag@MnO_2 NRs

The silver decorated α-MnO_2 Nano rods (Ag@MnO_2 NRs) were synthesized by a simple hydrothermal method and were characterized through, X-ray powder diffraction (XRD), Fourier transform infrared spectroscopy (FTIR), and transmission electron microscopy (TEM) analysis. The XRD pattern of α-MnO_2 NRs and Ag@MnO_2 NRs is depicted in Fig. 1A, indicating a number of distinct sharp diffraction peaks. The diffraction peaks in the XRD spectrum at 18.10°, 25.71°, 28.84°, 36.69°, 37.52°, 39.01°, 41.96°, 49.86°, 56.37°, 60.27°, 65.10°, and 69.71° are assigned to the planes (200), (220), (310), (400), (211), (330), (301), (411), (600), (521), (002) The XRD spectrum clearly shows high crystallinity and directional growth of α-MnO_2 NRs (221). In the XRD pattern, no contaminants or residues are detected, demonstrating the high purity of as-synthesized α-MnO_2 NRs.

The XRD pattern of Ag@MnO_2 revealed the presence of α-MnO_2 and metallic silver, with diffraction peaks at 38.12°, 44.28°, and 64.43° assigned to the crystal faces (111), (200), and (220) of silver indicating that silver nanoparticles had been successfully supported on the α-MnO_2 nanorods. Fig. 1B shows the FTIR spectra of as-synthesized MnO_2 and Ag@MnO_2. It can be seen that the FTIR spectrum of the α-MnO_2 showed very weak absorptions at 2310 cm^{-1}, and 1540 cm^{-1}, which correspond to the stretching and bending vibrations of water molecules or hydroxyl groups because the nano crystalline materials exhibit a high surface-to volume ratio. Peaks at 1080 cm^{-1} and 520 cm^{-1} correspond to the typical Mn-O stretching, bending, and wagging vibrations. The FTIR spectra of Ag@MnO_2 exhibits various peaks at 2598 cm^{-1}, 1413 cm^{-1}, and CH_2 in plane bending, respectively.

The morphologies and structural characteristics of the Ag@MnO_2 nanorods could be observed diametrically by TEM analysis. A typical TEM image of α-MnO_2 NRs shown in Fig. 2A evidently confirms nanorod-type surface morphology. The individual nanorods are clearly distinguishable. The clear lattice fringes illustrate that the nanorod is a single-crystal, and the interlayer space is about 0.7 nm, corresponding to the [110] plane of α-MnO_2.

TEM images in Fig. 2B reveal that silver nanoparticles are supported on α-MnO_2 nanorods. As shown in Fig. 2B, it is clearly observed that the surface of the MnO_2 nanorods is coated with many small silver particles. The full-range EDS spectra of α-MnO_2 NRs and Ag@ α-MnO_2 NRs are shown in Fig. 2. Four elements (C, Ag, Mn, and O) were identified from the full-survey-scan spectrum of the Ag@MnO_2 composite. The peak of Cu was caused by the Cu micro grid on which the product was placed.

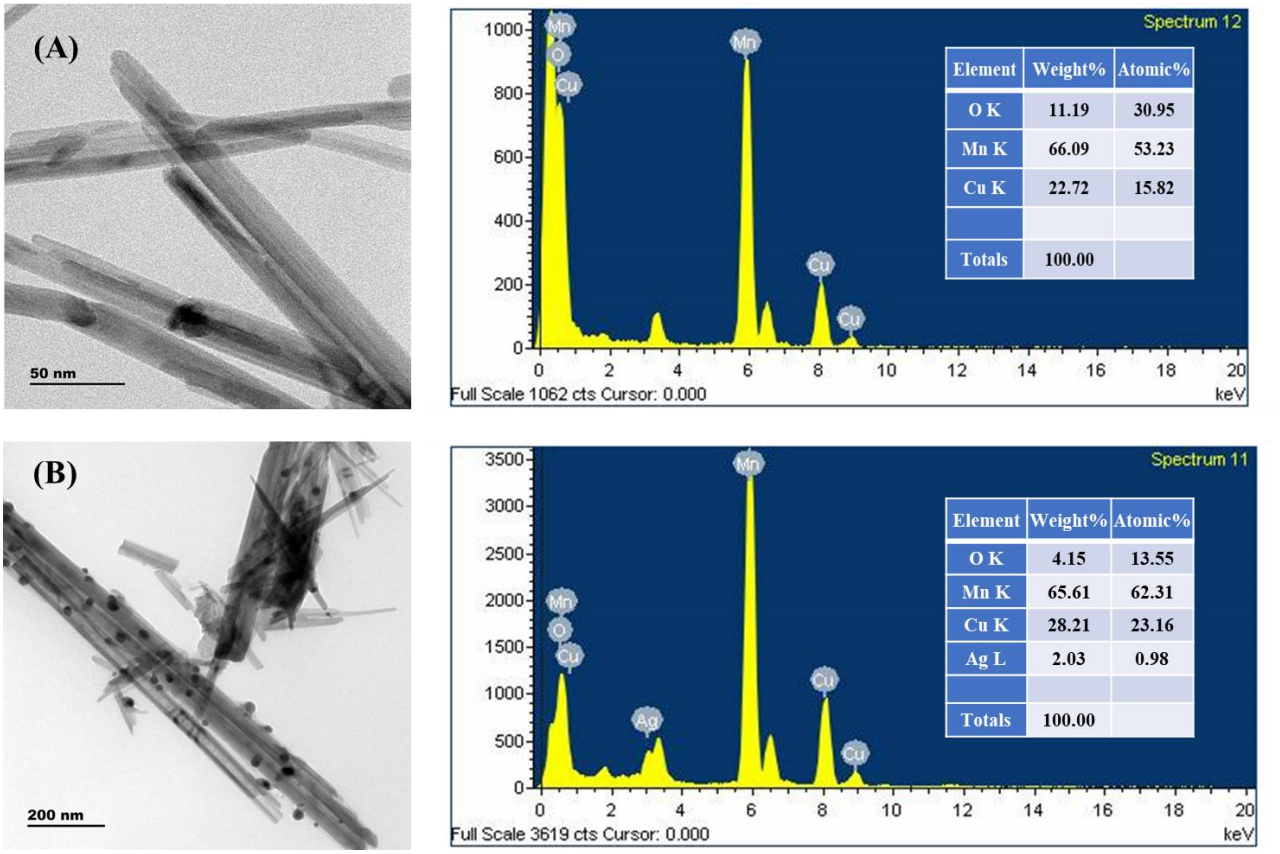


Fig. 2 TEM analysis and the corresponding EDS spectra of (A) α-MnO_2 NRs and (B) Ag@α-MnO_2 NRs.

3.2 SERS Detection of Thiocyanate

The feasibility of using the newly developed SERS substrate (Ag@MnO_2) to detect thiocyanate was investigated. SERS spectra was acquired using confocal Raman microscope (WITec alpha300 RA, Ulm, Germany) equipped with 532 nm laser. Both the material and the target analyte are active in this laser wavelength and 532 nm wavelength option is a workhorse for inorganic materials, offering maximum signal for samples that do not suffer from autofluorescence. Also, 532 nm is useful for Raman resonance experiments and for the study of metal oxide based materials. The excellent power stability, very low rms noise and perfect beam quality will meet all the requirements of most applications.

Copper (I) Thiocyanate (CuSCN) was used as the precursor for the preparation of different thiocyanate concentrations. A concentration of 1 M was used for the Raman spectra whereas 50 mM concentration was used for SERS. Fig. 3A shows the Raman spectrum of CuSCN in the regions of 20 cm^{-1} to 3500 cm^{-1}. There are four Raman peaks centred at 235 cm^{-1}, 420 cm^{-1}, 735 cm^{-1} and 2170 cm^{-1}, indicating CuSCN, which were well matched with the previous reports [11, 12]. The absorption peak at 753 cm^{-1} is caused by the C−S bond stretching vibration and the peak at 2170 cm^{-1} is attributed to the asymmetric stretching vibration of −C≡N bond, which is chosen as the characteristic peak for identifying of SCN^- due to its high intensity. The highest Raman peak at 2170 cm^{-1} showed an intensity enhancement of around 12,000 counts in the SERS spectra.

The physicochemical properties of plasmonically active nanoparticles are important parameters to consider when preparing nanostructures to produce substrates with a high SERS effect [13, 14]. The Raman intensity was found to be greatly enhanced when the Ag decorated α-MnO_2 nanorod was used as an efficient SERS substrate for the detection of thiocyanate (Fig. 3A). This massive enhancement is due to the strong localization of near field intensity, which results in the formation of so-called hot spots where the Raman signal from analyte molecules can be amplified orders of magnitude [15]. The greater enhancement of Ag@MnO_2 is explained by the higher concentration of Ag causing a more pronounced Plasmon excitation effect, which results in more efficient excitation of the Raman modes.

The enhancement factor can be calculated using the following Eq.:

$$Enhancement\ Factor(EF) = \frac{I_{SERS} \times C_{Raman}}{I_{Raman} \times C_{SERS}}, \quad (1)$$

where I_{SERS} = 11,642 a.u., C_{Raman} = 1 M, I_{Raman} = 1345 a.u., C_{SERS} = 50 mM, $EF = 11{,}642 \times 1/1345 \times 50 \times 10^{-3} = 0.17 \times 10^3$.

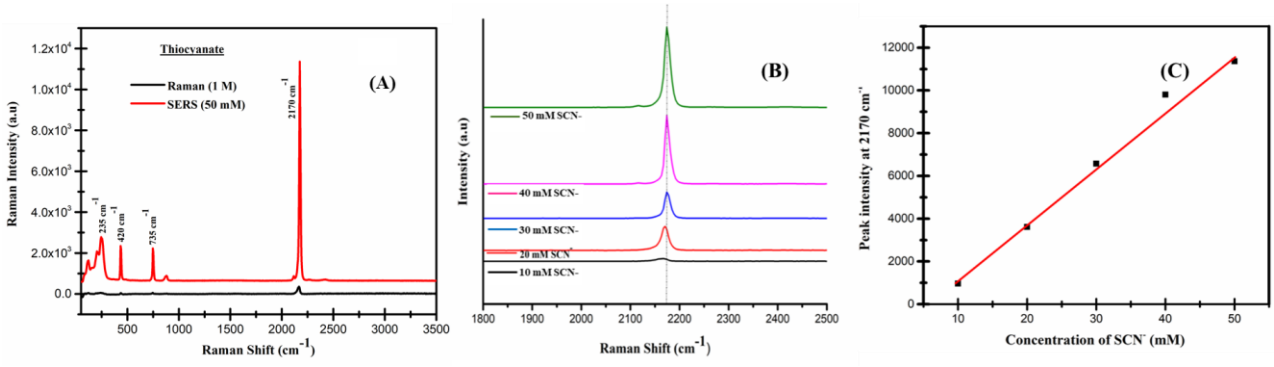


Fig. 3 Comparison of (A) Raman spectra of SCN^- and SERS spectra of SCN^- with Ag@MnO_2 as SERS substrate and (B) SERS spectra of different concentration of SCN^- (10 mM to 50 mM) and (C) the plot of peak intensity at 2170 cm^{-1} as a function of SCN^- concentration.

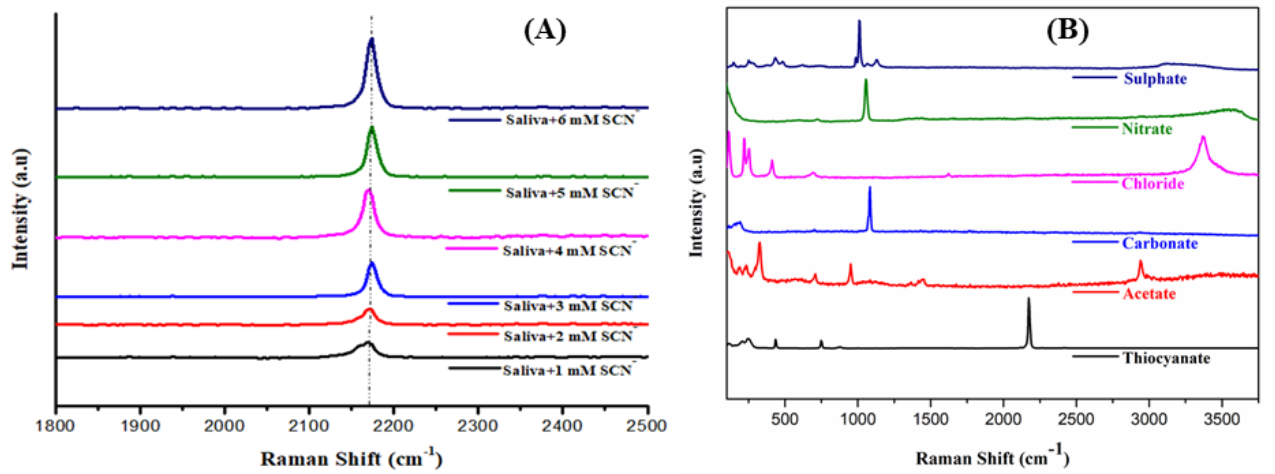


Fig. 4 (A) SERS spectra of saliva spiked with different concentrations of SCN^- (1 mM−6 mM) in Ag@MnO_2 SERS substrate and (B) the effect of interferents.

To assess the general applicability of Ag@MnO_2 for potential applications in bio-analytics, it was then used to detect thiocyanate (SCN^-) concentrations ranging from 10 mM to 50 mM as shown in the Fig. 3B. The SERS spectra showed increase in intensity with increase in the concentration of thiocyanate and the plot of peak intensity at 2170 cm^{-1} as a function of thiocyanate concentration was also found to be linear which is compatible with the existing literatures (Fig. 3C).

When SCN^- is added, a strong Raman band at 2170 cm^{-1} was appeared, which is attributed to the −CN stretching vibration mode. The results show that Ag@MnO_2 NRs can amplify the SCN^- Raman signal, and the SERS intensity at 2170 cm^{-1} can be used to detect the presence of SCN. To evaluate the ability of Ag@MnO_2 NRs to detect SCN^- in the human saliva, the saliva samples were spiked with different concentrations of the thiocyanate ranging from 1 mM to 6 mM. A SERS peak appears at around 2170 cm^{-1}, corresponding to the −C≡N stretching mode, which can be used to indicate the existence of SCN^- in human saliva [16−18]. By using the peak intensity at 2170 cm^{-1} to characterize the SERS signal, there exhibits a positive correlation between SERS intensity and ion concentration.

The SERS spectra of SCN^- with concentrations ranging from 1 mM to 6 mM are shown in Fig. 4A. The SERS intensity (2170 cm^{-1}) increased as expected with increasing thiocyante concentration, which is consistent with previous reports [19−22]. The developed substrate exhibited extremely high SERS activity and sensitivity, as well as exceptional signal stability and reproducibility, and can thus be used to distinguish between smokers and non-smokers and hence the risk of oral cancer.

The SERS sensor to detect SCN^- would be highly specific, because the Raman bands of most common chemical bonds are usually within the range of 500–2000 cm^{-1}, which is far away from the peak responsible for the –C≡N stretching mode (2170 cm^{-1}). As a proof of concept, the anions which shows the effect of interferents of other anions with the thiocyanate were studied. Acetate, carbonate, chloride, nitrate, and sulphate were the common anions interfering with the salivary thiocyanate. Thus, to study the effect of interferents, Ag@MnO_2 NRs were mixed with solutions containing 100 μM of different anion ions, including CH_3COOH^-, Cl^-, CO_3^{2-}, NO^{3-}, and SO_4^{2-}. The results shown in Fig. 4B indicate that the presence of these anions has little impact on the peak intensity at

2170 cm^{-1}. As a result, this peak can be confidentially used to indicate the concentration of SCN^- with high specificity.

4 Conclusion

Herein, we present a simple method for fabricating α-MnO_2 nanorods using a hydrothermal method, and then decorating these nanorod structures with Ag nanoparticles (AgNPs) using a wet chemical method. The feasibility of using the newly developed SERS substrate (Ag@MnO_2) to detect thiocyanate was investigated using the developed SERS substrate. The results show that Ag@MnO_2 NRs can amplify the SCN^- Raman signal, and the SERS intensity at 2170 cm^{-1} can be used to detect the presence of SCN. The SERS spectra of SCN^- with concentrations ranging from 1 to 6 mM was detected which is used to distinguish between the smokers and non-smokers and hence to predict the risk of oral cancer. This work could be further extended to real time saliva sample analysis for the detection of thiocyanate using the developed Ag@MnO_2 based SERS substrates, further extending its application to oral cancer diagnosis.

Acknowledgement

Authors wish to acknowledge DST-INSPIRE (DST/INSPIRE Fellowship/2020/IF200094) for the financial support. The authors also acknowledge the facilities and support provided by the management, PSG Sons and Charities, Coimbatore.

Ethical Approval

All procedures performed in this study were in accordance with the ethical standards. Ethical clearance was obtained from Institutional Human Ethics Committee, PSG Institute of Medical Science and Research, Coimbatore (Ref No: PSG/IHEC/2023Appr/FB/014) dated 23-02-2023 for the collection of human saliva samples.

Disclosures

The authors declare no conflict of interest.

References

1. M. Kumar, R. Nanavati, T. G. Modi, and C. Dobariya, "Oral cancer: Etiology and risk factors: A review," Journal of Cancer Research and Therapeutics 12(2), 458–463 (2016).
2. M. T. Ashby, A. C. Carlson, and M. J. Scott, "Redox buffering of hypochlorous acid by thiocyanate in physiologic fluids," Journal of the American Chemical Society 126(49), 15976–15977 (2004).
3. A. Madiyal, V. Ajila, S. G. Babu, S. Hegde, S. Kumari, M. Madi, S. Achalli, P. Alva, and H. Ullal, "Status of thiocyanate levels in the serum and saliva of non-smokers, ex-smokers and smokers," African Health Sciences 18(3), 727–736 (2018).
4. R. B. Silwal, B. Ojha, D. Bajracharya, and G. Silwal, "Correlation of Salivary Thiocyanate levels and Oral Cytological Changes in Smokers," Journal of College of Medical Sciences-Nepal 16(4), 259–266 (2020).
5. K. Tsuge, M. Kataoka, and Y. Seto, "Cyanide and thiocyanate levels in blood and saliva of healthy adult volunteers," Journal of Health Science 46(5), 343–350 (2000).
6. K. Guze, H. C. Pawluk, M. Short, H. Zeng, J. Lorch, C. Norris, and S. Sonis, "Pilot study: Raman spectroscopy in differentiating premalignant and malignant oral lesions from normal mucosa and benign lesions in humans," Head & Neck 37(4), 511–517 (2015).
7. A. Musumeci, D. Gosztola, T. Schiller, N. M. Dimitrijevic, V. Mujica, D. Martin, and T. Rajh, "SERS of semiconducting nanoparticles (TiO2 hybrid composites)," Journal of the American Chemical Society 131(17), 6040–6041 (2009).
8. X. Liu, L. Shi, W. Jiang, J. Zhang, and L. Huang, "Taking full advantage of KMnO4 in simplified Hummers method: A green and one pot process for the fabrication of alpha MnO2 nanorods on graphene oxide," Chemical Engineering Science 192, 414–421 (2018).
9. X. Zhao-Hui, L. Zhao-Lin, M. Fang-Wei, S. Li-Ping, H. Li-Hua, and Z. Hui, "Hydrothermal Synthesis of alpha-MnO2 Nanorods and Their Electrochemical Performances," Chinese Journal of Inorganic Chemistry 28(4), 691–697 (2012).
10. H. Luo, Y. Yang, B. Yang, Z. Xu, and D. Wang, "Silver/manganese dioxide nanorod catalyzed hydrogen-borrowing reactions and tert-butyl ester synthesis," Journal of Chemical Research 45(7-8), 708–715 (2021).
11. Y. Feng, R. Mo, L. Wang, C. Zhou, P. Hong, and C. Li, "Surface enhanced Raman spectroscopy detection of sodium thiocyanate in milk based on the aggregation of Ag nanoparticles," Sensors 19(6),1363 (2019).
12. A. Nizamuddin, F. Arith, J. Rong, M. Zaimi, A. S. Rahimi, and S. Saat, "Investigation of copper (I) thiocyanate (CuSCN) as a hole transporting layer for perovskite solar cells application," Journal of Advanced Research in Fluid Mechanics and Thermal Sciences 78(2), 153–159 (2020).
13. Q. Tong, W. Wang, Y. Fan, and L. Dong, "Recent progressive preparations and applications of silver-based SERS substrates," TrAC Trends in Analytical Chemistry 106, 246–258 (2018).

14. Y. Zhang, R. J. Liu, X. Ma, X. Y. Liu, Y. X. Zhang, and J. Zhang, "Ag nanoparticle decorated MnO 2 flakes as flexible SERS substrates for rhodamine 6G detection," RSC Advances 8(66), 37750–37756 (2018).
15. T. Jiang, L. Zhang, H. Jin, X. Wang, and J. Zhou, "In situ controlled sputtering deposition of gold nanoparticles on MnO2 nanorods as surface-enhanced Raman scattering substrates for molecular detection," Dalton Transactions 44(16), 7606–7612 (2015).
16. L. Wu, Z. Wang, S. Zong, and Y. Cui, "Rapid and reproducible analysis of thiocyanate in real human serum and saliva using a droplet SERS-microfluidic chip," Biosensors and Bioelectronics 62, 13–18 (2014).
17. A. Hussain, H. Pu, and D. W. Sun, "SERS detection of sodium thiocyanate and benzoic acid preservatives in liquid milk using cysteamine functionalized core-shelled nanoparticles," Spectrochimica Acta Part A: Molecular and Biomolecular Spectroscopy 229, 117994 (2020).
18. Z. Wang, C. Ma, Y. Wu, J. Gu, C. Zhu, L. Li, and G. Chen, "A sensitive method for detecting sodium thiocyanate using AgNPs and MIL-101 (Fe) combined as SERS substrate," Vibrational Spectroscopy 117, 103311 (2021).
19. F. PulliShery, G. S. Panchmal, and S. SiDDique, "Salivary thiocyanate, uric acid and pH as biomarkers of periodontal disease in tobacco users and non-users-an in-vitro study," Journal of Clinical and Diagnostic Research 9(7), ZC47–ZC50 (2015).
20. Z. Ma, Y. Zhai, Z. Chen, H. Yang, and F. Wang, "Preparation of QSS@ AuNPs and Solvent Inducing Enhancement Strategy for Raman Determination of Salivary Thiocyanate," ACS Applied Materials & Interfaces 13(5), 5966–5974 (2021).
21. M. P. Noland, R. J. Kryscio, R. S. Riggs, L. H. Linville, L. J. Perritt, and T. C. Tucker, "Saliva cotinine and thiocyanate: Chemical indicators of smokeless tobacco and cigarette use in adolecents," Journal of Behavioral Medicine 11, 423–433 (1988).
22. I. M. Colceriu-Șimon, M. Hedeșiu, V. Toma, G. Armencea, A. Moldovan, G. Știufiuc, B. Culic, V. Țărmure, C. Dinu, I. Berindan-Neagoe, and R. I. Știufiuc, "The effects of low-dose irradiation on human saliva: A surface-enhanced raman spectroscopy study," Diagnostics 9(3), 101 (2019).

Laser-Induced Crystallization of Standard Proteins on Ultra-Hydrophobic Surface and Characterization Using Raman Spectroscopy

B. Sudarshan Acharya, Sajan D. George, and Abdul Ajees Abdul Salam*
Department of Atomic and Molecular Physics, Manipal Academy of Higher Education, Manipal 576104, Karnataka, India

***e-mail:** abdul.ajees@manipal.edu

Abstract. Structural information helps to understand the function of the proteins and provides potential protein-ligand interactions of new drugs. X-ray crystallography is a powerful technique to determine the structure in three-dimensional geometry. However, obtaining high-quality single crystals remains an obstacle in macromolecular crystallography. Laser-induced crystallization is emerging as an alternative technique to circumvent this problem. In this study, we have prepared ultra-hydrophobic surfaces and used them for protein crystallization. Three model proteins, lysozyme, ferritin, and proteinase K, with distinct hydrophobicity, were used for this study. The protein droplet placed on three surfaces (non-siliconized, siliconized, and candle soot films) is exposed to a diode laser (785 nm, 75 mW). Ultra-hydrophobic candle soot surfaced coverslips rapidly yielded the crystals in conventional and laser-exposed droplets. Proteinase K nucleated faster than the lysozyme/ferritin on candle soot coated surface, compared to the regular coverslips suggesting that ultra-hydrophobic surfaces assisted laser-induced crystallization will play an essential role in protein crystallization.
© 2023 Journal of Biomedical Photonics & Engineering.

Keywords: protein crystallization; ultra-hydrophobic surfaces; laser-induced crystallization.

Paper #7785 received 25 Feb 2023; revised manuscript received 20 Jul 2023; accepted for publication 21 Jul 2023; published online 4 Sep 2023. doi: 10.18287/JBPE23.09.030312.

1 Introduction

Proteins are essential for cell functioning because they produce required elements like cytoskeletons, metabolic enzymes, and signal-transmitting factors. Determination of the three-dimensional (3D) structure of proteins is essential to know its function [1]. X-ray crystallography is a gold standard technique to determine the 3D structure of the protein [2]. Protein structure determination using X-ray crystallography involves the following steps: (i) designing of the desired plasmid, (ii) cloning and expression of plasmids, (iii) large-scale purification of desired proteins, (iv) crystallization and optimization of purified proteins, (v) collecting X-ray diffraction data and refining the structure, and (vi) analyzing the 3D structure and predicting the function of the particular protein [3, 4]. However, the success of an X-ray diffraction technique purely depends on the quality of the single crystal [2]. Except for crystallization, other steps involved in protein structure determination through X-ray crystallography are a bit easier due to highly improved modern technologies [5]. Producing high-quality crystals of the preferable size is tedious, time-consuming, and the primary bottleneck. Nucleation and crystal growth are two steps in crystallization [6]. Nucleation is the first step of the crystallization process, which decides the property of the end product [5]. Thermodynamically, the proteins and small molecules will crystallize in the same fashion. In both cases, crystallization happens in a supersaturated state. In the case of small molecules, the supersaturation state is generally achieved by cooling the solvent from a higher temperature to room temperature. In the case of proteins,

This paper was presented at the International Conference on Nanoscience and Photonics for Medical Applications – ICNPMA, Manipal, India, December 28–30, 2022.

getting the protein into a supersaturation state and maintaining it in the same state is very difficult due to the precipitation problem. Vapor diffusion, batch crystallization, dialysis, and free interface diffusion are the conventional methods introduced to get protein into a supersaturated state [2, 5]. Various nucleation promoters known as nucleants and hydrophobic surfaces have been used to induce nucleation [7, 8]. These methods have little reproducibility probability due to the fragility and softness of protein crystals [1]. Laser-induced crystallization is an alternative and promising technique to crystallize small and biomolecules. Its advantages include accelerated growth of high-quality crystals, increased nucleation probability, broad applicability, polymorph selectivity, and spatiotemporal controllability [9].

In 1996, Garetz et al. reported the laser-induced crystallization of urea using a nanosecond laser of wavelength 1064 nm [10]. However, the limitation of the method is that it requires aged sample solutions and longtime laser exposure. The aging of the solution and longtime laser exposure is impropriating for biomolecules. Later several researchers used a femtosecond laser to crystallize different molecules, including proteins [11]. Unlike femtosecond lasers, a few molecules crystallized using the continuous-wave (CW) laser. Rungsimanon et al. reported the crystallization of glycine using a CW laser of wavelength 1064 nm and with a power of 1.1 W. In this case, the nucleation is due to an optical phenomenon known as laser trapping [12]. Caciagli et al. reported the laser-induced crystallization of colloids under the influence of the optofluidic force in the oil-water interface [13]. After that, several crystallization experiments are carried out using CW lasers [14–16].

In most cases, high-energy lasers, the pulsed laser beam from nanosecond to femtosecond duration, or several watts of CW lasers are used to induce nucleation. This is unsuitable in the case of the crystallization of biomolecules, especially proteins. Such factors may lead to the denaturation of biomolecules and/or structural disorders [6, 9, 17]. To overcome these problems, nucleants are introduced in laser-induced crystallization, known as photothermal laser-induced crystallization [9]. Recently our group crystallized lysozyme protein and all-natural amino acids using a novel technique called nucleate-assisted laser-induced crystallization [6, 9]. This study uses biocompatible materials such as coconut coir and peacock feathers as nucleants [6]. A combination of CW laser sources with biocompatible nucleants rapidly yielded the crystals (in seconds) with very low laser power (2–60 mW). In the current study, we present the effect of hydrophobic surfaces on the growth of three proteins using conventional and laser-induced crystallization methods.

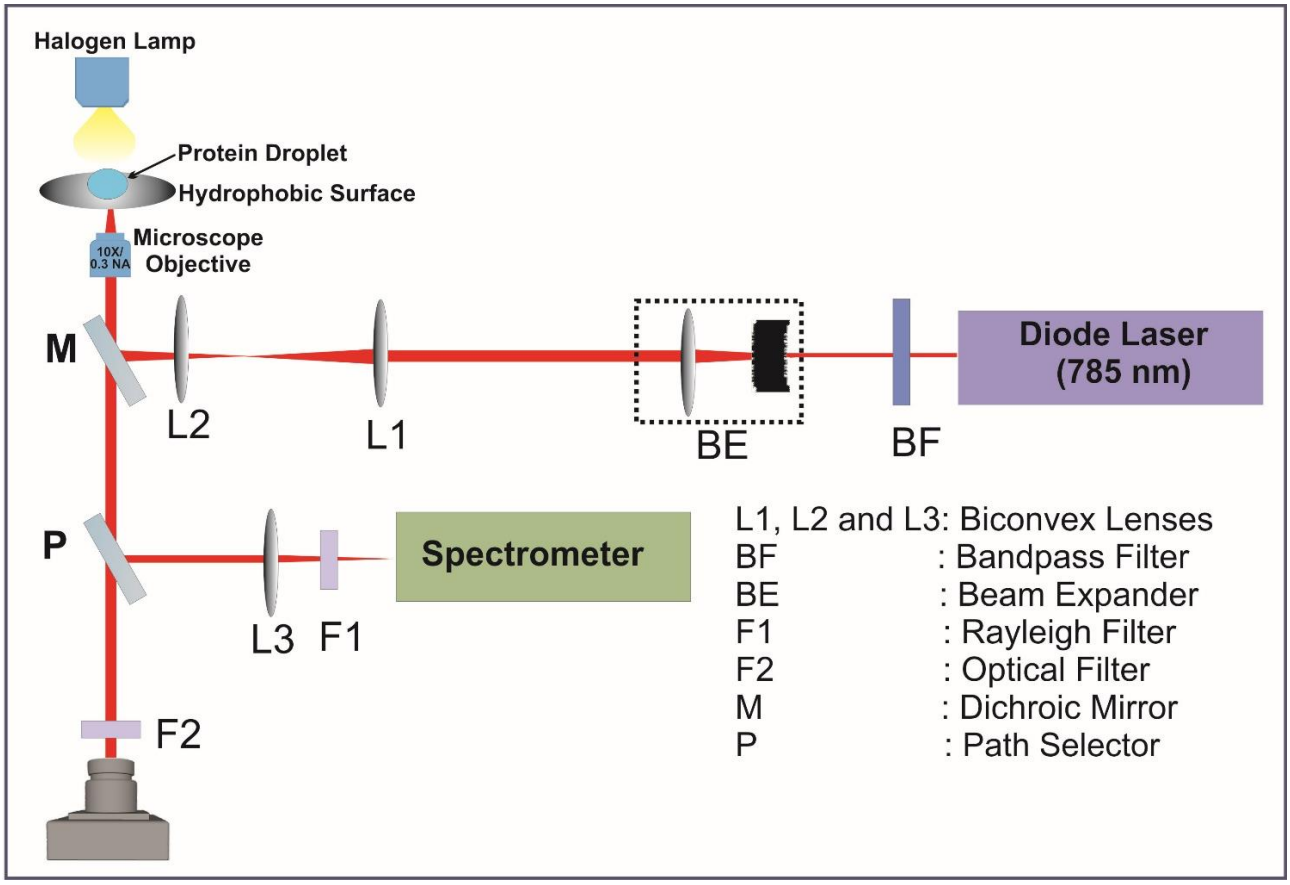


Fig. 1 A schematic diagram of the optical setup used for laser-induced crystallization and Raman spectroscopy is shown.

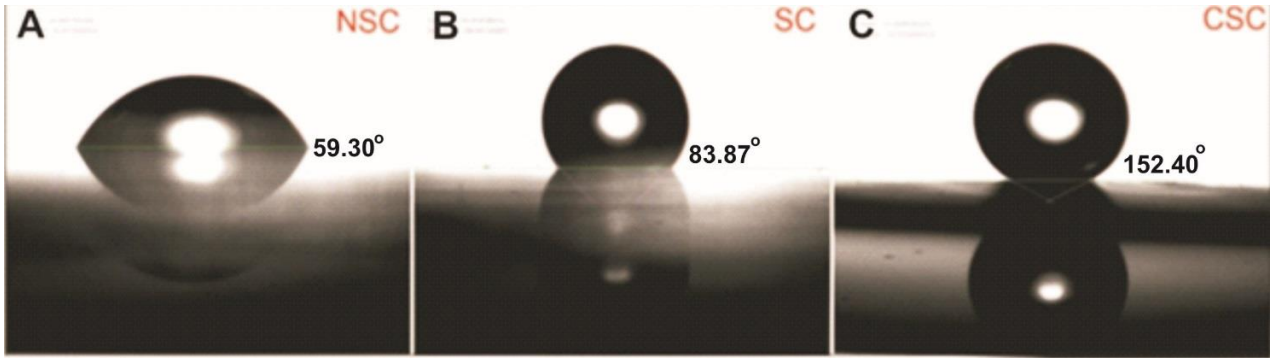


Fig. 2 Contact angle measurements of (A) NSC (59.30°), (B) SC (83.87°), and (C) CSC (152.4°), respectively.

Table 1 Proteins and chemicals selected for crystallization and time taken for crystallization.

Sl. No.	Protein	Protein solution	Well buffer	Time is taken for crystallization (in hours)					
				NSC		SC		CSC	
				Conventional	Laser	Conventional	Laser	Conventional	Laser
1	Lysozyme (Sigma #L-6876) 40 mg/ml	100 mM NaOAc (pH 4.8)	1 M NaCl, 0.1M NaOAc (pH 4.8)	18	4	12	4	12	6
2	Proteinase K (Sigma #P-2308) 20 mg/ml	25mM Tris (pH 7.5)	1.2 M $(NH_4)_2SO_4$, 0.1 M Sodium Cacodylate (pH 6.2)	12	6	12	6	6	2
3	Ferritin (Sigma #F4503) 20 mg/ml	Distilled water	0.8 M $(NH_4)_2SO_4$, 60 mM $CdSO_4$, and 0.1 M Tris (pH 7.5)	32	32	32	18	12	6

2 Materials and Methods

2.1 Chemical and Proteins

The analytical grade chemicals required for the study were purchased from SRL (India), Sigma Aldrich (USA), and Merck (USA). Non-siliconized coverslips were purchased from Blue Star (India) and siliconized coverslips from Hampton Research (USA) and used for protein crystallization without any modifications. Proteins for this study were obtained from Sigma Aldrich and used without further purification. The desired amount of protein samples is either dissolved by deionized water or suitable buffers based on the solubility, pH, and stability. The details of the buffer conditions for each protein are given in Table 1.

2.2 Synthesis of Ultra-hydrophobic Surface

Three types of 22 mm glass coverslips (Hampton Research, HR3-254), namely (1) non-siliconized (NSC), (2) siliconized (SC), and (3) candle soot film (CSC) was used for this crystallization study. Candle soot films (CSC) were prepared in four steps. In the first step, the 5 µl of polydimethylsiloxane (PDMS) solution was uniformly coated on coverslips using a spin coater. In the second step, these PDMS-coated coverslips were exposed to candle soot such that the candle soot flame covers the entire surface. The coverslips were incubated at 85 °C for 2 h in the third step. In the final stage, the dried coverslips were washed once using distilled water and incubated again at 85 °C for 15 min.

2.3 Contact Angle Measurement

To understand the hydrophobicity of the coverslips, the contact angle was measured with a 20 µl water droplet placed on NSC, SC, and CSC coverslips using a commercial contact angle meter (model: HO-IAD-CAM-01B, Halmarc, India). The experiment was repeated three times in each case, and the average of contact angles was calculated.

2.4 Crystallization

The hanging drop method was used to crystallize all the proteins using Linbro 24 well plates (HR3-110; Hampton Research, Aliso Viejo, CA). 5 µl volume of protein solutions was pipetted on the coverslips and mixed with an equal volume of well-buffers given in Table 1.

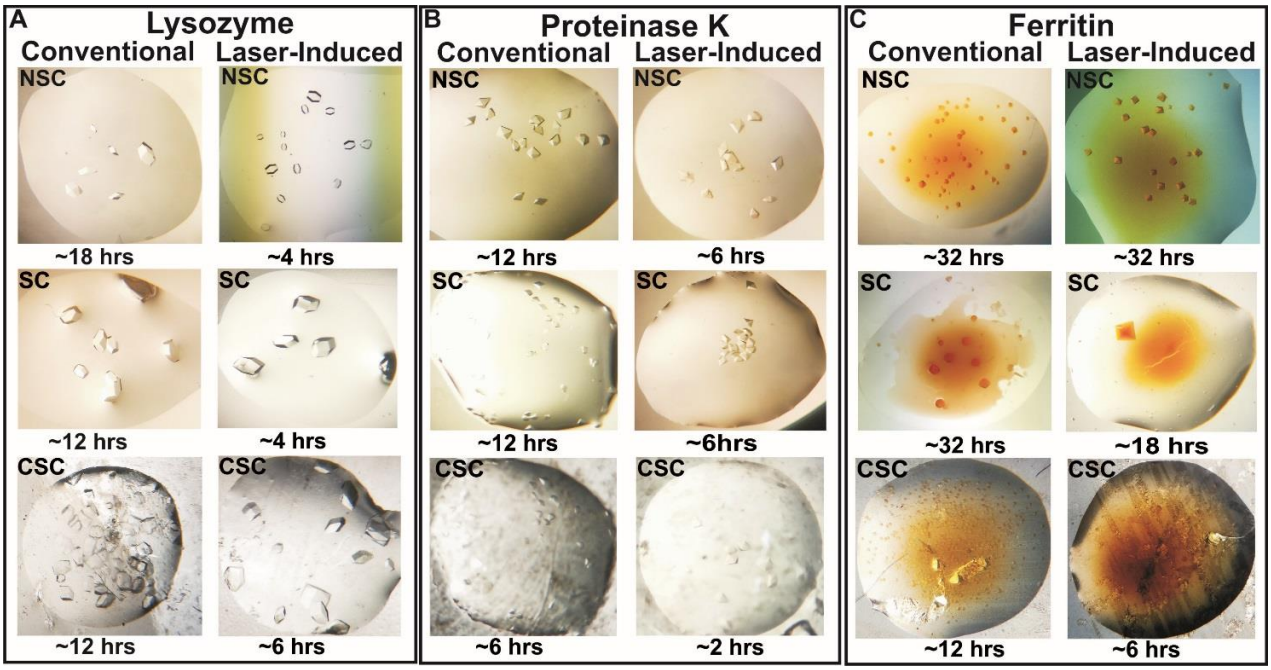


Fig. 3 Conventional and laser-induced crystallization results of the (A) lysozyme, (B) proteinase k, and (C) ferritin protein crystallized on three different surfaces.

Then the drops were subjected to the diode laser (Starbright Diode Laser, Torsana Laser Tech, Denmark) beam of wavelength 785 nm with 75 mW laser power for one minute. A microscope monitored laser-exposed mixtures to identify the protein crystals and eliminate the false positive crystals. After the laser exposure, the crystallization plates were placed at a constant temperate of 19 °C in a clean environment without disturbance. The plates were observed every 2 h for the initial 6 h. After that, the plates were followed every 6 h up to the initial 24 h and then every day for a few more days. Protein's physical and chemical properties were analyzed using the *ProtParam* online tool (https://web.expasy.org/cgi-bin/protparam/ protparam).

2.5 Optical Setup for Crystallization and Characterization

Crystallization of proteins and characterization were carried out by a micro-Raman arrangement built around a CW diode laser (785 nm wavelength, Starbright, Denmark) [6, 9]. The experimental setup used for crystallization is built around an inverted microscope, as shown in a schematic diagram (Fig. 1). The laser beam (~2 mm diameter) was expanded using manual beam expanders (BE) to a size of 9 mm.

A 1:1 telescopic arrangement and a dichroic mirror (M1) with high reflectivity at 785 nm were used to steer the expanded beam to the back aperture of a microscope objective (60X objective of 0.85 NA). A CCD camera (Nikon Eclipse Ti-U, Japan) captured images of grown crystals through an inverted microscope with a 10× objective of 0.3 NA under a halogen lamp. The protein crystals were characterized by Raman spectroscopy. Raman signals were measured (60× objective of 0.85 NA) by a spectrometer (Horiba Jobin Yvon iHR320) coupled with a liquid-nitrogen-cooled CCD detector (Symphony CCD-1024×256-OPEN-1LS). In all our experiments, Raman spectra of protein crystals were recorded at a constant laser power of 12 mW using 60 s integration time as described [6, 9].

3 Results and Discussion

3.1 Contact Angles of Three Different Surfaces

The contact angles for NSC, SC, and CSC are 59.30º, 83.87º, and 152.4º, respectively. It suggests that the CSC is ultra-hydrophobic compared to the other two surfaces because the contact angle of the candle soot films is greater than 150º (Fig. 2).

3.2 Crystallization of Proteins on the Ultra-Hydrophobic Surface

The proteins lysozyme, proteinase K, and ferritin were initially crystallized in the conventional protein crystallization method using the hanging drop method. The results are shown in Table 1 and Fig. 3. In the conventional method, the lysozyme crystals were observed on SC and CSC after 12 h and 18 h on NSC. The proteinase K crystals were observed at 12 h on NSC and SC coverslips and 6 h in CSC coverslips. The ferritin crystals took 32 h to grow on NSC and SC coverslips and 12 h on CSC. Later the protein crystallization experiments were repeated using the laser-induced crystallization method, and the results are summarized in Table 1 and Fig. 3. In the case of lysozyme, the formation of the crystals was observed in laser-induced droplets placed in NSC, SC within ~4 h and ~6 h in CSC coverslip.

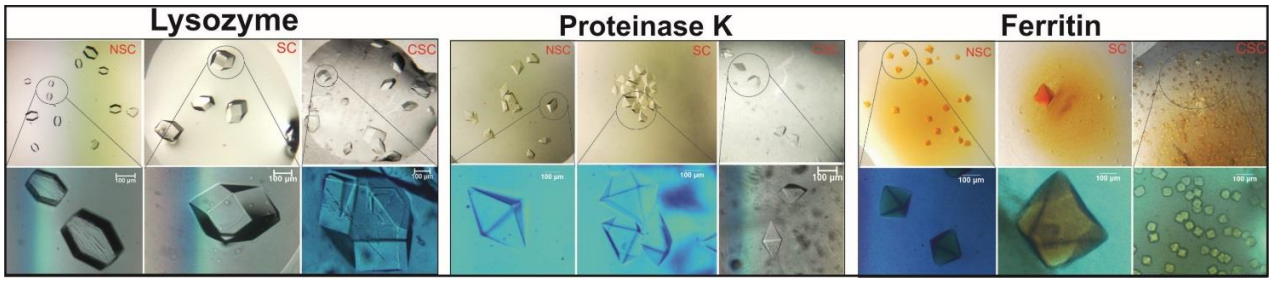


Fig. 4 Microscopic view of protein crystals crystallized on three different surfaces by laser-induced crystallization.

Table 2 Raman bands and assignments for single lysozyme crystal in the spectral region of 500–1800 cm^{-1}.

Band frequency (cm^{-1})	Assignments	Band frequency (cm^{-1})	Assignments
506	ν(S–S) ggg	#1258	amide III (random coil)
528	ν(S–S) ggt	#1289	amide III (α-Helix)
573	Tryptophan	*1292	amide III (α-Helix)
643	Tyrosine	1312	δ(CH_2)
694	Methionine ν(C–S)	1336	Tryptophan (Fermi doublet)
723	Cysteine ν(C–S)	1358	Tryptophan (Fermi doublet)
759	Tryptophan (W18 mode)	1386	Cα-H bending
833	Tyrosine (Fermi doublet)	1389	Proline
855	Tyrosine (Fermi doublet)	1407	Histidine
872	Tryptophan	1423	Tryptophan
896	Main chain vibration ν(Cα–C)	1442	Glycine
929	Main chain vibration ν(Cα–C)	1444	CH deformational vibrations
1003	Phenylalanine (F1 mode)	1456	CH deformational vibrations
1025	Phenylalanine	1467	δ(CH_2)
1048	ν(C–N)	1486	Tryptophan
1072	ν(C–N)	1513	amide II
1102	Proline, Alanine, σ(Cα–N), σ(C–C)	1549	δ(CH_3)
1127	Tryptophan σ(C–C), σ(C–N)	1576	Phenylalanine
1154	δ(CH_3)	1602	Phenylalanine (ring mode)
1175	Tyrosine, δ(CH_3)	1613	Tyrosine
1208	Tyrosine, Phenylalanine, Tryptophan	1615	Tyrosine, Tryptophan
#1231	amide III (β-sheet)	1654	amide I (α-helix)
*1242	amide III (β-sheet)		

The band frequencies marked with * correspond to the lysozyme crystal grown on NSC by the conventional method, and the frequencies marked with # correspond to the crystals grown on SC and CSC.

Laser-induced crystals of proteinase K were observed in NCS and SC within ~6 h and CSC within ~2 h. The ferritin crystals took a similar time (~32 h) to grow on NSC surfaces for conventional and laser-induced methods. However, the SC (~18 h) and CSC (~6 h) surfaces yielded the ferritin crystals faster in the laser-induced method than in the conventional method. In addition, the crystal size of all three proteins is significantly bigger in the laser-induced method droplets compared to the conventional method in most of the cases (Fig. 4).

3.3 Structural Studies Using Raman Spectroscopy

Raman spectrum of three proteins were recorded in the range of 500–1850 cm^{-1} for the analysis, called as fingerprint region of the protein [18, 19]. Analysis of this region will provide information about the vibrations of aromatic amino-acid residues, disulfide bonds, protein secondary structure dynamics based on amide I and

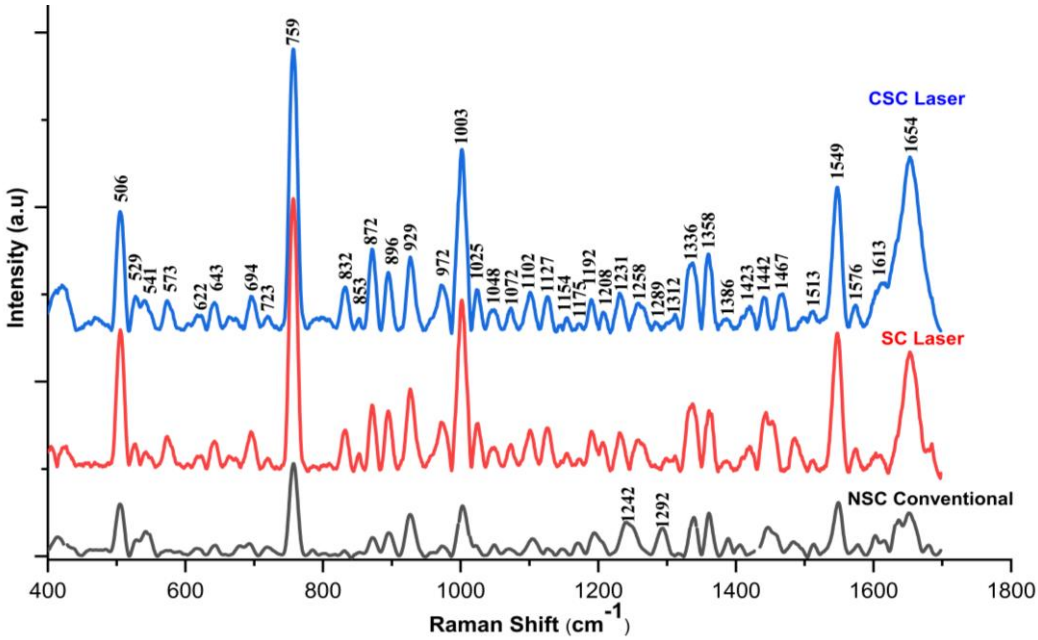


Fig. 5 Raman spectra of lysozyme crystals grown on the NSC surface using the conventional method and those grown on SC and CSC using the laser-induced method.

amide III bands, and modes related to polypeptide backbone [20]. Knowing the positions of the amide I and amide III bands helps interpret the dynamics of protein secondary structure [9, 18]. Raman spectra can be used to characterize the secondary structure conformation changes of proteins [9, 21]. We have used Raman spectroscopy to confirm the structural modifications of the proteins taken for this study.

In order to verify whether the laser source and/or the three surfaces used to grow the crystals caused any structural changes in any of these three proteins, Raman spectra of lysozyme, proteinase K, and ferritin protein crystals grown on non-siliconized coverslip (NSC) using the conventional crystallization method the protein crystals grown on siliconized coverslip (SC), and candle soot film (CSC) surfaces using laser-induced crystallization method were recorded. The frequency assignments for Raman spectra of lysozyme, proteinase k, and ferritin crystals are summarized in Tables 2–4, respectively. In lysozyme protein, around 40 peaks were measured for each case (Table 2), and detailed molecular vibrations were assigned for all the peaks. The signature five major peaks (506 cm^{-1}, 759 cm^{-1}, 1003 cm^{-1}, 1506 cm^{-1}, and 1654 cm^{-1}) and tryptophan doublet (1336 cm^{-1} and 1358 cm^{-1}) are observed for all three lysozyme crystals. The Raman spectra recorded for lysozyme crystals grown using the conventional crystallization method on the NSC surface, and the Raman spectra recorded for lysozyme crystals grown on SC, and CSC surfaces using the laser-induced crystallization method are similar. A few minor differences are observed for crystals grown on NSC and SC surfaces in comparison with the crystals grown on CSC surfaces. For example, the lysozyme crystals grown on the NSC surface using the conventional method showed two additional minor peaks (1242 cm^{-1} and 1292 $cm^{-1)}$. Similarly, three minor peaks (1231 cm^{-1}, 1258 cm^{-1}, and 1289 $cm^{-1)}$ are observed for crystals grown using laser-induced crystallization methods on SC and CSC surfaces, and these peaks correspond to amide III bands. The Raman spectrum of lysozyme proteins such as the amide I (1600–1700 cm^{-1}), amide III (1220–1300 cm^{-1}), C–C stretches (901–960 cm^{-1}), and disulfide (500–550 cm^{-1}) reported by the previous reports are matching with the current study [18, 20, 22]. The Raman spectrum of proteinase K protein yields 26 peaks with a major peak at 976 cm^{-1}, which belongs to the tryptophan vibration mode. All three proteinase K Raman spectra recorded for the crystals grown under conventional (NSC) and laser-induced (SC and CSC) methods showed similar range, and there are no major or minor differences are noted (Table 3). Similarly, the Raman spectrum recorded for the ferritin crystals yielded 28 peaks for those grown under NSC, SC, and CSC conditions. Once again, the ferritin crystal also showed a major peak at 976 cm^{-1} (Table 4).

4 Discussion

4.1 Crystallization

4.1.1 Effect of Hydrophobic Surfaces

Protein crystallization and 3D structure determination play a crucial role in various fields, including drug design, drug formulations, drug delivery, the pharmaceutical industry, biomaterial manufacture, food packaging, food delivery, and structural biology [6]. The protein crystallization process can be controlled by surface modification due to the hydrophobic interactions of proteins. The air/solution, oil/solution, microfluidic, and nanoparticle interfaces are studies conducted for several

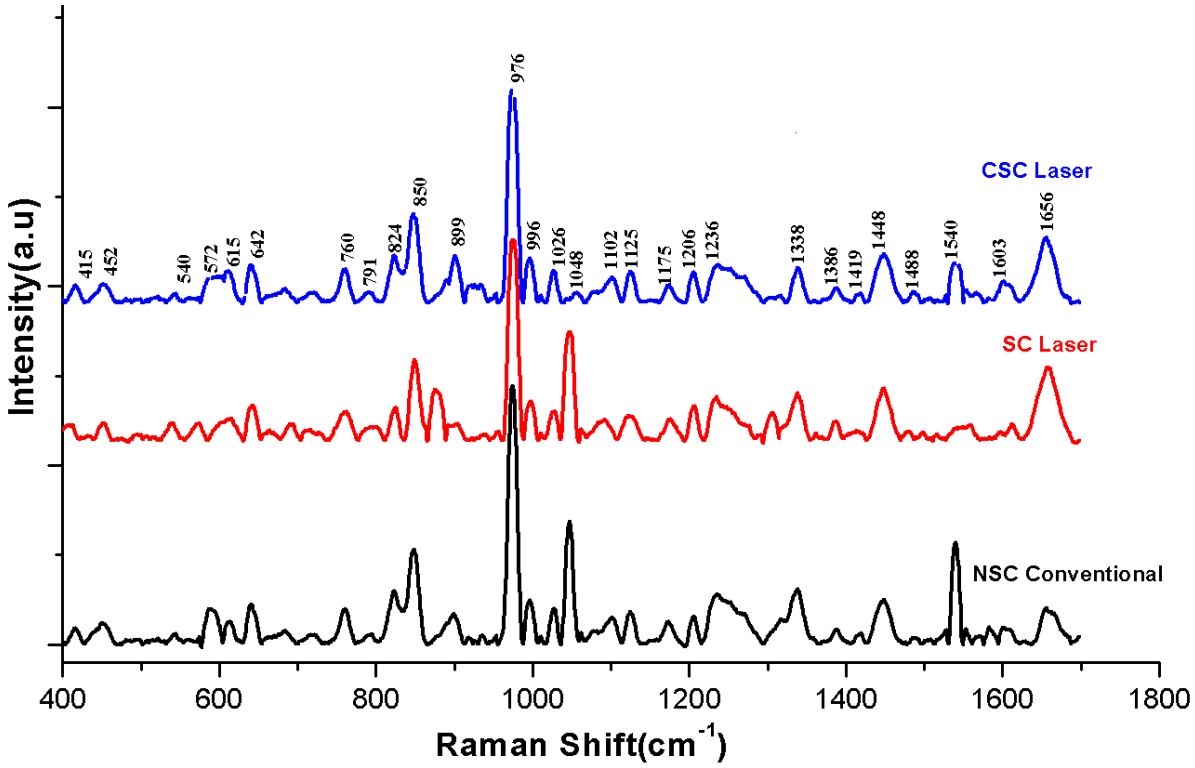


Fig. 6 Raman spectra of proteinase k crystals grown on the NSC surface using the conventional method and those grown on SC and CSC using the laser-induced method.

Table 3 Raman bands and assignments for proteinase k single crystal in the spectral region of 500–1800 cm^{-1}.

Band frequency (cm^{-1})	Assignments	Band frequency (cm^{-1})	Assignments
540	ν(S–S)	1102	Proline, Alanine, σ(Cα–N), σ(C–C) (stretching)
572	Tryptophan/Cytosine, Guanine	1125	Tryptophan σ(C–C), σ(C–N)
615	C–C twisting of protein	1175	Tyrosine, δ(CH_3)
642	Tyrosine	1206	Phenylalanine
760	Tryptophan, δ(ring)	1236	amide III (β- sheet)
791	Pyrimidine	1338	Tryptophan
824	Tyrosine (Fermi doublet)	1386	Cα-H bending
850	Tyrosine (Fermi doublet)	1419	δ(CH_2) aliphatic side chains
876	ν(C–C), hydroxyproline	1448	C–H (deformation)
976	Tryptophan	1488	Phenylalanine/Guanine (N7)
996	Phenylalanine	1540	amide II (N–H bending vibration)
1026	Phenylalanine	1603	Phenylalanine (ring mode)
1048	Phenylalanine, ν(C–N)	1656	amide I (α-helix)

proteins and proved effective in controlling protein nucleation [23–27]. Siliconized coverslips coated with poly-L-lysine and hexamethyl-D-disilane are used to grow the lysozyme crystals to understand the thermodynamics of homogenous and heterogeneous nucleation processes [28]. Lysozyme protein is coated on the coverslips and used as a thin film to grow the protein crystals, yielding bigger protein crystals than the conventional hanging drop method [29]. Surface modification by adding various nucleants is another popular method routinely used to accelerate protein growth [6, 9, 30, 31]. Surface modification-based crystallization has several advantages; (i) increasing possibilities to get desired crystal sizes, shapes, and forms without changing the buffer conditions, pH, and temperature, (ii) significantly reducing the nucleation time, (iii) obtaining the protein crystals at very low supersaturation level and optimization, (iv) expedite the overall crystallization process, and (v) cost reduction to develop new pharmaceutical products [32]. The current work uses the simple and cost-effective CSC surface modification technique, showing several advantages.

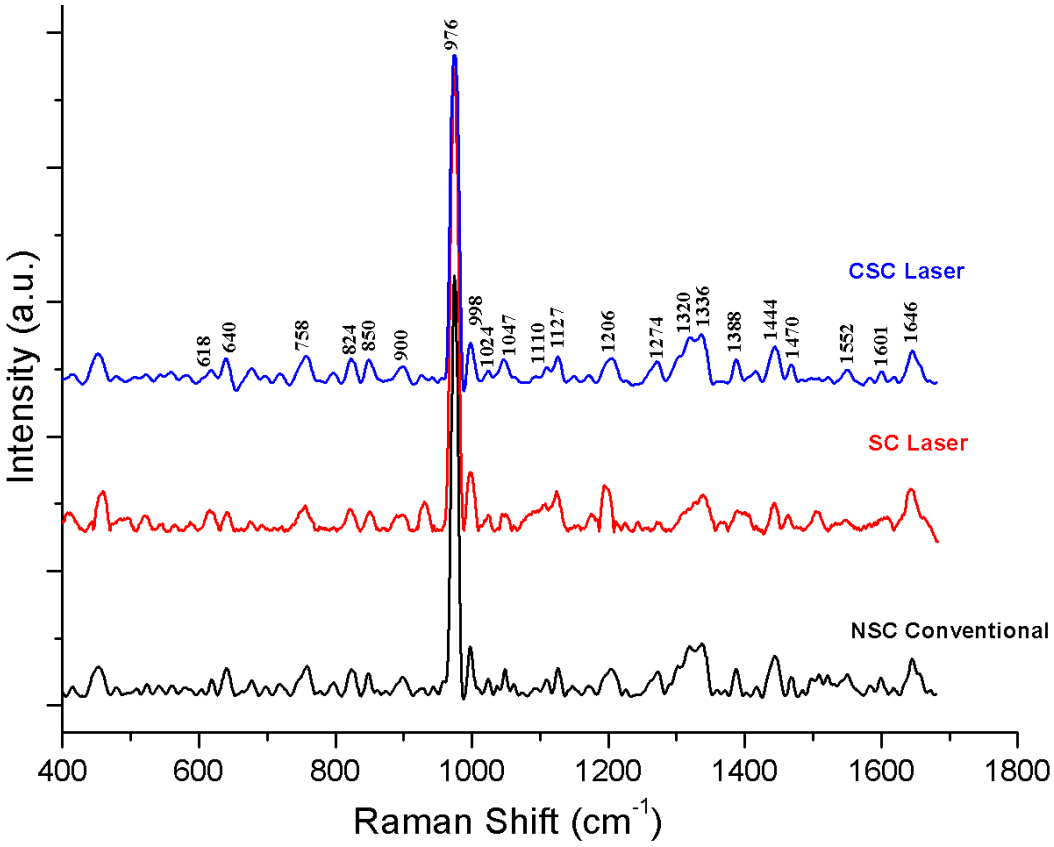


Fig.7 Raman spectra of ferritin crystals grown on the NSC surface using the conventional method and those grown on SC and CSC using the laser-induced method.

Table 4 Raman bands and assignments for ferritin single crystal in the spectral region of 500–1800 cm^{-1}.

Band frequency (cm^{-1})	Assignments	Band frequency (cm^{-1})	Assignments
521	S–S disulfide stretching	1127	ν(C–N)
619	C–C twisting	1197	Tryptophan ring breathing
640	C–S stretching & C–C twisting	1206	Hydroxy-proline, tyrosine
758	Tryptophan	1274	amide III (α-helix)
824	Tyrosine (Fermi doublet)	1320	CH deformation
850	Tyrosine (Fermi doublet)	1336	δ(CH_3) δ(CH_2) twisting
896	Tryptophan	1388	CH_3 band
900	C–C stretching vibration	1444	CH_2 deformation
932	Skeletal C–C, α-helix	1470	C=N stretching
976	Tryptophan	1548	amide II, Tryptophan
998	ν(C–C)	1552	Tryptophan
1024	ν(C–N)	1601	amide I (C=O stretching)
1047	ν(C–N)	1608	Tyrosine, Tryptophan, Phenylalanine
1110	C–C and C–N stretching	1646	amide I (α-helix)

The CSC surface generally yielded the protein crystals faster than the NSC and SC surfaces (Table 1 and Fig. 3). For example, proteinase K crystals were observed ~12 h on the NSC surface, whereas the time is reduced to 6 h on the CSC surface. The CSC surface under the laser-induced crystallization method yielded crystals faster than NSC and SC surfaces. Almost 50% time reduction is observed for all three protein crystals grown on the CSC surface using a laser-induced crystallization technique. The nucleation time is reduced to half when the hydrophobicity of the coverslip is increased. A similar trend is also observed for ferritin.

In addition, proteins' hydrophobic or hydrophilic nature shows some interesting results. Lysozyme comprises 129 amino acids with a molecular weight of 14.3 kDa. The theoretical pI is 9.32, and the

hydropathicity (GRAVY) is −0.472. The proteinase K contains 279 amino acids (molecular weight 28.9 kD), the theoretical pI is 7.80, and the hydropathicity (GRAVY) is −0.228. The ferritin is ~20 kDa protein comprised of 165 amino acids with a theoretical pI of 9.76, and the hydropathicity (GRAVY) is −0.378. The increasing positive value of grant average hydropathicity (GRAVY) indicates a greater hydrophobicity. The proteinase K is poorly water-soluble than lysozyme. water-soluble than lysozyme.

It should be noted that proteinase K crystallized faster in CSC coverslips than the other two proteins. This indicates that proteinase K can be crystallized faster on the CSC surfaces. Lysozyme has a hydrophilic surface and prefers to crystallize on hydrophilic surfaces. Thus, the results suggest that surface chemistry certainly plays an essential role in the crystallization of proteins and may influence nucleation.

4.1.2 Effect of Laser on Crystal Growth

Laser-induced crystallization method is an emerging alternative technique for growing small and macromolecule crystals. We have produced various small molecules (NaCl, KCl, chalcone compounds, and amino acids) and proteins (lysozyme) using CW and ultrafast laser sources [6, 9]. In the current study, we are interested in studying the effect of hydrophobic surfaces on protein crystal growth using conventional and laser-induced crystallization techniques. The study was conducted for their proteins, namely lysozyme, ferritin, and proteinase K using conventional and laser-induced crystallization methods in three different hydrophobic surfaces NSC, SC, and CSC. The results suggest that in general, the laser-induced crystallization method helps to obtain the crystals faster on all three surfaces, except ferritin under NSC. The ferritin crystals took ~32 h to grow on NSC surfaces for conventional and laser-induced methods. Thus, the results showed that in terms of crystal growth time, the laser-induced crystallization method did not show any advantage on the ferritin crystals growth on the NSC surface. At the same time, the same ferritin protein crystals were grown in ~18 h under the laser-induced method on the SC surface, which is ~1.8 times faster than the crystals grown using the conventional method (Table 1 and Fig. 3C). Similarly, the crystals grown on CSC surfaces on both conventional and laser-induced crystallization methods yielded the crystals faster. The ferritin crystals were grown on the CSC surface within 6 h under the laser-induced crystallization method, which is ~5.3 faster than the crystals grown on NSC surfaces. A similar trend is observed for proteinase K crystals grown in NSC and SC surfaces. However, the proteinase K crystals have grown much faster than lysozyme and ferritin on the CSC surface within ~2 h. Apart from the time reduction, the laser-induced method reduced the nucleation sites. Due to this effect, the crystals are bigger than those in the conventional method (Fig. 5). This phenomenon was observed and reported [6, 9, 11]. In the case of ferritin, a large number of small crystals were observed with few bigger crystals on CSC. This shows a high nucleation probability (Fig. 4). Compared with the conventional the laser-induced crystallization technique yielded the crystals faster in all three cases, and crystals grown on SC and CSC are highly diffractive [6, 7].

We notice that the probability of finding crystals on the focal region of the laser is maximum in most cases (Figs. 3 and 4). In the case of proteinase k, the protein crystals are concentrated at the focal area. In the case of ferritin, we observed only one single crystal growth with a large size. The CSCs are ultra-hydrophobic and highly biocompatible, with higher contact angle values than the other two surfaces [33]. In general, we observed that the crystal growth rate is high on CSC in conventional and laser-induced crystallization techniques. This is mainly due to the porous nature of the material [33, 34]. There is an increase in the solute concentration due to the trapping of solute molecules inside the pores, and pore walls provide free energy, which drives the adsorption of solute molecules. Due to this, a supersaturated state will form at pores, which leads to nucleation [35, 36]. So, these pores present on the surface will act as nucleation sites.

4.2 Raman Spectroscopic Studies

Raman spectroscopy is used to validate the structural properties of the protein [37]. Compared with the solution, protein crystals have a narrower Raman band with less peak broadening [38]. Generally, in solution, the molecules are subject to constant movement and frequent intermolecular collisions [37]. The vibrational modes are used to analyze the protein structures. The CONH group of proteins, which forms the peptide bond, is associated with nine vibrational modes. The amide I band ranges from 1600 cm^{-1} to 1700 cm^{-1} helps study the proteins' C=O (~80%) and C–N (~20%) stretching contributions. The amide II band ranges from 1480 cm^{-1} to 1580 cm^{-1} is helpful in the study of the out-of-phase combination of the NH bending and CN stretching vibrations. The amide III band ranges from 1220 cm^{-1} to 1400 cm^{-1} in-phase combination of the NH bending and CN stretching vibrations. It should be noted that the side chain conformational changes of the proteins can be analyzed using intensity changes of amide III bands [39]. The amide II bands are very sensitive to the backbone conformational changes of the proteins. Hence secondary structural information such as α-helix (1300 cm^{-1}), β-sheet, and random coil (1240 cm^{-1}) can be analyzed using amide III bands. Amide IV (625−770 cm^{-1}), amide V (640−800 cm^{-1}), and amide VI (540−600 cm^{-1}) are helpful to study the conformational changes of OCN bending, out-of-plane CN bending, and out-of-plane C=O bending. The structural analysis of the proteins is mainly studied using amide I, II, and III bands.

The amide I band appears mainly due to C=O stretching vibrations, and in addition, there is the contribution from N–H bending, C–N stretching, and C–C–N deformations [20, 21]. Amide I peak in Raman spectra indicates the strength of hydrogen bonds formed by dipole-dipole interactions between C=O and N–H groups of amides [20]. In the Raman spectra recorded for

all three lysozyme crystals (Fig. 5), the amide I band from α-helix appeared at 1654 cm^{-1}, which matches well with the literature [18, 20]. Similarly, the amide I band for proteinase k and ferritin crystals (Fig. 6) appeared at 1656 cm^{-1} (α-helix) and 1646 cm^{-1} (α-helix) (Fig. 7), respectively [19]. For the disordered protein structures, the amide I band occurs at a higher wavenumber region of 1680–1695 cm^{-1} [9, 19, 22]. This implies that the 3D structure of all three proteins taken for this study is unaltered by laser or CSC.

The amide II bands are observed at 1513 cm^{-1} for lysozyme, at 1540 cm^{-1} for proteinase k, and at 1548 cm^{-1} ferritin crystals and are well supported by the literature [20, 40, 41]. Similarly, the amide-III bands at 1231 cm^{-1} (β-sheet) and 1258 cm^{-1} (random coil) are observed for lysozyme crystals. In addition, two minor peaks at 1242 cm^{-1} (β-sheet) and 1292 cm^{-1} (α-helix) are observed for the lysozyme crystals grown on NSC coverslips using conventional crystallization methods. A similar observation is also found in the literature for lysozyme protein [21, 42, 43]. For proteinase K the amide III bands are observed at 1236 cm^{-1} (β-sheet), and in the case of ferritin at 1274 cm^{-1} (α-helix), similar observations have already been reported [19]. Thus, as we discussed earlier amide III bands are very sensitive to protein backbone conformation. The protein profiles recorded for all three proteins match the literature, thus confirming that the protein structures are not undergoing conformational changes.

In all three proteins, the tryptophan peaks showed the highest intensity at 759 cm^{-1} for lysozyme and 976 cm^{-1} for the other two proteins. Lysozyme has a peak at 1003 cm^{-1}, which corresponds to the F1 mode of phenylalanine and is well supported by the literature [20, 41]. The peak observed around 872 cm^{-1} is a signature lysozyme peak known as the W17 mode of tryptophan. W17 mode is an important marker for forming a strong hydrogen bond of the tryptophan-28 indole ring, which matches the literature [21]. The lysozyme protein has six tryptophan residues. Four of them are solvent exposed and situated on the outer surface of the lysozyme. The W17 mode indicates that tryptophan residues of lysozyme are involved in a very strong hydrogen bonding [9].

Lysozyme protein has four disulfide bridges. The peak at 506 cm^{-1} (ggg confirmation) and 528 cm^{-1} (ggt confirmation) correspond to vibrations of disulfide bonds between cysteine residues of lysozyme [18, 20]. Cys34-Cys123 and Cysl78-Cys249 are the two disulfide bonds of the proteinase k, and the Raman peak at 540 cm^{-1} (Fig. 7) corresponds to the vibrations of disulfide bonds of proteinase k [41, 44]. In the case of ferritin, S–S disulfide stretching is observed at 521 cm^{-1} and confirmed by the literature [41]. Rygula et al. reported that the band related to the stretching vibration of disulfide bonds is not observed for ferritin due to the absence of disulfide bridges in the protein [19]. In the current study, we have prepared the ferritin solution using distilled water, and there is a high possibility that the due to oxidation of cysteine residues the disulfide bonds appeared [45–47].

5 Conclusion

In macromolecular X-ray crystallography, except crystallization, all other steps are automated. Most challenges are solved using advances in experimental techniques and artificial intelligence-enabled high-end computational systems. Obtaining large enough crystals, which helps to collect high-resolution diffraction data, and subsequent atomic resolution 3D structures from protein crystals are still considered to be one of the bottlenecks in structural biology. Optimizing several crystallization variable parameters such as temperature, pH, buffer conditions, salts, ions, additives, and detergents makes the crystallization process challenging. Most of the time, the available amount of protein is also limited, restricting the number of crystallization trials. To overcome these issues, the high-throughput crystallization process involving data collection using micron-sized protein crystals through synchrotron sources, X-ray free-electron lasers, data collection techniques like serial synchrotron crystallography, and serial femtosecond crystallography have been successfully utilized. However, developing suitable protein crystals for these studies is still inevitable. In this work, we have crystallized the lysozyme, proteinase K, and ferritin proteins in three different surfaces: NSC, SC, and CSC, using conventional and laser-induced (CW 785 nm laser) crystallization methods. We have produced the protein crystals faster and bigger using ultra-hydrophobic coverslips made up of CSC. We have proved that the protein crystals in CSC can be grown more quickly than NSC and SC coverslips. For all three proteins, both conventional and laser-induced methods, the hydrophobic CSC surface yielded the crystals faster.

The CSC coverslips are easy to prepare and cost-effective. The hydrophobicity of the CSC surfaces can be easily customized based on the protein's hydrophobic properties. In addition, laser-induced crystallographic studies accelerate the crystallization process and help us to grow suitable diffraction-quality crystals in less than 24 h. Proteinase K yielded the crystals within 2 h, and lysozyme and ferritin took 6 h. The Raman spectroscopy results unambiguously proved that neither the CSC nor laser sources do not alter the protein structure. Thus, the current proposed study might be beneficial for obtaining the protein crystals rapidly. The study can be extended to more proteins, especially membrane proteins which are difficult to purify and crystallize.

6 Acknowledgment

Abdul Ajees Abdul Salam acknowledges the research grant provided by the Manipal Academy of Higher Education (MAHE) under intramural funding (MAHE/DREG/PhD/IMF/2019).

Disclosures

The authors declare no conflict of interest.

References

1. M. Kashii, H. Kitano, Y. Hosokawa, H. Adachi, Y. Mori, T. Sasaki, H. Masuhara, K. Takano, H. Matsumura, and T. Inoue, "Femtosecond laser processing of protein crystals in crystallization drop," Japanese Journal of Applied Physics 44(6L), L873 (2005).
2. M. A. Dessau, Y. Modis, "Protein crystallization for X-ray crystallography," Journal of Visualized Experiments 47, e2285 (2011).
3. A. Moreno, "Advanced methods of protein crystallization," Protein Crystallography. Methods in Molecular Biology 1607, A. Wlodawer, Z. Dauter, M. Jaskolski (Eds.), Humana Press, New York (2017).
4. J. M. Keith (Ed.), "Data, sequence analysis and evolution. Preface," Methods in Molecular Biology 452, Totowa, NJ (2008).
5. A. McPherson, J. A. Gavira, "Introduction to protein crystallization," Acta Crystallographica Section F: Structural Biology Communications 70(1), 2–20 (2014).
6. S. Thippeshappa, S. D. George, A. Bankapur, S. Chidangil, D. Mathur, and A. A. A. Salam, "Effect of biocompatible nucleants in rapid crystallization of natural amino acids using a CW Nd:YAG laser," Scientific Reports 8, 16018 (2018).
7. C. N. Nanev, E. Saridakis, L. Govada, S. C. Kassen, H. V. Solomon, and N. E. Chayen, "Hydrophobic Interface-Assisted Protein Crystallization: Theory and Experiment," ACS Applied Materials & Interfaces 11(13), 12931–12940 (2019).
8. T. A. J. Grell, M. A. Pinard, D. Pettis, and K. Aslan, "Rapid crystallization of glycine using metal-assisted and microwave-accelerated evaporative crystallization: The effect of engineered surfaces and sample volume," Nano Biomedicine and Engineering 4(3), 125–131 (2012).
9. T. Shilpa, S. D. George, A. Bankapur, and S. Chidangil, A. K. Dharmadhikari, D. Mathur, S. M. Kumar, K. Byrappa, and A. A. A. Salam, "Effect of nucleants in photothermally assisted crystallization," Photochemical & Photobiological Sciences 16(6), 870–882 (2017).
10. B. A. Garetz, J. E. Aber, N. L. Goddard, R. G. Young, and A. S. Myerson, "Nonphotochemical, polarization-dependent, laser-induced nucleation in supersaturated aqueous urea solutions," Physical Review Letters 77(16), 3475–3476 (1996).
11. T. Shilpa, S. G. Bhat, V. R. Rodrigus, S. George, A. K. Dharmadhikari, C. Santhosh, and A. A. Ajees, "Small and macromolecules crystallization induced by focused ultrafast laser," Proceedings of the Indian National Science Academy 81(2), 517–523 (2015).
12. T. Rungsimanon, K. I. Yuyama, T. Sugiyama, and H. Masuhara, "Crystallization in unsaturated glycine/D2O solution achieved by irradiating a focused continuous wave near infrared laser," Crystal Growth & Design 10(11), 4686–4688 (2010).
13. A. Caciagli, R. Singh, D. Joshi, R. Adhikari, and E. Eiser, "Controlled Optofluidic Crystallization of Colloids Tethered at Interfaces," Physical Review Letters 125(6), 068001 (2020).
14. K. I. Yuyama, K.-D. Chang, J. R. Tu, H. Masuhara, and T. Sugiyama, "Rapid localized crystallization of lysozyme by laser trapping," Physical Chemistry Chemical Physics 20(9), 6034–6039 (2018).
15. J. R. Tu, A. Miura, K. I. Yuyama, H. Masuhara, and T. Sugiyama, "Crystal growth of lysozyme controlled by laser trapping," Crystal Growth & Design 14(1), 15–22 (2014).
16. J. J. K. Chen, K.-I. Yuyama, T. Sugiyama, and H. Masuhara, "Bubble generation and molecular crystallization at solution surface by intense continuous-wave laser irradiation," Applied Physics Express 11(8), 085502 (2018).
17. S. Pathak, J. A. Dharmadhikari, A. A. Thamizhavel, D. Mathur, and A. K. Dharmadhikari, "Growth of micro-crystals in solution by in-situ heating via continuous wave infrared laser light and an absorber," Journal of Crystal Growth 433, 43–47 (2016).
18. E. Pechkova, G. Maksimov, E. Parshina, E. Maksimov, N. Kutusov, N. Brazhe, I. Tarasova, S. Fiordoro, and N. Claudio, "Raman spectroscopy of protein crystal nucleation and growth," American Journal of Biochemistry and Biotechnology 10(3), 202–207 (2014).
19. A. Rygula, K. Majzner, K. M. Marzec, A. Kaczor, M. Pilarczyk, and M. Baranska, "Raman spectroscopy of proteins: A review," Journal of Raman Spectroscopy 44(8), 1061–1076 (2013).
20. A. V. Frontzek, L. Paccou, Y. Guinet, and A. Hédoux, "Study of the phase transition in lysozyme crystals by Raman spectroscopy," Biochimica et Biophysica Acta (BBA)-General Subjects 1860(2), 412–423 (2016).
21. V. Kocherbitov, J. Latynis, A. Misiuì, J. Barauskas, and G. Niaura, "Hydration of lysozyme studied by Raman spectroscopy," The Journal of Physical Chemistry B 117(17), 4981–4992 (2013).
22. G. Anderle, R. Mendelsohn, "Fourier Transform-Infrared Studies of the Amide III Spectral Region," Biophysical Journal 52(1), 69–74 (1987).
23. B. R. Silver, V. Fülöp, and P. R. Unwin, "Protein crystallization at oil / water interfaces," New Journal of Chemistry 35(3), 602–606 (2011).
24. R. Silver, J. M. A. Grime, New Approaches to Protein Crystallization, Ph.D. Thesis, University of Warwick (2013).

25. Y.-S. Jun, D. Kim, and C. W. Neil, "Heterogeneous Nucleation and Growth of Nanoparticles at Environmental Interfaces," Accounts of Chemical Research 49(9), 1681–1690 (2016).
26. J. R. Hunter, P. K. Kilpatrick, and R. G. Carbonell, "Lysozyme Adsorption at the Air / Water Interface," Journal of Colloid and Interface Science 137(2), 462–482 (1990).
27. C. J. J. Gerard, G. Ferry, L. M. Vuillard, J. A. Boutin, N. Ferte, R. Grossier, N. Candoni, and S. Veesler, "A Chemical Library to Screen Protein and Protein–Ligand Crystallization Using a Versatile Microfluidic Platform," Crystal Growth & Design 18(9), 5130–5137 (2018).
28. D. Tsekova, S. Dimitrova, and C. N. Nanev, "Heterogeneous nucleation (and adhesion) of lysozyme crystals," Journal of Crystal Growth 196(2–4), 226–233 (1999).
29. E. Pechkova, C. Nicolini, "Accelerated protein crystal growth by protein thin film template," Journal of Crystal Growth 231(4), 599–602 (2001).
30. T. Yamazaki, Y. Kimura, P. G. Vekilov, E. Furukawa, M. Shirai, H. Matsumoto, A. E. S. V. Driessche, and K. Tsukamoto, "Two types of amorphous protein particles facilitate crystal nucleation," Proceedings of the National Academy of Sciences 114(9), 2154–2159 (2017).
31. E. Saridakis, S. Khurshid, L. Govada, Q. Phan, D. Hawkins, G. V Crichlow, E. Lolis, S. M. Reddy s, and N. E. Chayen, "Protein crystallization facilitated by molecularly imprinted polymers," Proceedings of the National Academy of Sciences 108(27), 11081–11086 (2011).
32. F. Artusio, R. Pisano, "Surface-induced crystallization of pharmaceuticals and biopharmaceuticals : a review," International Journal of Pharmaceutics 547(1–2), 190–280 (2018).
33. X. Lin, S. Park, D. Choi, J. Heo, and J. Hong, "Mechanically durable superhydrophobic PDMS-candle soot composite coatings with high biocompatibility," Journal of Industrial and Engineering Chemistry 74, 79–85 (2019).
34. B. N. Sahoo, S. Nanda, J. A. Kozinski, and S. K. Mitra, "PDMS/camphor soot composite coating: towards a self-healing and a self-cleaning superhydrophobic surface," RSC Advances 7(25), 15027–15040 (2017).
35. E. Saridakis, N. E. Chayen, "Towards a 'universal' nucleant for protein crystallization," Trends in Biotechnology 27(2), 99–106 (2009).
36. C. N. Nanev, E. Saridakis, and N. E. Chayen, "Protein crystal nucleation in pores," Scientific Reports 7, 35821 (2017).
37. M. A. Hough, "Challenges and solutions for the analysis of in situ, in crystallo micro-spectrophotometric data," Acta Crystallographica Section D: Biological Crystallography 71, 27–35 (2015).
38. G. Gouadec, P. Colomban, "Raman Spectroscopy of nanomaterials: How spectra relate to disorder, particle size and mechanical properties," Progress in Crystal Growth and Characterization of Materials 53(1), 1–56 (2007).
39. N. Kuhar, S. Sil, T. Verma, and S. Umapathy, "Challenges in application of Raman spectroscopy to biology and materials," RSC Advances 8(46), 25888–25908 (2018).
40. N. A. Nevskaya, Y. N. Chirgadze, "Infrared spectra and resonance interactions of amide-I and II vibrations of α-helix," Biopolymers: Original Research on Biomolecules 15(4), 637–648 (1976).
41. A. C. S. Talari, Z. Movasaghi, S. Rehman, and I. U. Rehman, "Raman spectroscopy of biological tissues," Applied Spectroscopy Reviews 50(1), 46–111 (2015).
42. C. Camerlingo, M. Lisitskiy, M. Lepore, M. Portaccio, D. Montorio, S. D. Prete, and G. Cennamo, "Characterization of human tear fluid by means of surface-enhanced raman spectroscopy," Sensors 19(5), 1177 (2019).
43. N. S. Myshakina, Z. Ahmed, and S. A. Asher, "Dependence of Amide Vibrations on Hydrogen Bonding," Journal of Physical Chemistry B 112(38), 11873–11877 (2008).
44. C. Betzel, G. P. Pal, and W. Saenger, "Three-dimensional structure of proteinase K at 0.15-nm resolution," European Journal of Biochemistry 178(1), 155–171 (1988).
45. B. Xu, N. D. Chasteen, "Iron oxidation chemistry in ferritin. Increasing Fe/O2 stoichiometry during core formation," Journal of Biological Chemistry 266(30), 19965–19970 (1991).
46. K. D. Welch, M. E. Van Eden, and S. D. Aust, "Modification of ferritin during iron loading," Free Radical Biology and Medicine 31(8), 999–1006 (2001).
47. A. M. Koorts, M. Viljoen, "Ferritin and ferritin isoforms I : Structure – function relationships , synthesis , degradation and secretion," Archives of Physiology and Biochemistry 1(113), 30–54 (2007).

Cardiovascular Marker Proteins Detection in the Blood Serum Using an LSPR Chip Based on Au Nanobipyramid

Prajna N. D.[1], Tom Devasia[2], and Rajeev K. Sinha[1,3*]

[1] Department of Atomic and Molecular Physics, LG-1, Academic Block 5, Manipal Academy of Higher Education, Manipal 576104, Karnataka, India

[2] Department of Cardiology, Kasturba Medical College, Manipal 576104, Karnataka, India

[3] Department of Physics, Birla Institute of Technology Mesra, Ranchi 835215, Jharkhand, India

***e-mail:** rajeev.sinha@bitmesra.ac.in

Abstract. The localized surface plasmon resonance (LSPR) based technology allows the fabrication of inexpensive biosensors with very simple design for the detection of diseases. In the present work, we systematically fabricated an LSPR sensor chip using Au nanobipyramids (Au NBPs). Au NBPs with longitudinal LSPR band in the near-IR region (~900nm) exhibiting higher refractive index (RI) sensitivity are used for the sensor chip fabrication. The immobilized Au NBPs on a silanized glass coverslip were chemically modified using 11-mercaptoundecanoic acid (11-MUA) and Octanethiol monolayer, followed by activation using EDC-NHS chemistry for the immobilization of the protein molecules. For cardiovascular marker protein detection, monoclonal antibodies were immobilized on the sensor chip, and the marker proteins were detected from the blood serum obtained from the patients. Cardiovascular marker proteins N-terminal pro-B-type natriuretic peptide and cardiac troponin T (CTnT) were successfully detected on the fabricated LSPR sensor chip. © 2023 Journal of Biomedical Photonics & Engineering.

Keywords: localized surface plasmon resonance (LSPR); Au nanobipyramids; alkanethiol monolayer; NT-proBNP; cardiac troponin T (CTnT).

Paper #8973 received 11 May 2023; accepted for publication 14 Jun 2023; published online 14 Sep 2023. doi: 10.18287/JBPE23.09.030313.

1 Introduction

The localized surface plasmon resonance (LSPR) properties of metal nanoparticles have been utilized in different fields such as photocatalysis [1], biosensing [2–5], optical filters [6], nanophotonics [7] and surface-enhanced Raman scattering [8, 9]. These nanoparticles can be synthesized using physical and chemical methods. Among physical methods, electron beam lithography [10, 11], nanosphere lithography [12, 13], and the growth of nanostructure, particularly nanorods using oblique angle deposition techniques [14], have gained enormous interest. Although these physical methods can provide well-defined nanostructures on the substrates, these methods are expensive and need a skilled workforce to operate the equipment. On the other hand, chemical methods are inexpensive and are explored extensively. However, several byproducts appear in chemical synthesis along with the main product [15]. Also, the dispersion in the size of nanoparticles is another major concern in the chemical synthesis method. The use of capping molecules to prevent aggregation also leads to their inferior performance [15]. In the past decade, advancement in the separation and purification of colloidal nanoparticles and their immobilization on substrates paves the way to fabricate nanoparticle-based sensor chips for various applications.

Gold (Au) nanobipyramids (NBPs) are a unique nanostructure being synthesized using chemical methods [16–20]. These nanoparticles, similar to nanorods, show transverse and longitudinal LSPR bands due to transverse and longitudinal oscillation of surface electrons. The longitudinal LSPR band of nanorods and NBPs can be easily tuned from visible to infrared spectral regions. However, compared to nanorods, NBPs show narrow plasmon resonance, which is a critical factor in sensing applications and provides better spectral

resolution when the nanoparticles are immobilized on a substrate.

Although most of the sensing applications involving nanoparticles synthesized using a chemical route have been performed in colloidal solution, scattered works show nanoparticle immobilization on a substrate and their sensing applications [16, 21–24]. The availability of selected conjugating molecules allows the immobilization of nanostructures on transparent substrates such as glass or quartz. It has been observed that the refractive index of coupling molecules between glass and nanostructure alters the plasmonic property significantly [24]. Any such modulation may lead to a change in the sensing capability. Therefore, the suitability of the substrate surface is also essential for immobilizing the nanostructure.

Cardiovascular diseases (CVD) are among the most pronounced cause of mortality in humans, and nearly 32% of deaths occur due to CVD [25, 26]. During myocardial infarction, the level of specific cardiac marker proteins gets elevated. Early detection of these proteins is of utmost importance for the on-time diagnosis of CVD. The noticeable CVD marker proteins include cardiac troponin I (CTnI), cardiac troponin T (CTnT), N-terminal pro-B-type natriuretic peptide (NT-proBNP), and myoglobin. Several methods have been used to detect CVD marker proteins [26–28]. Recently we have used Au thin film-based SPR to detect CTnI and CTnT [29]. There are only a few reports on the detection of cardiac marker proteins using the nanostructure-based LSPR technique. L. Tang et al. discussed the LSPR biosensing method using gold nanorods to detect cardiac biomarkers [30]. The group has developed a multiplexed gold nanorod biosensor using gold nanorods of different aspect ratios to detect multiple cardiac biomarkers. The gold nanorods synthesized using the seed-mediated growth method were terminated with carboxylic groups and immobilized with antibodies to detect cardiac troponin I (cTnI) and myoglobin (MG). Y. M. Bae et al. developed an LSPR substrate using gold nanoparticles for detecting two prominent cardiovascular biomarkers, namely low-density lipoprotein (LDL) and high-density lipoprotein (HDL) [31]. T. Liyanage et al. discussed using triangular gold nanoprisms (Au TNPs) in LSPR biosensors to detect cTnT biomarkers in human body fluids [32]. The chip-based LSPR sensors developed by the group were more sensitive compared to the commercial biosensor.

In the present work, the focus is on two objectives. First, we aim to develop an LSPR-based sensor chip utilizing Au NBPs systematically. The NBPs exhibiting longitudinal plasmon band in the near-IR spectral reason were selected as they show higher RI sensitivity [33]. For efficient immobilization of Au NBPs, surfactant CTAB was removed, followed by the surface modification of NBPs for the CVD marker protein antibody immobilization. As the second objective, we show the successful detection of the cardiac marker proteins NT-proBNP and CTnT from the blood serum sample of cardiac patients on the prepared LSPR sensor chip.

2 Materials and Methods

2.1 Materials

For the synthesis and conjugation of gold nanobipyramids, tetrachloroauric(III) acid trihydrate ($HAuCl_4 \cdot 3H_2O$), cetyltrimethylammonium chloride (CTAC), cetyltrimethylammonium bromide (CTAB), 11-mercaptoundecanoic acid (11-MUA), 4-mercaptophenylboronic acid (MPBA), nitric acid (HNO_3), silver nitrate ($AgNO_3$), 8-hydroxyquinoline (HQL), (3-mercaptopropyl)trimethoxysilane (MPTMS), 1-ethyl-3-(3-Dimethylaminopropyl)carbodiimide hydrochloride (EDC), anti-Troponin T monoclonal antibody, bovine serum albumin (BSA), and human serum were procured from Sigma Aldrich. Anti-human NT-proBNP monoclonal antibody (clone 1312), CTnI, anti-Troponin I monoclonal antibody, hydrogen peroxide, sulfuric acid, were procured from Merck. 1-Octanethiol, ethanol was procured from Alfa Aesar. N-hydroxysuccinimide (NHS) and sodium borohydride ($NaBH_4$) were procured from Spectrochem. L-ascorbic acid (AA) was procured from Loba Chemie Pvt Ltd. Citric acid was procured from Qualigens fine chemicals.

2.2 Experimental Methods

2.2.1 Synthesis of Au NBPs

The seed-mediated approach reported earlier is used to synthesize the Au NBPs [33, 34]. Briefly, the seed nanoparticles were prepared by adding 72 μL of 0.25 M HNO_3 and 80 μL of 25 mM $HAuCl_4$ to 8mL of 66 mM CTAC. The solution is mixed well, followed by adding 100 μL of freshly prepared 50 mM $NaBH_4$ in NaOH. The solution color was changed to brownish orange. After 1 min of stirring, 60 μL of 0.1 M citric acid was added, and the seed solution was heated at 85 ^oC for 1 h in a water bath. For the growth solution preparation, 20 mL of 46.5 mM CTAB, 200 μL of 25 mM $HAuCl_4$, 165 μL of 5 mM $AgNO_3$, and 255 μL of 0.4 M ethanolic HQL were mixed. In a beaker, 200 μL of seed solution was added, followed by 20 mL of growth solution and incubation of the mixture solution in a hot-air oven at 85 ^oC for 10 min.

The synthesized Au NBPs were purified by centrifuging the colloidal solution at 8000 rpm thrice. For the immobilization of Au NBPs on the MPTMS-modified glass surface, the excess of CTAB was removed, keeping ~70 μL supernatant after the second wash.

2.2.2 Fabrication of LSPR Sensor Chip

For the sensor chip fabrication, glass coverslips were cleaned glass coverslips in piranha solution (1:3 ratio of H_2O_2 and conc. H_2SO_4). The cleaned glass coverslips were incubated in 10% MPTMS in ethanol overnight. Excess of MPTMS was removed by mild sonication of the substrates in ethanol two times. To ascertain the MPTMS functionalization, the water contact angle of the substrates before and after the silanization process was

investigated using a lab-built contact angle setup [35]. Contact angle measurements were performed with a 10 µL water droplet and the analysis was carried out using the 'drop analysis' plugin in the ImageJ software [36, 37]. For the immobilization of Au NBPs, the MPTMS-coated glass coverslips were incubated in purified Au NBPs solutions for about 3 h.

The Au NBPs immobilized substrate was immersed in acetone for ~1 h to remove the remaining CTAB bilayer from the NBPs surface [38, 39], followed by immersion in an ethanolic solution of 1-Octanethiol, 11-MUA, and MPBA in 3:1:1 ratio. The carboxylic-COOH groups of 11-MUA were activated by a 1:1 mixture of 400 mM EDC and 100 mM NHS crosslinkers.

For the immobilization of the NT-proBNP antibody, the EDC-NHS modified sensor chip was incubated with 50 µL of 100 µg/mL of NT-proBNP antibody in PBS buffer (pH:7.4) for 3 h. The sensor chip was rinsed with PBS buffer and DI water after incubation. CTnT monoclonal antibody was also immobilized on the sensor chip using a similar approach.

2.2.3 Blood Sample Collection and Serum Separation

The blood samples (3 mL) were collected from 3 CVD patients with informed consent from the intensive care unit, department of Cardiology, kasturba medical college, Manipal. The collected blood samples were centrifuged at 3000 rpm for 10 min. The supernatants containing serum were separated and stored at −20 ºC. Ethical approval was obtained from the institutional ethical committee (IEC number IEC551/2020), Kasturba Medical College & Hospital, for all the work related to human blood.

2.2.4 Bulk RI Sensing Using Au NBPs Substrate

The bulk refractive index sensitivity experiments were performed to ensure the successful removal of the CTAB bilayer from the Au NBPs surface. The experiments were performed with the substrate before and after the acetone treatment. For experiments, methanol (1.326 RI), water (1.33 RI), ethanol (1.36 RI), and toluene (1.496 RI) were used as sample mediums. Besides bulk RI sensitivity experiments, the absorption spectra of the sensor chip were also recorded after each step of the functionalization process. All these measurements were carried out using our lab-built setup described elsewhere [40].

3 Results and Discussion

3.1 Effect of Seed Age in Au NBPs Synthesis

The quality of seed nanoparticles plays a critical role in forming monodispersed and reproducible Au NBPs [41]. Factors affecting the quality of seed nanoparticles include the concentration of reducing agent, surfactant, temperature, and seed aging. As mentioned in the experimental section, the prepared seeds were heated at 85 ºC before their use for the Au NBPs synthesis. The heat-treated seeds were further aged to improve the seed quality. Fig. 1(a) shows the effect of aging time on the seed nanoparticles. It is evident from the figure that the absorption spectrum of seed nanoparticles, immediately after synthesis, has a distinct but less pronounced LSPR band. The aging of nanoparticles for more than 15 min shows a strong increase in the intensity of the LSPR band. Fig. 1(b) shows the normalized absorption spectra of Au NBPs prepared using aged seed nanoparticles. It is evident from the figure that the longitudinal LSPR band shifts towards a higher wavelength with an increase in the seed aging time. Therefore, seed nanoparticles aged up to 60 min were used in the following work.

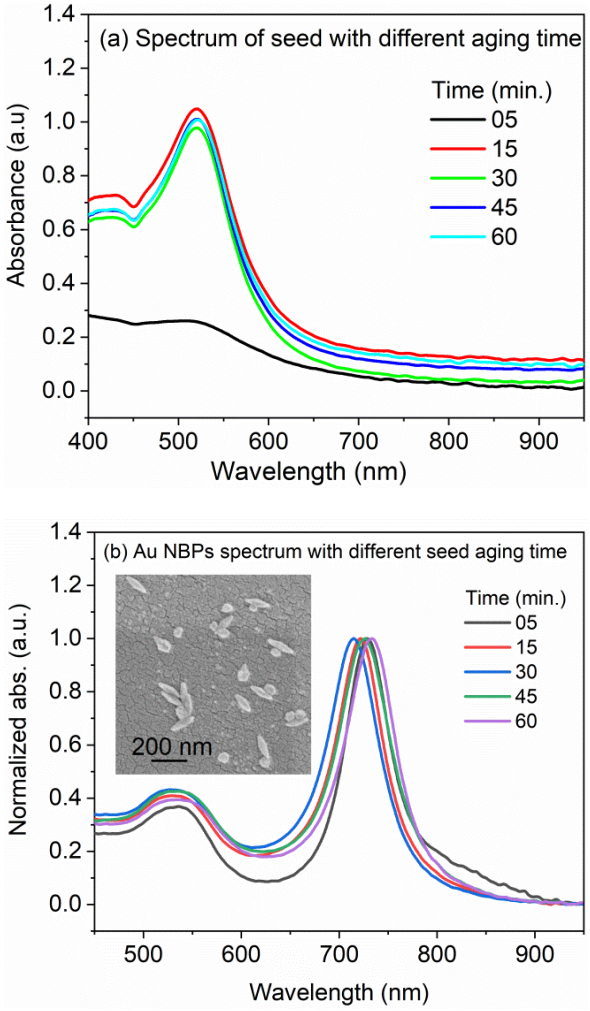


Fig. 1 Absorption spectra of (a) seed nanoparticles with different aging times and (b) Au NBPs synthesized using seed nanoparticles of different ages. Inset in (b) figure shows the FESEM image of the synthesized Au NBPs.

3.2 Purification and Immobilization of Au NBPs

Glass coverslips as an LSPR substrate were used in the following work. Before immobilization, the coverslips were cleaned with piranha solution (1:3 ratio of H_2O_2 and

conc. H_2SO_4). The cleaned glass coverslips were incubated in 10% MPTMS in ethanol overnight. The measurement of the water contact angle ascertained the silanization of coverslips. Figs. 2(a) and (b) show the contact angle images before and after the silanization process. As seen in Fig. 2, the water contact angle on the piranha-treated substrate was 21.8º indicating the hydrophilic nature of the substrate [42]. The water contact angle was increased to 64.6º after the silanization process with MPTMS due to the partial hydrophobic nature of the MPTMS-coated substrate [43].

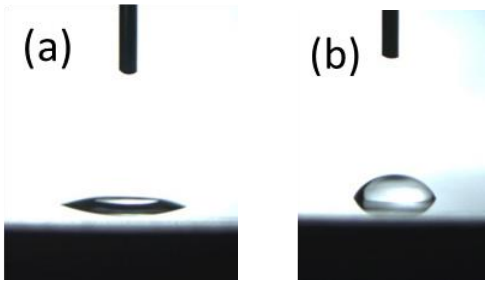


Fig. 2 Water contact angle (a) on piranha solution treated coverslip (contact angle: 21.8º), (b) on MPTMS coated coverslip (contact angle: 64.6º)

In the synthesis of Au NBPs, the CTAB forms a bilayer around NBPs, preventing them from aggregation. Due to the CTAB bilayer formation around nanoparticles, the NBPs acquire an overall positive surface charge. The immobilization of Au NBPs on the substrate is strongly hindered by the electrostatic repulsion between positively charged NBPs, resulting in lower NBPs density on the substrate [44]. Removal of CTAB from the NBPs surface can improve the Au NBPs immobilization and RI sensitivity. However, the complete removal of CTAB by several washing steps using centrifugation can cause shape deformation and aggregation of NBPs. For the successful immobilization of the Au NBPs on the glass substrates, optimization of the number of washing cycles and centrifugation time are performed. A constant centrifugation rate at 8000 rpm was maintained in all washing cycles.

For the removal of CTAB, 2 approaches were used. In the first approach, the Au NBPs colloidal solution was centrifuged at 8000 rpm for 5 min, and the supernatant was discarded. This washing process was repeated 3 times. Figs. 3(a) and (b) show the LSPR spectra of Au NBPs as-synthesized and after 3 washing cycles, respectively. It was observed that the longitudinal LSPR band shifts towards a lower wavelength after 3 washing steps. Also, the intensity ratio of longitudinal to transverse LSPR bands changes from 2.61 to 0.97. The observed changes could be due to the complete removal of CTAB. It has been observed earlier that the complete removal of CTAB can cause the aggregation of nanoparticles along with the deformation of Au NBPs. The observed blue shift could be due to the aggregation of particles, whereas the decrease in the longitudinal to transverse intensity (L/T) ratio could be due to the deformation of Au NBPs. An effort was made to immobilize the nanostructures on the MPTMS-modified glass substrates. The corresponding LSPR spectrum of the substrate is shown in Fig. 3(c). The broad spectrum from the substrate clearly shows that the Au NBPs get aggregated on the substrate surface.

In the second approach, to avoid aggregation or deformation of Au NBPs, the presence of CTAB was ensured by leaving a small amount (~100 μL) of supernatant after each centrifugation step of the colloidal solution. Figs. 4(a) and (b) show the LSPR spectra of Au NBPs as prepared and after 3 washing cycles, respectively. It is evident from the figure that the longitudinal band after 3 washing steps shows a slight blue shift of 5 nm. However, the L/T ratio improved from 2.61 to 3.6, indicating the suppression of aggregation and deformation of Au NBPs. The Au NBPs, obtained after centrifugation, were immobilized on the MPTMS-modified glass coverslips. Fig. 4(c) shows the spectrum of immobilized Au NBPs. It is evident that though the absolute absorbance decreases upon immobilization, the L/T ratio is maintained.

The immobilization of Au NBPs on silanized coverslips was further improved by optimizing the immobilization time. Fig. 5 shows the absorption spectra of immobilized Au NBPs after an immobilization time of 45 min and 3 h. A substantial increase in absorption was observed with higher immobilization time. It is also observed that upon immobilization, the FWHM of the spectrum increases marginally, along with a small red shift of the longitudinal LSPR band. The observed increase in the FWHM and redshift could be due to substrate and MPTMS, which is used as a linker molecule between glass and Au NBPs.

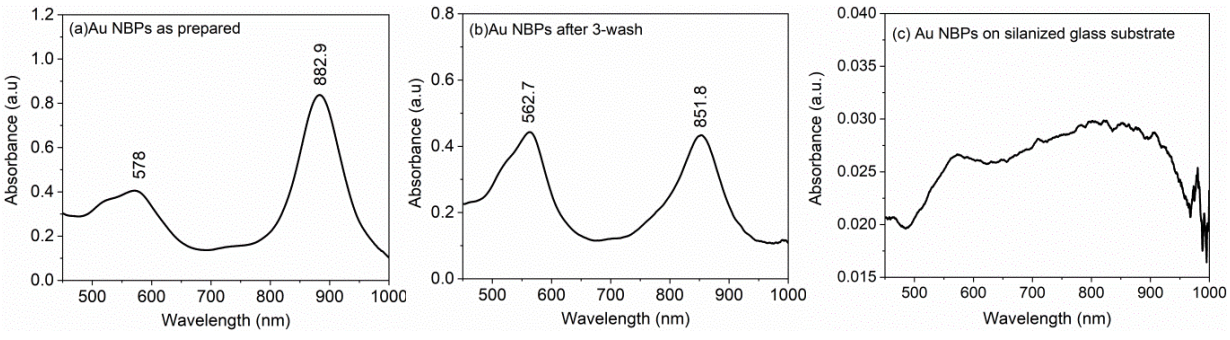


Fig. 3 Absorption spectra of Au NBPs (a) as-synthesized, (b) after 3 washes with complete removal of the supernatant, and (c) on MPTMS functionalized glass coverslip.

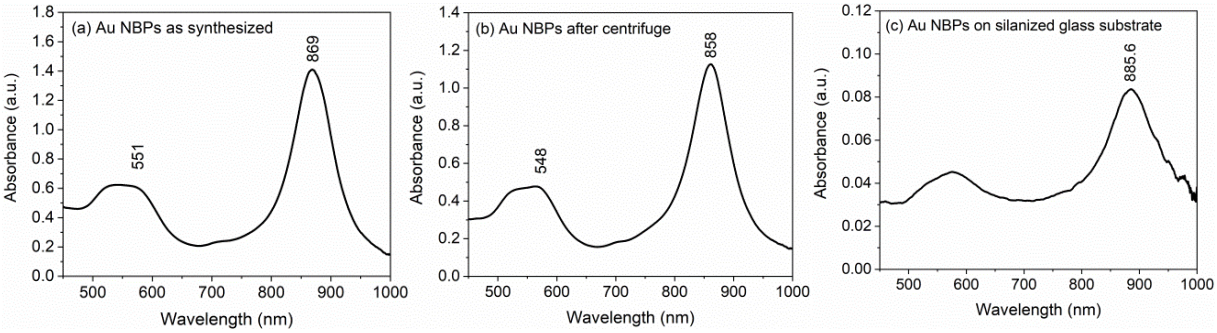


Fig. 4 Absorption spectra of Au NBPs (a) as-synthesized, (b) after 3 washes with partial removal of the supernatant, and (c) on the MPTMS functionalized glass coverslip.

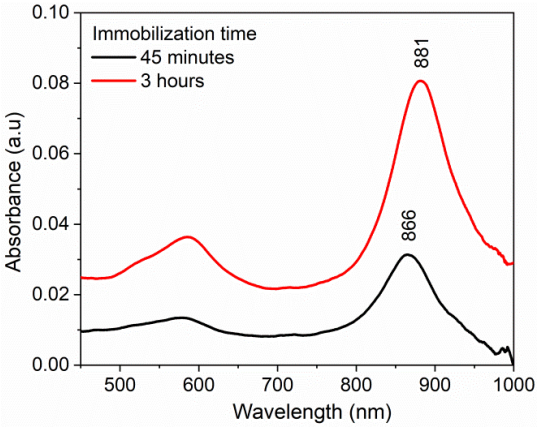


Fig. 5 Au NBPs immobilized on MPTMS-modified glass coverslip with an incubation time of 45 min and 3 h.

3.3 Surface Functionalization of Au NBPs

3.3.1 Non-Specific Binding (NSB) of BSA on the Sensor Chip

The Au NBPs immobilized on the MPTMS-treated glass coverslips were further modified for the immobilization of the protein molecules. It has been observed that acetone is helpful in the removal of the CTAB [38]. The immobilized Au NBPs were treated with acetone for 1 h to remove CTAB from the Au NBPs surface. The immobilized NBPs were treated with an ethanolic mixture of Octanethiol and 11-MUA (3:1 ratio), followed by the acetone treatment. The use of Octanthiol with 11-MUA ensures that the 11-MUA with –COOH terminal group is immobilized on the NBPs surface without any steric hindrance. It is well known that for protein conjugation, the terminal group –COOH of 11-MUA needs further modification, which is performed by incubating the substrate in the 1:1 mixture of EDC (0.4 M) and NHS (0.1 M) for 1 h.

The suitability of the EDC-NHS-modified substrate for protein conjugation was investigated using bovine serum albumin (BSA). The substrate is incubated in BSA solution in PBS buffer (10 µg/mL) for this. To prevent any temperature-dependent degradation of BSA, the incubation process was performed at 2−8 ºC. The LSPR spectra were recorded at each stage and are shown in Fig. 6. The figure shows that after the removal of CTAB by acetone, the longitudinal band in the LSPR spectrum shifts towards a lower wavelength of ~8.5 nm. The immobilization of 11-MUA and Octanethiol leads to the shift of the LSPR wavelength to red by 1.8 nm. The EDC-NHS modified substrate shows a further increase in the LSPR band maximum wavelength by 12.3 nm. The BSA further shifts the LSPR band maximum by 9 nm. The observed wavelength shifts are expected and corroborate our earlier results [33].

The non-specific binding of protein appeared as a common issue in SPR and LSPR measurements. In several reported works, polyethylene glycol that imparts hydrophilicity to the substrate surface is utilized to prevent non-specific binding. However, due to the long polymeric chain and size of PEGs, degradation of sensing performance was observed. The present work uses a small thiolated molecule, 4-mercaptoboronic acid (MPBA), as a non-specific binding-preventing molecule.

MPBA has a −SH group in a phenyl ring group and boronic acid with 2 hydroxyl groups at the para position. After the EDC-NHS treatment of a self-assembled monolayer of alkanethiols, MPBA binds to the Au NBPs surface and prevents the non-specific binding of protein molecules on the NBPs surface. In the experiments reported here, 115 mM concentration of MPBA was used.

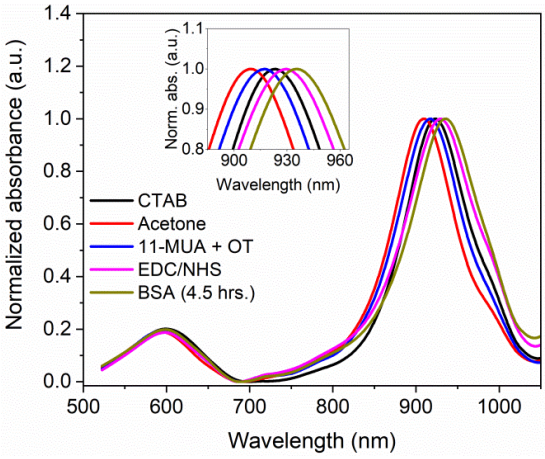


Fig. 6 Absorption spectra of the sensor chip at different functionalization stages. Inset shows the expanded spectral region of the longitudinal LSPR band.

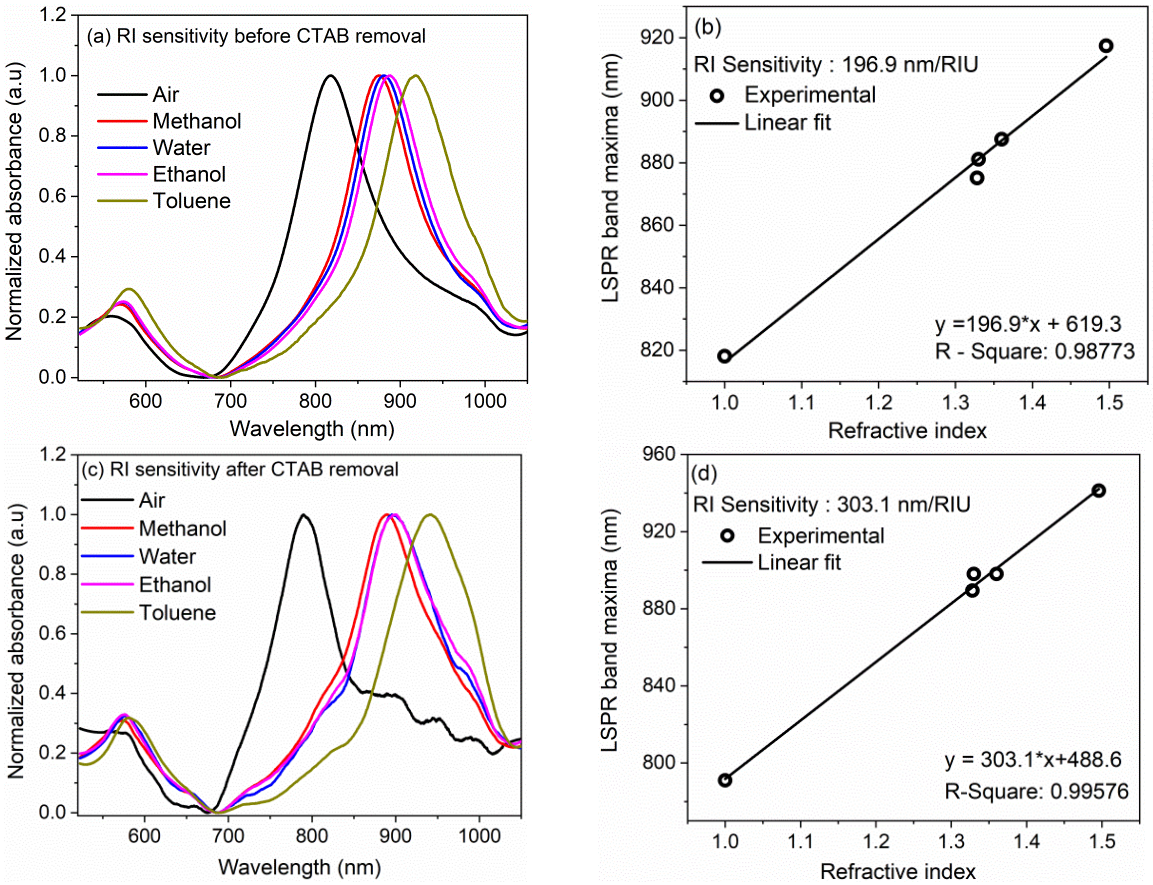


Fig. 7 (a) LSPR spectra of Au NBPs in different refractive index media before the removal of CTAB, (b) linear fit to the longitudinal band maxima position before CTAB removal, (c) LSPR spectra of Au NBPs in different refractive index media after the removal of CTAB, and (d) linear fit to the longitudinal band maxima position after CTAB removal.

3.3.2 Bulk RI Sensing of LSPR Sensor Chip

The replacement of CTAB with thiolated molecules was ascertained by examining the refractive index sensitivity of the sensor substrates. For the RI sensitivity measurement, methanol, water, ethanol, and toluene were standard samples. The RI sensitivity experiments were performed on immobilized NBPs with CTAB and immobilized NBPs after functionalization with thiolated molecules. Fig. 7(a) shows the LSPR spectra of the sensor substrate with immobilized CTAB-capped Au NBPs. The figure shows a clear wavelength shift in the sample medium from water to toluene. Fig. 7(b) shows the LSPR band maxima plotted against the RI of samples. The slope of the linear fit to the data represents the RI sensitivity. For the NBPs without acetone treatment immobilized on the sensor substrate, the RI sensitivity of 196.9 nm/RIU was observed. Figs. 7(c) and (d) show similar plots for the Au NBPs immobilized on sensor substrate, followed by acetone treatment and thiolation of immobilized NBPs. In this case, the RI sensitivity of 303.1 nm/RIU was obtained, 105 nm/RIU higher than the CTAB-capped immobilized NBPs. Our earlier work observed similar behavior where CTAB was replaced with 11-MUA [33]. The observed increase in the RI sensitivity is due to the replacement of the CTAB bilayer on the NBPs surface by thiolated molecules, which makes the nanostructure more accessible and sensitive towards the sample medium.

3.4 CVD Biomarker Detection from Clinical Samples

3.4.1 Detection of NT-proBNP

NT-proBNP is a cardiac marker protein in the bloodstream. The B-type natriuretic peptide (BNP) plays a vital role in maintaining homeostasis in the cardiovascular system, serving as a counter-regulatory hormone for volume and pressure overload. The increase in the level of NT-proBNP in the bloodstream indicates insufficient blood pumping by the heart. Therefore, the level of NT-proBNP is widely measured in clinical applications for the diagnosis, risk stratification, and management of patients with heart failure. Early detection of elevated levels of NT-proBNP in the bloodstream is helpful in the timely treatment of the problems associated with heart failure.

The prepared sensor chips with immobilized Au NBPs were utilized to detect cardiac marker protein NT-proBNP. For the detection, the sensor chip was treated with acetone for 1 h, followed by incubation in the 3:1:1 mixture of Octanethiol, 11-MUA, and MPBA overnight.

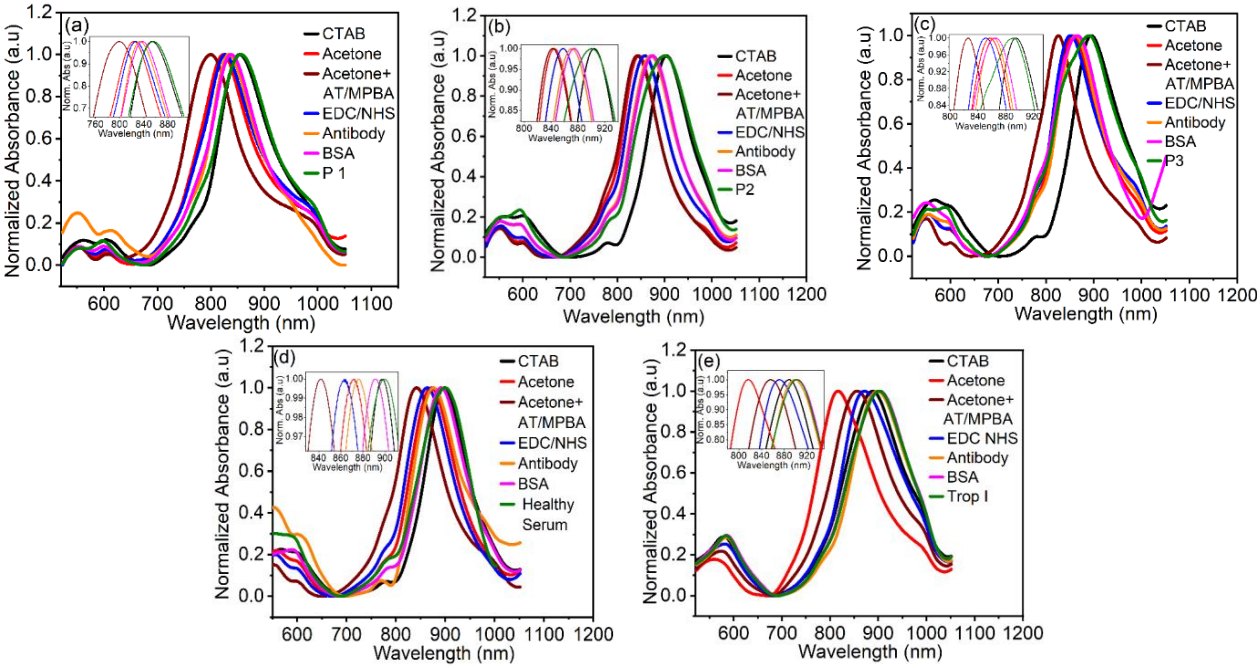


Fig. 8 LSPR spectra of the substrate at different functionalization and detection stages of NT-proBNP (a) for the blood serum of patient 1, (b) for the blood serum of patient 2, (c) for the blood serum of patient 3, (d) for commercial human serum, and (e) specificity determination using CTnI on NT-proBNP antibody immobilized sensor chip.

Table 1 LSPR band positions of sensor chip at different stages of functionalization and detection of NT-proBNP.

Coverslip (CS)	**LSPR band position (nm) at different functionalization stages**				
	a	b	c	d	e
before acetone	855.2	904.6	895.4	897.8	888
after acetone	823.6	845.3	857.7	871.7	817.5
after alkane thiols (AT)	798.6	842.7	825.9	843	856.4
after EDC/NHS	828.01	857.9	851.5	863.8	872.6
after antibody	835.2	871.1	862.4	876.7	898.4
after BSA	838.8	874.5	864.6	891.6	902.2
after cardiac patient serum	856.5	898.6	887.9	–	–
after commercial serum	–	–	–	898.6	–
after 100 ng/mL CTnI	–	–	–	–	901.6

After washing with ethanol, the terminal −COOH groups of 11-MUA were activated using EDC and NHS. After activation of the NBPs surface, the sensor chip was incubated in 100 µg/mL NT-proBNP monoclonal antibody for 4 h. The antibody-immobilized sensor chip was treated with 1% (10 mg/mL) BSA for 30 min to lower the non-specific binding. The cardiac marker protein NT-proBNP was detected in the serum sample of cardiac patients. The sensor chip with immobilized monoclonal antibody blocked for non-specific binding was incubated in the blood serum and separated from cardiac patients' blood for 2 h. Subsequently, the LSPR spectra were recorded. Figs. 8(a–c) show the LSPR spectra of the sensor chip at different functionalization and detection of NT-proBNP from the 3 patients marked as P1, P2, and P3. Fig. 8(d) corresponds to the response of the NT-proBNP antibody immobilized chip toward the commercially obtained blood serum of a healthy human. The detection specificity of NT-proBNP was ensured by using CTnI protein (100 ng/mL) diluted in PBS buffer. Fig. 8(e) shows the response of the CTnI on the NT-proBNP antibody immobilized sensor chip. The LSPR band maxima observed in these figures are listed in Table 1. It is also evident from the table that a substantial redshift in the LSPR band maxima position occurs when the sensor chip is treated with the serum of cardiac patients, whereas the presence of troponin I do not show a significant band position shift ensuring the specificity of the measurements.

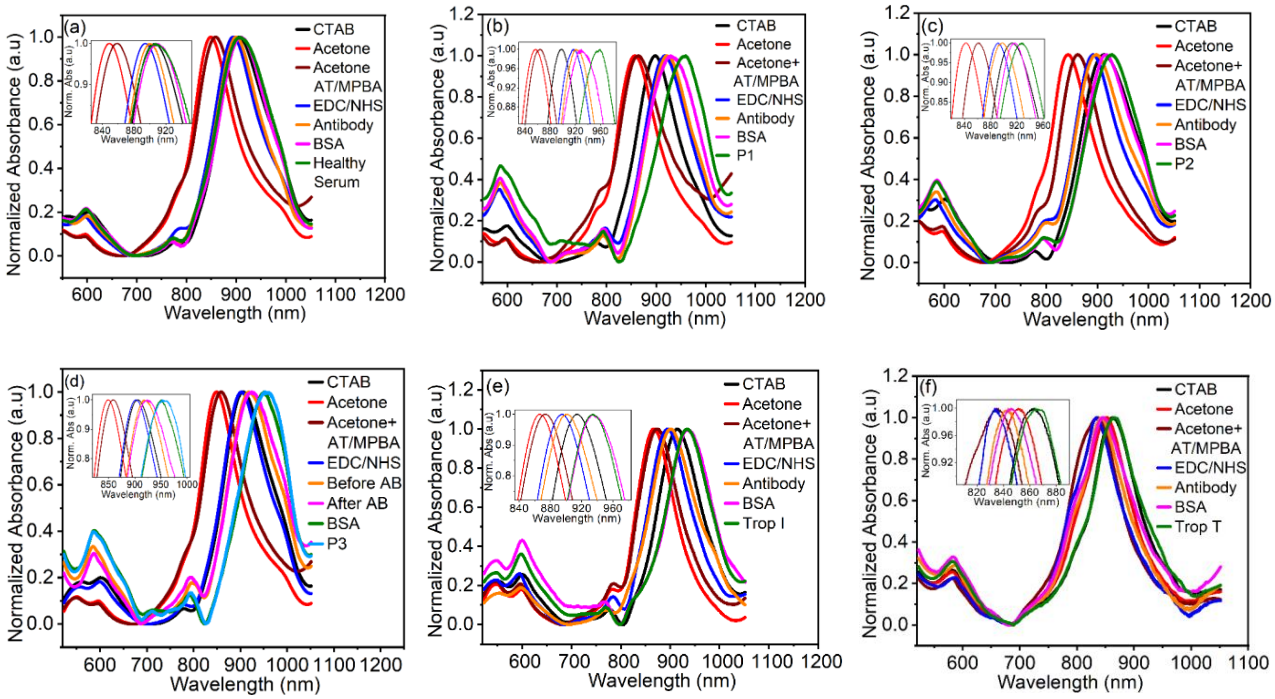


Fig. 9 LSPR spectra of the substrate at different functionalization and detection stages of NT-proBNP (a) for commercial human serum (b), for blood serum of patient 1, (c) for blood serum of patient 2, (d) for blood serum of patient 3, (e) specificity determination using CTnI, and (f) CTnT spiked in commercial human serum.

Table 2 LSPR band positions of sensor chip at different stages of functionalization and detection of CTnT.

Coverslip (CS)	**LSPR band positions (nm) at different functionalization stages**					
	a	b	c	d	e	f
before acetone	905.9	898.2	913.6	906.3	914.8	862.9
after acetone	849.2	857.4	843.1	849.4	867.3	851.3
after alkane thiols (AT)	858.8	864.2	862.2	859	873.7	834.8
after EDC/NHS	894.5	917.4	892	920.2	895	835.2
after antibody	900.3	923.2	898.1	925.2	901.4	842.7
after BSA	910.6	931.5	917	949.7	936.9	846.6
after patient serum	–	955.6	927.5	955	–	–
after commercial serum	908.6	–	–	–	–	–
after 100 ng/mL CTnI	–	–	–	–	934.9	–
after 100 ng/mL CTnT	–	–	–	–	–	864.7

3.4.2 Detection of Cardiac Troponin T (CTnT)

The prepared LSPR chip is used for the detection of another cardiac marker protein CTnT. Prior to the detection of CTnT, a monoclonal antibody specific to CTnT is immobilized on the EDC-NHS modified sensor chip by using a 50 µg/mL solution of CTnT. To avoid non-specific binding, the substrates were treated with 1% (10 mg/mL) BSA for 30 min. For the detection of CTnT, the antibody-immobilized sensor chip was incubated in the blood serum and separated from the cardiac patient blood samples for 2 h. As mentioned earlier, the LSPR spectra were recorded at each step of the functionalization of the sensor chip and detection of CTnT. Figs. 9(a–f) show the absorption spectra at different stages of sensor chip functionalization for 6 sensor chips. Corresponding Table 2 lists the LSPR band maxima position at each stage of sensor functionalization. The insets in Fig. 9 show the expanded spectral region adjacent to the longitudinal band maxima for clarity purposes. It is clearly evident from Fig. 9(f) and Table 2 that the LSPR band maxima shift 18 nm towards red after CTnT incubation. Similarly, red shifts in the LSPR band maxima are also seen for the blood serum of patients 1, 2, and 3 by ~24, ~10, and ~5 nm, respectively. A blue shift of nearly 2 nm was seen for the healthy serum and CTnI (100 ng/mL). The clear absence

of red shift for CTnI confirms the specificity of the sensor chip. Also, it is very much evident that CTnT can be detected from the patient's blood serum easily using the developed approach.

4 Conclusions

The Au NBPs with longitudinal LSPR band in the near-IR spectral region were synthesized using a seed-mediated approach. After removing a significant amount of capping molecule CTAB, successful immobilization of the nanostructure is demonstrated on the MPTMS silanized glass coverslips. The immobilized Au NBPs were further functionalized using 11-MUA and Octanethiol after completely removing CTAB using acetone. The removal of CTAB was investigated using RI sensitivity measurements. It was found that the RI sensitivity before the removal of CTAB was 197 nm/RIU, which becomes 303 nm/RIU after the removal of CTAB. Successful fabrication of the sensor chip is demonstrated after activation of the terminal group of 11-MUA with EDC-NHS treatment, followed by immobilization of antibodies of CTnT and NT-proBNP. Successful detection of the corresponding marker proteins was also shown with blood serum collected from cardiac patients. The specificity of the prepared sensor chip is also shown using another cardiac marker protein, CTnI. The approach demonstrated in the present work will be extremely helpful in the fabrication of LSPR sensor chips for detecting cardiac marker proteins in blood serum samples with very high specificity.

Acknowledgments

Financial support from the Department of Science and Technology (DST) India under the project grant number IDP/BDTD/11/2019 is gratefully acknowledged. Prajna N D acknowledges the TMA Pai Ph.D. fellowship from the Manipal Academy of Higher Education (MAHE).

Disclosures

The authors declare no conflict of interest.

References

1. S. Lv, Y. Du, F. Wu, Y. Cai, and T. Zhou, "Review on LSPR assisted photocatalysis: effects of physical fields and opportunities in multifield decoupling," Nanoscale Advances 4(12), 2608–2631 (2022).
2. H. Zhang, X. Zhou, X. Li, P. Gong, Y. Zhang, and Y .Zhao, "Recent Advancements of LSPR Fiber-Optic Biosensing: Combination Methods, Structure, and Prospects," Biosensors 13(3), 405 (2023).
3. T. Ghodselahi, T. Neishaboorynejad, and S. Arsalani, "Fabrication LSPR sensor chip of Ag NPs and their biosensor application based on interparticle coupling," Applied Surface Science 343, 194–201 (2015).
4. Y. Ziai, C. Rinoldi, P. Nakielski, L. D. Sio, and F. Pierini, "Smart plasmonic hydrogels based on gold and silver nanoparticles for biosensing application," Current Opinion in Biomedical Engineering 24, 100413 (2022).
5. B. Sepúlveda, P. C. Angelomé, L. M. Lechuga, and L. M. Liz-Marzán, "LSPR-based nanobiosensors," Nano Today 4(3), 244–251 (2009).
6. Y. Song, V. Tran, and J. Lee, "Tuning plasmon resonance in magnetoplasmonic nanochains by controlling polarization and interparticle distance for simple preparation of optical filters," ACS Applied Materials & Interfaces 9(29), 24433–24439 (2017).
7. N. C. Lindquist, P. Nagpal, K. M. McPeak, D. J Norris, and S.-H. Oh, "Engineering metallic nanostructures for plasmonics and nanophotonics," Reports on Progress in Physics 75(3), 036501 (2012).
8. M. Fan, G. F. Andrade, and A. G. Brolo, "A review on recent advances in the applications of surface-enhanced Raman scattering in analytical chemistry," Analytica Chimica Acta 1097, 1–29 (2020).
9. R. Pilot, R. Signorini, C. Durante, L. Orian, M. Bhamidipati, and L. Fabris, "A review on surface-enhanced Raman scattering," Biosensors 9(2), 57 (2019).
10. G. Barbillon, J.-L. Bijeon, J. Plain, M. L. de la Chapelle, P.-M. Adam, and P. Royer, "Electron beam lithography designed chemical nanosensors based on localized surface plasmon resonance," Surface Science 601(21), 5057–5061 (2007).
11. Y. Lin, Y. Zou, Y. Mo, J. Guo, and R. G. Lindquist, "E-beam patterned gold nanodot arrays on optical fiber tips for localized surface plasmon resonance biochemical sensing," Sensors 10(10), 9397–9406 (2010).
12. T. R. Jensen, M. D. Malinsky, C. L. Haynes, and R. P. Van Duyne, "Nanosphere lithography: tunable localized surface plasmon resonance spectra of silver nanoparticles," The Journal of Physical Chemistry B 104(45), 10549–10556 (2000).
13. C. L. Haynes, R. P. Van Duyne, "Nanosphere lithography: a versatile nanofabrication tool for studies of size-dependent nanoparticle optics," The Journal of Physical Chemistry B 105(24), 5599–5611 (2001).
14. J. D. Driskell, S. Shanmukh, Y. Liu, S. B. Chaney, X.-J. Tang, Y.-P. Zhao, and R. A. Dluhy, "The use of aligned silver nanorod arrays prepared by oblique angle deposition as surface-enhanced Raman scattering substrates," The Journal of Physical Chemistry C 112(4), 895–901 (2008).
15. S. Kaabipour, S. Hemmati, "A review on the green and sustainable synthesis of silver nanoparticles and one-dimensional silver nanostructures," Beilstein Journal of Nanotechnology 12(1), 102–136 (2021).

16. H. Chen, X. Kou, Z. Yang, W. Ni, and J. Wang, "Shape-and size-dependent refractive index sensitivity of gold nanoparticles," Langmuir 24(10), 5233–5237 (2008).
17. N. R. Jana, L. Gearheart, and C. J. Murphy, "Seed-Mediated Growth Approach for Shape-Controlled Synthesis of Spheroidal and Rod-like Gold Nanoparticles Using a Surfactant Template," Advanced Materials 13(18), 1389–1393 (2001).
18. M. Liu, P. Guyot-Sionnest, "Mechanism of Silver(I)-Assisted Growth of Gold Nanorods and Bipyramids," The Journal of Physical Chemistry B 109(47), 22192–22200 (2005).
19. X. Zhang, M. Tsuji, S. Lim, N. Miyamae, M. Nishio, S. Hikino, and M. Umezu, "Synthesis and Growth Mechanism of Pentagonal Bipyramid-Shaped Gold-Rich Au/Ag Alloy Nanoparticles," Langmuir 23(11), 6372–6376 (2007).
20. Y. Xu, X. Wang, L. Cheng, Z. Liu, and Q. Zhang, "High-yield synthesis of gold bipyramids for in vivo CT imaging and photothermal cancer therapy with enhanced thermal stability," Chemical Engineering Journal 378, 122025 (2019).
21. S. Barbosa, A. Agrawal, L. Rodríguez-Lorenzo, I. Pastoriza-Santos, R. A. Alvarez-Puebla, A. Kornowski, H. Weller, and L. M. Liz-Marzán, "Tuning size and sensing properties in colloidal gold nanostars," Langmuir 26(18), 14943–14950 (2010).
22. S. M. Marinakos, S. Chen, and A. Chilkoti, "Plasmonic detection of a model analyte in serum by a gold nanorod sensor," Analytical chemistry 79(14), 5278–5283 (2007).
23. H. R. Hegde, S. Chidangil, and R. K. Sinha, "Refractive index sensitivity of Au nanostructures in solution and on the substrate," Journal of Materials Science: Materials in Electronics 33(7), 4011–4024 (2022).
24. H. R. Hegde, S. Chidangil, and R. K. Sinha, "Refractive index and formaldehyde sensing with silver nanocubes," RSC advances 11(14), 8042–8050 (2021).
25. G. A. Roth et al., "Global, regional, and national age-sex-specific mortality for 282 causes of death in 195 countries and territories, 1980–2017: a systematic analysis for the Global Burden of Disease Study 2017," The Lancet 392(10159), 1736–1788 (2018).
26. J. A. Reyes-Retana, L. C. Duque-Ossa, "Acute Myocardial Infarction Biosensor: A Review From Bottom Up," Current Problems in Cardiology 46(3), 100739 (2021).
27. S. Upasham, A. Tanak, and S. Prasad, "Cardiac troponin biosensors: where are we now," Advanced Health Care Technologies 4, 1–13 (2018).
28. A. Qureshi, Y. Gurbuz, and J. H. Niazi, "Biosensors for cardiac biomarkers detection: A review," Sensors and Actuators B: Chemical 171–172, 62–76 (2012).
29. R. K. Sinha, "Wavelength modulation based surface plasmon resonance sensor for detection of cardiac marker proteins troponin I and troponin T," Sensors and Actuators A: Physical 332, 113104 (2021).
30. L. Tang, J. Casas, "Quantification of cardiac biomarkers using label-free and multiplexed gold nanorod bioprobes for myocardial infarction diagnosis," Biosensors and Bioelectronics 61, 70–75 (2014).
31. Y. M. Bae, S. O. Jin, I. Kim, K. Y. Shin, and D. Heo, "Detection of biomarkers using LSPR substrate with gold nanoparticle array," Journal of Nanomaterials 2015, 302816 (2015).
32. T. Liyanage, A. Sangha, and R. Sardar, "Achieving biosensing at attomolar concentrations of cardiac troponin T in human biofluids by developing a label-free nanoplasmonic analytical assay," Analyst 142(13), 2442–2450 (2017).
33. P. N. Deviprasada, R. K. Sinha, "Highly Stable 11-MUA Capped Gold Nanobipyramid for Refractive Index Sensing," Journal of Biomedical Photonics & Engineering 9(1), 010308 (2023).
34. D. Chateau, A. Desert, F. Lerouge, G. Landaburu, S. Santucci, and S. Parola, "Beyond the concentration limitation in the synthesis of nanobipyramids and other pentatwinned gold nanostructures," ACS Applied Materials & Interfaces 11(42), 39068–39076 (2019).
35. R. K. Sinha, "A simple and inexpensive surface plasmon resonance setup for phase detection using rotating analyzer ellipsometric method," Laser Physics 30(2), 026202 (2019).
36. C. A. Schneider, W. S. Rasband, and K. W. Eliceiri, "NIH Image to ImageJ: 25 years of image analysis," Nature Methods 9(7), 671–675 (2012).
37. A. F. Stalder, T. Melchior, M. Müller, D. Sage, T. Blu, and M. Unser, "Low-bond axisymmetric drop shape analysis for surface tension and contact angle measurements of sessile drops," Colloid Surfaces A 364(1–3), 72–81 (2010).
38. J. Casas, M. Venkataramasubramani, Y. Wang, and L. Tang, "Replacement of cetyltrimethylammonium bromide bilayer on gold nanorod by alkanethiol crosslinker for enhanced plasmon resonance sensitivity," Biosensors and Bioelectronics 49, 525–530 (2013).
39. A. Wijaya, K. Hamad-Schifferli, "Ligand Customization and DNA Functionalization of Gold Nanorods via Round-Trip Phase Transfer Ligand Exchange," Langmuir 24(18), 9966–9969 (2008).
40. H. Hegde, C. Santhosh, and R.K. Sinha, "Seed mediated synthesis of highly stable CTAB capped triangular silver nanoplates for LSPR sensing," Materials Research Express 6(10), 105075 (2019).
41. A. Sánchez-Iglesias, N. Winckelmans, T. Altantzis, S. Bals, M. Grzelczak, and L. M. Liz-Marzán, "High-yield seeded growth of monodisperse pentatwinned gold nanoparticles through thermally induced seed twinning," Journal of the American Chemical Society 139(1), 107–110 (2017).

42. M. Ghorbanpour, C. Falamaki, "A novel method for the fabrication of ATPES silanized SPR sensor chips: Exclusion of Cr or Ti intermediate layers and optimization of optical/adherence properties," Applied Surface Science 301, 544–550 (2014).
43. H. Jung, C. K. Dalal, S. Kuntz, R. Shah, and C. P. Collier, "Surfactant activated dip-pen nanolithography," Nano Letters 4(11), 2171–2177 (2004).
44. A. R. Ferhan, L. Guo, and D. H. Kim, "Influence of ionic strength and surfactant concentration on electrostatic surfacial assembly of cetyltrimethylammonium bromide-capped gold nanorods on fully immersed glass," Langmuir 26(14), 12433–12442 (2010).

Motion Estimation of Handheld Optical Coherence Tomography System using Real-Time Eye Tracking System

Abira Bright B., Lakshmi Parvathi M., and Vani Damodaran*
Department of Biomedical Engineering, SRM Institute of Science and Technology, Kattankulathur 603203, Tamil Nadu, India

***e-mail:** vanid@srmist.edu.in

Abstract. Optical coherence tomography (OCT) is the clinical golden standard for cross-sectional imaging of the eye. The majority of clinical ophthalmic OCT systems are table-top devices that need the patient to align with the chinrest in order to capture a motion-free image. Portable OCT devices are used to perform retinal imaging on infants or patients who are confined to beds. Eye movements and relative motion between the patient and the imaging probe make interpretation and registration challenging and become a barrier to high-resolution ocular imaging. Thus, an OCT scanner with an automated real-time eye tracking system and a movement mapping for correction mechanism is required to overcome such motions. The aim of this work is to develop an algorithm to track pupil motion and allow motion-corrected imaging of the retina without the requirement of chinrest, fixation of the target, or seating chair and to minimize the requirement of skillset to operate and to correct motion artifacts. Two algorithms based on landmark and threshold were developed, capable of identifying and monitoring eye movements. The acquired output value of both algorithms was compared with the manually calculated actual center value of the pupil. The average deviation from the actual location was found to be 0.2∼0.6 for the landmark and 0.4∼0.9 for the threshold-based algorithm. In this study, it is observed that iris localization and gaze direction estimation is more accurate in the landmark-based system compared to the threshold-based eye-tracking system. © 2023 Journal of Biomedical Photonics & Engineering.

Keywords: optical coherence tomography (OCT); depth Camera; eye tracking; gaze tracking.

Paper #8306 received 28 Feb 2023; revised manuscript received 11 Aug 2023; accepted for publication 16 Aug 2023; published online 15 Sep 2023. doi: 10.18287/JBPE23.09.030314.

1 Introduction

Optical Coherence Tomography (OCT) is a non-invasive, high-resolution imaging system [1] that provides structural data on biological tissues [2]. It is the gold standard for imaging retinal [3]. Both the anterior and posterior portions of the eye are imaged using it [4]. However, major OCT systems are tabletop devices that are only available in imaging rooms in eye care facilities. Additionally, to operate and align these systems, qualified ophthalmic personnel are required. Only patients who can sit straight, use a chinrest arrangement, and fixate their attention on a target can use these devices. As a result, OCT imaging cannot be performed outside the clinic and for elderly, infant, and bedridden patients. Handheld OCT probes [5] and image registration methods [6] can be used to overcome these barriers of table top systems.

Handheld OCT systems suffer from two issues, i.e. operator stability and patient movement. Operator stability refers to the stability of the probe holding, and patient movement, refers to eye and head movement. Eye movements can be classified into Saccadic movement and Smooth pursuit movement [7]. Humans perform multiple saccades to align their visual axis with the subject of interest, and rapid eye movement help, to

This paper was presented at the International Conference on Nanoscience and Photonics for Medical Applications – ICNPMA, Manipal, India, December 28–30, 2022.

correct the position error between the eye's visual axis and the subject. Smooth pursuit eye movements help stabilize the projection of the moving subject onto the fovea and correct any velocity error between the eye and the subject [8]. These movements can cause distortion while acquiring retinal images which directly affects the image quality [9, 10]. Image registration, a sort of digital motion correction, helps to eliminate motion artifact's caused by operator tremors and/or patient movements. These image registration techniques, however, are unable to repair large-scale motion distortions that result in data loss owing to misalignment, necessitating the use of steady-handed, highly qualified operators [11]. The most effective way to overcome the issues is to design. An eye-tracking system to track eye movements and generate input to the OCT scanner for motion compensation. This feature would make the imaging system more robust and user-friendly.

Numerous real-time eye-tracking systems are available, typically electrooculography, contact lens techniques, limbus tracker, dual Purkinje, and video-based pupil tracking. However, video-based tracking is more advantageous over other methods due to its high resolution, flexibility, precision, and accuracy tracking techniques [12]. As cost-effective alternatives, these systems are employed with linguistic tools like OpenCV and Visual C [13]. The quality of the camera and the speed of the programme rely on software performance time [10, 11].

In this work, the development of a pupil-tracking system using a depth camera is described. The pupil tracking was performed using two algorithms. The outcomes are assessed and compared to identify the better performing algorithm.

2 Methodology

Eye movements are unavoidable during OCT imaging, especially in live subjects. Eye tracking allows real-time monitoring of these movements and helps correct motion artifacts, ensuring high-quality images even in the presence of patient movements. With eye tracking, OCT systems can work more efficiently. The system can automatically follow the eye's movements, reducing the need for manual adjustments and potentially speeding up the imaging process. In order to track the eye movement, it is important to use high resolution camera to detect very small changes. An eye tracker continuously records eye movements, which will be given as the input to the scanning system of the OCT system in order to align with the eye precisely. The tracking system involves image acquisition using a depth camera and the eye is isolated from the detected face. The acquired eye images are pre-processed to remove morphological noises caused by light reflection in the iris. The iris is then detected using threshold and landmark based algorithm. The detected iris region is then tracked to estimate gaze as shown in Fig. 1.

2.1 Image Acquisition

The eye is imaged using the Intel Real Sense Depth Camera D435i. This camera consists of a cutting-edge stereo-edge system (stereo depth baseline 1080p RGB), equipped with an inertial measurement unit (IMU) for detecting rotations and motions. The specification of the camera is presented in Table 1.

Table 1 Specification of Real Sense Camera D435i.

Pixel	1280 × 800
Resolution	720 p
Frame Rate	30 fps
(L × B × H)	36.5 × 19.4 × 10.5 mm
Focal Length	1.93 mm
Interface	USB

The required software packages and wrappers, namely the Intel RealSense SDK (Software Development Kit) from Github and Python wrappers were downloaded from the Python Platform. Real-time data acquisition and image processing were performed in Python.

The pupil is the dark circular aperture in the center of the eye that controls the amount of light entering the eye. By analyzing the position and movement of the pupils, eye-tracking systems can infer valuable information about a person's gaze direction. In this work, two eye-tracking methods are adopted, one is threshold based and the other is landmark-based. The subject is instructed to sit at approximately 7 cm (the minimum distance for the depth camera being utilized) from the camera, and both algorithms are used to assess eye movement in various directions.

In order to verify both the algorithm's performance, the pupil movement in each frame is measured. The number of pixel needs to be mapped with distance in mm. In order to estimate what a pixel represents in mm, a graph sheet is used. The graph sheet is placed at 7 cm from the camera and imaged. The number of pixels occupying one column (1 cm width) is estimated using Euclidean distance and is found to be 70 pixels as shown in Fig. 2 and each pixel represents 0.148 mm.

All the images were assessed manually to locate the center and movement of the eye in a different direction, this was used as ground truth to analysis the accuracy of the algorithm.

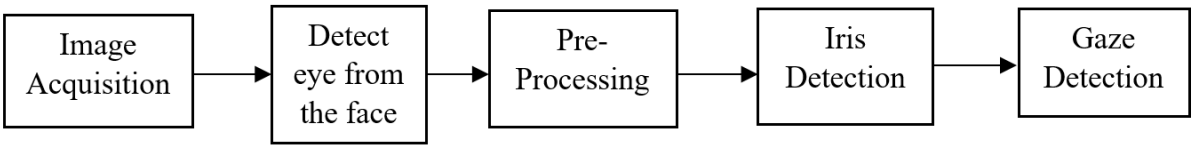


Fig. 1 Overview of gaze tracking algorithm.

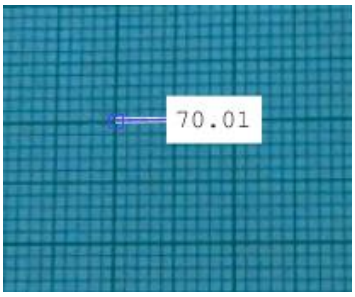


Fig. 2 Pixel to distance calculation using graph sheet.

2.2 Threshold-Based Eye Tracking

In threshold based eye tracking method, real-time RGB images are acquired using RealSense Depth D435i Camera. The face is detected using Haar features [9]. Haar features are a key component in the Viola-Jones face detection algorithm, which is a widely used and efficient method for detecting faces in images. The Viola-Jones algorithm is based on the principle of cascaded classifiers and uses Haar-like features to represent regions of an image and distinguish between facial and non-facial regions [14]. The threshold-based eye tracking algorithm flowchart is shown in Fig. 3.

A rectangular bounding box is marked surrounding the face region and eye region as shown in Fig. 4(a). Bounding boxes are used for region localization and isolation of the entire the region of interest (ROI) from an image as shown in Fig. 4(b). Once the bounding box is placed around the eye region, the pupil is tracked. The RGB is converted to a grayscale image as shown in Fig. 4(c). The grayscale is then converted to a binary image by thresholding (a threshold value of 70 is used) as shown in Fig. 4(d). All the pixel values greater or less than the threshold value are assigned to the maximum or minimum value respectively. The thresholding step clearly separates the ROI, i.e differentiating the sclera from the iris.

Once the pupils are detected, their positions are localized within the image. This allows the system to determine the precise position of the pupil. To track the pupils over time, the system establishes associations between the detected pupils in consecutive frames. After the pupils are continuously tracked, the eye-tracking system analyses the movement patterns and infers the person's gaze direction.

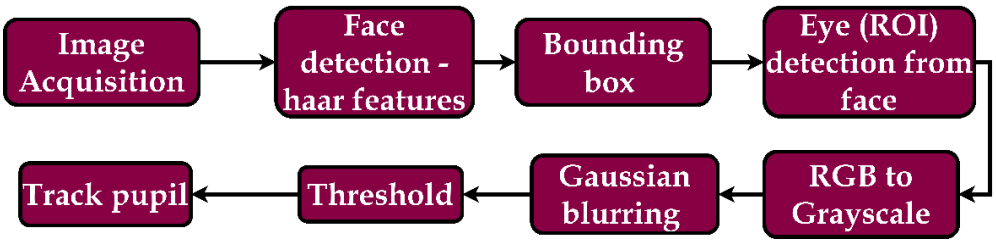
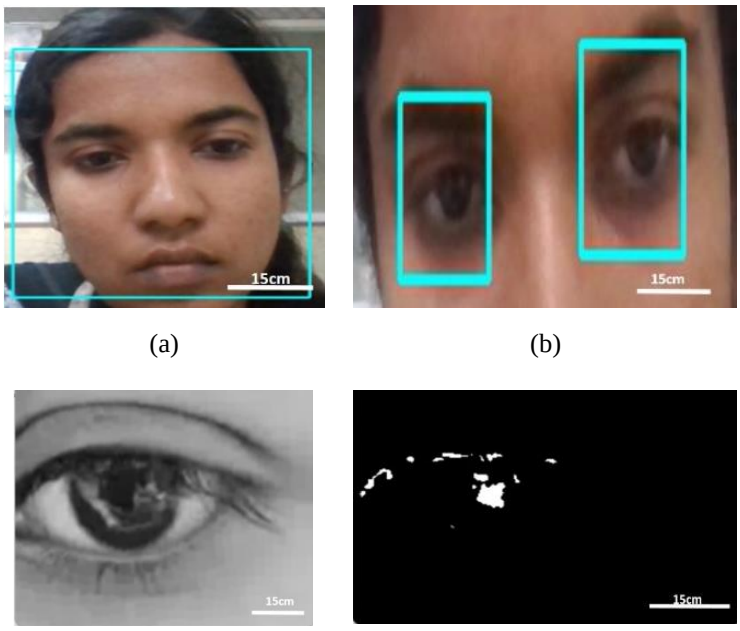


Fig. 3 Threshold based eye tracking algorithm flowchart.



(a) (b)

(c) (d)

Fig. 4 Threshold based eye tracking (a) face detection using Haar features, (b) bounding box for eye detection, (c) RGB to gray scale image, and (d) thresholding for iris detection.

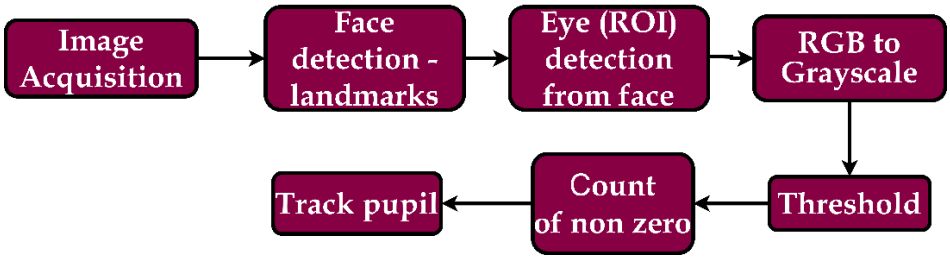


Fig. 5 Landmark based eye tracking algorithm flowchart.

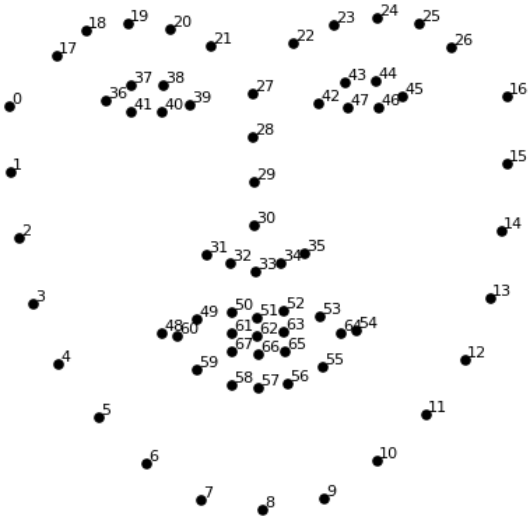


Fig. 6 Facial landmarks with 68 points from the machine learning library Dlib.

2.3 Landmark-Based Eye Tracking

In Landmark based method, a mesh model is used to identify different features in the face. The data is acquired from the Real Sense Depth D435i Camera. The video data is converted to frames, the RGB frames are converted to Grayscale. The overall algorithm flowchart is shown in Fig. 5.

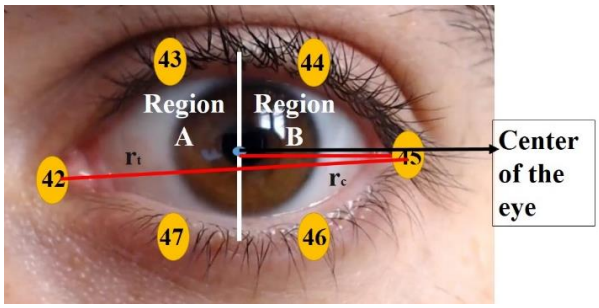
The machine learning library Dlib [15] based 68 landmark mesh model is used in this work to identify eye as shown in Fig. 6. This model processes the grayscale frame and returns 68 landmarks for each detected face. These landmarks are used to ensure accuracy irrespective of the age of the patient and the size of the face. The ROI (region of interest) is extracted by selecting the landmarks which denote the eye region ((right eye (36–41), left eye (42–47))).

This method measures angular eye position relative to the face movement using facial landmarks and measures eye position relative to these landmarks. It creates a mesh of the approximate eye region and separates the eye region from the original frames by using media Dlib. In order to identify the iris, the ROI region is thresholded. A threshold of 70 was chosen after multiple trials. The grayscale images are converted into binary images based on the chosen threshold.

For processing only one eye is taken (left eye) as shown in Fig. 7(a). Eye landmarks 43 and 44 which are in the upper region, and 46 and 47 from the bottom region are averaged and a vertical line is drawn to form the reference center point. The line divides the eye region as left and right region as shown in Fig. 7(b). To localize the iris position, the non-zero pixels are counted in each region. When the eye looks to the right the non-zero value is higher on the left side and vice versa. This help in detecting the direction in which the eye has moved.



(a)



(b)

Fig. 7 (a) Right eye landmarks, (b) eye movement detection by dividing eye into regions and calculating non-zero value in both regions.

An iris position ratio is computed in this study to precisely locate the iris. As a starting point, the eye's right landmark is used. The distance of the center of the eye from this reference point is measured and denoted as r_c as shown in Fig. 7(b). The r_t denotes the measurement of the distance between the left and right landmarks of the eye. In order to determine whether the iris is close to or far from the right landmark of the eye, i.e. to estimate if the iris is left, center, or right, the ratio of the two measured distances is used. The iris position ratio k value is represented in Eq. (1). Three categories comprise the calculated ratio value: non-zero values in A < B correspond to the left, A = B to the center, and A > B to the right. These values are derived based on measurements of various eye images.

$$k = \frac{r_c}{r_t}. \quad (1)$$

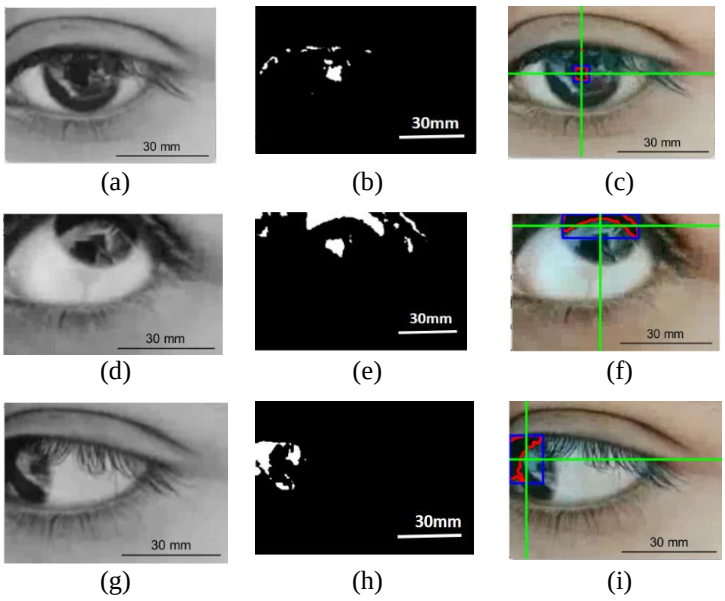


Fig. 8 Threshold-based eye tracking (a, d, g) extracted eye regions showing eyes in different positions; (b, e, h) extracted eye image is thresholded to identify the direction of gaze from (a), (d), and (g), respectively; (c, f, i) pupil is detected and gaze direction is determined to see if the eye is the center, up and right direction, respectively.

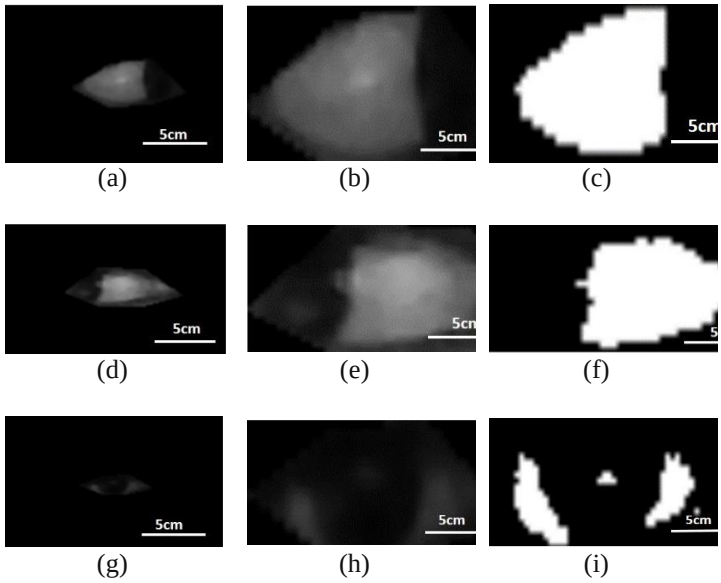


Fig. 9 Landmark-based real-time eye tracking system (a, d, g) the eye region is extracted from the face; (b, e, h) eye region landmarks are used to exclude the eyelashes and extract only the eye region from the frame (a), (d), and (g) respectively; (c, f, i) the extracted eye region is contoured to identify the direction of the eye movement and the gaze direction is identified as right, left and center respectively.

3 Result and Discussions

Two eye-tracking systems were developed and the performance of both algorithms on gaze tracking were assessed. Both the eye tracking algorithm were tested on 10 frames. The images include different positions of the iris and the precise location and tracking of these movements using threshold based algorithm and landmark based algorithm are as shown in Fig. 8 and Fig. 9, respectively.

In the threshold-based method, once the eye region is separated from the face, thresholding is used to isolate the iris alone. The center of the iris is then estimated and shown as a marker in the original image for live tracking of the eye.

The tracking output of the landmark-based algorithm was tested in different eye directions and under different light conditions as shown in Fig. 9. The eye is first extracted from the face image as shown in Fig. 9(a). Using the landmarks of the eye, the lashes are eliminated and only the eye region is extracted as shown in Fig. 9(b). Based on thresholding, the iris and the surrounding sclera are identified and the total number of non-zero pixels to the left and right of the

center of the iris is calculated in order to identify position of the eye A < B eyelooking left, A = B eye is at the center, A > B eye looking right) as shown in Fig. 9(c).

Table 2 Comparison of average deviation observed for threshold, landmark, and manual method in the estimation of center of iris.

Frames	Threshold	Landmark	Actual center
1	1.6	1.2	1.0
2	0.9	0.6	0.4
3	1.2	1.0	0.9
4	0.85	0.6	0.5
5	1.0	0.5	0.4
6	0.7	0.4	0.4
7	0.65	0.5	0.5
8	0.9	0.5	0.4
9	1.1	1.0	0.95
10	0.85	0.7	0.7

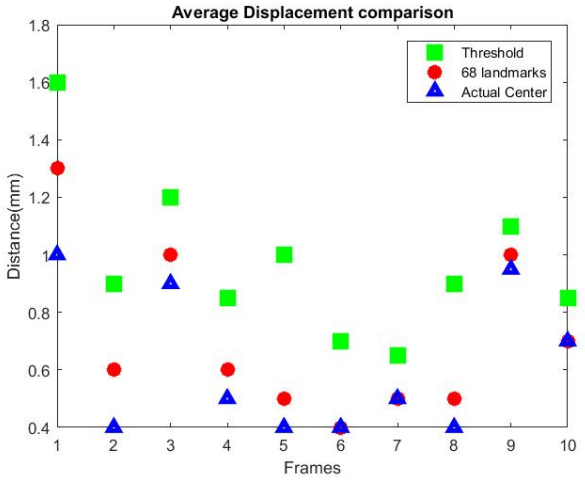


Fig. 10 Average deviation observed for threshold and landmark-based methods.

The individual frames are also assessed manually to identify the actual position of the iris by locating the center of the iris. The average deviation of these measured values is used as ground truth to assess the accuracy of the threshold and landmark based algorithms as shown in Table 2.

For landmark-based displacement, the average deviation was found to be in the range of approximately 0.2~0.6 whereas for the threshold-based system, the deviation was approximately 0.4~0.9. Hence, the iris localization and gaze direction estimation are more accurate in landmark-based system than threshold-based eye tracking systems. A graphical representation of the average deviation is shown in Fig. 10. It can be observed that the landmark-based system has a higher correlation with the actual center compared to threshold-based algorithm.

4 Conclusion

In order to automatically align the handheld imaging system, tracking of the eye is important. Two algorithms were developed and tested for iris detection and gaze tracking. The threshold-based algorithm uses a bounding box technique and the landmark-based algorithm uses 68 landmarks to precisely locate the iris. The movement of the iris is tracked to estimate the position of the eye. A total of 10 frames were used to analyze the efficiency of the algorithms. The average deviation from the manually calculated iris position is estimated for both algorithms and found to be 0.2~0.6 and 0.4~0.9 for threshold and landmark respectively. It is clearly observed that the landmark-based algorithm tracks the iris better. Future work on improving the facial landmark system and implementation of the same on a handheld OCT system is underway.

Acknowledgement

This work was supported by the SERB-funded Startup-grant project No: SRG/2020/002076.

Disclosures

The authors declare no conflict of interest.

References

1. V. Mazlin, P. Xiao, K. Irsch, J. Scholler, K. Groux, K. Grieve, M. Fink, and A. C. Boccara, "Optical phase modulation by natural eye movements: application to time-domain FF-OCT image retrieval," Biomedical Optics Express 13(2), 902–920 (2022).
2. J. A. Izatt, M. R. Hee, E. A. Swanson, C. P. Lin, D. Huang, J. S. Schuman, C. A. Puliafito, and J. G. Fujimoto, "Micrometer-Scale Resolution Imaging of the Anterior Eye In Vivo With Optical Coherence Tomography," Archives of Ophthalmology 112(12), 1584–1589 (1994).
3. E. A. Swanson, J. A. Izatt, M. R. Hee, D. Huang, C. P. Lin, J. S. Schuman, C. A. Puliafito, and J. G. Fujimoto, "In vivo retinal imaging by optical coherence tomography," Optics Letters 18(21), 1864–1866 (1993).

4. U. Schmidt-Erfurth, S. Klimscha, S. M. Waldstein, and H. Bogunović, "A view of the current and future role of optical coherence tomography in the management of age-related macular degeneration," Eye 31(1), 26–44 (2017).
5. W. Jung, J. Kim, M. Jeon, E. J. Chaney, C. N. Stewart, and S. A. Boppart, "Handheld Optical Coherence Tomography Scanner for Primary Care Diagnostics," IEEE Transactions on Biomedical Engineering 58(3), 741–744 (2011).
6. N. D. Shemonski, F. A. South, Y.-Z. Liu, S. G. Adie, P. S. Carney, and S. A. Boppart, "Computational high-resolution optical imaging of the living human retina," Nature Photonics 9(7), 440–443 (2015).
7. P. J. Rosenfeld, M. K. Durbin, L. Roisman, F. Zheng, A. Miller, G. Robbins, K. B. Schaal, and G. Gregori, "ZEISS AngioplexTM Spectral Domain Optical Coherence Tomography Angiography: Technical Aspects," in OCT Angiography in Retinal and Macular Diseases, F. Bandello, E. H. Souied, and G. Querques (Eds.), S. Karger AG, 56, 18–29 (2016).
8. H. Singh, J. Singh, "Human eye tracking and related issues: A review," International Journal of Scientific and Research Publications 2(9), 1–9 (2012).
9. Z. R. Cherif, A. Nait-Ali, J. F. Motsch, and M. O. Krebs, "An adaptive calibration of an infrared light device used for gaze tracking," in IMTC/2002. Proceedings of the 19th IEEE Instrumentation and Measurement Technology Conference (IEEE Cat. No.00CH37276), 2, Anchorage, AK, USA, 1029–1033 (2002).
10. W. Wang, Y. Huang, and R. Zhang, "Driver gaze tracker using deformable template matching," In Proceedings of 2011 IEEE International Conference on Vehicular Electronics and Safety, Beijing, China, 244–247 (2011).
11. N. H. Cuong, H. T. Hoang, "Eye-gaze detection with a single WebCAM based on geometry features extraction," In 2010 11th International Conference on Control Automation Robotics & Vision, Singapore, 2507–2512 (2010).
12. S. Das, S. K. Swar, S. Laha, S. Mahindar, S. Halder, H. Koushik, and S. Deb, "Design approach of Eye Tracking and Mind Operated Motorized System," International Journal of Innovative Research in Science, Engineering and Technology (An ISO 3297: 2007 Certified Organization) 5(8), 14349–14357 (2016).
13. I. García, S. Bronte, L. M. Bergasa, N. Hernández, B. Delgado, and M. Sevillano, "Vision-based drowsiness detector for a realistic driving simulator," In 13th International IEEE Conference on Intelligent Transportation Systems, Funchal, Portugal, 887–894 (2010).
14. B. S. Kim, H. Lee, and W. Y. Kim, "Rapid eye detection method for non-glasses type 3D display on portable devices," IEEE Transactions on Consumer Electronics 56(4), 2498–2505 (2010).
15. D. E. King, "Dlib-ml: A machine learning toolkit," The Journal of Machine Learning Research 10, 1755–1758 (2009).

Differences in the Effect of 40%-Glucose on the Optical Properties of Healthy and Stromal-Sarcoma Ovaries in Cats

Aleksey A. Selifonov[1*] and Valery V. Tuchin[2,3,4]

[1] Education and Research Institute of Nanostructures and Biosystems, Saratov State University, Saratov 410012, Russia
[2] Institute of Physics and Science Medical Center, Saratov State University, Saratov 410012, Russia
[3] Laboratory of Laser Molecular Imaging and Machine Learning, Tomsk State University, Tomsk 634050, Russia
[4] Laboratory of Laser Diagnostics of Technical and Living Systems, Institute of Precision Mechanics and Control, FRC "Saratov Scientific Centre of the Russian Academy of Sciences," Saratov 410028, Russia

***e-mail:** peshka029@gmail.com

Abstract. Differences in diffuse reflectance and total transmittance of healthy and sarcoma cat ovarian tissue were determined using integrating sphere spectroscopy and confirmed by histological analysis. The effective diffusion coefficient determined from the analysis of the kinetics of the diffuse reflectance was found equal to $D = (7.5 \pm 0.9)10^{-7}$ cm^2/s for healthy tissue and $D = (1.4 \pm 0.2)10^{-6}$ cm^2/s for sarcoma. In healthy tissue, optical clearing occurred with the formation of two UV transparency windows: (18 ± 4) nm wide centered at 225 nm and (50 ± 12) nm wide centered at 375 nm. For the ovary with sarcoma, the formation of only one transparency window centered at 380 nm and a width of (43 ± 11) nm was observed. © 2023 Journal of Biomedical Photonics & Engineering.

Keywords: ovarian tissues; cancer; glucose; total transmittance spectra; diffuse reflectance spectra; diffusion coefficient; optical clearing efficiency.

Paper #8986 received 3 Jun 2023; revised manuscript received 11 Jul 2023; accepted for publication 11 Jul 2023; published online 15 Sep 2023. doi: 10.18287/JBPE23.09.030315.

1 Introduction

Ovarian cancer is the fifth leading cause of death for women with cancer worldwide [1]. More than 70% of cancers are only diagnosed at an advanced stage. If ovarian cancer is detected in the initial stages, then the complete remission is 94%, while the detection of a tumor in the later stages reduces the chance of survival to 45% [2]. Overall, the five-year survival prognosis for ovarian cancer remains unfavorable at 46% [3]. The prognosis is closely related to the stage at the time of diagnosis: survival > 70% after 5 years in stage I or II, survival from 20 to 40% in stage III or IV [3, 4]. Despite the advances in modern medicine, the five-year survival of patients with this diagnosis has not increased much over the past half century [4]. Modern research of the problem of early diagnosis and effective treatment of cancer of the reproductive system combines surgical advances, the study of genomics and precision therapy. For example, in advanced economies, patients with ovarian, fallopian tube, or primary peritoneal cancer should undergo genetic risk assessment, and germline and somatic testing. Germline testing refers to the use of blood or saliva to test for genes that are expected to be identical throughout the body, while somatic testing focuses on genes in a tumor and may affect treatment. In modern clinical practice, it is very difficult to take into account gene mutations in the treatment of specific patients. Interdisciplinary precision medicine research is required because genomic mutations between histological subtypes of ovarian cancer are often observed [5]. Routine ultrasound examination of women does not provide accurate verification of benign and malignant changes [6]. Biological markers are often used to specifically detect epithelial ovarian cancer and metastatic ovarian carcinoma, in particular in the HE4, CA 125, RMI, and ROMA algorithms [7]. To date, the most effective biological diagnostic tool for diagnosing ovarian cancer is the combination of CA125 and HE4 [8]. However, there is no exact probability of detecting malignant changes in the early stages using the above algorithms and tumor markers, since the results are influenced by factors such as smoking or contraception that combines estrogen with progestin, endometriosis, benign changes, etc. [9, 10]. It is important to differentiate early malignant ovarian tumors from benign

ovarian tumors. Therefore, examinations are necessary and should be prioritized in order to advise the patient (monitoring, treatment or examination) according to the lesion, and first of all, taking into account the patient's medical history. Actively developing optical systems may have good prospects for the early detection of cancer, in particular of the reproductive system [11]. However, when using optical systems in clinical medical practice, strong light scattering of biological tissues prevents radiation from passing into deep layers and obtaining ultra-precise images. One of the approaches to solving this problem can be the optical clearing method, which is implemented using optical clearing agents: poly- and monosaccharides, alcohols, dimethyl sulfoxide, etc. [12].

In this work, to realize the main goal of the study, namely, to reliably determine the differences in the optical and diffusion properties of normal and tumor ovarian tissue, 40% aqueous glucose solution was chosen as an optical clearing agent. The objects of the study were clinically healthy ovaries of cats and ovaries with neoplasms in the form of stromal sarcoma, which was confirmed by histological studies. Determination of spectral and kinetic characteristics at optical clearing was carried out in the wavelength range of 200–800 nm by the method of diffusion reflection spectroscopy. Such parameters were determined as the effective diffusion coefficient of 40% glucose in healthy and pathological tissue, as well as the efficiency of optical clearing with finding new virtual windows of tissue transparency.

2 Materials and Methods

For *ex vivo* studies, ovaries from outbred cats aged 5 to 10 years obtained after ovariectomy and ovariohysterectomy in a veterinary hospital were used. A total of 6 samples from 3 ovaries from different cats diagnosed as "clinically healthy" and 6 samples from 2 ovaries from one animal with suspected malignancy were examined. To clarify the diagnosis, we carried out histological examination of the samples no later than 48 h after removal. To do this, a part of the sample was manually cut from each ovary with a scalpel and fixed in 10% buffered formalin. The remaining parts of the ovaries were kept frozen until optical measurements were taken. For histological examination of all samples, hematoxylin-eosin staining was used. To obtain histological scans, an Aperio AT2 digital slide converter (on-screen diagnostic scanner) equipped with a LED light source and calibration tools was used.

For optical measurements, 6 sections from healthy and 6 sections from pathological ovaries were used. The thickness of tissue sections (samples) was measured with an electron micrometer (Union Source CO., Ltd., China, Ningbo). The measurements were carried out at several points of the sample and averaged. The accuracy of each measurement was ± 0.01 mm. The average thickness of the sections of the ovaries was (0.80 ± 0.09) mm. To measure the diffuse reflectance spectra (DRS) and total transmission spectra (TTS) of tissue samples in the spectral range of 200–800 nm, a Shimadzu UV-2550 double-beam spectrophotometer (Japan, Tokyo) with an integrating sphere was used (Fig. 1).

The light source was a halogen lamp with filtering in the studied spectral range. The limiting resolution of the spectrometer was 0.1 nm. Prior to measurements, the spectra were normalized using a $BaSO_4$ reference reflector with a suitable reflectivity for the entire spectral range, including UV. All measurements were carried out at room temperature (~25 °C) and normal atmospheric pressure. Each sample of the studied tissue was fixed with double-sided adhesive tape in a special frame with a window of 0.5 × 0.5 cm in a quartz cuvette so that the tissue sample was pressed against the wall of the cuvette and subjected to optical measurement of DRS or TTS, as shown in Fig. 1. The study used 40% aqueous glucose solution (Grotex LLC, Russia, St. Petersburg).

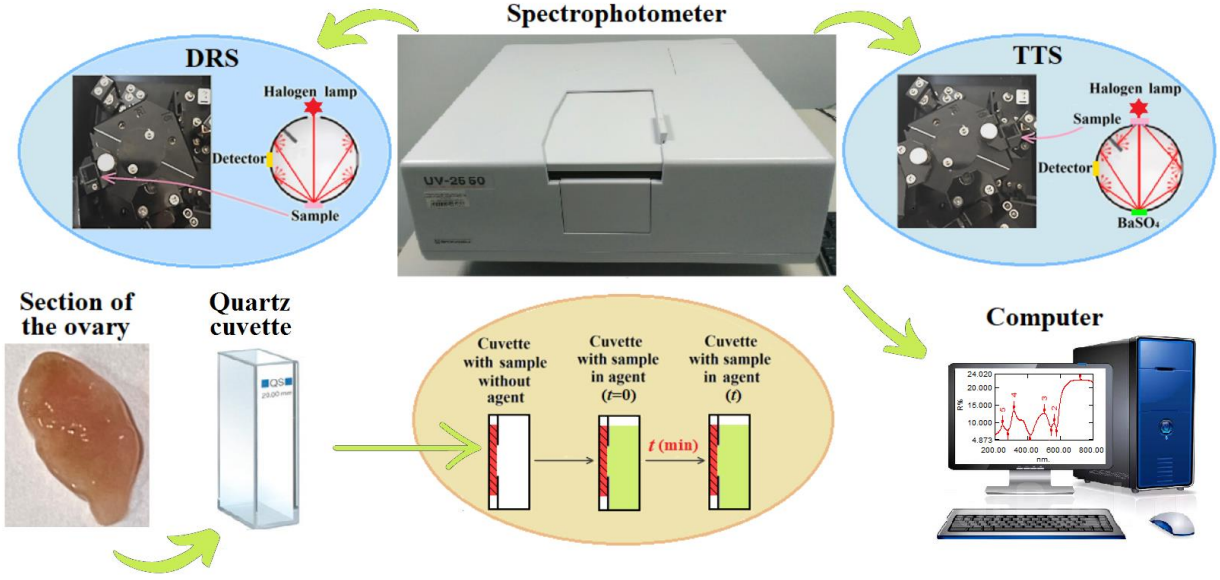


Fig. 1 Scheme of the experimental setup for measuring diffuse reflectance spectra (DRS) and total transmission spectra (TTS) of cat ovarian tissue samples.

For optical measurements, 6 sections from healthy organs and 6 sections from malignant ovaries were used, 3 of which were used to study the kinetics of DRS and 3 to measure TTS.

The protocol of the Local Ethical Committee with permission to conduct animal studies (No. 4 dated 1 November 2022) was issued by the Saratov State Medical University named after V. I. Razumovsky, which is responsible for providing permissions to conduct animal studies for Saratov region.

3 Calculations

The determination of the tissue diffusion coefficient of glucose/interstitial water is based on the measurement of DRS kinetics (Fig. 2). The process of transport of glucose/tissue water in a sample can be described in terms of the free diffusion model [13, 14]. For a plane-parallel tissue sample of a finite thickness, using Fick's second law and the modified Bouguer-Beer-Lambert law, an expression for the difference $\Delta A(t, \lambda)$ between the effective optical density at the current time $A(t, \lambda)$ and at the initial time $A(t = 0, \lambda)$, can be obtained [11−14].

For TTS measurements

$$I(t,\lambda) = I_0 \exp[-\mu_{eff}(t,\lambda)L(\lambda)],$$

where $I(t,\lambda)$ is the transmitted intensity of light, I_0 is the incident intensity of light, and

$$\mu_{eff}(t,\lambda) = \sqrt{3\mu_a[\mu_a + \mu_s'(t)]},$$

t is the time in seconds during which 40%-glucose is applied, λ is the wavelength in nm, $\mu_{eff}(t, \lambda)$ is the effective coefficient of light attenuation in the tissue, 1/cm; $\mu_s'(t) = \mu_s(1-g)$, 1/cm; g is the scattering anisotropy factor (varies from −1 to 1, for many biological tissues, $g \cong 0.93$) [11]; $L(\lambda)$ is the average pathlength of photons, in the transmission mode $L(\lambda) \cong l$, l is the thickness of the sample, cm.

Then,

$$\begin{aligned}\Delta A(t,\lambda) &= A(t,\lambda) - A(t=0,\lambda) = \mu_{eff}(t,\lambda)L(\lambda) = \\ &= [\mu_{eff}(t,\lambda) - \mu_{eff}(t=0,\lambda)]L(\lambda) \sim \\ &\sim C_0\left\{1 - \exp(-\frac{t}{\tau})\right\}L(\lambda),\end{aligned} \quad (1)$$

where $\Delta\mu_{eff}(t, \lambda)$ is the difference between the effective coefficient of attenuation of light in the tissue $\Delta\mu_{eff}(t, \lambda)$ at the current time and at the initial time, 1/cm;

$$\tau = \frac{4l^2}{\pi^2 D}, \quad (2)$$

D is the diffusion coefficient of the glucose molecules, cm^2/s; and C_0 is the initial concentration of the glucose, mol/l.

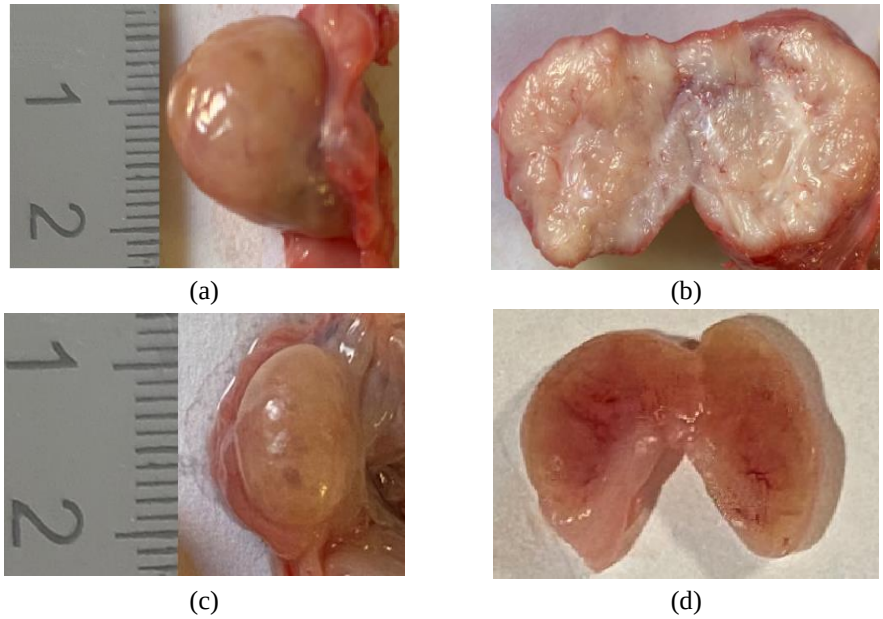
For DRS measurements:

$$A = -\log R(t,\lambda), \quad (3)$$

where $R(t, \lambda)$ is the diffuse reflectance coefficient, and

$$L(\lambda) \cong 2l_d\,,\ (l_d)^{-1} = \mu_{eff} l_d.$$

The recorded DRS [$R(\lambda)$, %] are converted using the standard Kubelka–Munk algorithm to optical density $A(\lambda)$ spectra (Shimadzu UV-2550 spectrophotometer software). Glucose is a well-known effective optical clearing agent and is often used in tissues [12, 13]. To evaluate the efficiency of optical clearing of *ex vivo* tissue samples, TTS measurements are usually used, and the efficiency parameter Q is calculated as:



(a) (b) (c) (d)

Fig. 2 Photos of the examined ovaries of cats. Whole (a) and in section (b) ovary with stromal sarcoma, whole (c) and in section (d) healthy ovary.

$$Q\ (\%) = \{T(t, \lambda)) - T(t = 0, \lambda)\}/T(t = 0, \lambda), \quad (4)$$

where $T(t = 0, \lambda)$ is the (total transmission coefficient, %) of the tissue sample for a specific wavelength λ at the initial time, and $T(t, \lambda)$ is the same at the current time.

The bars on the DRS and TTS graphs represent the boundaries of the confidence interval, found as:

$$\sigma = (t_s \mathrm{SD})/(\sqrt{n}), \quad (5)$$

where t_s is Student's coefficient, SD is the standard deviation, $n = 3$, and $p = 0{,}95$.

4 Results and Discussion

4.1 Histological Examination

The histological examination confirmed preliminary clinical diagnoses for ovarian stromal sarcoma tissue (Figs. 3(c, a) and 3(d, b)) and healthy tissue (Figs. 3(c) and 3(d)).

4.1.1 Histology of the Ovary with Stromal Sarcoma

From the outpatient chart: the animal was lethargic, inactive, ate little, and lost weight over the past two months. Over the past three days, the animal's condition has deteriorated significantly, vomiting bile.

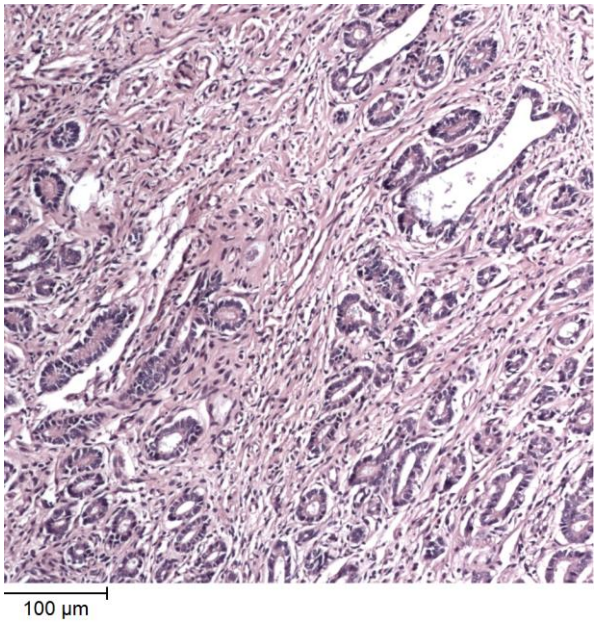
The ovary is a large, nonencapsulated, monophasic, highly cellular tumor with aggressive invasive growth. Tumor cells are fusiform, with clear intercellular boundaries, high nuclear-cytoplasmic ratio, homogeneous weakly eosinophilic cytoplasm, polymorphic hyperchromic nuclei with finely dispersed chromatin, and 1–2 eosinophilic nucleoli visible at 400 magnification (Fig. 3(a)). The degree of nuclear atypia is high; tumor cells form short intertwining bundles, solid fields. The stroma is poorly developed connective tissue with poor vascularization due to thick-walled vessels of medium caliber of irregular shape. Mitotic activity accounts for 16 mitoses per 10 fields of view at a magnification of 400 (2.37 mm^2). Extensive fields of tumor necrosis are determined. Lymphovascular invasion in the volume of the studied material is not determined. A focal moderate polymorphocellular subacute infiltrate is also determined, represented by lymphocytes, plasma cells, macrophages, neutrophils.

Histological conclusion: the histological picture is most consistent with a malignant mesenchymal tumor, ovarian sarcoma. Given the morphology, stromal sarcoma can be assumed [15].

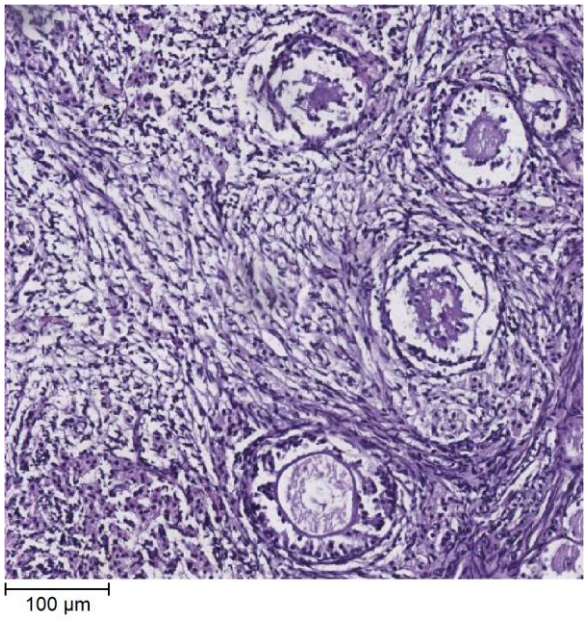
4.1.2 Histology of Healthy Ovary

The ovary has a preserved histological structure (Fig. 3(b)). The cortical substance is well developed, prevails over the stroma (2:1), multiple follicles are visualized at different stages of maturation. The corpus luteum is not visualized. Stroma is represented by a typical theca-tissue without edema, poorly developed, small-focal fresh hemorrhages are noted in it. The vessels are thin-walled, full-blooded.

Conclusion: an ovary with a healthy histological structure.



(a)



(b)

Fig. 3 Photo of a fragment of the histological preparation of the ovary: stromal sarcoma (a), healthy (b).

4.2 Spectrophotometric Studies

DRSs of samples from healthy and malignant ovaries of cats measured before and after interaction with glucose are shown in Figs. 4(a) and 4(c). In the UV range, the initial DRS of ovarian samples have obvious dips characteristic of the absorption bands of amino acid residues of connective tissue proteins in the form of collagen and reticular fibers, hemoglobin, and

porphyrins. In the region of about 415–420 nm and 540–580 nm, the observed dips correspond to the absorption bands of oxyhemoglobin (415, 542, and 576 nm). Water absorption in the measured range of 200–800 nm is insignificant. The diffusion coefficient of glucose/interstitial water in the samples was determined by the least squares method of the experimental curve segment, which characterizes the change in optical density on time of exposure to glucose at selected wavelengths. In Figs. 4(b) and 4(d), the kinetics of DRS during interaction with 40% glucose for 1 healthy and 1 malignant tissue samples are presented. The difference between the effective optical density at the current time and at the initial time ΔA was calculated from experimental data for each sample and then averaged for three the most sensitive to change of scattering wavelengths: 600, 700, and 800 nm.

It can be seen that the interaction of glucose with samples of healthy and malignant ovarian tissue leads to a gradual decrease in the reflectance in the entire studied wavelength range mostly due to decrease of tissue scattering and also some decrease of tissue absorption. Reduction of scattering is provided by refractive index matching of tissue scatterers and interstitial fluid, tissue dehydration, and better packing of collagen fibers [12, 13]. These effects are caused by two factors: the outflow of intracellular water together with hemoglobin from the tissue due to osmosis and the diffusion of glucose into the tissue (Fig. 5).

The time course of the DRS indicates a decrease in light scattering and, accordingly, makes it possible to unambiguously relate the rate of diffusion of glucose molecules to the rate of change in DRS. Using Eq. (1), we found τ (diffusion time), which for an ovarian tissue samples with sarcoma was 30.0 ± 1.8 min, and for healthy ovarian samples 57.3 ± 3.6 min. In the study of healthy and pathological human colorectal mucosa, similar differences in the values of τ were found, 3.9 min (colorectal carcinoma) and 5.0 min (healthy tissue) [16]. Also diffusion time of 22.3 min was found for glycerol/interstitial water in healthy cat ovarian tissue in follicular phase and 17.7 min – in luteal phase [17].

From experimental data presented in Figs. 4(b) and 4(d), the average diffusion coefficient for 40%-glucose in ovarian samples with sarcoma (n = 3) was found as $D = (1.4 \pm 0.2)\cdot 10^{-6}$ cm^2/s and for healthy tissue (n = 3) as $D = (7.5 \pm 0.9)\cdot 10^{-7}$ cm^2/s.

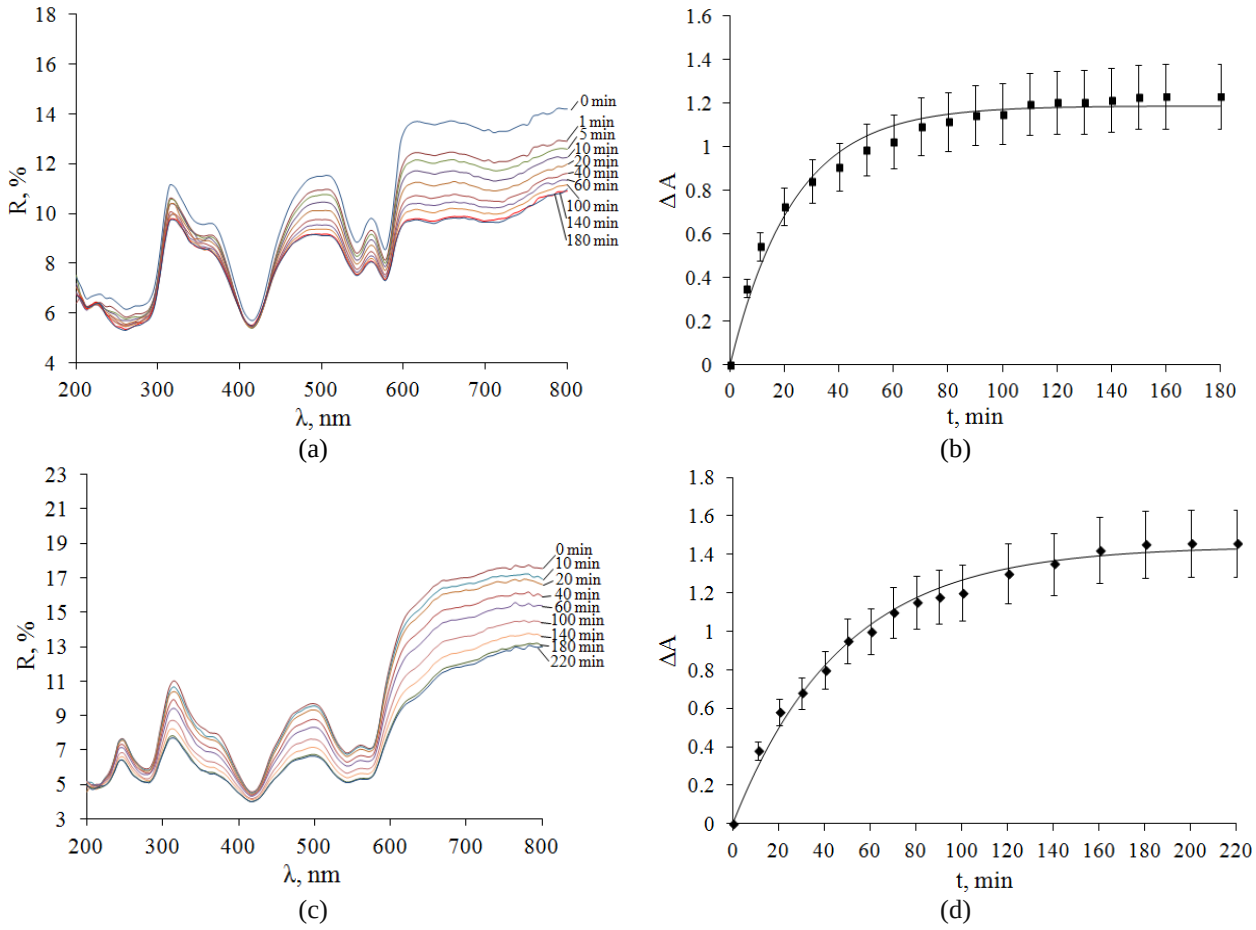


Fig. 4 DRS of cat ovarian tissue samples when immersed in 40% glucose: stromal sarcoma (a), healthy tissue (c). The respective kinetics of the difference in effective optical density $\Delta A(t, \lambda)$ at 600, 700, and 800 nm and then averaged (see Eq. (1)) of the studied ovarian samples. Experimental data marked as symbols, corresponding approximation of experimental data within the framework of the free diffusion model: stromal sarcoma (b), healthy tissue (d) marked as solid curves.

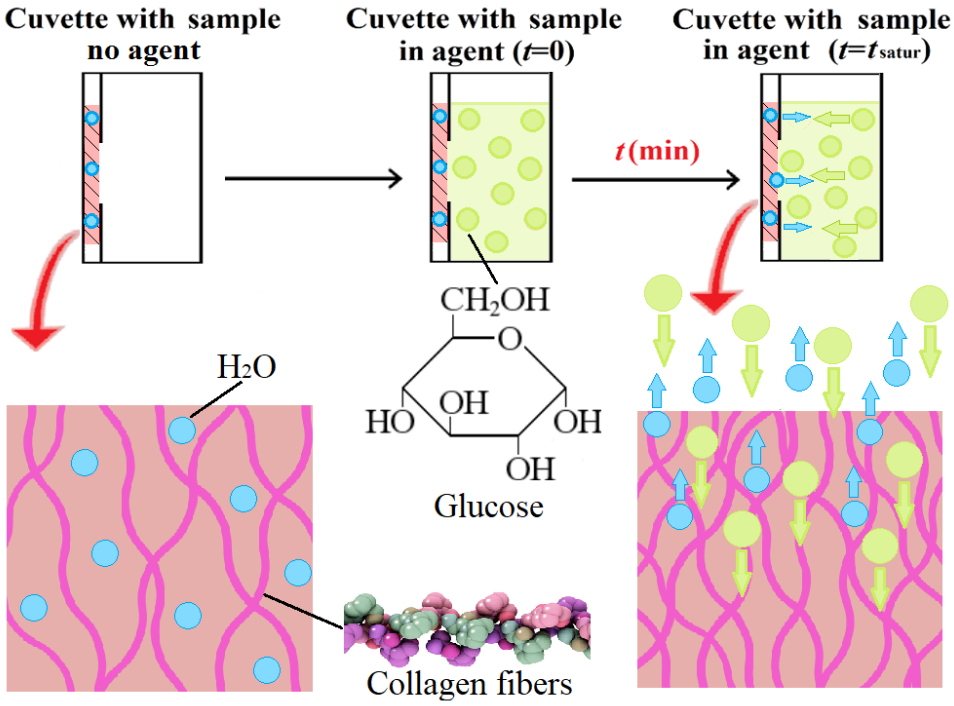


Fig. 5 Diagram showing the interaction of 40%-glucose with ovarian tissue.

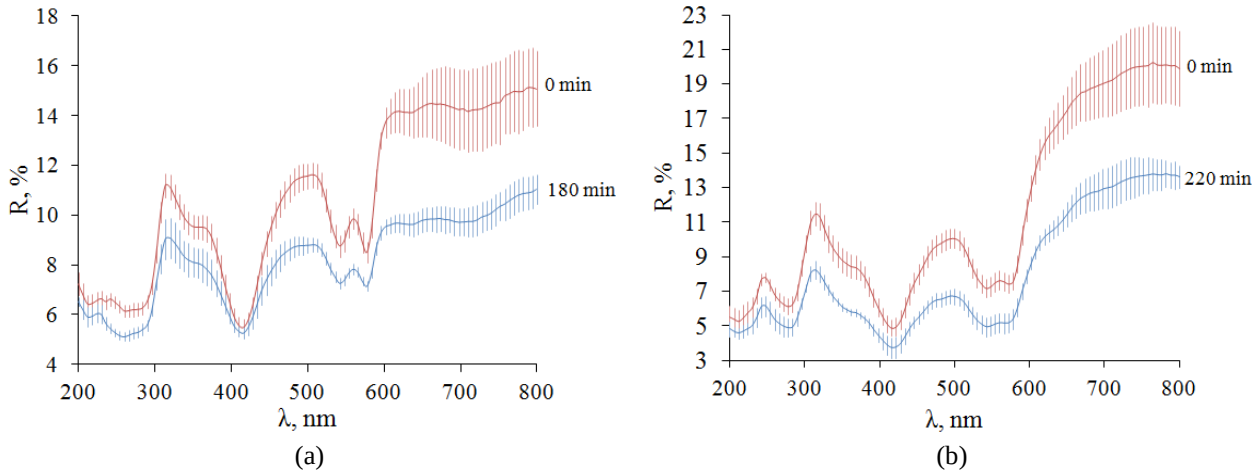


Fig. 6 DRS in the range from 200 to 800 nm of cat ovary tissue before and after immersion in 40 %-glucose: ovaries with sarcoma (n=6) (a), healthy ovaries (n=6) (b).

The effective diffusion coefficients for glycerol/interstitial water in healthy ovarian samples in follicular phase was determined as $D = (1.9 \pm 0.2)\cdot 10^{-6}$ cm^2/s, and in the luteal phase as $D = (2.4 \pm 0.2)\cdot 10^{-6}$ cm^2/s [17], which is expectably faster than for glucose diffusion in healthy tissue due to bigger molecule size in comparison with water and glycerol. The diffusion coefficient for 40%-glucose solution in the healthy gum was determined as $(4.1 \pm 0.8)\cdot 10^{-6}$ cm^2/s, which is much higher than in healthy ovarian tissue and explained by difference in structure [18].

DRS of the studied ovary samples were averaged over 6 healthy and 2 malignant samples before and after interaction with 40% glucose, which are presented in Fig. 6.

TTS of the samples with sarcoma and healthy tissue, before and after interaction with glucose are shown in Fig. 7. In the UV range, the transmission spectra of the samples under study have pronounced dips characteristic to the absorption bands of proteins and blood hemoglobin and correlate with diffuse reflection spectra (Fig. 4 (a, c)).

The total transmittance increases with time over the entire wavelength range with respect to the initial state of the sample (before immersion in glucose), which indicates a decrease in light scattering of the samples as a result of its immersion in glucose.

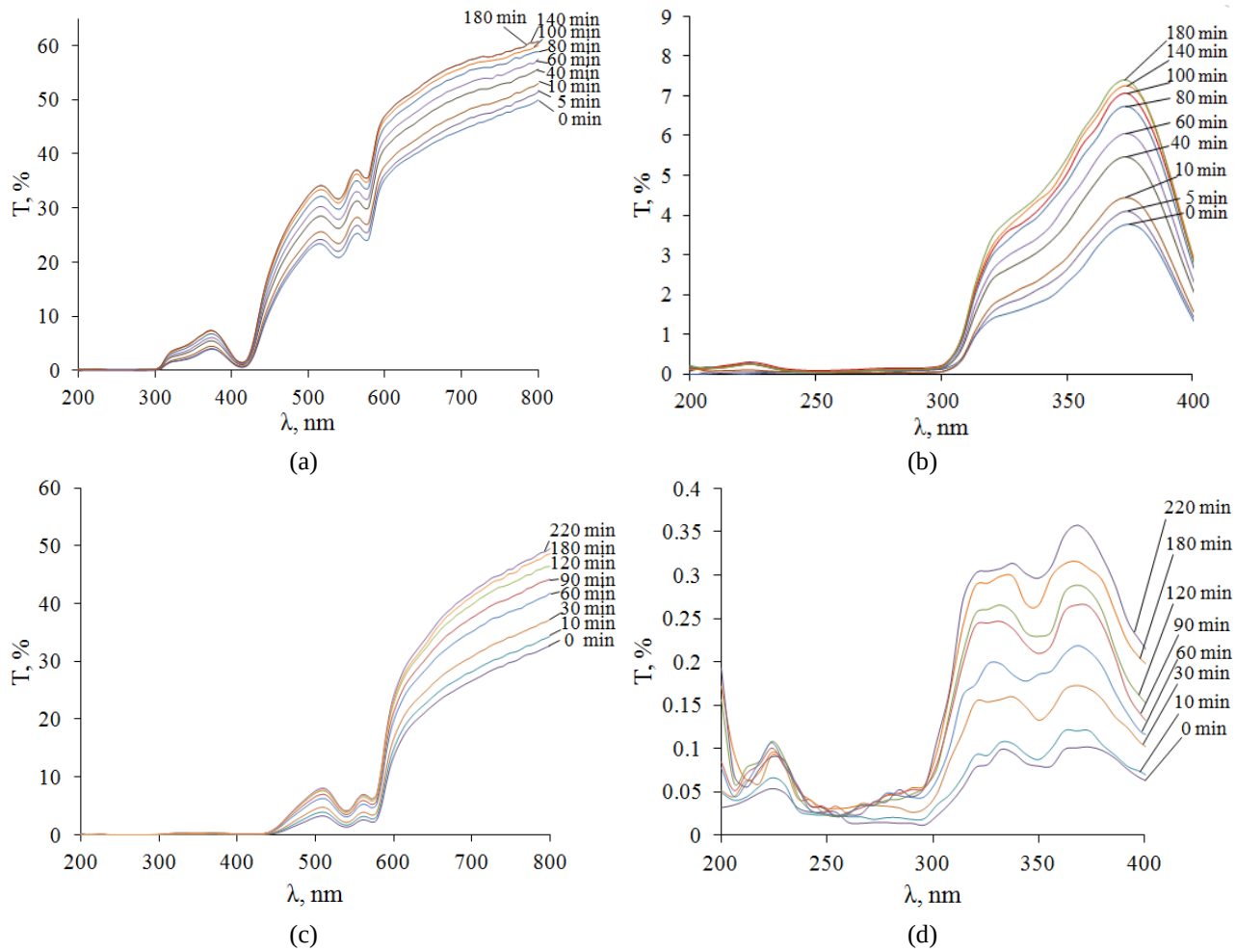


Fig. 7 TTS of cat ovarian tissue samples during immersion in 40%-glucose: an ovary with sarcoma ((a) in the range from 200 to 800 nm, (b) in the range from 200 to 400 nm); a healthy ovary ((c) in the range from 200 to 800 nm, (d) in the range from 200 to 400 nm).

The total transmittance for sarcoma is larger compared to the healthy tissue in the entire studied wavelength range. So, from 300–420 nm, we observe an increase in T from 3.9% to 7.4% after 180 min of interaction of the pathological tissue with 40%-glucose. For healthy tissue, T in the entire UV region does not exceed 0.1% before interaction and 0.36% after interaction with 40%-glucose. In the case of pathological tissue, the absolute values of the transmittance vary from 22.2% to 32.4% (at 500 nm), from 35.8% to 47.4% (at 600 nm), from 44.3% to 56.6% (at 700 nm), and from 50.1% to 60.8% (at 800 nm). In the case of healthy ovarian tissue, the transmittance varies from 3.2% to 7.6% (at 500 nm), from 14.2% to 25.0% (at 600 nm), from 26.5% to 41.7% (at 700 nm), and from 32.7% to 49.6% (at 800 nm). Thus, 40%- glucose is an effective optically clearing agent [12].

In Fig. 8, ovary TTS averaged over 6 healthy and 2 malignant samples before and after interaction with 40% glucose are presented.

After completing immersion of the samples, it can be seen that in healthy tissue, optical clearing occurred with the formation of two UV transparency windows: (18 ± 4) nm wide centered at 225 nm and (50 ± 12) nm wide centered at 375 nm (Figs. 8(a) and 8(b)). For the ovary with sarcoma, the formation of only one transparency window centered at 380 nm and a width of (43 ± 11) nm was observed (Figs. 8(c) and 8(d)). The efficiency of optical clearing of biological tissue Q is an important characteristic of the interaction of tissue with an OCA. Using experimental data and Eq. (4), parameter Q was calculated for 40%-glucose action on healthy and sarcoma ovarian tissues (Fig. 9).

In healthy ovarian samples, the efficiency of optical clearing was about 260% in the range from 200–450 nm, up to 290% at 450 nm, 160% at 500 nm, 230% at 550 nm; no more than 80% from 600 to 800 nm. In ovarian samples with sarcoma, optical clearing efficiency is no more than 100% from 200 to 450 nm, and no more than 50% from 500 to 800 nm. Similar results were obtained when using highly concentrated glycerol for the optical clearing of healthy colorectal tissues and in polyposis pathologies, as well as healthy gingival tissue [19].

In the literature, there are a large number of studies of various diseases and areas of interest in the human body, conducted using animal tissue samples [20, 21]. The effectiveness of the study of the reproductive system of cats has been shown using the ultrasound method [22] and X-ray with contrast agents [23],

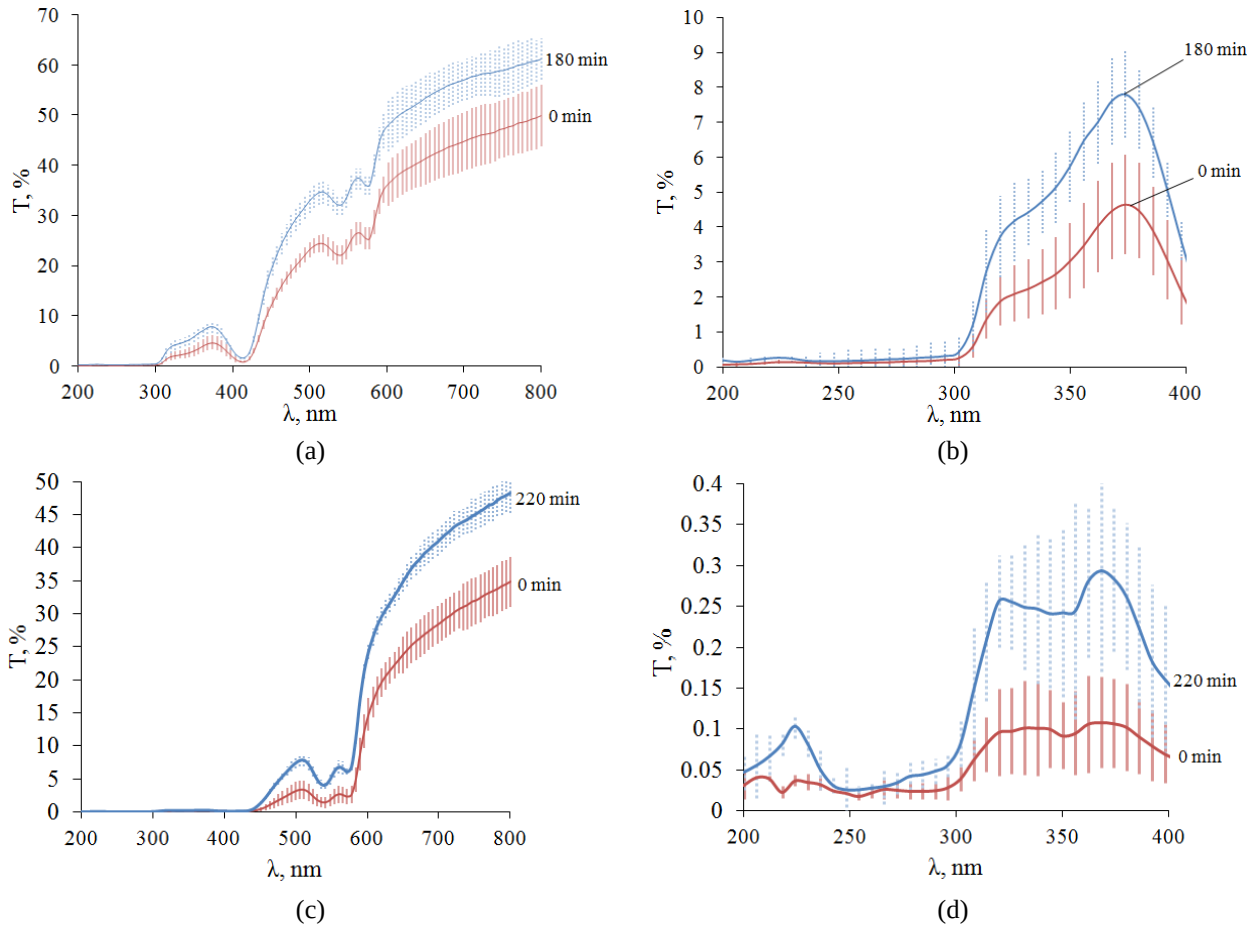


Fig. 8 Averaged TTS of cat ovary tissue before and after immersion in 40%-glucose: spectra of ovaries with sarcoma (n=6) from 200 nm to 800 nm (a), from 200 nm to 400 nm (b), spectra of healthy ovaries (n=6) from 200 nm to 800 nm (c), from 200 nm to 400 nm (d).

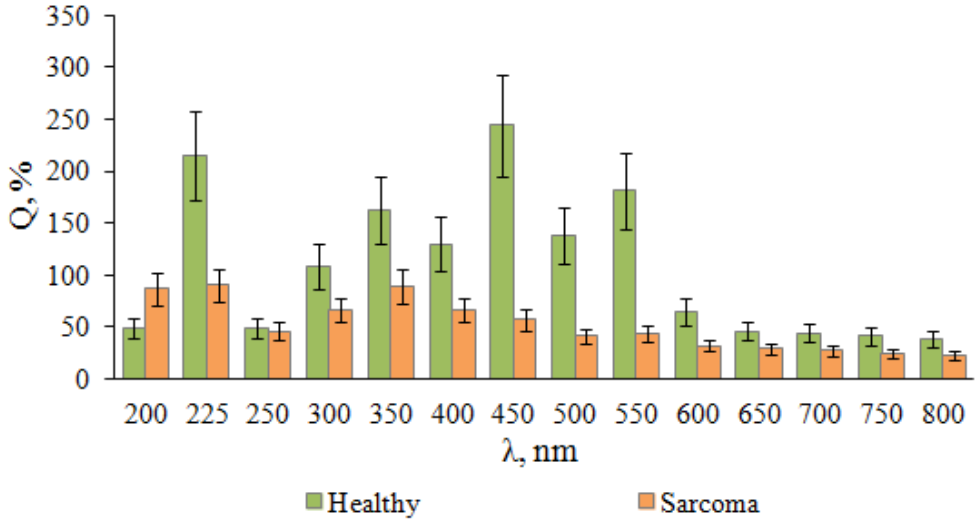


Fig. 9 Efficiency (Q, %) of tissue optical clearing after exposure to 40%-glucose during 180 min for stromal sarcoma and 220 min for healthy tissue.

the neuroanatomy of the brain of cats was studied using the methods of cryosection, magnetic resonance imaging and computed tomography [24], nuclear medicine application refers to a method in which radioactive compounds are injected into an animal to be examined, followed by imaging and measurement of the radiation emitted [25], etc. However, there are a lack of optical methods for studying tissues of the reproductive system of domestic mammals, in particular, cats and

dogs, which indicates the relevance of the ongoing research.

5 Conclusion

Differences in the perfusion-kinetic parameters of the healthy ovaries and with sarcoma at 40%-glucose action were revealed. The diffusion coefficient was determined as $D = (7.5 \pm 0.9) \cdot 10^{-7}$ cm^2/s for healthy tissue and $D = (1.4 \pm 0.2) \cdot 10^{-6}$ cm^2/s for stromal sarcoma. Glucose diffusion coefficient in the tumor ovarian tissue is greater than in the healthy tissue, which is due to bigger content of free water and the ability of the malignant tissue to induce uptake of glucose as an energy for growth.

For healthy tissue, in the UV region two virtual windows were found, one with a center at 225 nm and (18 ± 4) nm wide and another centered at 375 nm and (50 ± 12) nm wide. In the ovary samples with the stromal sarcoma, the formation of a single transparency window in the UV spectral region with a center at 380 nm and a width of (43 ± 11) nm was observed. The results obtained allow us to recommend 40%-glucose as an effective agent for optical clearing, which can be used in clinical practice at topical application.

Acknowledgments

Work was supported by the Russian Science Foundation Grant No. 22-75-00021.

Disclosures

The authors declare no conflicts of interest. The funders had no role in the design of the study; in the collection, analyses, or interpretation of data; in the writing of the manuscript; or in the decision to publish the results.

References

1. V. Dochez, H. Caillon, E. Vaucel, J. Dimet, N. Winer, and G. Ducarme, "Biomarkers and algorithms for diagnosis of ovarian cancer: CA125, HE4, RMI and ROMA, a review," Journal of Ovarian Research 12, 28 (2019).
2. H. Falconer, U. Joneborg, K. Krawiec, K. Palsdottir, M. Bottai, and S. Salehi, "Ultra-radical upfront surgery does not improve survival in women with advanced epithelial ovarian cancer; a natural experiment in a complete population," Gynecologic Oncology 159(1), 58–65 (2020).
3. S. Aust, R. Schwameis, T. Gagic, L. Müllauer, E. Langthaler, G. Prager, C.Grech, A. Reinthaller, M. Krainer, D. Pils, C. Grimm, and S. Polterauer, "Precision Medicine Tumor Boards: Clinical Applicability of Personalized Treatment Concepts in Ovarian Cancer," Cancers 12(3), 548 (2020).
4. F. G. Lawton, E. J. Pavlik, "Perspectives on Ovarian Cancer 1809 to 2022 and Beyond," Diagnostics 12(4), 791 (2022).
5. N. Lapke, C.-H. Chen, T.-C. Chang, A. Chao, Y.-J. Lu, C.-H. Lai, K.T. Tan, H.-C. Chen, H.-Y. Lu, and S.-J. Chen, "Genetic alterations and their therapeutic implications in epithelial ovarian cancer," BMC Cancer 21(1), 499 (2021).
6. E. J. Pavlik, E. Brekke, J. Gorski, L. Baldwin-Branch, R. Miller, C. P. DeSimone, C. S. Dietrich, H. S. Gallion, F. R. Ueland, and J. R.van Nagell Jr., "Ultrasonographic Visualization of the Ovaries to Detect Ovarian Cancer According to Age, Menopausal Status and Body Type," Diagnostics 12(1), 128 (2022).
7. N. Carreras-Dieguez, A. Glickman, M. Munmany, G. Casanovas, N. Agustí, B. Díaz-Feijoo, A. Saco, B. Sánchez, L. Gaba, and M. A. Angeles, "Comparison of HE4, CA125, ROMA and CPH-I for Preoperative Assessment of Adnexal Tumors," Diagnostics 12, 226 (2022).
8. P. Phinyo, J. Patumanond, P. Saenrungmuaeng, W. Chirdchim, T. Pipanmekaporn, A. Tantraworasin, T. Tongsong, and C. Tantipalakorn, "Diagnostic Added-Value of Serum CA-125 on the IOTA Simple Rules and Derivation of Practical Combined Prediction Models (IOTA SR X CA-125)," Diagnostics 11(2), 173 (2021).
9. T. Karlsson, T. Johansson, J. Höglund, W. E. Ek, and A. Johansson, "Time-Dependent Effects of Oral Contraceptive Use on Breast, Ovarian, and Endometrial Cancers," Cancer Research 81(4), 1153–1162 (2021).
10. C. J. Dunton, M .L. Hutchcraft, R. G. Bullock, L. E. Northrop, and F. R. Ueland, "Salvaging Detection of Early-Stage Ovarian Malignancies When CA125 Is Not Informative," Diagnostics 11(8), 1440 (2021).
11. V. V. Tuchin (Ed.), Handbook of Optical Biomedical Diagnostics, Volume 1: Light-Tissue Interaction, 2 ed., SPIE Press, Bellingham, WA (2016). ISBN: 9781628419092.
12. V. V.Tuchin, D. Zhu, and E. A. Genina (Eds.), Handbook of Tissue Optical Clearing : New Prospects in Optical Imaging, 1st ed., CRC Press, Boca Raton (2022). ISBN: 9781003025252.
13. E. A. Genina, A. N. Bashkatov, and V. V. Tuchin, "Tissue optical immersion clearing," Expert Review of Medical Devices 7(6), 825–842 (2010).
14. A. Kotyk, K. Janacek, "Membrane transport an interdisciplinary approach," Biomembranes 9, 3–348 (1977).
15. D. J. Meuten (Ed.), Tumors in Domestic Animals, 5th ed., John Wiley & Sons (2017). ISBN: 9780813821795.
16. S. Carvalho, N. Gueiral, E. Nogueira, R. Henrique, L. Oliveira, and V. V. Tuchin, "Glucose diffusion in colorectal mucosa - a comparative study between normal and cancer tissues," Journal of Biomedical Optics 22(9), 091506 (2017).
17. A. A.Selifonov, A. S. Rykhlov, and V. V.Tuchin, " The Glycerol-Induced Perfusion-Kinetics of the Cat Ovaries in the Follicular and Luteal Phases of the Cycle," Diagnostics 13(3), 490 (2023).

18. A. A. Selifonov, V. V. Tuchin, "Determination of the Diffusion Coefficient of 40%-Glucose in Human Gum Tissue by Optical Method," Optics and Spectroscopy 128(6), 766–770 (2020).
19. I. Carneiro, S. Carvalho, R. Henrique, A. Selifonov, L. Oliveira, and V. V. Tuchin, "Enhanced Ultraviolet Spectroscopy by Optical Clearing for Biomedical Applications," IEEE Journal of Selected Topics in Quantum Electronics 27(4), 1–8 (2021).
20. A. K. LeBlanc, C. N. Mazcko, "Improving human cancer therapy through the evaluation of pet dogs," Nature Reviews Cancer 20(12), 727–742 (2020).
21. J. D. Schiffman, M. Breen, "Comparative oncology: what dogs and other species can teach us about humans with cancer," Philosophical Transactions of the Royal Society B: Biological Sciences 370(1673), 20140231 (2015).
22. T. Conze, A. Wehrend, "Sonographic imaging of physiological ovaries in the cat," Tierarztliche Praxis. Ausgabe K, Kleintiere/heimtiere 45(3), 199–203 (2017).
23. Tanjila Hasan, M. M. Hossan, N. Tahsin, M. A. Hossain, and A. M. Uddin, "Pyometra in a Cat: A Clinical Case Report. A Review of Literature," Biomedical Journal of Scientific & Technical Research 37(5), 29851–29856 (2021).
24. H. Rizk, N. A. Shaker, and E. Yahya, "Cat brain neuroanatomy using cryosectioning, magnetic resonance and computed tomography imaging modalities," International Journal of Veterinary Science 9(3), 385–390 (2020).
25. M. Nordin, A. Osman, R. Shaari, M. Arshad, A. Kadir, M. Farhan, M. F. H. Reduan, and M. Luqmannordin, "Recent Overview of Mammary Cancer in Dogs and Cats: Classification, Risk Factors and Future Perspectives for Treatmen," Journal of Agriculture and Veterinary Science 10(8), 64–69 (2017).

Spectrometer Design for an 840 nm Spectral Domain Optical Coherence Tomography System

Lakshmi Parvathi M., Abira Bright B., and Vani Damodaran*
Department of Biomedical Engineering, Faculty of Engineering and Technology, SRM Institute of Science and Technology, Kattankulathur 603203, Tamil Nadu, India

***e-mail:** vanid@srmist.edu.in

Abstract. In this paper, the design and performance of a custom-built spectrometer for Spectral Domain Optical Coherence Tomography (SD-OCT) imaging for a near-infrared wavelength range centered around 840 nm is presented. Two configurations of spectrometers based on reflective and transmission type grating and achromatic doublet lens were analyzed and the spectrometer performance characteristics are studied. The spectrometer is designed to work best with a light source whose wavelength is 840 ± 46 nm. A line scan camera captures multiple wavelengths simultaneously. In order to achieve higher resolution and imaging depth, a 2048-pixel array linear line scan camera from Basler was chosen. The line scan camera's detector has a length and width of 14.3 mm and 7 μm, respectively. The spectrometer design was simulated using Zemax software and the design parameters are described in this paper. © 2023 Journal of Biomedical Photonics & Engineering.

Keywords: spectrometer, Zemax simulation, transmission type grating, reflective type grating.

Paper #8305 received 28 Feb 2023; revised manuscript received 1 Sep 2023; accepted for publication 5 Sep 2023; published online 25 Sep 2023. doi: 10.18287/JBPE23.09.030316.

1 Introduction

Optical coherence tomography (OCT) provides a high-resolution (1–15 μm) cross-sectional imaging of biological tissues which makes it a powerful tool in clinical diagnosis. The depth of imaging is restricted to 1~2 mm due to optical scattering in tissues [1].

In most of the commercial OCT systems, spectral domain OCT (SD-OCT) is employed due to high-speed acquisition capability. This technique is based on Michelson interferometer, the broadband light source in the near infrared region is used as a source. Using a beam splitter the light is made to illuminate two arms, one with the sample and other with reference mirror. The backreflected light from both the arms interfere at beam splitter and moves to the spectrometer. Spectrometer records intensity of all wavelengths. The recorded spectral information in converted to k-space and then an inverse Fourier transform is applied to extract depth versus intensity profile also known as A-scan [2].

The spectrometer plays a major role in the quality of image and the depth of imaging. The spectrometer is typically made up of a diffraction grating, focusing lens and single array CCD camera or detector. In order to improve the SD-OCT performance, it is crucial to assess the spectrometer's parameters. The choice of light source (central wavelength and spectral width), the focusing optics in the spectrometer and the detector parameters affects the spectrometer performance. For SD-OCT imaging systems, numerous spectrometer designs and arrangements have been put out thus far [3–5].

A prism is used to linearize spectrum data in wavenumber followed by grating [6]. With this method, the processing time is reduced, the depth-dependent sensitivity fall-off is improved and numerical interpolation is eliminated. In addition to using a prism, it can be created using reflecting optics, which removes the chromatic aberration and improve quality of image. Kamal et al. presented a spectrometer for OCT imaging with high quality which takes the chromatic aberration in account along with optical resolution and detector array resolution. A planer reflecting grating, an off axis parabolic cylindrical mirror and a CCD array detector make up the proposed imaging spectrometer. Reflective optics focusing improves the clarity of the spectrometer [7].

Three optical frequency windows, 840, 1050, and 1310 nm, are frequently utilized in OCT imaging because

This paper was presented at the International Conference on Nanoscience and Photonics for Medical Applications – ICNPMA, Manipal, India, December 28–30, 2022.

of the technological limits of detectors and the availability of light sources. For anterior segment imaging, practical 840 nm hybrid retinal/corneal Fourier-domain OCT systems are fast and sensitive enough.

The choice of source wavelength in the OCT system depends on the application that it is being considered for. An OCT system's axial resolution is inversely related to the light source's bandwidth and proportionate to the square of the centre wavelength. Therefore, the wider bandwidth and shorter wavelength offer superior resolution. For instance, in retinal imaging, a spectral window centred at 840 nm with a bandwidth of 40 nm is commonly utilised to attain maximum axial resolution (~7 μm). Additionally, water strongly absorbs light with a wavelength of 1310 nm, resulting in a retinal exposure that is less than 7% of the power incident on the cornea. In contrast, the retina receives practically all of the 840 nm wavelength light that strikes the eye without being absorbed. The sensitive retinal tissue is not typically exposed to 1310 nm light, hence much higher power levels can be utilized on the eye without harm. The SLED source from EXALOS (EXS210006-03) is chosen as a light source.

So, the optical design of a spectrometer for a light source centered at 840 nm with a bandwidth of 46 nm is presented in the following sections. In this work, two grating-based line scanning spectrometer models are introduced. The first is based on a reflecting grating and the second is based on a transmission grating. On the basis of their optical capabilities, the two are compared. The optical studio Zemax was used to create and implement each spectrometer.

2 Methodology

The four main parts of a conventional SD-OCT spectrometer are the beam lead (collimator), the dispersive element (diffraction grating), the collecting optics (a focusing lens), and the detector (CCD camera). Since these optics play a major role in the resolving capability of the OCT system, the detector specification is taken into account early in the spectrometer design process.

2.1 Theory and Properties

Eq. (1) illustrates the connection between the diffracted angle and the wavelength of the transmission and reflected grating

$$d[\sin(\theta_i) \pm \sin(\theta_d)] = m\lambda, \quad (1)$$

where d is the grating period, θ_d is the diffraction angle, θ_i is the incident angle, m is the diffraction order, and λ is the wavelength.

Theoretically, an SD-OCT system's axial resolution is provided by following:

$$\Delta z = \frac{2\ln 2}{n\pi}\frac{\lambda_0^2}{\Delta\lambda}, \quad (2)$$

where λ_0 is the center wavelength, n is the sample's refractive index and $\Delta\lambda$ is the optical source's bandwidth. It should be noted that the axial resolution is inversely proportional to source's bandwidth and this value is only possible if the source's complete bandwidth can be detected by the detector.

The light source in use has a bandwidth of 46 nm and a central wavelength of about 840 nm. Based on bandwidth, the spectral range between λ_{min} = 817 nm and λ_{max} = 863 nm was taken into consideration. As said, the coherence light source determines the axial resolution and is computed using Eq. (2). The theoretical axial resolution in air, taking the provided light source into account is 6.764 μm.

2.2 Detector

In order to achieve optical source-restricted axial resolution without reducing the imaging range, utilize an ideal technique such that the maximal imaging depth and axial resolution are chosen at the design stage.

The maximum imaging depth is determined by the optical source parameters and the overall detector pixel count. As a result, by choosing the pixel spacing to be half of the theoretical axial resolution, the imaging depth is improved while the axial resolution is maintained.

The maximum imaging depth is determined by the optical source parameters and overall detector pixel count. As a result, by choosing the pixel spacing to be half of the theoretical axial resolution, the imaging depth is improved while the axial resolution is maintained. The imaging depth can be expressed as in Eq. (3) if the testing sample's absorption and scattering characteristics are ignored

$$Z_{\max} = \frac{1}{4}\frac{\lambda_0^2}{\Delta\lambda}N, \quad (3)$$

where λ_0 is the central wavelength, $\Delta\lambda$ is the spectral bandwidth's full width at half maximum, and N is the number of pixels of the detector. Theoretical imaging depth in air is determined to be 7 mm using the optical source parameters used and N = 2048 pixels.

2.3 Diffraction Grating

The light can be spectrally dispersed over the detector using a prism or grating. Since grating offers two unique advantages, it is typically used. It offers better resolution than prism to start. Second, this occupies lesser space in the spectrometer design. The resolution of the spectrometer is significantly influenced by the grating's characteristics. Resolving power (R), a dimensional less number that describes gratings is determined by following Eq. (4):

$$R = \frac{\lambda}{\delta\lambda} = mM, \quad (4)$$

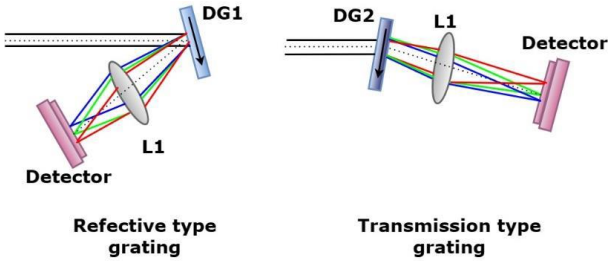


Fig. 1 Spectrometer configurations.

where M is the number of grooves illuminated on the grating, λ is the maximum wavelength, δλ is the highest spectral resolution that a grating can achieve, and m is the diffraction order.

For a particular grating shape, where the scattered light returns in the same direction as the incident light ($\theta_i = \theta_d$), the efficiency is maximized. Littrow condition is the name given to this condition. As a result, the grating equation for Littrow configuration becomes as following Eq. (5):

$$[\sin(\theta_i) = \sin(\theta_d)] = \frac{m\lambda}{2d}. \quad (5)$$

2.4 Spectrometer Optical Resolution

The transmission and reflective grating-based spectrometer design was created using the Zemax software. The light source used in the simulation is a Super-Luminescent Light Emitting diode (SLED) with a central wavelength of 840 nm and a bandwidth of 46 nm (Exalos EXS210006-03).

Fig. 1 represents the schematic diagram of both spectrometer configurations. The achromatic doublet lens with a focal length of 100 mm is used for focusing the rays from the grating. A commercial Basler ral2048-80km line scan camera (12-bit camera, 80 kHz line rate and 2048 pixels, each of size 7 µm × 7 µm) was considered in the simulation. The optical components utilized to execute the two spectrometer design are summarised in Table 1.

In the present work, light beam of width 2 mm was used to evaluate the imaging performance. In Zemax simulation, for performance analysis three wavelengths 817 nm, 840 nm, and 863 nm are used. In the simulation, a collimated beam of diameter 2 mm is made incident on the dispersive element. The grating (DG1/DG2) separates the various wavelengths in the source spectrum and this is made incident on the line scan camera. The distance between the grating and line scan array is optimized to obtain maximum resolving power.

3 Results and Discussions

3.1 Transmission Grating

In transmission grating type spectrometer, the light incident on the grating (DG 2) is dispersed as individual wavelength at different angles as it passes through the grating. This beam is then focused onto the detector array using an achromatic doublet lens (L1). The distance between the optical components are as follows: the grating is placed at 10 mm from the point of light entry into the spectrometer, distance between the grating and the focusing lens is 10 mm and the optical distance between the lens and detector is 97.040 mm.

3.2 Reflection Grating

In reflection grating type spectrometer, the light incident on the grating (DG1) is dispersed as individual wavelength at different angles as it passes through the grating. This beam is then focused onto the detector array using the lens (L1). The distance between the optical components are as follows: the grating is place at 100 mm from the point of entry into the spectrometer, the distance between the grating and lens is 50 mm and the optical distance between the lens and detector is 97 mm. Fig. 2 illustrates the Zemax ray diagram for both the spectrometer design.

The 3D enclosure design of the spectrometer is designed using Autodesk Fusion 360 and the design is 3D printed using the 3D printer (Ultimaker 3). The design is made such that the grooves matches the dimension of the individual components of the spectrometer. The design and the 3D printed output is shown in Fig 3.

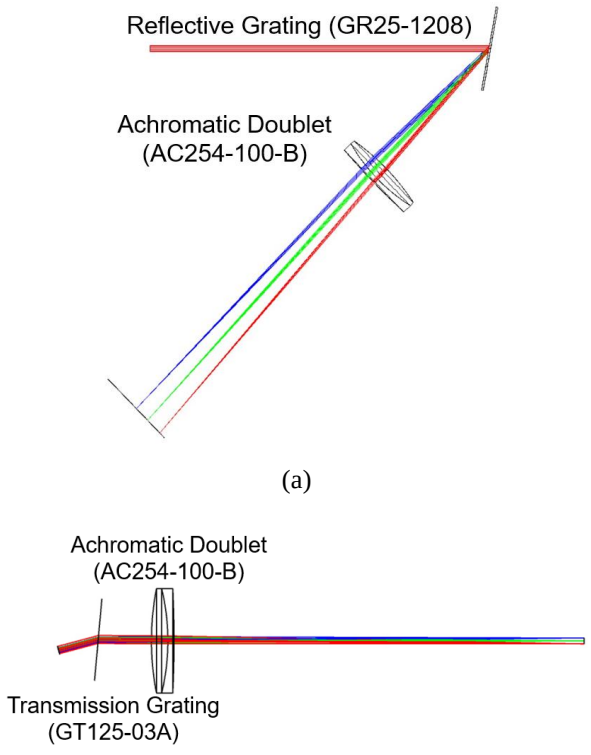


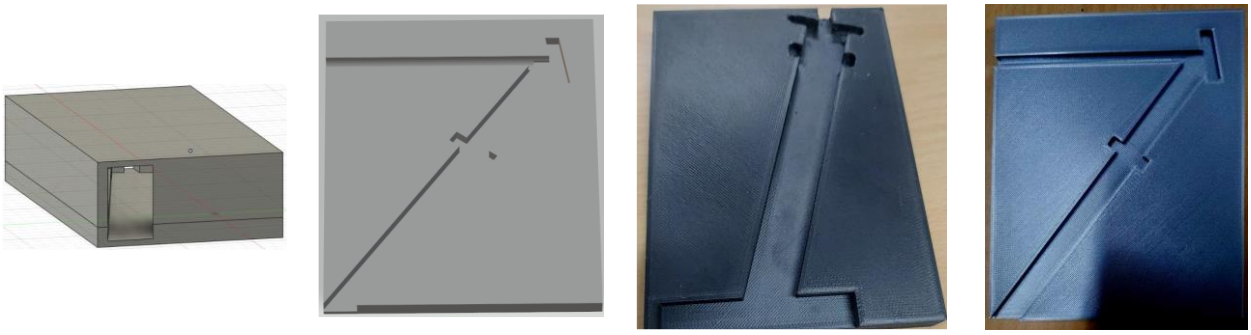
Fig. 2 Ray diagram for the (a) reflective type and (b) transmission type spectrometer design.

Table 1 The optical components utilized to execute the two spectrometer design.

Acronynm	Description	Part Number	Manufacturer
L1	Achromatic doublet Lens f = 100 mm	AC254-100-B	Thorlabs
DG1	Ruled reflective diffraction grating, 1200 grooves/mm	GR25-1208	Thorlabs
DG2	NIR Transmission grating, 300 grooves/mm	GTi25-03A	Thorlabs
Detector	Line scan camera 2048 pixel, 12 bits, line rate 80 kHz, each pixel size is 7 µm × 7 µm	racer raL2048-80km	Basler

Table 2 Evaluation of Spectrometer performance.

Sensor size (mm)	Beam diameter falling in the sensor (mm)	Number of pixels covered in detector	Resolution (nm)	Imaging depth (mm)	Sensor size (mm)
Transmission	14.3	1.434	205	0.22	0.786
Reflective		10.080	1440	0.031	5.52



(a) (b) (c) (d)

Fig. 3 The 3D design (a) transmission type (total enclosure), (b) reflective type (base) and the 3D printed output, (c) transmission type (base), and (d) reflective type spectrometers (base).

3.3 Comparison

By comparing the two spectrometric designs the refractive grating has a better spread of the wavelength in the detector. The coverage on the detector is higher in the reflective type than in the transmission type. This ensures higher resolving capacity and greater depth of imaging. The comparision of the spectrometers is described in Table 2.

4 Conclusion

The contribution of the spectrometer to SD-OCT system performance is investigated, and general design consideration for the spectrometer for an 840 nm system are outlined. The importance of spectrometer design and the impact of the selected optic source, central wavelength, bandwidth, grating and line scan camera have been studied using Zemax Optic Studio and its performance has been evaluated. It is found that the reflective type grating has a better spread on the detector and hence results in a higher spectral resolution of 0.031 nm/pixel in comparison to the transmission type grating which gives a resolution of 0.22 nm/pixel. The theoretical imaging depth for reflective type is 5.52 mm and that of transmission type is 0.786 mm. Thus the reflective type is found to be a better choice for SD-OCT system.

Acknowledgements

This work was supported by the SERB-funded Startup-grant project No: SRG/2020/002076.

Disclosures

The authors declare no conflict of interest.

References

1 P. H. Tomlins, R. K. Wang, "Theory, development and applications of optical coherence tomography," Journal of Physics D: Applied Physics 38(15), 2519 (2005).

2 S. Samadi, J. Dargahi, and S. Narayanaswamy, "Design and Optimization of a Linear Wavenumber Spectrometer Spectrometer with Cylindrical Optics and Line Scaning Optical Coherence Tomography," Sensors 21(19), 6463 (2021).

3 P. Xi, K. Mei, T. Brauler, C. Zhou, and Q. Ren, " Evaluation of spectrometric parameters in spectral-domain optical coherence tomography," Applied Optics 50(3), 366–372 (2011).

4 B. Potsaid, I. Gorczynska, V. J. Srinivasan, Y. Chen, J. Jiang, A. Cable, and J. G. Fujimoto, "Ultrahigh speed Spectral/Fourier domain OCT ophthalmic imaging at 70,000 to 312500 axial scan per secong," Optic Express 16(19), 15149–15169 (2008).

5 M. Kamal, S. Narayanswamy, and M. Packirisamy, "Design of spectrometer for high-speed line field optical coherence tomography," Proceedings of SPIE 8007, 80071J (2011).

6 Z. Hu, A. M. Rollins, "Fourier domain optical coherence tomography eith a linear in wavenumber spectrometer," Optical Letters 32(24), 3525–3527 (2007).

7 M. Kamal, N. Sivakumar, and M. Packirisamy, "Design of a spectrometr for all-reflective optics-based line scan Fourier domain optical coherence tomography," Proceedings of SPIE 7750, 775020 (2010).

Design of a Photonic Integrated Device with an on-Chip k-Clock and Tunable Reference Arm for Swept-Source Optical Coherence Tomography

Ivan V. Stepanov*, Evgeniy A. Talynev, Anton A. Ivanov, Ruslan V. Kutluyarov, and Elizaveta P. Grakhova
Ufa University of Science and Technology, 32 Zaki Validi str., Ufa 450076, Russia

***e-mail:** stepanov.iv@ugatu.su

Abstract. The paper presents a photonic integrated circuit (PIC) design that offers a high degree of integration of building blocks required to implement a swept-source optical coherence tomography (SS-OCT) system. The device includes an interferometer, sample arm, k-clock, and a tunable reference path integrated on a single chip implemented based on the silicon nitride fabrication platform. The PIC elements are optimized to perform low losses and minimal dispersion around a central operation wavelength of 1310 nm, which is critical for applications such as OCT. The device was simulated using Ansys Lumerical software. Simulation results show that the proposed PIC provides precise control of the scanning depth with a resolution of 0.725 nm/mV. Also, the frequency of the OCT signal does not exceed 17 GHz for scanning distances below 5 mm. © 2023 Journal of Biomedical Photonics & Engineering.

Keywords: optical coherence tomography; photonic integrated circuits; swept-source OCT; integrated k-clock; tunable reference path.

Paper #8962 received 27 Apr 2023; revised manuscript received 14 Jul 2023; accepted for publication 14 Jul 2023; published online 28 Sep 2023. doi: 10.18287/JBPE23.09.030317.

1 Introduction

Photonics opens prospects in the medical diagnostics especially in the non-invasive visualization methods. Thus, optical coherence tomography (OCT) has found wide application in scientific medical research and clinical practice due to the possibility of non-contact and highly sensitive visualization of the structure of tissues and organs and their pathological changes. High scanning speed virtually eliminates motion artifacts, and precision allows for an objective quantitative assessment of microstructural changes at the level of cell layers. Thereby, OCT has proven itself well in ophthalmology [1–3], oncology [4–6], neurosurgery [7, 8], urology [9, 10], gynecology [11], and other fields of medicine [12–14].

The potential advantages of integrated photonics, such as mechanical stability, miniaturization, the ability to integrate many components on a single chip, and low cost, are of great interest in OCT [15]. In addition, the possibility of implementing new form factors of diagnostic probes based on photonic integrated circuits (PIC) can significantly expand the opportunities of OCT [16], for example, for intraoperative studies, in which an objective assessment of tumor boundaries plays an essential role.

Full integration of the optical and optoelectronic parts of the OCT device is an intricate problem that attracts many researchers around the world. Most of the effort is on Fourier-domain OCT techniques, including spectral-domain OCT (SD-OCT) [17] and swept-source OCT (SS-OCT) [18], because they demonstrate superior scan speeds and axial imaging resolution. For published solutions, the integration of individual system elements on the PIC, such as interferometers [19, 20], arrayed waveguide gratings [17, 21], reference arm [22], or even combinations of several components [18, 23, 24], has been reported. However, total integration has yet to be achieved, even though researchers report the feasibility of an integrated radiation source [23, 25]. To date, experiments with PIC for OCT use an external source.

The main disadvantages of PIC-based OCT systems are high losses and dispersion compared to the fiber

implementation, which negatively affects the signal-to-noise ratio, and hence the imaging resolution. At the same time, a significant part of the losses is associated with interconnections between integral and discrete parts [15]. To reduce these losses, solutions for optimizing devices for coupling and decoupling light on PIC are presented [18, 26]. However, the high integration of elements on a chip is again a much more reliable and robust solution. For example, in Ref. [25], a multi-channel SS-OCT scheme is proposed, simultaneously performing measurements at several points of the sample, increasing the measurement speed by a factor of several. Such scaling in large systems is impossible due to the complexity of configuration, maintenance, and the need for many additional components.

Thus, this paper proposes one more step towards a fully integrated SS-OCT system. To this end, in addition to the conventional interference scheme and the sample arm, we propose implementing two key components of SS-OCT on the PIC to improve the system's performance: an integrated k-clock and an adjustable reference arm.

The SS-OCT systems suffer from a drift of the light source sweep over time [27], which happens due to the phase instability of the laser [28]. Therefore, the system includes an optical clock (k-clock) to strictly synchronize the swept-source sweep and the digital signal processing cycle to prevent visualization errors. Moreover, the integrated k-clock provides more minor time delays and losses than discrete devices because of smaller dimensions and the number of interconnections and eliminates the need for additional signal post-processing for phase calibration [29]. In the research, the k-clock is implemented with a tunable unbalanced Mach-Zender Interferometer and balanced photodetectors.

Fixed optical delay lines that are used in conventional SS-OCT systems as reference arm cannot provide to adjust the visualization depth, which is essential for some applications. In turn, Bragg gratings [30], microresonators [31], and photonic crystals [32] used to implement the optical delay tuning on the chip are significantly limited in bandwidth. For wideband operation, researchers offer different methods such as thermo-optical effect [22], microelectromechanical systems [33] that can be utilized in wideband operations. Thus, Ref. [22] demonstrates the possibility of increasing the scanning depth of the OCT system by 0.6 mm due to the use of a silicon PIC containing only a tunable reference arm based on platinum microheaters and a thermo-optic effect. Nevertheless, implementing long delay lines while keeping a low loss and small footprint remains challenging. In the research, the adjustment of the optical delay in the reference arm is realized in a small footprint with a gold heater 5 μm wide.

The paper is organized as follows. Section 2 describes the SS-OCT system concept with an integrated k-clock and tunable reference arm. Section 3 depicts issues of the PIC components design and simulation. Section 4 shows the results PIC performance analysis. The outlook for the system implementation is presented in Section 5, while the conclusion is given in Section 6.

2 The Concept of PIC with an Advanced Level of Components Integration for Application in SS-OCT

The scheme for SS-OCT with the proposed photonic integrated device is presented in Fig. 1. The design was carried out for a silicon nitride platform (Si_3N_4) that provides minimal loss compared with other semiconductor platforms for PIC fabrication. In this case, the drawback of such a solution is the absence of integrated photodiodes [34]. This problem can be subsequently solved with heterogeneous integration. However, in the research, we utilized discrete photodiodes connected to the PIC through edge couplers.

The device is operating as follows. The light from the narrowband sweeping laser (in the range from 1260 to 1360 nm) is coupled to the PIC through the edge coupler (EC). A 95/5 multimode interference coupler (MMI) divides the input light between the OCT interference scheme and the integrated k-clock segment.

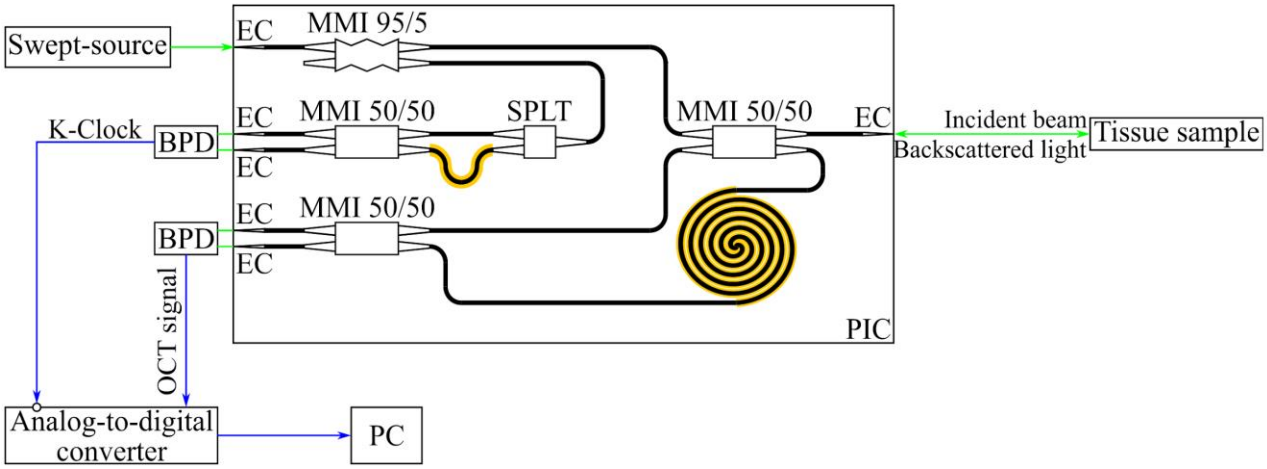
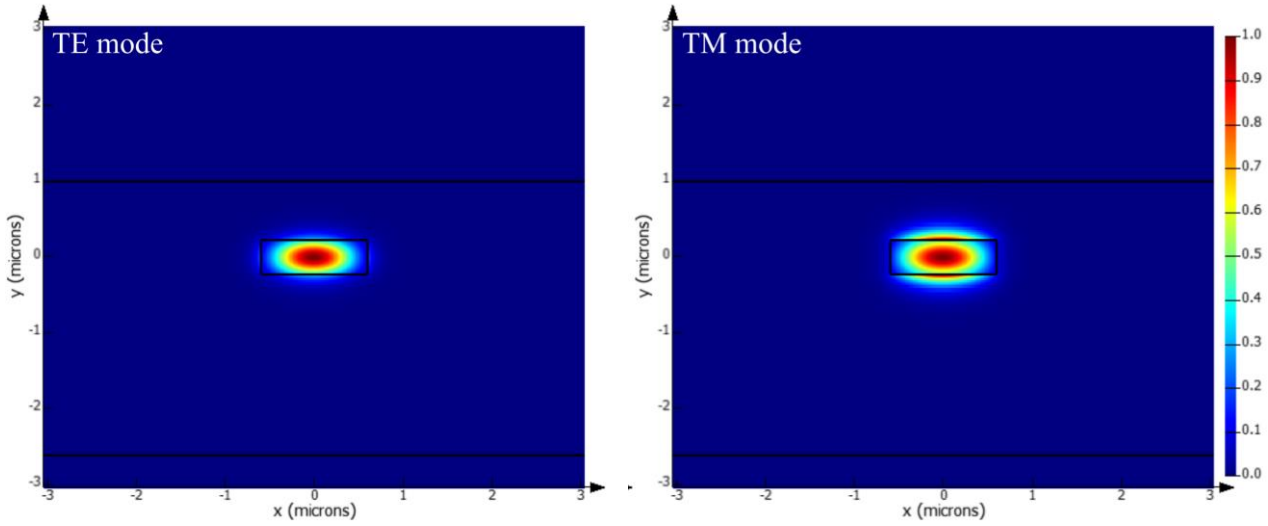


Fig. 1 PIC-based SS-OCT system scheme: EC – edge coupler, MMI – multimode interference coupler, SPLT – splitter, BPD – balanced photodiode, PIC – photonic integrated circuit, PC – personal computer. Blue lines represent electrical signals and green – optical. Thick black lines show waveguides inside the PIC, yellow – heaters.



(a) (b)

Fig. 2 TE- (a) and TM-mode (b) field intensity in the waveguide cross-section.

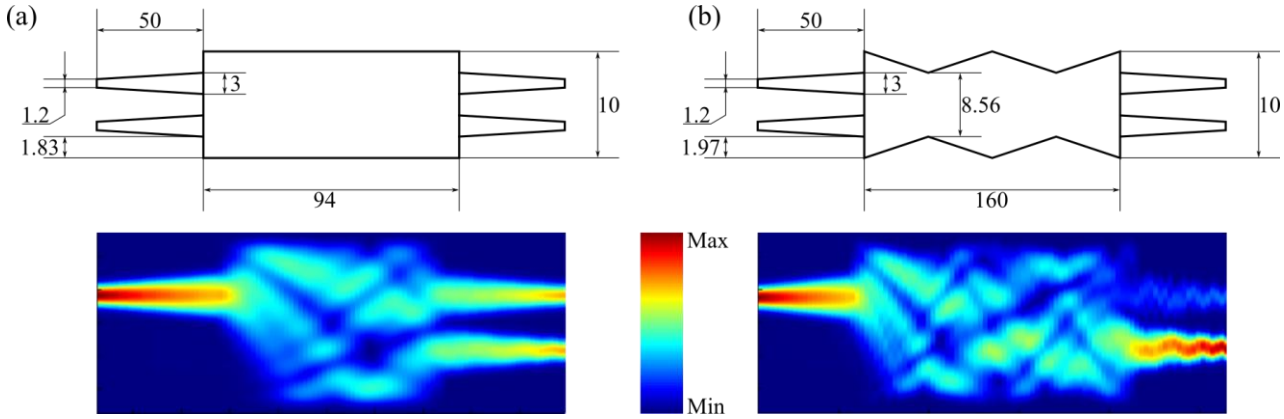


Fig. 3 Dimensions of the multimode interference couplers (top) with different coupling ratios and field distributions (bottom): (a) 50/50, (b) 95/5. All dimensions are given in μm.

In the OCT part, light is divided equally by 50/50 MMI between the sample arm and reference arm. In the first, through the EC, incident light illuminates the test sample, backscatters in the tissue, and is collected back to the PIC through the same waveguide. At the same time, the second half of the optical power passes through the reference arm (tunable delay line) to interfere with backscattered light after the second 50/50 MMI.

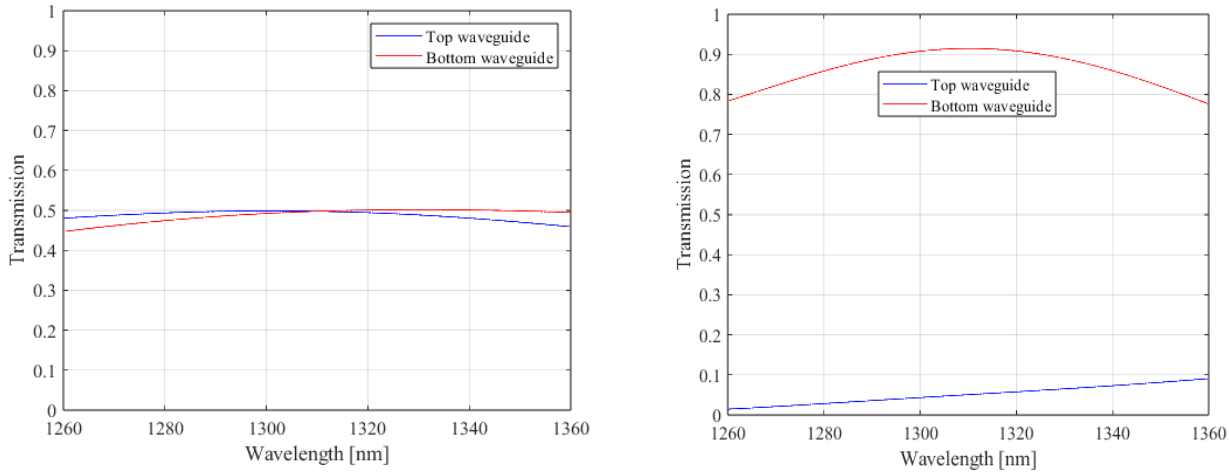
Simultaneously 5% of the optical power in the k-clock arm goes to the unbalanced Mach-Zehnder interferometer (MZI). The length difference of the MZI's arms is calculated to provide a 3 dB transmission at the starting wavelength of the laser sweep. This condition offers zero amplitude at the balanced photodiode (BPD) output with a frequency corresponding to the period of the laser. When such a signal from the BPD output is connected to the inverted input of the analog-to-digital converter (ADC) board, the required signal is generated to launch the digital processing cycle of the received OCT signal. To reduce the influence of possible manufacturing errors on the transmission characteristics and to adjust the k-clock signal period, the MMI's long arm could be upgraded with the heaters.

The delay line length is calculated to provide a zero delay point located as close to the PIC fringe as possible to reduce the attenuation of the already low-power backscattered light when propagating in free space and, respectively, to increase the visualization depth. Zero delay point corresponds to the equal optical path at the reference and sample arms. The operation of the tunable reference arm will be described in the next chapter.

The applied MMIs in the scheme can be replaced with wideband directional couplers (DC). However, DC's characteristics are more sensitive to fabrication errors [35].

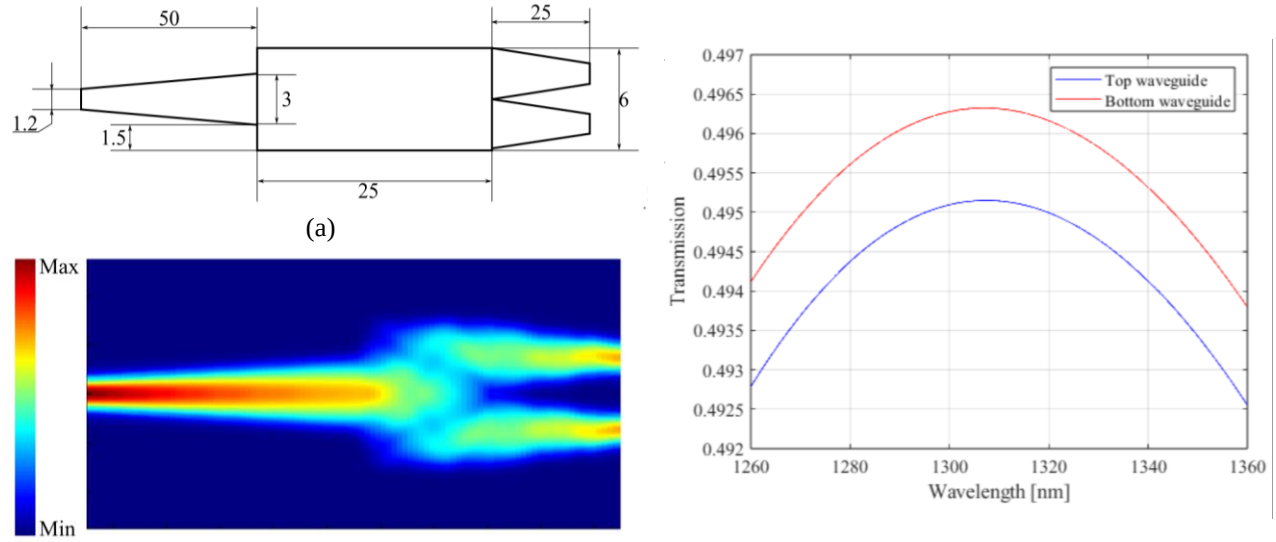
3 PIC Components Design and Simulation

PIC design contains the following elements: waveguides, MMIs with coupling coefficients 95/5 and 50/50, splitter (MMI with one input and two outputs), and heaters for tunable elements. Simulation of the components was performed in the ANSYS Lumerical software.



(a) (b)

Fig. 4 Transmission spectra of the 50/50 MMI (a) and 95/5 MMI (b).



(a) (b) (c)

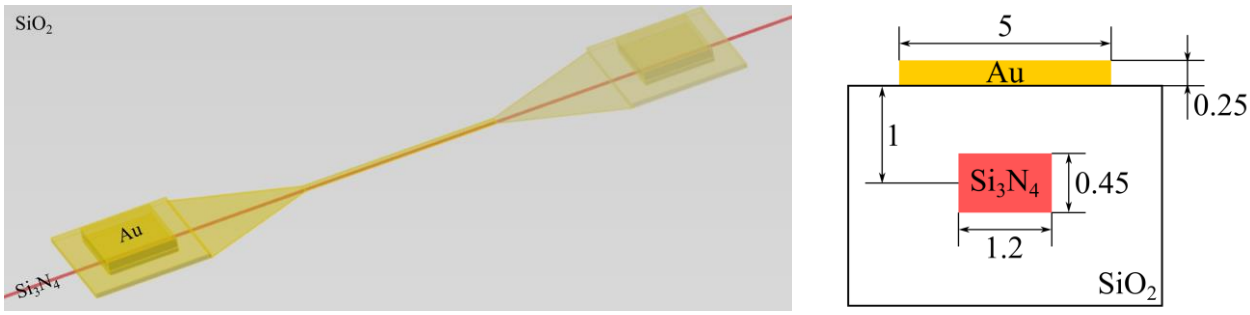
Fig. 5 Dimensions (a), field distribution (b), and transmission spectra (c) of the splitter MMI.

As mentioned earlier, the proposed PIC is developed for the Si_3N_4 (silicon nitride) platform, which provides minimal loss and higher system sensitivity. The waveguide's dimensions equal 1200×450 nm were chosen to keep single-mode operation and close to zero dispersion around 1300 nm. The waveguide simulation was performed using the finite difference Eigenmode method in the Lumerical MODE software. The TE-and TM-mode field distributions in the waveguide cross-section are presented in Fig. 2.

Dimensions of the 50/50 and 95/5 MMIs were calculated by the approach presented in Refs. [36, 37], respectively. The components we further simulated in a Lumerical MODE software, but the Eigenmode expansion method was used in this case. We optimized the geometry of MMI using the same software to achieve the desired operation mode. The final MMIs dimensions with field distributions are presented in Fig. 3. Transmission spectra of the MMIs are provided in Fig. 4. The transmission spectra of 50/50 MMI has a shift of 20 nm between the output waveguides; however, it could be compensated during MZI design. Particle swarm optimization can be applied to flatten the proposed MMIs' transmission spectra. Nevertheless, proposed MMI structures are the most robust to fabrication errors.

Compared to discrete directional couplers, the MMI on PIC offer less flat transmission spectra. However, integrated components are much smaller than discrete [38–41].

Instead of using a conventional waveguide splitter, we applied MMI with one input and two outputs since it is easier to fabricate and is more tolerant of manufacturing errors. The 1×2 MMI length was calculated according to Ref. [36]. The MMI's optimized dimensions, field distribution, and transmission spectra are presented in Fig. 5.



(a) (b)

Fig. 6 Simulation model of the heater in Lumerical DEVICE (a) and heater cross-section (b). All dimensions are in μm.

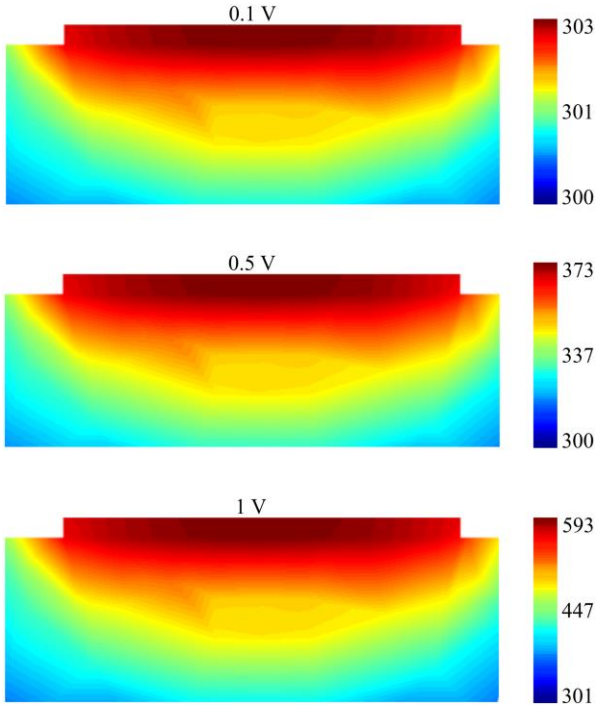


Fig. 7 Heat dissipation profile simulation in Lumerical DEVICE for different voltages. All temperatures are in Kelvins [K].

The electric heater simulation was performed using the finite element method in the Lumerical DEVICE package. A three-dimensional view of the model is presented in Fig. 6. First, we obtained the device temperature dependence from the applied voltage and next exported it to the Lumerical MODE to calculate effective index variation. Corresponding heat dissipation profiles for different used voltage ratings are provided in Fig. 7. The waveguide temperature dependence on the applied to the heater voltage is depicted in Fig. 8. Corresponding effective index dependence on the applied to the heater voltage is depicted in Fig. 9.

In the simulation, the heater length equals 100 μm, and this assumption was made to decrease computational requirements. The heater is represented by a gold microstrip line with dimensions of 5 × 0.25 μm and is deposited on the glass layer with 1 μm thickness.

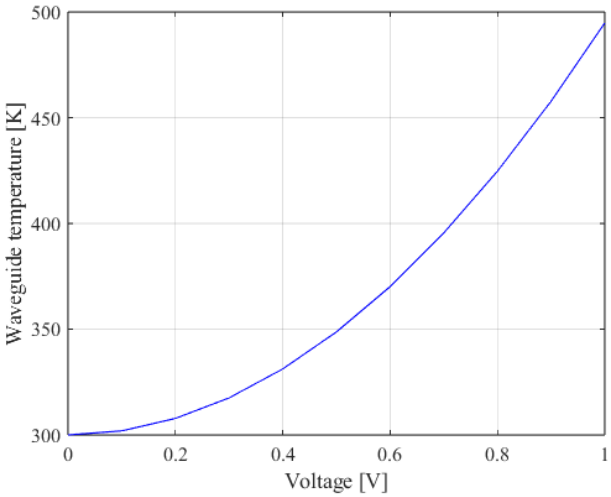


Fig. 8 Waveguide temperature dependence from applied to the heater voltage.

The waveguide temperature deviation range is 200 K with a maximum achieved value of 500 K for a 1 V applied voltage.

That corresponds to the waveguide fundamental TE mode effective index change by $4.5 \cdot 10^{-3}$ (Fig. 9). Such results are within tolerance for silicon photonics [42, 43], which means that heating does not significantly affect the mode propagating in the waveguide, which ensures minimum losses.

Waveguide temperature shift leads to the relative change in the optical path length. This change can be calculated as follows [22]:

$$\Delta l_{OPL} = \varepsilon \cdot \Delta T \cdot l_0,$$

where ε is the thermo-optical coefficient of the Si_3N_4 that equals $2.45 \cdot 10^{-5}$ RIU/°C, ΔT is the temperature shift, and l_0 is the length of the waveguide. The waveguide length variation due to temperature change is depicted in Fig. 10.

Thus, for the heater voltage up to 1 V, the relative change in the optical path length reaches 100 μm.

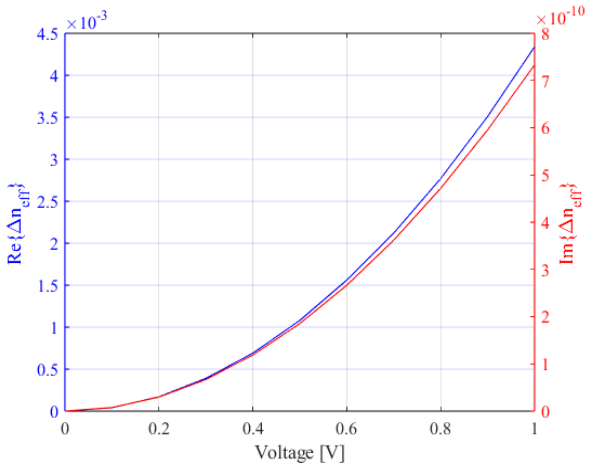


Fig. 9 Waveguide effective index dependence from applied to the heater voltage.

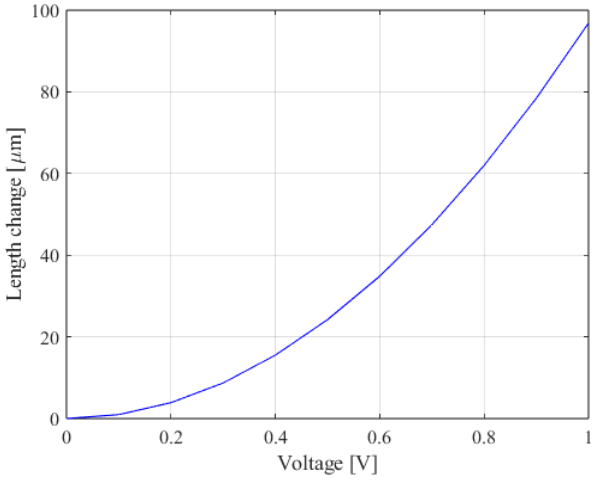


Fig. 10 The optical path tuning range vs the applied voltage to the heater.

4 Simulation Results of the Photonic Integrated Device Performance

The PIC simulation model based on the topology presented in Fig. 1 and designed components was performed in Lumerical INTERCONNECT using scattering matrices apparatus. Commercial SS-OCT systems have a sweep rate of 100 kHz [29], corresponding to the sweeping period of 10 μs. Since the zero delay point calculation is based on the operating wavelength band and waveguide lengths and does not depend on the laser sweeping period, the latter was set to 10 ns for a reasonable simulation time.

The first simulation step was k-clock characterization to ensure an equal transmission coefficient at the desired wavelength. Obtained transmission spectra of the integrated k-clock are depicted in Fig. 11. It is worth noting that this MZI is designed for the calculated MMI transmission spectra.

As can be seen from Fig. 11, the free spectral range (FSR) of the k-clock's MZI is equal to 100 nm. It is necessary to prevent the ADC's false start within the swept-source period. For example, if the wavelength sweep of the source is equal to 50 nm, then the FSR value should be higher than 50 nm.

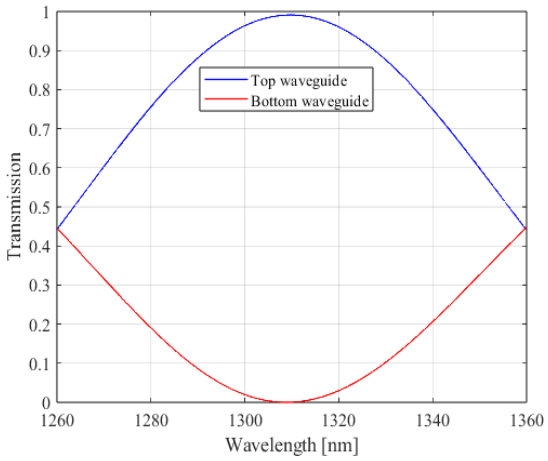
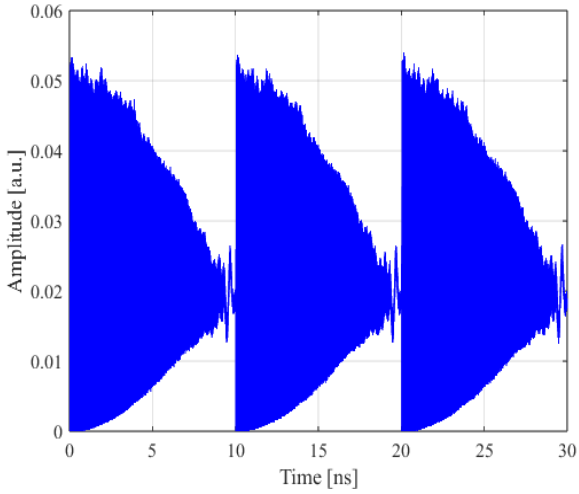
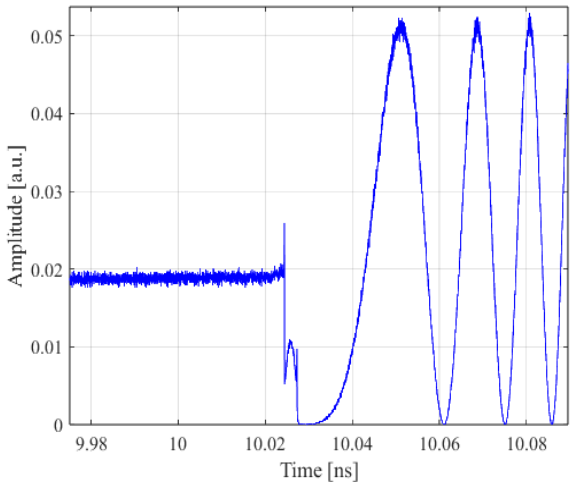


Fig. 11 The integrated k-clock transmission spectra.



(a)



(b)

Fig. 12 The electrical clock signal in the time domain at the output of BPD (a) and its transition between the first and the second sweeping period of the laser (b).

The following simulation step is the PIC operation in three periods of the swept-source. The main goal of this stage is to get the dependence of the electrical signal frequency at the output of the OCT arm from the distance to the optical inhomogeneity in the test tissue sample, in which the incident beam is backscattered. We applied an optical mirror with a 0.99 reflection coefficient to imitate such a layer in a tissue sample. This mirror is connected with an interference scheme through the edge coupler and air volume.

The k-clock operation in the time domain for three sweeping periods of the laser is shown in Fig. 12.

Ripples on the timing diagram arise from the 95/5 MMI transmission coefficient irregularity. These amplitude deviations have almost no effect on the trigger work, and the time delay of the trigger is about 0.03 ns.

The output signal frequency dependence vs a distance between the chip fridge and backscattering layer in the tissue sample for different voltages applied to the heater is presented in Fig. 13. Zero delay point shift between 0 V and 1 V is 0.047 mm. The maximum zero delay point shift is 0.063 mm. The reference path tuning time is about 1 μs [44].

From the Gaussian interpolation, we obtained a trend line that shown in Fig. 14. We calculated a delay line tuning resolution of about 0.725 nm/mV by this trend.

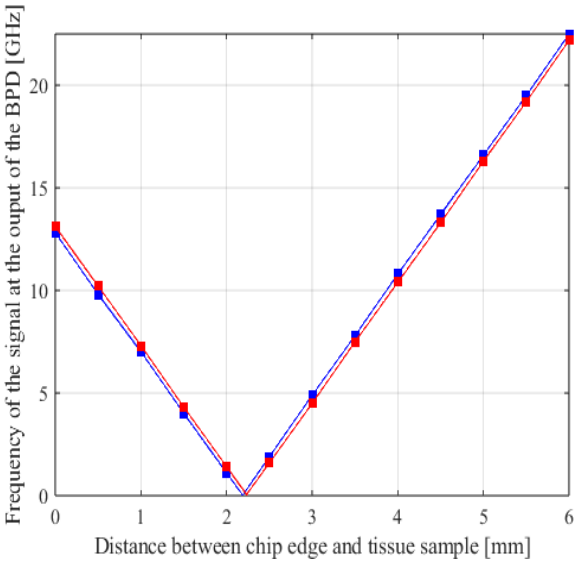


Fig. 13 BPD's output signal frequency dependence on the distance to the backscattering layer in the tissue sample for two voltages applied to heater – 0 V (blue line) and 1 V (red line).

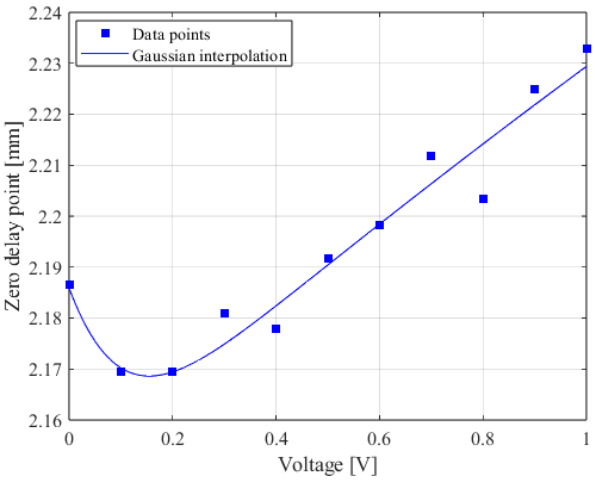


Fig. 14 Zero delay point dependence from applied to the heater voltage.

5 Discussion

The achieved scanning depth variation is lower than was demonstrated in Ref. [22, 33]. However, these solutions do not provide the full potential of integrated photonics. First, the presented devices provide integration of only one system/s component on the PIC, leading to an additional loss at the connections. Also, our reference arm can be implemented as Archimedes' spiral with a total footprint of about 800 × 800 μm for the Si_3N_4 platform. This value is comparable to the device footprint presented in Ref. [33] (about 300 × 600 μm) and much lower than that shown in Ref. [22] (8 mm^2). It is worth noting that the tuning range of the scanning depth can be increased by using different waveguide materials with higher thermal coefficients (for example, silicon) or with true-time delay device integration [45]. Also, a longer reference path can be utilized in thermal tuning [22].

Another approach to expand the tunability of the reference path is effective index contrast between two states increasing. Phase change materials can provide a more effective index difference between distinct states [46]. For example, the effective index change for $Ge_2Sb_2Te_5$ deposited on the Si_3N_4 waveguide reaches 0.1 [47] for other states in the second transparency window when thermo-optical effect leads to the effective index change of order of 10^{-3} (as shown in Fig. 9).

To further improve system performance, a fast Fourier transform can be implemented in the optical domain on the PIC [48], removing the high-performance digital signal processors and significantly reducing the SS-OCT system's cost.

Another possible optimization of the proposed device can be implemented by replacing the Mach-Zehnder interferometer in the k-clock arm with a microring resonator with an FSR value above 100 nm [49]. This replacement provides for further reducing the footprint of the device.

6 Conclusion

In the paper, we presented a PIC design for the SS-OCT with a high integration degree of the system's components. The proposed PIC is developed for the Si_3N_4 platform. Although, the PIC topology is compatible with different fabrication platforms after the corresponding redesign and optimization of the components.

Simulation results in the Lumerical software show that OCT electrical signal frequency does not exceed 17 GHz for scanning depths up to 5 mm. This frequency fits the 3 dB bandwidth of the most integrated and discrete high-speed photodiodes [34]. The integrated k-clock shows a minor start time error equal to 0.03 ns that can be compensated with proper heating. An integrated tunable reference path controls the zero delay point position from 2.17 to 2.23 mm. With a voltage resolution of 1 mV, our tunable reference path provides a scanning depth change resolution of about 0.725 nm.

Acknowledgments

The research is supported by the Ministry of Science and Higher Education of the Russian Federation within the state assignment for the Ufa University of Science and Technology (agreement No. 075-03-2021-014) and conducted in the research laboratory "Sensor systems based on integrated photonics devices" of the Eurasian Scientific and Educational Center.

Disclosures

The authors declare that they have no conflict of interest.

References

1 E. Vaghefi, S. Hill, H. M. Kersten, and D. Squirrell, "Multimodal Retinal Image Analysis via Deep Learning for the Diagnosis of Intermediate Dry Age-Related Macular Degeneration: A Feasibility Study," Journal of Ophthalmology 2020, 7493419 (2020).

2 G. Quellec, K. Lee, M. Dolejsi, M. K. Garvin, M. D. Abramoff, and M. Sonka, "Three-Dimensional Analysis of Retinal Layer Texture: Identification of Fluid-Filled Regions in SD-OCT of the Macula," IEEE Transactions on Medical Imaging 29(6), 1321–1330 (2010).

3 E. A. Rank, S. Nevlacsil, P. Muellner, R. Hainberger, M. Salas, S. Gloor, M. Duelk, M. Sagmeister, J. Kraft, R. A. Leitgeb, and W. Drexler, "In vivo human retinal swept source optical coherence tomography and angiography at 830 nm with a CMOS compatible photonic integrated circuit," Scientific Reports 11, 21052 (2021).

4 J. Wang, Y. Xu, and S. A. Boppart, "Review of optical coherence tomography in oncology," Journal of Biomedical Optics 22(12), 121711(2017).

5 L. Van Manen, J. Dijkstra, C. Boccara, E. Benoit, A. L. Vahrmeijer, M. J. Gora, and J. S. D. Mieog, "The clinical usefulness of optical coherence tomography during cancer interventions," Journal of Cancer Research and Clinical Oncology 144(10), 1967–1990 (2018).

6 N. Acharya, S. K. Melanthota, M. Khokhar, S. Chakrabarti, D. Gopal, D. S. Mallya, and N. Mazumder, "Types of Optical Coherence Tomography for Cancer Diagnosis: A Systematic Review," Journal of Biomedical Photonics & Engineering 8(1), 010201 (2022).

7 Y. Fan, Y. Xia, X. Zhang, Y. Sun, J. Tang, L. Zhang, and H. Liao, "Optical coherence tomography for precision brain imaging, neurosurgical guidance and minimally invasive theranostics," Bioscience Trends 12(1), 12–23 (2018).

8 K. Hartmann, K.-P. Stein, B. Neyazi, and I. E. Sandalcioglu, "Theranostic applications of optical coherence tomography in neurosurgery?" Neurosurgical Review 45, 421–427(2022).

9 J. E. Freund, M. Buijs, C. D. Savci-Heijink, D. M. de Bruin, J. J. M. C. H. de la Rosette, T. G. van Leeuwen, and M. P. Laguna, "Optical Coherence Tomography in Urologic Oncology: a Comprehensive Review," SN Comprehensive Clinical Medicine 1, 67–84 (2019).

10 H.-W. Wang, Y. Chen, "Clinical applications of optical coherence tomography in urology," IntraVital 3(1), e28770 (2014).

11 M. Kirillin, T. Motovilova, and N. Shakhova, "Optical coherence tomography in gynecology: a narrative review," Journal of Biomedical Optics 22(12), 121709 (2017).

12 W. Drexler, J. G. Fujimoto (Eds.), Optical Coherence Tomography: Technology and Applications, Springer Cham (2015). ISBN: 978-3-319-06418-5.

13 F. T. Nguyen, A. M. Zysk, E. J. Chaney, J. G. Kotynek, U. J. Oliphant, F. J. Bellafiore, K. M. Rowland, P. A. Johnson, and S. A. Boppart, "Intraoperative Evaluation of Breast Tumor Margins with Optical Coherence Tomography," Cancer Research 69(22), 8790–8796 (2009).

14 J. G. Sun, S. G. Adie, E. J. Chaney, and S. A. Boppart, "Segmentation and correlation of optical coherence tomography and X-ray images for breast cancer diagnostics," Journal of Innovative Optical Health Sciences 6(02), 1350015 (2013).

15 E. A. Rank, A. Agneter, T. Schmoll, R. A. Leitgeb, and W. Drexler, "Miniaturizing optical coherence tomography," Translational Biophotonics 4(1–2), e202100007 (2022).

16 J. Sancho-Durá, K. Zinoviev, J. Lloret-Soler, J. L. Rubio-Guviernau, E. Margallo-Balbás, and W. Drexler, "Handheld multi-modal imaging for point-of-care skin diagnosis based on akinetic integrated optics optical coherence tomography," Journal of Biophotonics 11(10), e201800193 (2018).

17 R. M. Ruis, A. Leinse, R. Dekker, R. G. Heideman, T. G. van Leeuwen, and D. J. Faber, "Decreasing the Size of a Spectral Domain Optical Coherence Tomography System With Cascaded Arrayed Waveguide Gratings in a Photonic Integrated Circuit," IEEE Journal of Selected Topics in Quantum Electronics 25(1), 1–9 (2019).
18 V. D. Nguyen, N. Weiss, W. Beeker, M. Hoekman, A. Leinse, R. G. Heideman, T. G. Van Leeuwen, and J. Kalkman, "Integrated-optics-based swept-source optical coherence tomography," Optics Letters 37(23), 4820 (2012).
19 G. Yurtsever, B. Považay, A. Alex, B. Zabihian, W. Drexler, and R. Baets, "Photonic integrated Mach-Zehnder interferometer with an on-chip reference arm for optical coherence tomography," Biomedical optics express 5(4), 1050 (2014).
20 G. Yurtsever, N. Weiss, J. Kalkman, T. G. van Leeuwen, and R. Baets, "Ultra-compact silicon photonic integrated interferometer for swept-source optical coherence tomography," Optics Letters 39(17), 5228 (2014).
21 B. I. Akca, B. Považay, A. Alex, K. Wörhoff, R. M. De Ridder, W. Drexler, and M. Pollnau, "Miniature spectrometer and beam splitter for an optical coherence tomography on a silicon chip," Optics Express 21(14), 16648 (2013).
22 X. Ji, X. Yao, Y. Gan, A. Mohanty, M. A. Tadayon, C. P. Hendon, and M. Lipson, "On-chip tunable photonic delay line," APL Photonics 4(9), 090803 (2019).
23 E. A. Rank, R. Sentosa, D. J. Harper, M. Salas, A. Gaugutz, D. Seyringer, S. Nevlacsil, A. Maese-Novo, M. Eggeling, P. Muellner, R. Hainberger, M. Sagmeister, J. Kraft, R. A. Leitgeb, and W. Drexler, "Toward optical coherence tomography on a chip: in vivo three-dimensional human retinal imaging using photonic integrated circuit-based arrayed waveguide gratings," Light: Science & Applications 10, 6 (2021).
24 E. A. Rank, S. Nevlacsil, P. Muellner, R. Hainberger, A. Maese-Novo, M. Duelk, S. Gloor, M. Voelker, N. Verwaal, G. Meinhardt, M. Sagmeister, J. Kraft, P. Morrissey, M. Jezzini, Z. Quan, P. O'Brien, S. Richter, M. Kempe, D. Seyringer, and W. Drexler, "Spectral domain and swept source optical coherence tomography on a photonic integrated circuit at 840nm for ophthalmic application," in European Conference on Biomedical Optics, Munich, Germany, 11078_29 (2019).
25 S. Nevlacsil, P. Muellner, A. Maese-Novo, M. Eggeling, F. Vogelbacher, M. Sagmeister, J. Kraft, E. Rank, W. Drexler, and R. Hainberger, "Multi-channel swept source optical coherence tomography concept based on photonic integrated circuits," Optics Express 28(22), 32468 (2020).
26 L. Chang, N. Weiss, T. G. Van Leeuwen, M. Pollnau, R. M. De Ridder, K. Wörhoff, V. Subramaniam, and J. S. Kanger, "Chip based common-path optical coherence tomography system with an on-chip microlens and multi-reference suppression algorithm," Optics Express 24(12), 12635 (2016).
27 R. V. Kutluyarov, D. M. Fatkhiev, G. S. Voronkov, and A. K. Sultanov, "Devices for backscattered and reflected signals processing based on integrated photonics," SPIE Proceedings 11516, 115160X (2020).
28 S. Song, J. Xu, S. Men, T. T. Shen, and R. K. Wang, "Robust numerical phase stabilization for long-range swept-source optical coherence tomography," Journal of Biophotonics 10(11), 1398–1410 (2017).
29 K. S. Park, E. Park, H. Lee, H.-J. Lee, S.-W. Lee, and T. J. Eom, "Phase stable swept-source optical coherence tomography with active mode-locking laser for contrast enhancements of retinal angiography," Scientific Reports 11(1), 16636 (2021).
30 M. Burla, L. R. Cortés, M. Li, X. Wang, L. Chrostowski, and J. Azaña, "Integrated waveguide Bragg gratings for microwave photonics signal processing," Optics Express 21(21), 25120–25147 (2013).
31 Y. Liu, A. Wichman, B. Isaac, J. Kalkavage, E. J. Adles, T. R. Clark, and J. Klamkin, "Tuning Optimization of Ring Resonator Delays for Integrated Optical Beam Forming Networks," Journal of Lightwave Technology 35(22), 4954–4960 (2017).
32 A. Melloni, A. Canciamilla, C. Ferrari, F. Morichetti, L. O'Faolain, T. F. Krauss, R. De La Rue, A. Samarelli, and M. Sorel, "Tunable Delay Lines in Silicon Photonics: Coupled Resonators and Photonic Crystals, a Comparison," IEEE Photonics Journal 2(2), 181–194 (2010).
33 M. Rahim, P. Akkary, N. Jamaleddine, F. Nabki, and M. Menard, "An integrated silicon-on-insulator continually tunable optical delay line for optical coherence tomography," in 2013 IEEE 56th International Midwest Symposium on Circuits and Systems (MWSCAS), Columbus, OH, USA, 709–712 (2013).
34 J. Liu, S. Cristoloveanu, and J. Wan, "A Review on the Recent Progress of Silicon-on-Insulator-Based Photodetectors," Physica Status Solidi (a) 218(14), 2000751 (2021).
35 Y. Fei, L. Zhang, T. Cao, Y. Cao, and S. Chen, "Ultracompact polarization splitter–rotator based on an asymmetric directional coupler," Applied Optics 51(34), 8257 (2012).
36 L. B. Soldano, E. C. M. Pennings, "Optical multi-mode interference devices based on self-imaging: principles and applications," Journal of Lightwave Technology 13(4), 615–627 (1995).
37 J. D. Domenech, J. S. Fandino, B. Gargallo, and P. Munoz, "Arbitrary Coupling Ratio Multimode Interference Couplers in Silicon-on-Insulator," Journal of Lightwave Technology 32(14), 2536–2543 (2014).
38 "2X2 Fiber Optic Coupler 1310nm/1550nm Single Mode Double Window Fiber Splitter FC/UPC," Civil Laser (accessed 29 June 2023). [https://www.civillaser.com/index.php?main_page=product_info&products_id=2531].

39 "F-CPL-B22355-FCUPC Optical Fiber Coupler," Newport (accessed 29 June 2023). [https://www.newport.com/p/F-CPL-B22355-FCUPC].
40 "G&H Products: Fiber Optics: 850, 1060, 1300 nm Extended Wideband OCT Coupler (EWOC)," G&H (accessed 29 June 2023). [https://gandh.com/products/fiber-optics/wideband-couplers/850-1060-1300-nm-extended-wideband-oct-coupler-ewoc].
41 "1310 nm, 2x2 Single Mode Fused Fiber Optic Couplers/Taps," (accessed 29 June 2023). [https://www.thorlabs.com/newgrouppage9.cfm?objectgroup_id=8461].
42 J. Zheng, Z. Fang, C. Wu, S. Zhu, P. Xu, J. K. Doylend, S. Deshmukh, E. Pop, S. Dunham, M. Li, and A. Majumdar, "Nonvolatile Electrically Reconfigurable Integrated Photonic Switch Enabled by a Silicon PIN Diode Heater," Advanced Materials 32(31), 2001218 (2020).
43 M. A. Tran, C. Zhang, T. J. Morin, L. Chang, S. Barik, Z. Yuan, W. Lee, G. Kim, A. Malik, Z. Zhang, J. Guo, H. Wang, B. Shen, L. Wu, K. Vahala, J. E. Bowers, H. Park, and T. Komljenovic, "Extending the spectrum of fully integrated photonics to submicrometre wavelengths," Nature 610(7930), 54–60 (2022).
44 R. Soref, "Tutorial: Integrated-photonic switching structures," APL Photonics 3(2), 021101 (2018).
45 D. Melati, A. Waqas, Z. Mushtaq, and A. Melloni, "Wideband Integrated Optical Delay Line Based on a Continuously Tunable Mach–Zehnder Interferometer," IEEE Journal of Selected Topics in Quantum Electronics 24(1), 1–8 (2018).
46 X. Wang, H. Qi, X. Hu, Z. Yu, S. Ding, Z. Du, and Q. Gong, "Advances in Photonic Devices Based on Optical Phase-Change Materials," Molecules 26(9), 2813 (2021).
47 J. Faneca, S. Garcia-Cuevas Carrillo, E. Gemo, C. R. De Galarreta, T. Domínguez Bucio, F. Y. Gardes, H. Bhaskaran, W. H. P. Pernice, C. D. Wright, and A. Baldycheva, "Performance characteristics of phase-change integrated silicon nitride photonic devices in the O and C telecommunications bands," Optical Materials Express 10(8), 1778 (2020).
48 M. Ahmed, Y. Al-Hadeethi, A. Bakry, H. Dalir, and V. J. Sorger, "Integrated photonic FFT for photonic tensor operations towards efficient and high-speed neural networks," Nanophotonics 9(13), 4097–4108 (2020).
49 S. Kumar Bag, S. K. Varshney, "Ultrawide FSR microring racetrack resonator with an integrated Fabry–Perot cavity for refractive index sensing," Journal of the Optical Society of America B 38(5), 1669 (2021).